CLEARINGHOUSE FOR FEDERAL SCIENTIFIC AND TECHNICAL INFORMATION CFSTI
DOCUMENT MANAGEMENT BRANCH 410.11

LIMITATIONS IN REPRODUCTION QUALITY

ACCESSION # AD 605289

☒ 1. WE REGRET THAT LEGIBILITY OF THIS DOCUMENT IS IN PART UNSATISFACTORY. REPRODUCTION HAS BEEN MADE FROM BEST AVAILABLE COPY.

☒ 2. A PORTION OF THE ORIGINAL DOCUMENT CONTAINS FINE DETAIL WHICH MAY MAKE READING OF PHOTOCOPY DIFFICULT.

☐ 3. THE ORIGINAL DOCUMENT CONTAINS COLOR, BUT DISTRIBUTION COPIES ARE AVAILABLE IN BLACK-AND-WHITE REPRODUCTION ONLY.

☐ 4. THE INITIAL DISTRIBUTION COPIES CONTAIN COLOR WHICH WILL BE SHOWN IN BLACK-AND-WHITE WHEN IT IS NECESSARY TO REPRINT.

☐ 5. LIMITED SUPPLY ON HAND: WHEN EXHAUSTED, DOCUMENT WILL BE AVAILABLE IN MICROFICHE ONLY.

☐ 6. LIMITED SUPPLY ON HAND: WHEN EXHAUSTED DOCUMENT WILL NOT BE AVAILABLE.

☐ 7. DOCUMENT IS AVAILABLE IN MICROFICHE ONLY.

☐ 8. DOCUMENT AVAILABLE ON LOAN FROM CFSTI (TT DOCUMENTS ONLY).

☐ 9.

NBS 9/64

PROCESSOR: GL

Proceedings of the

FLUID AMPLIFICATION SYMPOSIUM

May 1964

Volume IV

H·D·L

HARRY DIAMOND LABORATORIES

FORMERLY: DIAMOND ORDNANCE FUZE LABORATORIES

ARMY MATERIEL COMMAND

WASHINGTON 25, D. C.

UNITED STATES ARMY MATERIEL COMMAND
HARRY DIAMOND LABORATORIES
WASHINGTON 25, D.C.

PROCEEDINGS OF THE
FLUID AMPLIFICATION SYMPOSIUM

Sponsored by the Harry Diamond Laboratories
26, 27, and 28 May 1964

Volume IV

CONTENTS

ATTACHMENT OF A JET TO A CURVED WALL.

by M. KADOSCH

1) Historical Account :

The physical phenomena applied in fluid amplifiers have been known for a very long time.

For instance, the phenomenon of attachment of a jet to a side wall at an angle with the normal exit direction of the jet was described by Young (1) as soon as 1800 : it was for that reason called "Young effect", in that country. The phenomenon of attachment to a plane or curved wall (for example, the contour of a bottle) is again described by H. Bouasse (2) and mathematically studied by L.C. Woods (3). Other ancient references are cited in the bibliography of the article (4).

In the years 1948-1950, a group of engineers of the "Société Nationale d'Etudes et de Construction de Moteurs d'Aviation" discovered the remarkable properties of the phenomenon obtained by combining the interference of a small obstacle or of an auxiliary transverse jet forming a fluid screen on a side of the main jet, with the phenomenon of attachment to a wall placed on the opposite side of this jet when this wall is curved (5) for applications, the chief properties were the following : by making the action of the material or fluid screen vary, the jet was deflected through attachment at a variable angle in a stable configuration ; by suppressing the screen action, the jet resumed a normal non-deflected outline ; finally and principally, the phenomenon was freed from the scale effect ; it could be used on the jet of the biggest jet engines. Consequently, the devices studied and developed by these engineers were mostly conceived with a view to the braking (thrust reverser) to the piloting (thrust vector control) of jet engines At the same time, the basic physical phenomena were studied in detail theoretically and experimentally, but the emphasis was laid particularly on the thrust, drag and lift properties

Our aim in this paper is to set forth what we have found, which, being directly applicable to fluid amplifiers remains of prevailing interest. Thus we hope to have given a satisfactory theoretical explanation, well supported by experi-

mental evidence, of the phenomena we were using. The ability of deviating the jet of a big jet engine is not perhaps fundamentally important for fluid amplifiers, but it is interesting to note that the schemes we were led to study thoroughly, somewhat differ from those which were selected for the fluid amplifiers with which we have been acquainted.

However, some parallelism could be drawn between the studies relating more particularly to propulsion and those peculiar to amplifiers ; for example one of the main features of our devices might be described as a momentum gain in a one-stage fluid amplifier.

In thrust vector control of rockets, a ratio of lateral thrust to controlling jet momentum in the range of 2, 5 to 3 is achieved.

In thrust reverser operation on jet engines the gain may be defined as the difference between forward thrust and reversed thrust divided by the momentum which would have been obtained from the controlling mass-flow if not bled off the compressor ; in actual such thrust reversers operating on jet planes this gain was between 10 and 30.

Finally, for the transformation of a continuous flow into a pulsating flow, we were led as soon as 1952, to propose and build laboratory models for a device much similar with that known under the name of "fluid flip-flop" except that its application was contemplated chiefly for propulsion systems (5).

Under such prospects, we hope to do useful work by resuming the description of the schemes to which we have been led, in terms adapted to fluid amplifiers. Thus we hope to show a possible way of progress and also that a satisfactory physical description of the used phenomena could be obtained.

2) Means of acting on a jet direction.

In order not to stay in abstractions, here are simple experiments effected in the years 1948-1950, relating to the combination of both means : deviation of a jet by an obstacle or a transverse jet, attachment to a curved or convex wall.

2) 1. Experiment n° 1

A De Laval nozzle was used : viz. a converging nozzle followed by a diverging venturi. Incidentally, this device is the fluid analogue of a detector : if run through in the usual direction (figure 1), the mass-flow is proportional to the exit section AB in subsonic flow ; if run through in the reverse direction (figure 2), the mass-flow is proportional to the section at throat CD, for the flow separates from the walls very close to CD ; in CD the pressure is much lower than the atmospheric pressure. Now if, in the reverse flow, a small obstacle is placed a little after throat CD (figure 3), on a part of the circumference, it causes a pressure unbalance and the jet comes and flattens itself on the remaining part. The deviation is very great. Both flows, figure (2) and (3), are stable ; the passage from the one to the other is of the flip-flop type.

2) 2. The purpose of Experiment n° 2, due to J. Bertin, is to show that the jet-wall interaction is reciprocal. Suppose that the De Laval nozzle figure 1 be two-dimensional and that parts CE and DF may revolve freely round small axes respectively in C and D. It may be shown that the pressure distribution results in bringing considerably closer together the mobile parts. In figure 5, only a part CE was set free ; it takes an equilibrium position when the resulting moment of the pressures round C vanishes (figure 4). This equilibrium position is also stable, with a jet strongly deflected round the immobilized wall and a very narrow passage section, obtained without blockage, since the sucked in wall is free with a horizontal motion.

2) 3. Experiments n° 3 and 4

In two-dimensional flow, figures 6 and 7 show the deviation obtained by combining a convex wall on the left and a transverse jet on the right ; on figure 6, it is noted that the convex wall has a radius such that if it acts alone, it produces a negligible deviation (no Young effect). The action of the jet causes a progressive deviation.

The existence of a critical wall radius, allowing this experiment is demonstrated in the following paragraph.

We think, to the best of our knowledge, that its systematic utilization in the way described below constitutes the main difference between the known schemes of fluid amplifiers, even if curved walls are present, and the schemes which we have studied and used.

3) A few explanations and physical descriptions.

The theoretical and experimental study of the former phenomena has formed the subject of other published works (4) (6) (7), to which we refer for the detail of our experimental results, mainly as concerns the variation of the curvature radius given to the convex attachment wall. The theoretical considerations given below have been worked out with a view to explaining these experiments.

3) 1. Balance of a curved flow.

In our mind, the purpose of the convex wall is to ensure the balance of a deflected flow from the start.

In aerodynamic terms, a jet driven sideways presents itself as a quasi-isentropic stream comprised between two adjacent zones of dissipative flow : boundary layer, or zone of mixing with the surrounding fluid. If two or more flow configurations exist, one of them at least is a curved flow. The essential condition of its stability is the condition of transverse balance, expressing that the centrifugal forces are balanced by a transverse pressure gradient (fig. 8) :

$$\frac{1}{\rho}\,\frac{\partial p}{\partial n} = \frac{v^2}{R}$$

3) 1.1. In the isentropic part of the stream, we moreover have :

$$dp + \rho v\, dv = 0$$

whence a partial intégration along the normal line IE crossing the stream is deduced :

$$v_I = v_E \exp \int_I^E \frac{dn}{R}$$

These inequalities (higher velocity and lower pressure on the wall) justify the presence of a convex wall which helps them to be checked.

Moreover, the velocity, or pressure difference is an increasing function of $\frac{h}{R_I}$, where h = IE, stream thickness.

3) 1.2. In the boundary layer along the wall, the fluid is slowed down, and the jet separates when the pressure reaches the surrounding pressure. If p_E is also the surrounding pressure, it will be noted that the boundary layer is subject to reascend a longitudinal difference of pressure $(p_E - p_I)$ equal to that which one will have managed to establish crosswise : in other words, the better the jet is attached in I, the more easily it separates farther on.

3) 1.3. This well-known description of the transverse balance of an isentropic stream accounts insufficiently, however, for the phenomenon of attachment to a curved wall, which necessitates the calculation of the longitudinal gradient. To this effect, a calculation of L.C. Woods (3) is used.

Consider figure 9 : At point M, where velocity v is at angle θ with the horizontal, it is admitted that the velocity potential is proportional to θ :

$$\varphi = \bar{v}\, r\theta = \frac{\theta}{\gamma}\varphi_D$$

$v = v_a$ in D, D', O'. $\bar{v}$, velocity mean value. It is then found that the velocity is given by the formulas :

$$v = v_a \exp\frac{\gamma u}{\sigma}$$

$$\cos u \cosh \sigma = \cosh \sigma \frac{\theta}{\gamma}$$

$$\sigma = \frac{\pi}{2}\frac{\bar{v}}{v_a}\frac{r\gamma}{h}$$

Parameter σ, whereon the velocity depends, is proportional to $\frac{r\gamma}{h} = \frac{OD}{OO'}$; it is, on the one hand, the aspect ratio of the attached part, on the other hand, the approximate ratio of the transverse gradient to the longitudinal gradient, on account of the important property of § 3. 1.2.

The longitudinal gradient is expressed by :

$$-v\frac{dv}{r\,d\theta} = \frac{V_a^2}{r}\exp\frac{2\gamma u}{\sigma}\ \text{cotang}\,u\ \tanh\sigma\frac{\theta}{\gamma}$$

By means of these formulas it is possible to link up the result of the tests with the behaviour of the isentropic stream.

3) 1.4. The most important conclusion of the tests is that, if the ratio $\frac{r}{h}$ varies, three flow conditions appear :

1) $r < 3\,h$ approximately. The jet is attached on a constant arc $\gamma_1 =$ 20 degrees approximately and is not deflected. The wall action is purely local (see fig.7).

In that case, σ is small enough, of order unity or less. The theoretical distribution of pressures at the wall is indicated by the pointed curve of figure (10). We approximately get :

$$v = v_a \exp\sqrt{\gamma^2-\theta^2}$$

The velocity neither depends on h, nor on r, nor even on $\bar{v}$, but only on the angles. It is uniform as soon as we move a little aside from the wall. The longitudinal gradient which the boundary must reascend cannot be calculated in D, where it is infinite, but at some point of arc OD, for example such as : $\theta = 0{,}8\,\gamma$

It is made non dimensional by being plotted against the length $l = r\,\gamma$ covered : $g = -\frac{v\,dv}{V_a^2}\frac{l}{r\,d\theta}$

$g_1 = \frac{4}{3}\gamma\exp(1{,}2\gamma)$ at point M.

The gradient increases with according to γ and its maximum value is $0{,}7$.

2) $r > 3\,h$. As soon as σ reaches such a value that the previous approximations are no longer satisfactory, it is theoretically found (figure 10) that the pressure curve is much more flattened, and, experimentally, that a true deviation appears, the effect of which is to increase still more the value of σ proportional to $\frac{r\gamma}{h}$.

The aspect ratio of the attached part of stream increases rapidly and conditions n° 3, very different from n° 1, are obtained.

3) Young effect. If $\frac{r}{h}$ and γ increasing separately, factor σ takes a high value, the transverse gradient is much bigger than the longitudinal gradient and the pressure curve (fig. 10) is so much flattened that the velocity does not vary over most of the length r_γ. The exponential interference of σ leads to the approximation :

$$u \# \frac{\pi}{2} \qquad v = v_a \exp \frac{h}{r}$$

This time the velocity depends only on h and not on θ, nor on γ.

Therefore, there is not only jet attachment, but overall deviation, the deviation phenomenon being defined by the fact that the wall action extends to the whole width of the jet, according to the law of velocity, and produces an increase of the attachment, which may be considerable.

The longitudinal gradient may be approximated by :

$$g_2 \# \gamma \exp 2\frac{h}{r} \exp \sigma\left(\frac{\theta}{\gamma} - 1\right)$$

It fades exponentially as a function of $(\frac{-r}{h})$; its theoretical value may be as low as 10^{-3} g_1. This exponential factor in $(\frac{-r}{h})$, which cannot be deduced from elementary considerations, annihilates the increase proportional to γ, which allows the effect of attachment to the curved wall.

3) 1.5. Comparison with the attachment on a flat wall.

In order to illustrate the preceding calculation, figure 11 represents a plane plate of length $\frac{1}{2}$l, to which a jet portion is attached, with an aspect ratio $\frac{l}{2h}$ constant. In the formulas, if r tends to the infinite and γ to zero, naturally $v = v_a$ is constant and gradient g is null.

Case n° 1. Low $\frac{l}{2h}$

If length $\frac{1}{2}$ l is curved at radius r, the jet remains attached up to a 20 degrees angle, then it separates, under the influence of gradient g_1.

Case n° 2. High $\frac{l}{2h}$.

If length $\frac{1}{2}$ l is curved at radius r, the jet may be

deflected practically to any angle, for gradient g_2 remains very small. The attachment phenomena is similar to that along a plane wall.

3) 2.0. Application to the above-described tests.

In most of the devices capable of being turned to account, r has a fixed value. The former mathematical description subordinates the attachment to the product $\frac{r\gamma}{h}$. In the quoted tests, r has a value such that the attachment does not occur when there is no external action : the jet sticks locally on a nearly constant arc : $\gamma_1 \# 0{,}35$ radian or 20 degrees ; and $r\gamma_1 < h$; the jet is not deflected ; parameter σ is of order unity, as in the 1st case above.

In all the tests, the primary effect of the external action is to create : a) a beginning of transverse unbalance, whence a small increase of γ of the "vector thrust control" type ; b) a beginning of decrease of h, whether or not due to a blockage resulting from control input. The important fact is that both effects contribute to increase σ, to decrease exponentially the resistance to attachment, therefore to increase γ still more, which results in a quick passage to the 2nd case above, where $r\gamma_2 \gg h$, σ ranging about 10.

In the experiment of figures (6) and (7), the variation of the attachment angle γ between γ_1 and γ maximum is progressive as function of the input ; the necessary input for the maximum deviation is a small fraction of the main mass-flow, on account of the exponential vanishing of the resistance to attachment, which also explains the possibility of flip-flop operations.

3) 3. Physical description

The former theory, although perfectly in accordance with experience, will perhaps appear sophisticated and little propitious to a correct description of boundary layers ; therefore, a physical interpretation of the formulas introduced, founding on conventional reasonings (8) (9), is given.

Consider (figure 12a) the balance of the non-deflect jet ; let us introduce a perpendicular blow (figure 12b), which deflects the jet, first by thrust vector control, and let us analyse the transient phenomena. If a fluid element of the isentropic stream is offset transiently by this action towards the inside of the boundary layer, it finds itself submitted there to a centrifugal force unbalanced by a pressure gradient, and therefore returns to the isentropic zone ; conversely, a slowed down element of boundary layer offset into the isentropic zone, without sufficient centrifugal force, would fall back into the boundary layer. Consequently, the new flow is stable and the thickness of the boundary layer is smaller, since the exchange of momentum between slow fluid and quick fluid is reduced by the primary deviation, which produces the additional deviation χ by recession of the separation point. On the side of the blow, on the contrary, the mixing zone between the isentropic stream and the surrounding gas tends to amplify itself by the transient offsets which do not die ; whence an increase of the vortex flux in AA', whereas it decreases along the convex wall ; both these effects contribute to bring about a circulation (and a lateral thrust), of which deviation χ is the index and which tends to decrease the velocities in AA' ; deviation χ stops when the vortex flux in AA' stops increasing thereby. Moreover, in the aspect ratios allowing Young effect, the mixing zone is strongly sucked in towards the curved wall, because the transverse field of pressures reaches the whole width h. The test figure (5) shows what occurs when the mixing zone is partly suppressed ; the main obstacle to deviation being suppressed, the jet evolves towards a deflected configuration with an appropriate similitude ratio.

This description is interesting because in an elbow the contrary may happen (fig.13) ; the boundary layer at the convex wall tends to thicken through accumulation of the slowed down fluid which starts a secondary flow along side walls, if there is no way for it to escape somewhere, as in figure (12).

The secondary flow will tend to occur if the side walls of the fluid amplifier are sufficiently near, so that fluid may flow from one wall to the other. The interference of a side aspect ratio has already been noticed by fluid amplifiers constructors.

4. Conclusions

In the applications to propulsion, as in those to fluid amplifiers, the phenomenon of attachment to a wall is first felt as an obstacle, if it is not controlled or controllable. The most often cited means of controlling in fluid amplifiers consists in bringing fluid between the wall and the jet to impede the low pressures created in the confined zones. We have had to use similar processes in the applications to propulsion, in order to impede the thrust losses in normal operation, and with a view to a better control of the deviation in reverse operation.

However, we have always deliberately used the wall curvature to impede attachment, so that it may occur only through the use of a control input. The results obtained in this direction have been recalled to mind and submitted for reflexion to the new users of these phenomena.

BIBLIOGRAPHY

(1) Young (T.) "Outlines of Experiments and Inquiries Respecting Sound and Light" (16 January 1800) Quoted by J.L. Pritchard :"The Dawn of Aerodynamics" Journal of the Royal Aeronautical Society, March 1957.

2) Bouasse (H.) Tourbillons (Delagrave, Paris) 1931, pp. 341, 347.

3) Woods (L.C.) Compressible Subsonic flow in two-dimensional Channels with mixed boundary conditions. The Quarterly Journal of Mechanics and Applied Mathematics, September 1954, VII, 263.

4) Kadosch (M.). Déviation des jets par adhérence à une paroi convexe. Le Journal de Physique et le Radium April 1958, XIX.

5) U.S. Patents n° 2,702,986
2,793,493
3,048,974
2,825,204

6) Kadosch (M.) Mécanisme de la Déviation des Jets Propulsifs D.Thesis, Paris, 5 January 1957 (Publications Scientifiques et techniques du Ministère de l'Air, n° BST 124)

7) Bertin (J.) and Kadosch (M.). Principes et Applications de la Striction Axiale et Directionnelle. Bulletin de la Société Française des Mécaniciens, 1958, n° 24.

8) Goldstein (S.). Modern Developments in Fluid Dynamics. 1938

9) Crocco (L.) and Lees (L.). A mixing theory for the interaction between dissipative flows and nearly isentropic streams. Journal of the Aeronautical Sciences, October 1952, XIX, pp. 649-676.

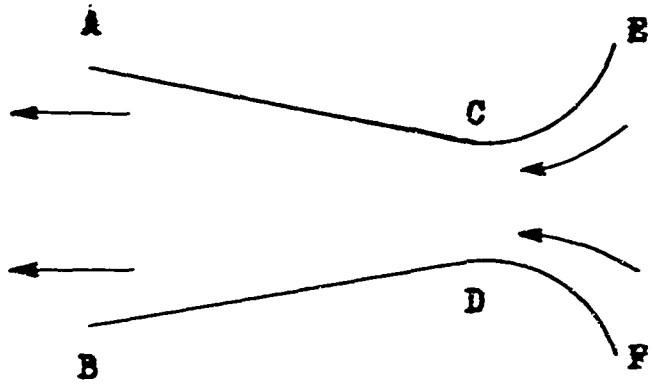

Fig. 1

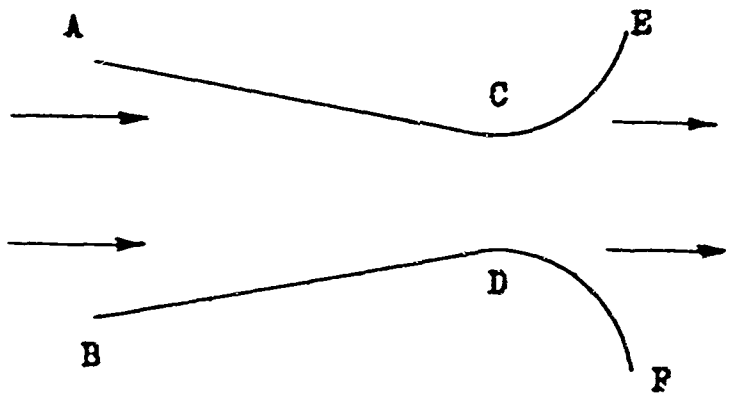

Fig. 2

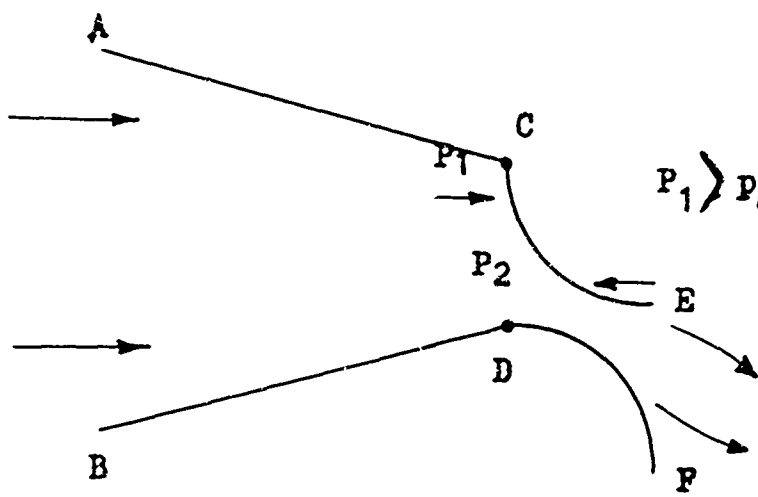

$P_1 \rangle P_a \rangle P_2$

Fig. 4

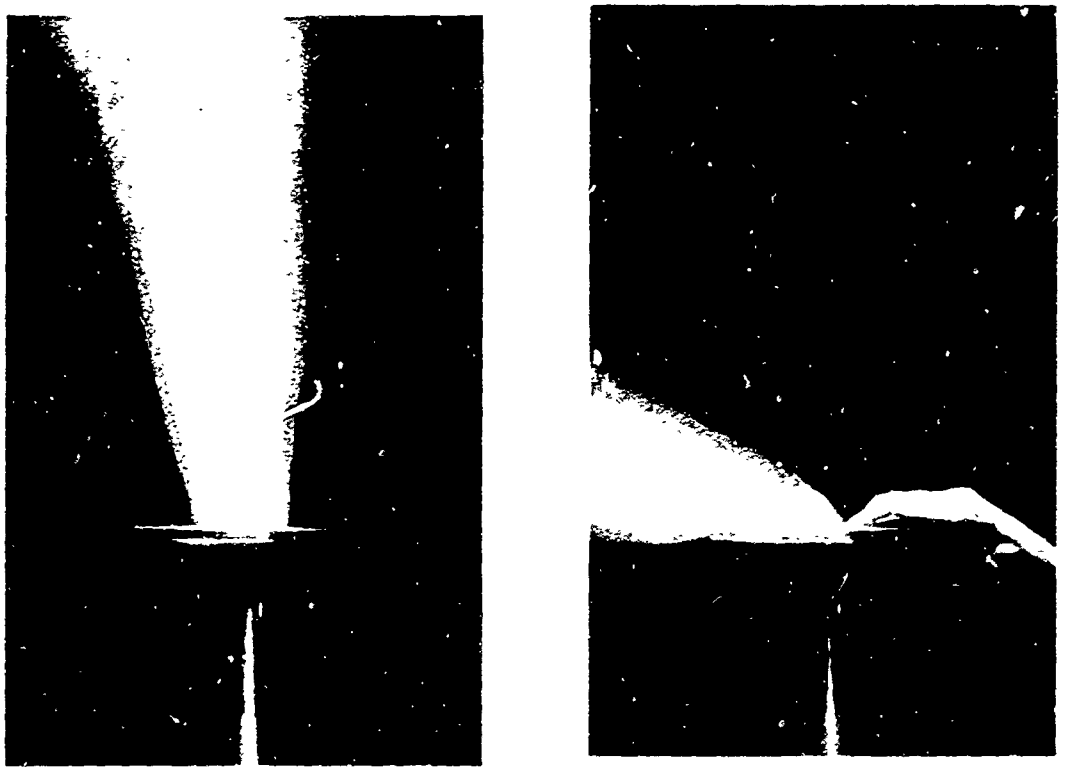

fig-3

fig. 5

fig. 6

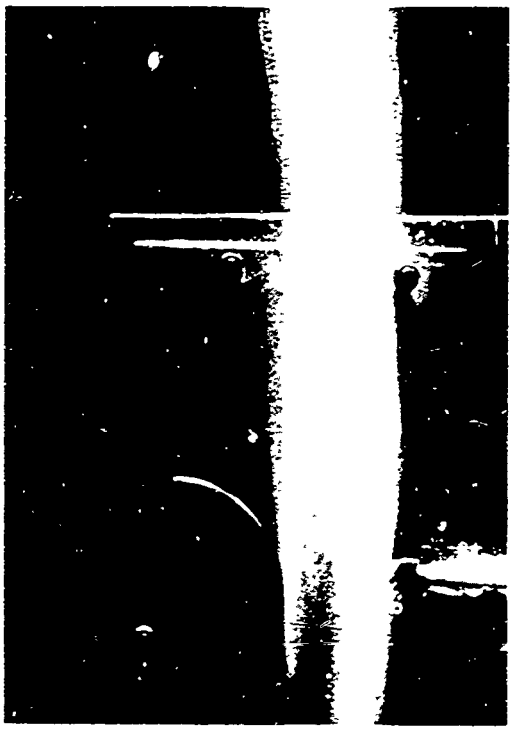

fig. 7

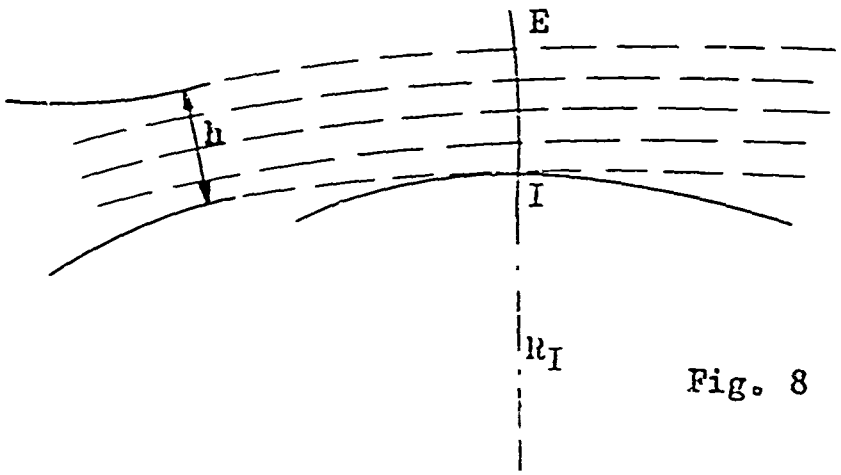

Fig. 8

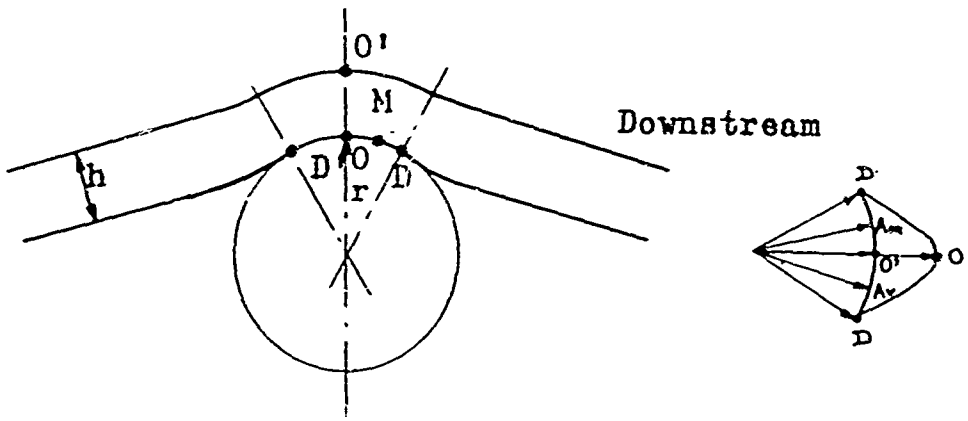

Fig. 9

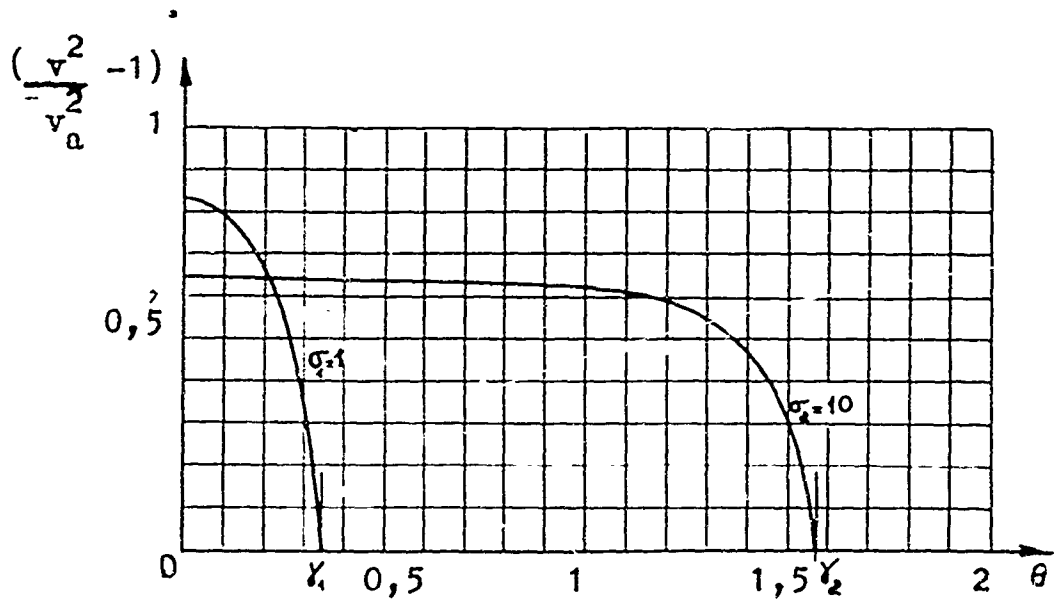

Fig. 10

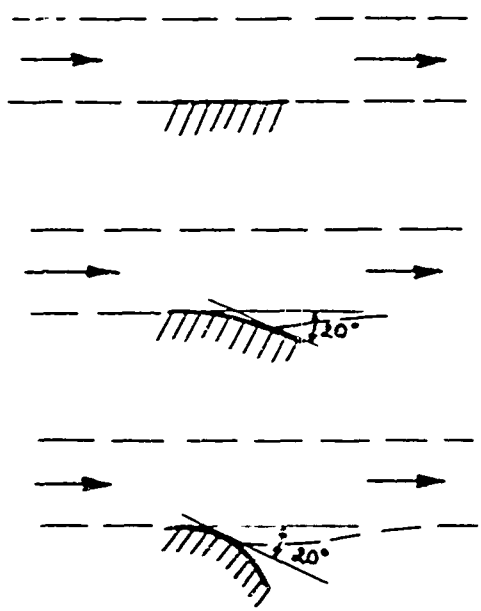

Fig. 11 a

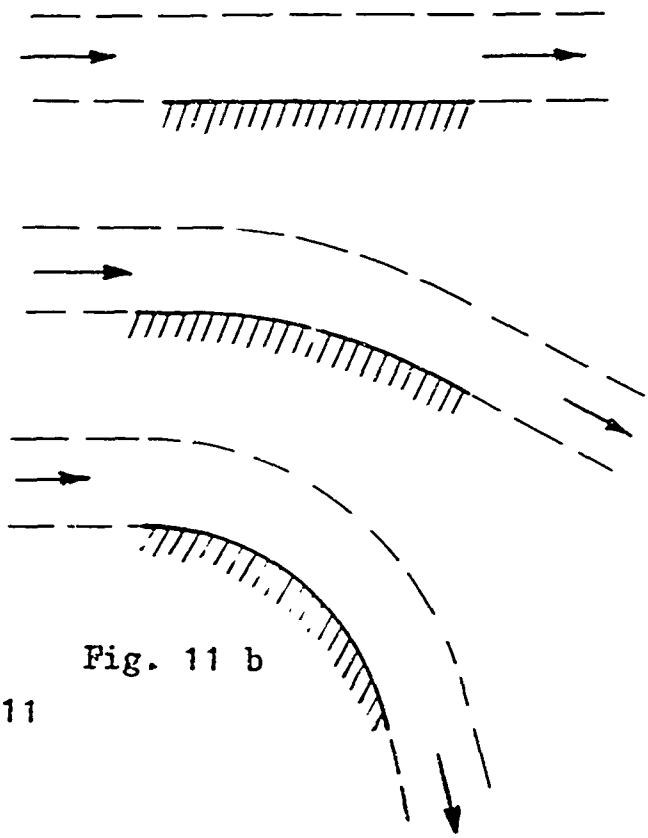

Fig. 11 b

Fig. 11

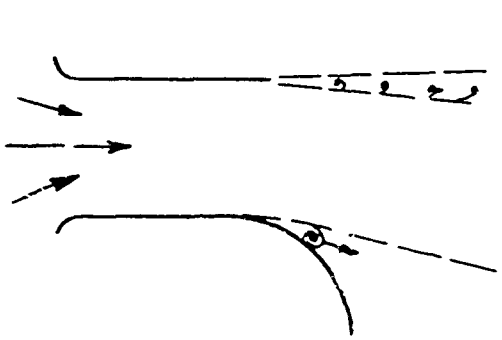

Fig. 12 a

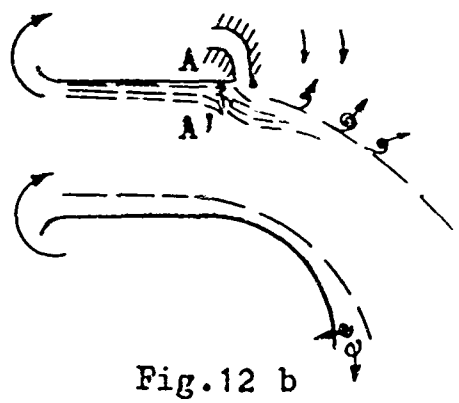

Fig.12 b

Fig. 12

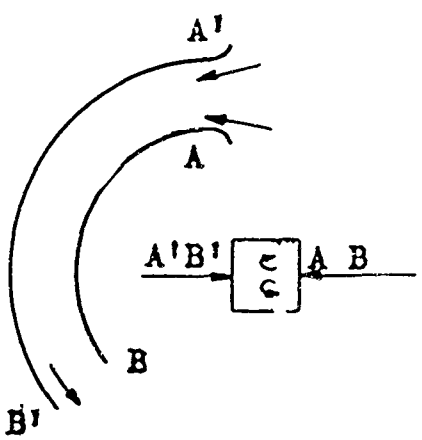

Fig. 13

SEPARATED FLOW IN CURVED CHANNELS WITH SECONDARY INJECTION[+]

by

H. A. Curtiss *
O. G. Feil **
D. J. Liquornik ***

Giannini Controls Corporation
Astromechanics Research Division
Malvern, Pennsylvania

Abstract

Injection of secondary fluid flow into a primary flow confined in a curved or straight channel is shown to be a powerful technique for use in fluid state amplification. The secondary injection continuously and progressively alters the separation characteristics of the confined primary flow, resulting in large proportional changes in the channel output flows. A fundamental experimental study of the method with incompressible, turbulent boundary layer flow in a range of varying curvature channels was conducted to learn about the flow characteristics and passage shape parameters relevant to proportional amplification. Several injection methods and velocities were investigated with the main emphasis on the effects of this injection on the flow characteristics within the channels. Preliminary analytical techniques which compared favorably with the experimental results were developed. An overall comparison of the mass flow and momentum gains obtainable for various injection and channel configurations is presented.

INTRODUCTION

When a secondary fluid is injected into the primary flow in a curved or straight channel, large changes in the resulting output flow characteristics are produced. These output flow changes result from alterations of separated flow boundaries within the channel which vary continuously and repeatedly as a function of the injection rate. Thus, the velocity distribution of the flow stream effluxing from the channel is redistributed, as a result of secondary injection such that the mass flow and stream momentum thru a fixed cross section of the channel exit vary proportionally with the injection flow rate. Since the secondary injection flow is

---

+ This work was carried out under the sponsorship of the United States Air Force Office of Scientific Research and forms the basis for AFOSR Scientific Report 64-0860.

* Chief, Applied Fluid Dynamics
** Staff Scientist
*** Director, Laboratory Services

substantially smaller than the primary stream flow, the net effect is an amplification; i.e., a large change in output flow with respect to a smaller input flow. Thus, the curved channel with secondary injection is itself a fluid state amplifier.

More importantly, the modulated channel output provides a basis for very large proportional flow amplification as exemplified in the Double Leg Elbow Amplifier [1,2*] concept. In this application the modulated channel output is combined with other flow phenomena in a single element configuration that has demonstrated differential flow gains of over 200. Such gains are far superior to those of any other reported fluid state proportional amplifier.**

Returning to a curved channel, we can visualize the effects of secondary injection in the typical sketch below. Here the channel is curved sufficiently that separation occurs without any injection on the inner wall with a boundary A-B and an exit velocity profile as indicated.

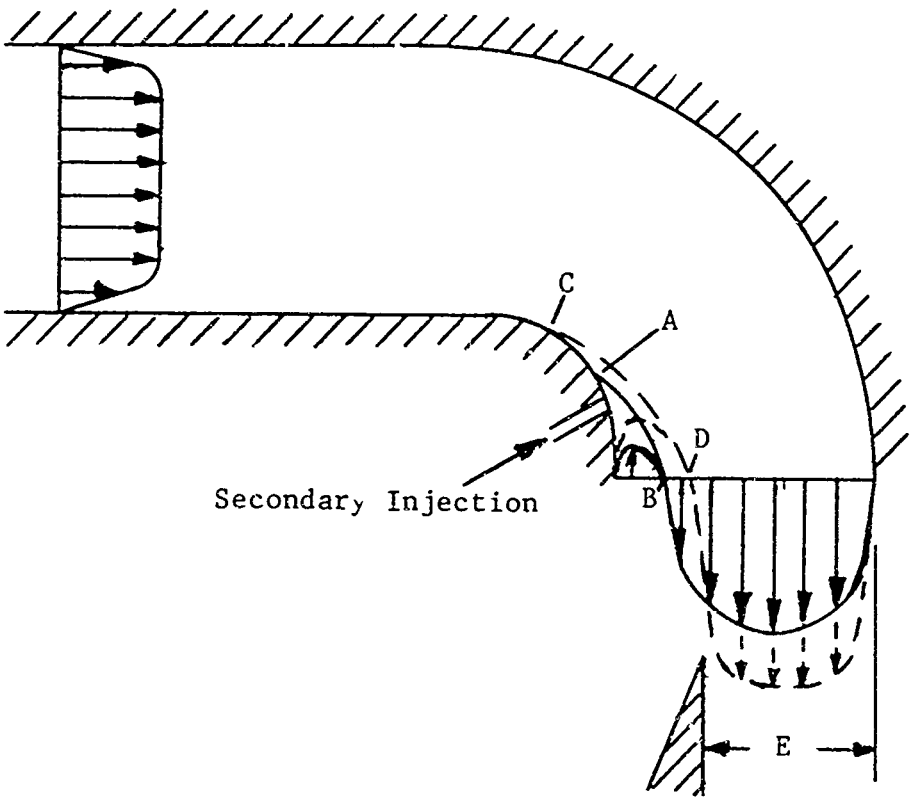

When secondary injection is applied, the separation boundary is changed to C-D and the resulting velocity profile is altered as shown. Through the region E above, the velocity and thus the mass, momentum, and energy flux change continuously in proportion to the secondary flow input.

* Superscripts refer to references at the end of the paper

** The authors are indebted to the Guidance and Control Branch of the Army Missile Command under the technical cognizance of Mr. T.G. Wetheral for sponsoring current studies in fluid state high gain amplifiers that utilize the methods described herein.

This paper is concerned with both the net results and the flow mechanisms involved in the above described phenomena. In our investigation we studied, both experimentally and theoretically, various channel curvatures, injection locations, injection directions, and channel aspect ratios. Several free stream velocities - all in the low speed or incompressible flow range-and a range of injection velocities were applied to the channels.

Before describing our work in this area, however, a word about prior results is in order. First, after a thorough search of the literature the authors could find no published work on the injection of a secondary flow into the separation region of a curved channel flow.

Next in importance, however, is our concern with the flow in channels of varying curvatures; particularly with relatively sharp bend radii where separation will occur naturally. In our experiments, the flows entering the channels were specifically arranged to have relatively thin turbulent boundary layers with a low turbulence core region. Again, however, existing literature in this area is also quite rare. In fact, no published theoretical work meeting these requirements is available, to the authors knowledge. All existing theory depends on one, or all, of three characteristics which do not apply for this work; i.e., exclusion of flow separation because of shallow turns, a fully developed inlet velocity profile, or a fully developed curved channel flow pattern (flow pattern independent of amount of turn).

On the other hand, some experimental work has been conducted on flow characteristics in rectangular curved passages, but again, most of it is not applicable for the same reasons mentioned above. The work of Hawthorne[3], Becker[4], and Brown and Marris[5] are in some ways applicable to this work although, in general, the curvatures were not as severe and channel aspect ratios were different than in the present investigation. Weske[6] conducted an extensive series of tests on sharp curvature bends but all of the upstream velocity profiles were fully developed except for one channel with a circular cross section.

In short, our investigation into curved channel separated flow with secondary injection was essentially started from scratch. The techniques we used for conducting the experimental portion of this program are described in the next section, which is followed by a theoretical development and analysis of the data in the remainder of this report.

EXPERIMENTAL TECHNIQUE

Models and Facilities

Five, two-dimensional, curved channels all of which are sketched in Fig. 1, were used for the experiments. Four of these channels, all with an aspect ratio (depth/width) of unity, were of different curvatures, as defined by the ratio of the inner radius to the outer radius (R). The curvatures ranged from straight (R = 1.0) to infinitely curved (R = 0). A fifth model with an aspect ratio of .208, but with the same radius ratio as one of the other channels (R = .4), was also utilized in these tests.

The models were, in general, instrumented with static pressure taps along the inner, outer, and bottom walls. Two methods of secondary injection were employed: (1) normal to the inner wall, or what we call cross flow at an angle, β, of 60 degrees from the turn (refer to Fig. 1 for symbol locations) and (2) parallel to the inner wall opposing the boundary layer of the primary flow, or what we call counter flow, at several β locations. The slots extended the full depth of the channel with a width of roughly .037 inches for all the injection slots. The width, w, for all channels was 1.2 inches. The table below summarizes the test configurations.

TABLE 1

R	h/w	r_{iw}	Cross flow location	Counter flow locations
0	1.0	0.0	zero radius	$\beta = 0$
0.2	1.0	0.3	$\beta = 60^o$	$\beta = 60^o$
0.4	1.0	0.6	$\beta = 60^o$	$\beta = 60,75$
0.4	0.208	0.8	$\beta = 60^o$	$\beta = 30,45,65,75$
1.0	1.0		$\frac{x}{w} = 1.4$ from exit	$\frac{x}{w} = 0.8$ from exit

An especially designed low turbulence plenum chamber supplied with dry, filtered air provided the input air for the channels. Six stages of screens in the plenum and a large contraction ratio assured the delivery of a relatively turbulence-free air, but with a turbulent boundary layer, to the test channels. The air was maintained at a constant temperature of $24^oC \pm 1^oC$ throughout the tests.

Fig. 2 shows the channels in some detail with their side plate removed, particularly the general arrangement of the cross flow injection slots. Fig. 3 shows a photo of the end of the plenum with the straight channel and the R = 0.4 curved channel attached in series. All of the curved channel tests were conducted in this arrangement with the straight channel providing the inlet except for the small aspect ratio channel which required a special adapter section.

Instrumentation

All static and pitot pressures were measured by means of a micro-manometer. Mass flow measurements of the secondary injection flow were obtained from differential pressure readings across a calibrated venturi. Velocity profiles were obtained both across and along each of the injection slots.

A fluorescent oil film technique[7] was used for boundary-layer flow visualization. This method consists simply of coating the walls of the channel with a light oil containing a fluorescent additive and observing

the oil film under an ultraviolet light. During a test, the air flow shear sweeps the oil along the surface such that the oil film develops a pattern indicative of the surface shear-intensity and direction.

Measurements of the local velocity and its angular direction were obtained by means of constant temperature hot wire anemometers with digital voltmeter readouts. All probes had tungsten wires 0.0002 inches in diameter and were approximately 0.040 inches long. The hot wires were calibrated at the beginning and end of each day's testing.

Local velocity measurements were made with single wire probes aligned so that the probe stem was approximately parallel to the mean flow direction. Boundary layer profiles were obtained by a long needle probe with the ends of the needles bent 90° to form a hook.

Local flow angle measurements were made by means of a hot wire anemometer X-probe using a unique method which is detailed in the Appendix. For the tests, the X-probe was attached to a watchmaker's lathe cross slide mounted on a movable, plexiglass channel sidewall as shown in Fig. 3. The X-probe was calibrated directly in this holder to establish the precise wire angles, θ_1 and θ_2. The local velocity and two-component angular direction were determined from the two voltage readings using the analysis described in the Appendix.

Inlet Flow Conditions

The straight channel was mounted directly to the inlet nozzle from the plenum chamber. In this nozzle, a boundary layer trip was placed downstream of the convergent section in order to fix the transition to turbulent boundary layers at a common location for all four walls. The velocity profiles at the nozzle exit were measured in order to determine the boundary layer parameters. For the curved channel tests, the straight channel was left in place as shown in Fig. 2 using it as an additional inlet section. Therefore, the velocity profiles measured at the exit of the straight channel give the inlet conditions for the curved channels. Fig. 4 shows these boundary layer profiles. The boundary layer parameters corresponding to all inlet boundary layer profiles are summarized in the following table:

TABLE 2

Straight Channel Inlet:

Ref. Inlet Velocity ft/sec	B.L. Thickness δ in.	Displacement Thickness δ_1 in.	Momentum Thickness δ_2 in.	Form Parameter $H = \delta_1/\delta_2$
25	0.10	.0061	.0051	1.19
50	0.13	.0107	.0087	1.23
100	0.13	.0127	.0097	1.31

TABLE 2 (Continued)

Curved Channel Inlet:

Ref. Inlet Velocity ft/sec	B.L. Thickness δ in.	Displacement Thickness δ_1 in.	Momentum Thickness δ_2 in.	Form Parameter $H = \delta_1/\delta_2$
25	0.19	.0257	.0182	1.42
50	0.15	.0140	.0108	1.29
100	0.15	.0121	.0100	1.23

The boundary layer velocity profiles shown in Fig. 4 were averaged for a number of profiles taken at each wall over a range of at least 1/2 channel width, excluding the immediate vicinity of the corners. The actual data points are not plotted for reasons of clarity; they showed a maximum scatter of $\pm$ 3% for the straight channel inlet and $\pm$ 1.5% for the curved channel inlet.

The Reynolds Number $(w\ u_o)/\nu$, used in these tests ranged from 1.5×10^4 to 6×10^4.

FLOW CHARACTERISTICS

Channel Flow Without Injection

1. STRAIGHT CHANNEL

The velocity distribution in the straight channel without injection was essentially uniform, except for the boundary layers on the walls. The boundary layers and their parameters are shown in Fig. 4 and in Table 2. It can be seen that for higher main stream velocities the changes of the boundary layer values are small. At lower velocities the boundary layer develops faster toward a "fully developed" velocity distribution in the channel as would be expected. The static pressure dropped almost linearly from a value of $\Delta P/q_o = 0.14$ at the inlet to zero at the exit of the straight channel.

2. CURVED CHANNEL

(a) Approximate Calculation of the Flow

The inlet velocity distribtuion shown in the previous section consists of a "potential flow core" with uniform velcotiy surrounded by boundary layers. The secondary flow which is always associated with real flow in curved channels is neglected in this first approximation; i.e., the flow is considered two-dimensional. The effect of curvature induced secondary flow is discussed later.

In all curved channels tested, the radii of curvature were small enough to cause flow separation at the inner wall. Although such a separation cannot be explained without consideration of the viscous forces acting mainly in the boundary layer, the assumption of inviscid, incompressible flow was made for a first approximate calculation of the flow configuration.

With the further assumption of uniform velocity distributions upstream of the curved channel and in the unstalled portion of the exit cross section, the size of the stalled exit area can be determined by the static pressure drop thru the channel. If this pressure difference is known from experiments, u_e can be calculated from Bernoulli's equation $p_o - p_e = \rho/2 \cdot (u_e^2 - u_o^2)$ and the exit flow area A_e is easily obtained from continuity.

To establish the separation boundary within the channel an assumption of the shape was made as will now be described. Since the channels considered here have a relatively strong curvature, the separation was assumed to start at the beginning of the curvature and a circular arc was used to connect this separation point with the point A_e marking the stalled exit area. The assumed circular arc starts tangentally from the straight part of the inner wall and therefore does not end perpendicular to the exit plane. In actuality, the separation point is located some distance downstream of the assumed location and the boundary of the stalled region will be as indicated by the dashed line in Fig. 5. However, the boundary layer can be expected to thicken upstream of the separation point, thus moving the "potential flow core" away from the wall and filling the wedge-shaped flow region bounded by the wall, the dashed line, and the assumed separation line.

Admittedly, the somewhat arbitrary way of establishing the separation line must fail for channels with very small radii of curvature as can be seen by considering the extreme case of a zero radius of curvature inner channel wall. In this case, the separation line would be a continuation of the upstream channel wall and at the same time would coincide with the exit plane.

This flow model is based on several significant simplifications and therefore cannot be expected to agree exactly with experimental data. However, it is questionable if further refinement based on the concept of two-dimensional flow, e.g., a boundary layer calculation to determine the separation point, would bring any significant improvement. The secondary flow due to the curvature might completely change the effects of the refinements. It is also undesirable to rely on more empirical data than necessary for this analysis since the applicability of the results would then be restricted by the limited range of geometrical configurations for which data are available. For the approximate calculation described here, only the static pressure difference between the inlet and exit of the channel need be known and this data can easily be obtained.

For the curved channels, the method described was used to determine the boundaries of the unstalled flow region. To determine the flow pattern within this region the potential flow distribution was calculated. This required a solution of the Laplace equation:

$$\frac{\partial^2 \Phi}{\partial x^2} + \frac{\partial^2 \Phi}{\partial y^2} = 0$$

where Φ is the flow potential ($u = \partial\Phi/\partial x$, $v = \partial\Phi/\partial y$). Except for simple geometric configurations and certain types of boundary conditions, it is

not possible to obtain a closed solution for the above equation. Of the graphical and numerical methods capable of a solution of the general case, the relaxation method is probably the best. A digital computer program * using over-relaxation was applied to determine the distribution of the stream function ($u = \partial\psi/\partial y$, $v = \partial\psi/\partial x$) in the channel. An example of a streamline pattern obtained by this method for channel R = 0.4 is shown in Fig. 5. From the streamlines, the velocities and static pressures can be calculated. To determine the pressure distributions along the walls, additional streamlines not shown in Fig. 5 were used. Their stream functions differed by 0.025 from the value for the inner wall (stream function 0.0) and the outer wall (stream function 1).

It should be noted that, although a potential flow solution is independent of the flow velocity, the method described here takes into account the variation of the inlet velocity, u_o, since a changed pressure drop in the channel (due to change of u_o) effects the size of the unstalled portion of the exit plane (A_e).

(b) Comparison with Experiments

The calculated unstalled flow boundary at the exit plane Ae using the pressure drop method is marked in the plot of measured velocity profiles which are described later (Fig. 17). The calculated boundary coincides reasonably well with the strong velocity gradient measured between the flow and the stalled region.

The solution for the unstalled flow region found by the described calculation method is compared with measured angular velocity directions, wall static pressure data, and exit velocity profiles in the paragraphs below.

The average flow directions as obtained from hot wire X-probe surveys along a perpendicular to the plane of curvature are indicated by the short straight lines in Fig. 5. The agreement with the directions of the streamlines is generally good.

The static pressure distributions along the inner and outer walls and across the bottom at $\beta = 50^\circ$ are shown in Fig. 6(a) in comparison with the calculated pressure. The calculated values along the side walls agree fairly well with the data. They all show higher values in the vicinity of the $\beta = 0$ position. This discrepancy could possibly be reduced by considering the increasing boundary layer thickness in that area. In the experimental data the pressure peak at the outer wall moves further downstream with decreasing radius of curvature, while the calculation does not show this effect. An improvement of the theoretical results could be obtained by assuming a non-uniform velocity distribution at the exit with decreasing velocities toward the outer wall. The measured exit velocity profiles (Fig. 16) show indeed, that the assumption of a uniform velocity distribution at the exit becomes less correct for decreasing radii of curvature.

The deviation between measured and calculated pressure distributions may also be partly due to the effect of the secondary flow. Such an effect is evident in the pressure distributions measured along a vertical line on

* The program was a slightly modified version of the one described in Ref. 8.

the outer wall, as described in section (c) below.

The pressure distribution across the channel for three channel curvatures at $\beta = 50^{o}$ is shown in Fig. 6(b). The calculation agrees very well with the data for the channel R = 0.4, but with poorer agreement, as expected, for the stronger curvature.

(c) Curvature Induced Secondary Flow Effects

The centrifugal forces resulting from flow in the curved channels creates a pressure field with increasing pressure toward the outer wall. The velocities in the boundary layers along the side walls are not large enough to balance these pressure forces. Therefore a circular motion called "secondary flow", is set up in a plane perpendicular to the channel walls. It forms two vortex type flows located symmetrically on both sides of the channel centerplane as shown in the sketch below.

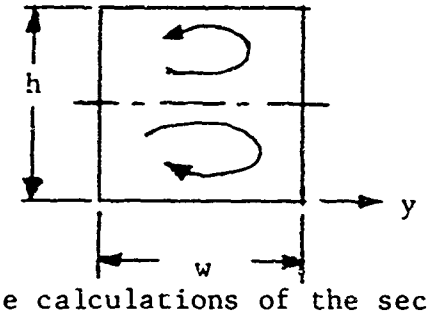

Attempts at quantitative calculations of the secondary flow, have been made but no complete general theory has been developed at this time. In the tests described here, the secondary and primary velocity components were calculated from flow angles measured by means of a hot wire anemometer X-probe. The disadvantage of this method is that the third flow component (z-component in this case) is included in both the u and v components. However, it can safely be assumed that the z-component is very small in the center portion of the unstalled flow region, a sufficient distance away from the outer wall, inner wall, and separation boundary, respectively. A typical primary and secondary profile is shown in Fig. 7 and a three dimensional representation of the same profiles is presented in Fig. 8. Near the channel exit, the secondary flow velocities outside the boundary layer reach values in the order of 10% of the reference inlet velocity, u_o, at the channel inlet.

Since the zero reference direction of the hot wire X-probe was perpendicular to radial lines from the center of curvature, it did not generally coincide with the average direction of the flow. Therefore, the secondary flow component was established from the X-probe data by iterations of the zero reference direction until continuity for the secondary flow component ($\int_o^h u dz = o$) was satisfied. As mentioned earlier, the average flow direction found by this method is compared with the potential flow solution at several locations in Fig. 5.

Similar X-probe surveys were conducted in the same channel with various injection flow rates. The results were not significantly different from those without injection.

Another effect of the secondary flow is indicated by the pressure variation on a vertical line (z-direction) along the outer wall. Measurements taken at $\beta = 50^{o}$ showed that the highest pressure occurred in the center plane. The decrease toward toward the two side walls amounts to approximately $\Delta p/q_{\infty} = 0.06$. It is remarkable that this amount is practically independent of the absolute pressure which varied for the different configurations used in these tests over a range of approximately 0.5 to 5 times the ambient pressure.

Channel Flow With Injection

1. STRAIGHT CHANNEL

Previously, a brief description of the flow pattern in straight and curved channels was given. In view of the application to fluid state amplification, it is of special interest to investigate the change of these flow patterns due to the injection of a control jet.

An approximate analytical method to calculate the flow in a straight channel with crosswise injection of a jet is presented below based on the following assumptions (see sketch below):

(a) Two-dimensional incompressible flow of an inviscid fluid. (The side with the port is called the "inner wall" in analogy to the curved channels).

(b) The jet width is small compared with the channel width.

(c) The main flow velocity profiles at the inlet, u_o, and at the exit, u_e, and the jet velocity, u_j, are uniform.

(d) The static pressure in each cross section of the main flow region is determined by the average velocity obtained from the continuity equation; i.e., there is no upstream effect from the injection. The resulting pressure distribution (ambient pressure = 0) along the walls is indicated qualitatively in the sketch below. In reality the pressure distribution will be more like the one indicated by the dashed lines.

(e) The static pressure in the stalled region is equal to ambient.

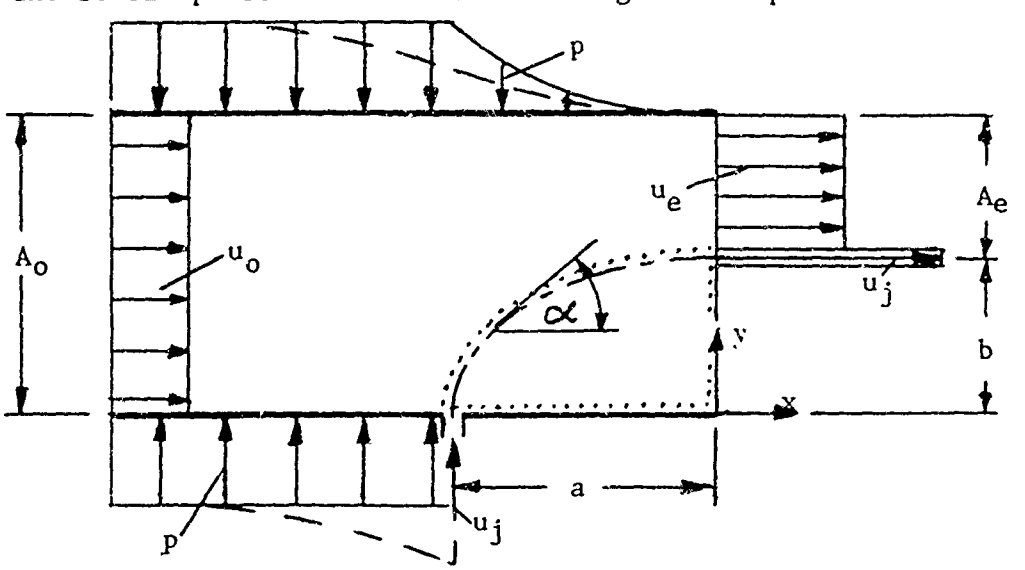

Applying the Bernoulli equation and the momentum equation in the x-direction to this flow model one obtains

$$\rho/2\, u_o^2 + p_o = \rho/2\, u_e^2 + p_e \tag{1}$$

and (by including continuity, $A_e/A_o = u_o/u_e$)

$$p_o A_o + \rho A_o u_o^2 = \rho\left(A_o u_o u_e + A_j u_j^2\right) + p_e A_e \tag{2}$$

Combining equations (1) and (2) for pe = 0 leads to

$$\left(\frac{u_e}{u_o}\right)^2 - 2\frac{u_e}{u_o} + 1 - 2\frac{A_j}{A_e}\left(\frac{u_j}{u_o}\right)^2 = 0 \tag{3}$$

from which follows

$$\frac{u_e}{u_o} = 1 + \sqrt{2\frac{A_j}{A_e}\left(\frac{u_j}{u_o}\right)^2} \tag{4}$$

The calculated values for A_e or

$$b = \frac{A_o - A_e}{h} \tag{5}$$

agree fairly well with experimental data, as will be shown later.

In applying this type of flow to fluid state amplification, the dimension b above is not alone sufficient to determine the optimum location of a pick-off. Were such a pickoff placed a distance b from the inner wall but too far downstream, the flows in the stalled and unstalled region would have mixed from diffusion and the amplification effect would be lost. For a pick-off location too close to the injection port, the main flow displacement would not be optimum. Therefore, the dimension "a" needs to be known.

To calculate "a" accurately, the location and shape of the jet centerline should be obtained from a detailed analysis. However, since there was not enough data available on a plane jet in a crossflow, a first approximation was made by assuming a shape of the jet and applying the momentum theorem in the y-direction to the control volume bounded by the dotted line on the above schematic. With the jet leaving the slot perpendicular to the wall and reaching a direction parallel to the wall at "a", the jet curve was assumed to be elliptic. Since the momemtum equation gives an integration of the forces and only the value of "a", not the complete jet shape, is to be calculated, this assumption should not prevent a reasonable result.

With the origin of the x-y coordinate system at the center of the assumed elliptic jet curve, (refer to the above sketch) the equation for the centerline becomes

$$y = b\sqrt{1 - (x/a)^2} \tag{6}$$

and the angle α in the above sketch can be expressed by

$$\alpha = \arctan\left(-\frac{x}{y}\frac{b^2}{a^2}\right) \tag{7}$$

Applying the continuity and Bernoulli's equations yields

$$\frac{p - p_e}{\rho/2\, u_c^2} = \left(\frac{u_e}{u_c}\right)^2 \left[1 - \frac{(1-b)^2}{(1-y)^2}\right] \tag{8}$$

for the pressure difference between the main stream and the stalled region (assumed equal to exit pressure) at any location x.

According to the momentum theorem, the integral of the y-component pressure forces, over the control volume (dotted line in the sketch) must equal the applied momentum (M_j) force in the y direction:

$$\int_{-\frac{a}{w}}^{0} \frac{p - p_e}{\rho/2\, u_c^2} (\cos\alpha)\, d\frac{x}{w} = \frac{A_j \rho u_j^2}{A_o \rho/2\, u_c^2} \tag{9}$$

Combining (6) to (9) and rearranging yields

$$\int_{-\frac{a}{b}}^{0} \left[1 - \left(\frac{1 - b/a}{1 - b/a\sqrt{1 - \frac{(x/b)^2}{(a/b)^2}}}\right)^2\right] \cos\left\{\operatorname{arctg}\left(\frac{x}{b}\cdot\frac{(b/a)^2}{\sqrt{1 - \frac{(x/b)^2}{(a/b)^2}}}\right)\right\} d\frac{x}{b} = 2\,\frac{A_1}{b}\left(\frac{u_1}{u_e}\right)^2 \tag{10}$$

Equation (10) has been evaluated numerically with resulting values of b and a plotted in Fig. 9 versus the ratio of jet and mainflow momentum.

A comparison of the above method with experimental data is indicated in Fig. 10 for the two injection ratios of u_j/u_o = 2 and 4. In view of the assumptions included in the calculation, the agreement is good.

For the injection rate of u_j/u_o = 2 and 4, the wall static pressure distribution is plotted in Fig. 11. A considerable deviation from the assumptions made above is the low pressure in the stalled region. The same type of distributions were measured for other injection rates and for different main stream velocities. The variation of the upstream pressure with injection is shown in Fig. 12 together with that of the curved channels.

Equation (4) can also be derived for counterflow injection. The result

$$\frac{u_e}{u_o} = 1 + 2\sqrt{\frac{A_j}{A_c}\left(\frac{u_j}{u_e}\right)^2} \tag{11}$$

gives higher values for b than with crossflow (see Fig. 9). Experimental data described later show indeed a further shifting of the velocity profiles of roughly the amount predicted.

No attempt has been made to calculate "a" in the same way as in the case of crossflow. It is believed that the viscous mixing effects are too large to be neglected here since the injection and the main flow not only have different velocities, but also opposing directions.

Additional information on velocity profiles in the straight channel is presented later in the section on Flow Modulation.

2. CURVED CHANNELS

The main effect of an injection at the inner wall on the flow in curved

channels is the enlargement of the stalled region. The resulting strong restriction of the exit area imposed on the main stream leads to a rising static pressure difference between inlet and exit with increasing injection as shown in Fig. 12. From the pressure drop thru the channel, the unstalle portion of the exit area can be calculated using Bernoulli's equation and continuity as before. The separation boundaries thus obtained are marked in Fig. 17. As in the case without injection, the calculated boundaries coincide with the strong velocity gradients.

The stalled area was made visible by means of a fluorescent oil technique as described earlier. Fig. 13(a) shows a photograph of the inner wall, and Fig. 13(b), the side wall of Channel R = 0.4. Bright regions represent stagnating flow. It can be seen that the separation line on the inner wall is not straight, but has a peak in the centerplane of the channel. The shape of the line can be explained by the curvature induced secondary flow, which has velocity components pointing toward the wall in the vicinity of the side walls and components pointing away from the inner wall in the center portion. The black streak in the picture of the bottom wall Fig. 13(b), indicates the curving secondary injection jet. From a series of such pictures the change of the separation point with injection can be established. Fig. 14 shows the movement of the peak point (center plane) of the separation line on the inner wall for Channel R = 0.4 as a function of injection velocities.

A further indication of the variation of the flow pattern with injection is the change of the pressure distributions along the turn walls. Fig. 15 gives these distributions for crossflow and two counterflow injection configurations in Channel R = 0.4. As indicated in Fig. 12 the pressure level rises with increasing injection rate. Fig. 15 shows how the various types of injection effect the shape of the wall pressure distribution. For the channels with different radius ratios, similar pressure variations were noted.

FLOW MODULATION

Use of Injection for Amplification

As mentioned earlier in this paper the injection of a secondary flow into the primary flow in an enclosed channel is well suited for direct flow amplification. The separation characteristics are altered by the injection, resulting in a redistribution of the stream velocity over a selected cross sectional area of the main channel. This redistribution is in proportion to the secondary injection and therefore provides a proportional mass flow, momentum or power gain as defined in any fluid state amplifier. However, the flow is merely pinched rather than deflected as in the usual fluid amplifier.

Since velocity profile changes are the essence of this amplification, we will begin by discussing the experimental velocity measurements. Velocity profiles measured at the channel exit for each of the unity aspect ratio channels used in these experiments are shown in Fig. 16(a) without secondary injection and in 16 (b) with a counterflow injection velocity of 3 times the entering main stream velocity. Data symbols are not shown to avoid loss of clarity. In the zero injection data, the separated region and the consequently higher velocity toward the outer wall of the curved channels is clearly evident. It should be pointed out that the data shown in Fig. 16 are the absolute velocities, not velocity components normal to the exit plane. The angular

deviation of the flow and thus the reduction in the normal component, increases as the bend becomes sharper; e.g., the normal component velocity data for Channel R = 0 in Fig. 16 is roughly 20% lower than the absolute velocity shown.

The secondary injection, as shown in 16(b), causes the width of the high velocity plateau to become smaller than without injection, but the velocity is higher. In the straight channel the injection induces a separation so that the redistributed velocity profile begins to approach that of the curved channels.

A typical example of the exit velocity profiles for various injection rates for a particular channel (Channel R = 0.4 with counterflow injection) is presented in Fig. 17. In this figure the shift of the exit profiles resulting from injection velocities increasing from zero to 4 times the entering stream velocity are clearly evident. Since the quantity of injection fluid is much less than the primary stream flow, this redistribution of the velocity profile results in amplification. It can be seen in Fig. 17 that the shift of the velocity profile is a direct function of the injection velocity. In the next subsection it will be shown that this profile shift is in general linearly proportional to the injection rate.

Gain Results

Referring again to Fig. 17, an integration of the velocity data over the region y_2-y_1 in the form $\int_{y_1}^{y_2} u\,dy$ represents the mass flux thru that area or the quantity of air that would flow thru a receiver passage if a corresponding splitter pickoff were located to receive flow in the cross sectional area between y_1 and y_2. To determine the maximum mass flow gains for each channel and injection configuration, integrations were carried out over a series of y_1 and y_2 values. These integrations assumed that the flow is two-dimensional, which is of course not exactly true in the curved channels. However, the exit velocity profiles in the z direction were nearly flat except in the low aspect ratio channel.

A typical example of integrated output mass flow as a function of counterflow injection mass flow for each of the unity aspect ratio channels is presented in the lower portion of Fig. 18. The corresponding mass flow gains, $\dot{G}_m$, are tabulated on the figure. These gains are of course only for the channels alone. When combined in a Double Leg Elbow amplifier for example, the overall differential output gain would be over 200 for most of the results shown. Note that the slope of the straight channel data and thus the gain is greater than any of the others, but it also has the smallest linear range.

High mass flow gain is not necessarily the most important feature to be gained from the modulated channels. Rather, it is the momentum slope that is the important factor. We say this because the use of the channel output for high gain amplification utilizes the momentum produced (see Appendix C of Ref 1, for example, for the governing equations) to deflect another stream. Thus, calculations of the momentum flux, or $\int_{y_1}^{y_2} u^2\,dy$ were also carried out for all of the data over the same set of integration limits. The momentum results for the above mentioned conditions are presented in the upper graph of Fig. 18 in the form of

$$\frac{\text{output momentum flux}}{\text{momentum flux over the same output cross section without injection}}$$

as a function of injection mass flows.

The important parameter is that which determines the ultimate amplification produced if the channel were used as part of a fluid state amplifier. This parameter is the output momentum produced per injection mass flow input, or $G_M/\dot{m} = \dfrac{\Delta\int_{y_1}^{y_2} u^2 dy \,/\, [\int_{y_1}^{y_2} u^2 dy]_{u_j=0}}{\Delta \dot{m}_j \,/\, \dot{m}_o}$. It is simply the slope of the momentum vs mass flow curve as shown typically in Fig. 18. The corresponding values of $G_M/\dot{m}$ are indicated on the figure.

One more item of real importance in evaluating the gain effectiveness of the channels is the energy flux characteristics, or in fluid state terms, the fluid power. To obtain the power characteristics we integrated much of the data in the form $\int_{y_1}^{y_2} u^3 dy$. Typically, power gains fall in the 1 - 2 range.

The final parameter of interest in evaluating the results is the injection power required, or $u_j^3 A_j / u_o^3 A_o$, to produce a given mass flow or momentum gain. This will be included in the overall discussion in the next subsection.

Returning to mass flow and momentum mass flow gain considerations. Mass flow gains of up to 5.3 were measured in the experiments; the highest gains occurring with counterflow injection in the straight channel. Momentum per mass flow gains of over 22 were obtained; with the highest values obtained in the low aspect ratio curved channel.

For a particular channel and type of injection, the gains vary as a function of receiver cross section width y_2-y_1), streamwise location of the receiving cross section, and streamwise location of the injection slots in the curved channels. In general, receivers extending from y_1/w = 1/3 or 1/2 to the outer channel wall were the most effective; the wider receiver being best for the straighter channels.

The influence of receiver cross section location with respect to the injection point was investigated in the straight channel wherein it was found that both the peak mass flow and the peak momentum per mass flow gain occur about 0.4 channel widths downstream of the counter-flow injection port. However, the peak momentum per mass flow occurs as a result of a wider receiver and decays much faster upstream than the mass flow gain. The results in the straight channel suggest, as mentioned earlier, that an optimum location for velocity redistribution will occur at the point downstream of the injection slot where the injection stream has been fully turned toward the flow direction. Downstream of this point the flows tend to diffuse and thus lose their identity.

In the curved channels, however, there does not appear to be a strong effect of streamwise location on the velocity redistribution. This is to be expected because the centrifugally induced secondary flows of the curved passage tend to maintain the profile integrity around the full turn. However, some data obtained in the low aspect ratio channel indicated that there may be a modest increase in gain for injections close to the natural separation point if the receivers are located a short distance downstream.

Further experiments indicated that the location of the injection port, using counterflow, with respect to the channel inner wall, is also a factor

in providing velocity redistribution. The effectiveness tends toward a maximum between 60 and 75 degrees around the turn. This result agrees to some extent with data published in Ref. 1 for a somewhat smaller aspect ratio channel (.625) that showed counter flow injection in the β = 70 to 80 degree region was the most effective.

One other effect should be mentioned before discussing the overall results; that is, the effect of absolute stream velocity on the gain results. A majority of the experiments were conducted at incoming primary velocities of 50 fps, but enough injection tests were also conducted at 100 fps to indicate that no major variations in the performance will result. The only significant difference with respect to gain effectiveness noted was in the straight channel where a somewhat greater injection velocity was required to initiate a significant main stream velocity redistribution. This would be the equivalent of bias flow in a fluid state amplifier. However, the eventual output slopes were not significantly altered.

Overall Comparisons

As mentioned earlier, the mass flow and momentum gains for all of the channels do not vary over a broad range, although a trend toward higher effectiveness with the straight channel is evident. Table 3 below briefly summarizes this information:

TABLE 3

Channel	Counterflow Injection		Crossflow Injection	
R	Max $G_{\dot{m}}$	Max $G_{M/\dot{m}}$	Max $G_{\dot{m}}$	Max $G_{M/\dot{m}}$
0	3.7	13.5	3.7	13.5
0.2	3.7	19.5	3.3	
0.4	4.3	18.1	3.5	13.3
0.4(h/w=.208)	4.3	22.3	2.8	8.5
1.0	5.2	21.2	4.9	19.9

The trends indicated in the above table can only be compared realistically, however, in terms of the energy required to produce these gains. Accounting for energy requirements will allow for minor variations in injection port geometry including velocity profile variations. This accounting is necessary since, as was shown in Ref. 1, decreasing the injection port size (and thus increasing the injection energy for a given flow) results in a direct improvement in gain. Therefore, for evaluating the gain data herein, the power required at a fixed injection velocity ratio of 2.0, which is within the linear range of all of the tests, was calculated for all of the test configurations. This factor, in the form of injection power per primary flow power, W_j/W_o, was used as a basis for comparing all of the gain results. In other words, the mass flow or momentum gain per injection power required is a figure of merit for evaluating any channel and injection port geometry.

On this basis the peak gains for each of the test channels are shown as a function of the radius ratio in Fig. 19. This figure makes the following trends apparent as listed below:

1. The counter flow injection method is more effective than cross flow injection.

2. For the counter flow injection method, the effectiveness improves as the channel becomes straighter.

3. For the cross flow injection method, channel curvature does not appear to be significant.

4. Effectiveness appears to decrease as the channel aspect ratio is reduced.

A word of caution must be raised at this point. Our program is still in progress and will extend further than reported herein. The test circumstances reported so far are not necessarily universal. The entering flow in all cases was made up of a low turbulence core and a relatively thin turbulent boundary layer. These conditions are not necessarily what is found in a fluid state amplifier where a more fully developed turbulent flow is likely. Our work will progress into this area. In the curved channels this is particularly important because of its effect on the natural separation point and on the generation of secondary flow. It should also be reiterated that the mass flow and momentum data from the gradually curved channels (R = 0.2 and 0.4) appear to be more nearly linear than in the straight channel, another item requiring further investigation. Moreover, concerning item 2 above, a more detailed probing of primary velocity profiles within the curved channel in the region nearer the natrual separation point may provide increased gain effectiveness as some preliminary data indicated.

Referring to item 4 above, it seems logical that the gain effectiveness would be less in a smaller aspect ratio channel because a much greater proportion of the flow thru a cross sectional area is in the boundary layer. For this case, the injection velocity, instead of acting mainly on the inner wall boundary layer, is also acting on the top and bottom boundary layer where its effectiveness is probably reduced.

In summation, however, it can be concluded that significant mass flow and momentum gains can be generated by injection induced separation in closed channels. The large changes in the primary or power flows are caused by, and vary continuously with, the small changes in the secondary injection flows when the injection flows are directed so that they can cause continuous changes in the primary flow boundary layer separation points.

CONCLUDING REMARKS

We have shown herein that large changes in the output flow of a curved or straight channel can be wrought thru judicious injection of a smaller secondary flow into the channel. The injection flow changes the separation characteristics of the primary flow such that a higher velocity, and thereby higher mass and momentum flux, is available over a selected downstream cross section of the channel.

A satisfactory analytical approach for the solution of the flow field in a curving channel was developed and compared with experimental results. With some further extension the approach will lead to a good understanding of separated flow in curved channels. Further, a method for calculating the primary flow redistributions from secondary injection into a straight channel was derived. This method compared well with measured data.

The extensive experimental data lead to some very interesting and hitherto unknown observations concerning injection into closed channels, particularly with respect to use in fluid state amplification. It was established, among other things, that the secondary injection method applied to any channel curvature can be effectively utilized for significant flow or momentum gain. Moreover, it is apparent that injection into the boundary layer, parallel but opposite to the primary stream is superior to crosswise injection and that a small aspect ratio channel is less effective than a unity aspect ratio channel for the inlet conditions tested.

The program reported here will be continued and expanded to include new test models and flow conditions to verify and generalize observations and conclusions to date and to continue to learn about the properties of these complex but important flows.

Acknowledgments

The encouragement and support of Capt. Lucius P. Gregg of the Air Force Office of Scientific Research is hereby greatfully acknowledged.

REFERENCES

1. Curtiss, H. A. and D. J. Liquornik, Research Studies in Proportional Fluid State Control Components, Giannini Controls Corporation Report Nr. ARD TR-013-01, September 1963.

2. Zisfein, M. B. and H. A. Curtiss, A High Gain Proportional Fluid State Flow Amplifier, to be presented at the Harry Diamond Lab Fluid Amplification Symposium in Washington D. C. May 1964.

3. Hawthorne, W. R., Secondary Circulation in Fluid Flow; Proceedings Royal Society of London A, Vol. 206, 1951.

4. Becker, E., Beitrag zur Berechnung von Sekundarstromungen, (Report on Analysis of Secondary Flow) Max-Planck-Institut fur Stromungsforschung Nr. 13, Gottingen, 1956.

5. Brown, O. G. and A. W. Marris, Turbulent Flow of Water in Plane Curved Channels of Finite Depth, presented at the ASME Winter Meeting, New York, 1962.

6. Weske, J.R., Experimental Investigation of Velocity Distributions Downstream of Single Duct Bends, NACA TN 1471, January 1948

7. Loving, D. L. and S. Katsoff, The Fluorescent Oil Film Method and Other Techniques For Boundary Layer Flow Visualization, NASA Memo 3-17-59L, March 1959.

8. Greenspan, D. and Yohe, M., On the Approximate Solution of $\Delta_u = F(u)$, Communications of the ACM, Vol. 6, Number 9, September 1963.

NOMENCLATURE

a	half-axis of ellipse, distance from injection slot
A	cross section area
A_e	unstalled portion of channel exit area
b	half-axis of ellipse, distance from inner wall
$G_{\dot{m}}$	mass flow gain, $\dot{m}_{output}/\dot{m}_j$
$G_{M/\dot{m}}$	momentum per mass flow gain, (defined on page 15)
h	channel height
H	boundary layer form parameter, δ_1/δ_2
$\dot{m}$	mass flow
M	momentum
n	exponent for correction of X-probe data
p	static pressure
Δp	pressure difference with respect to ambient, p - p ambient
q	velocity head, $1/2\rho u^2$
r	radius
R	radius ratio of channel inner to outer wall radius, r_{iw}/r_{ow}

u	primary velocity, x component
U	total velocity
v	secondary velocity, y component
V	voltage
w	channel width
W	power
x, y, z	coordinates
α	angle indicating slope of injection jet curve
β	turning angle of curved channels
γ	local flow angle
δ	boundary layer thickness
δ_1	displacement thickness
δ_2	momentum thickness
ϵ	angle between local flow angle and normal to hot wire
θ	X-probe wire angles with respect to a reference
ν	kinematic viscosity
ρ	density
Φ	velocity potential
ψ	stream function

Subscripts

e	exit
j	injection jet
iw	inner wall
ow	outer wall
o	inlet conditions
1,2	integration limits, X-probe wires

APPENDIX

Determination of the local flow angle γ from X-probe hot wire measurements.

Pictured below are sketches of the X-probe showing its alignment in relation to the air stream.

Each wire of the X-probe was individually calibrated for senstivity in yaw. Because of end effects a modified cosine equation was used as defined below:

$$U = U_1(\cos \epsilon_1)^{\frac{1}{n}} \quad (A1)$$

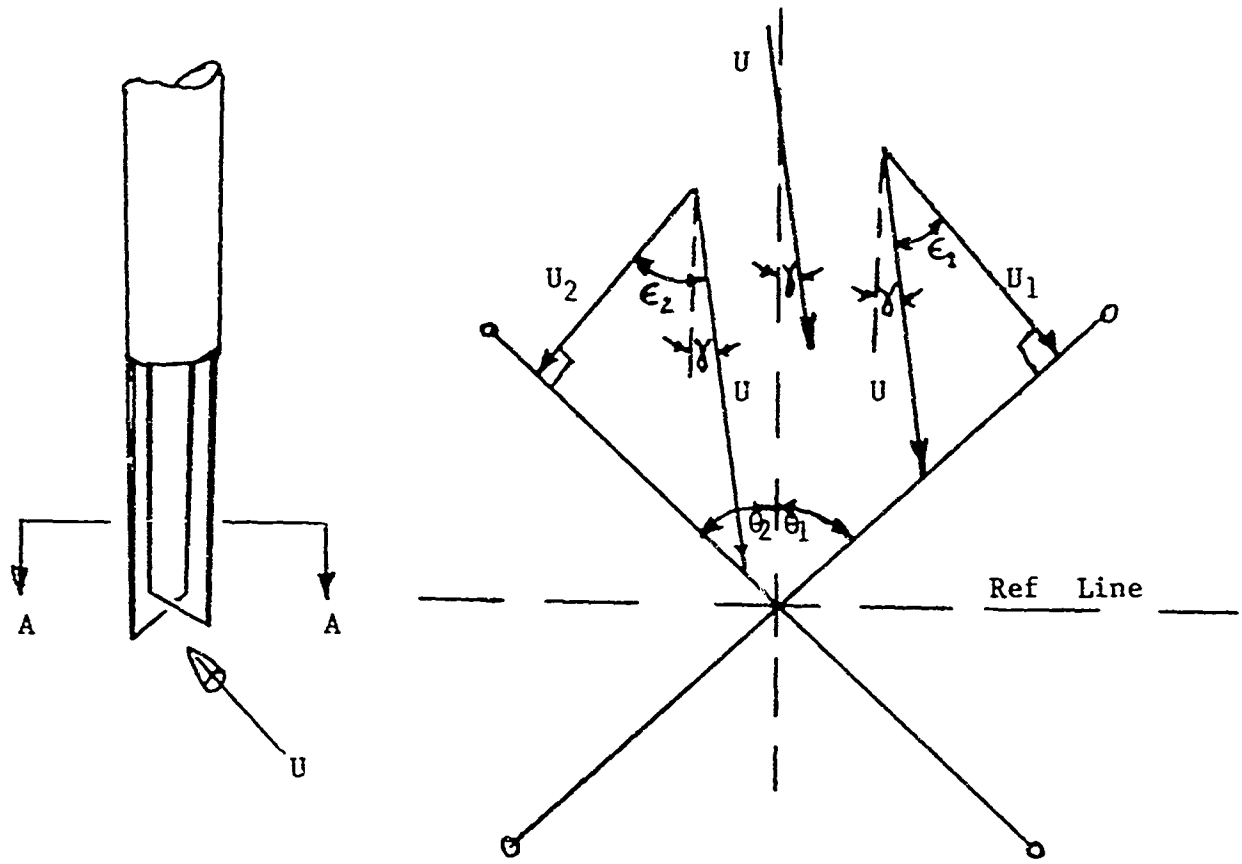

VIEW A-A

From view A-A

$$\theta_1 + \epsilon_1 + \gamma = 90^\circ \text{ and } \epsilon_1 = 90^\circ - (\theta_1 + \gamma)$$

substituting these in equation A1 we obtain

$$U_1 = U \sin(\theta_1 + \gamma)^{n_1} \tag{A2}$$

Following the same procedure for the other wire we obtain

$$U_2 = U \sin(\theta_2 - \gamma)^{n_2} \tag{A3}$$

Combining equations A2 and A3 to eliminate U gives

$$\frac{U_2}{U_1} = \frac{\sin(\theta_2 - \gamma)^{n_2}}{\sin(\theta_1 + \gamma)^{n_1}} \tag{A4}$$

The exponents, n_1 and n_2, were determined for each wire from yaw calibrations. The angles, θ_1 and θ_2, were determined by calibration after the X-probe was fixed in place in the movable plexiglass channel top. U_1 and U_2 were obtained from their respective voltage measurements during the run and by using their respective calibration curves $V_{1,2}^2 = A + B\sqrt{U_{1,2}}$, where A and B are constants. With these values the angle γ can be found by a trial and error solution. A computer program was wirtten which utilized the measured voltages, $V_{1,2}$ and solved for U_1 and U_2, then plugged these values into equation A4 and solved for γ.

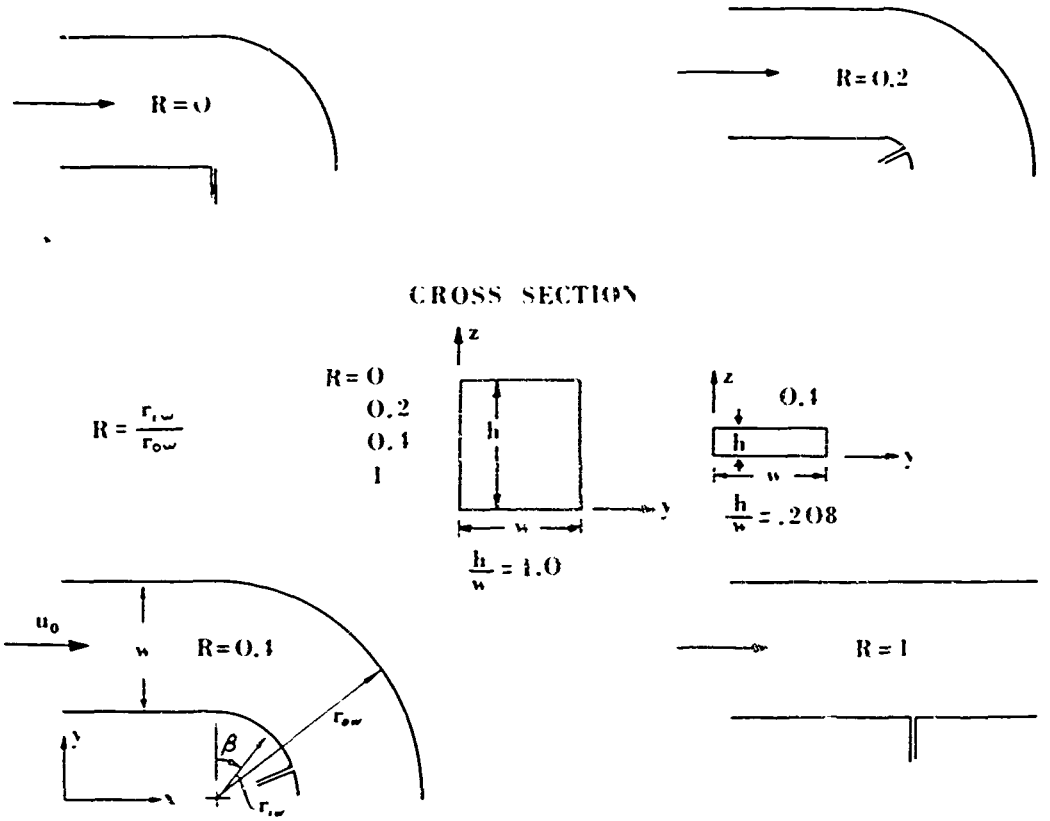

Fig. 1. Model diagrams

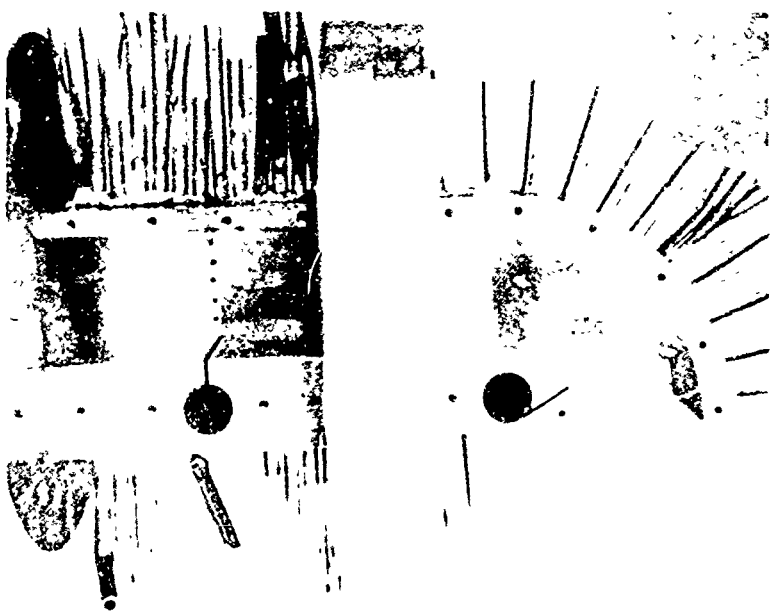

Fig. 2. Typical test configuration of channels with side wall removed

Fig. 3. View of typical test configuration with X-probe hot wire anemometer mounted on curved channel

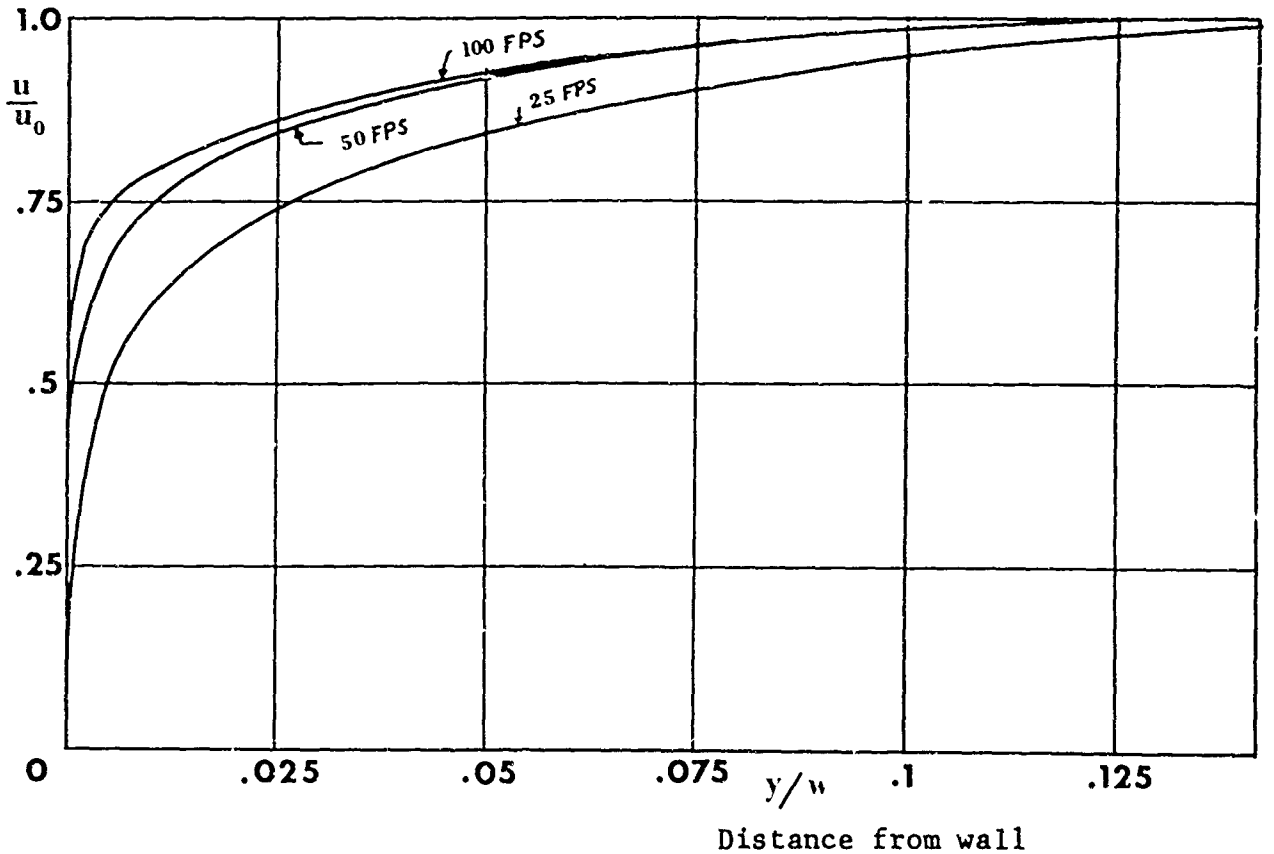

Fig. 4. Inlet boundary layer profiles at inlet to curved channels (exit of straight channel)

u_0

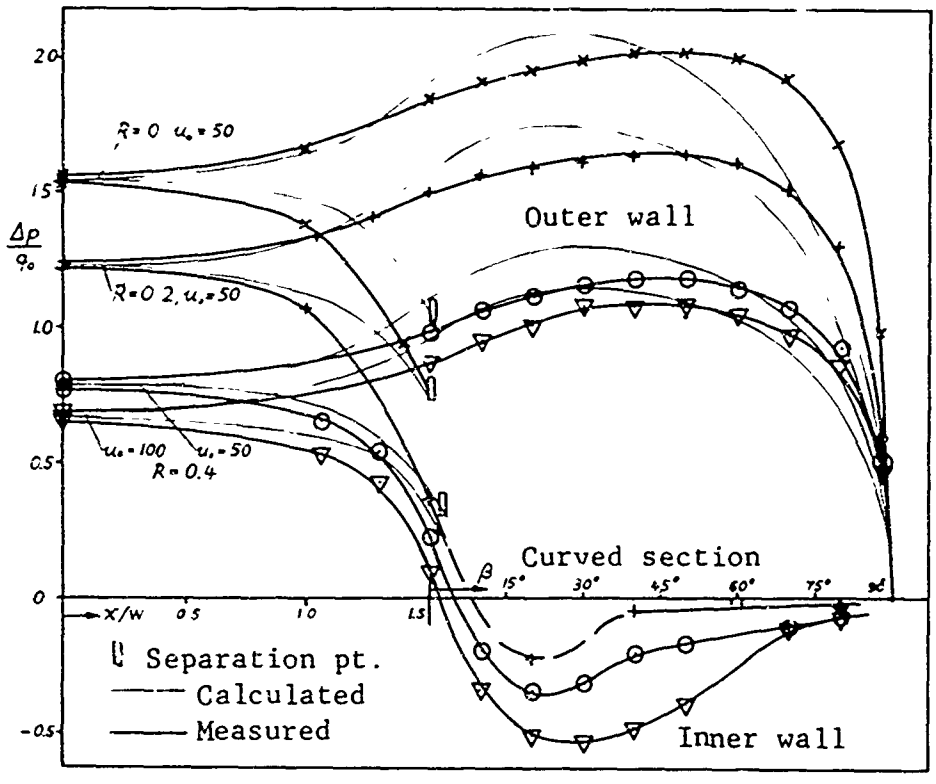

(a) Pressure distributions along channel inner and outer walls

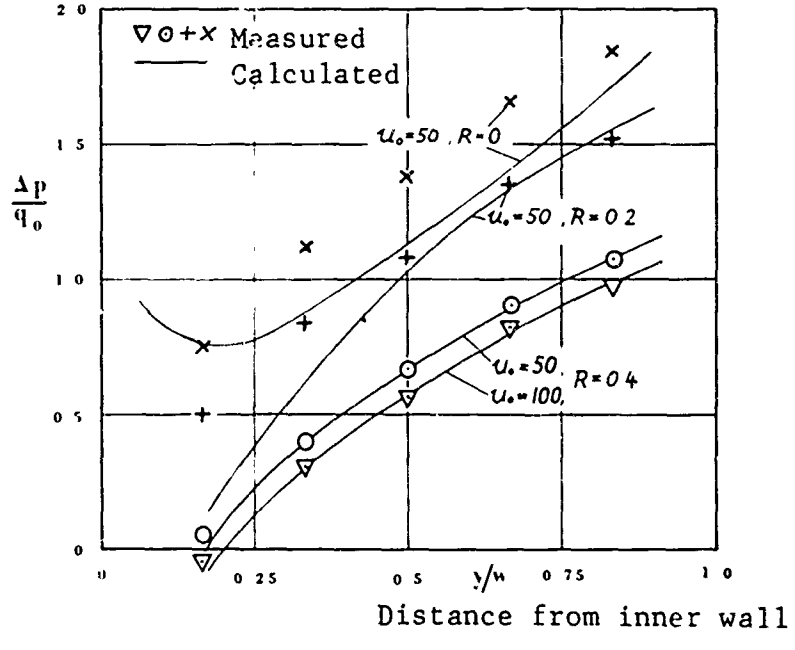

(b) Pressure distributions across channel at $\beta = 50^{o}$

Fig. 6 Channel wall pressure distributions without injection

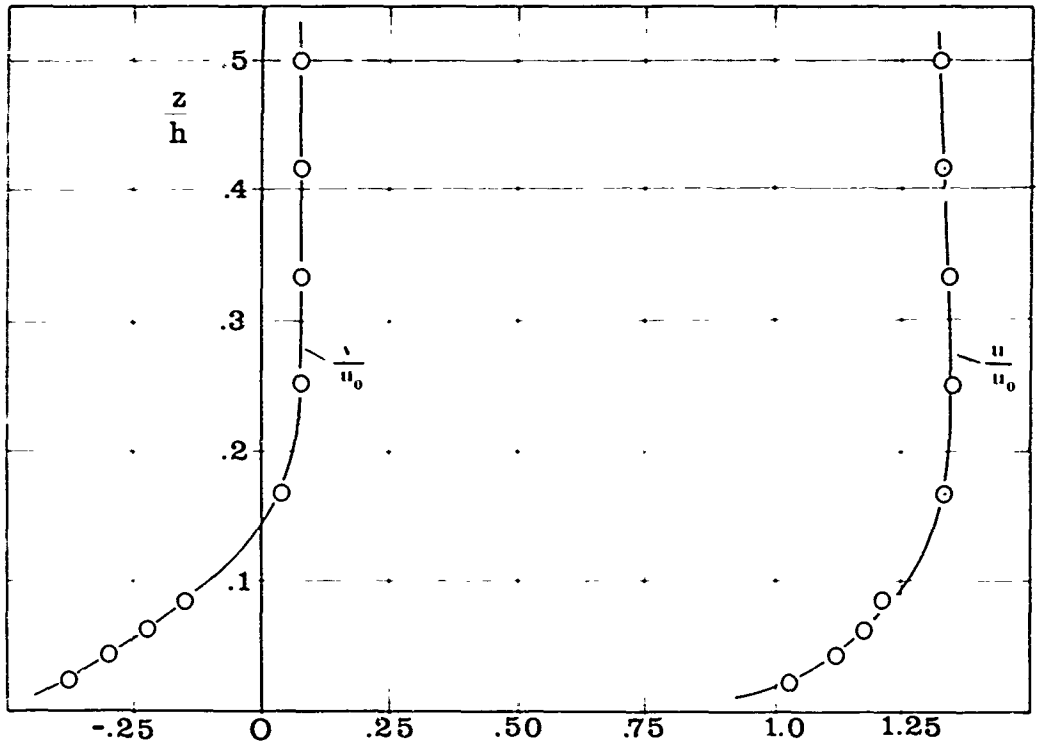

Fig. 7. Typical primary and secondary velocity profiles. Channel R = 0.4, location φ = 60°, y/w = 0.6, no injection

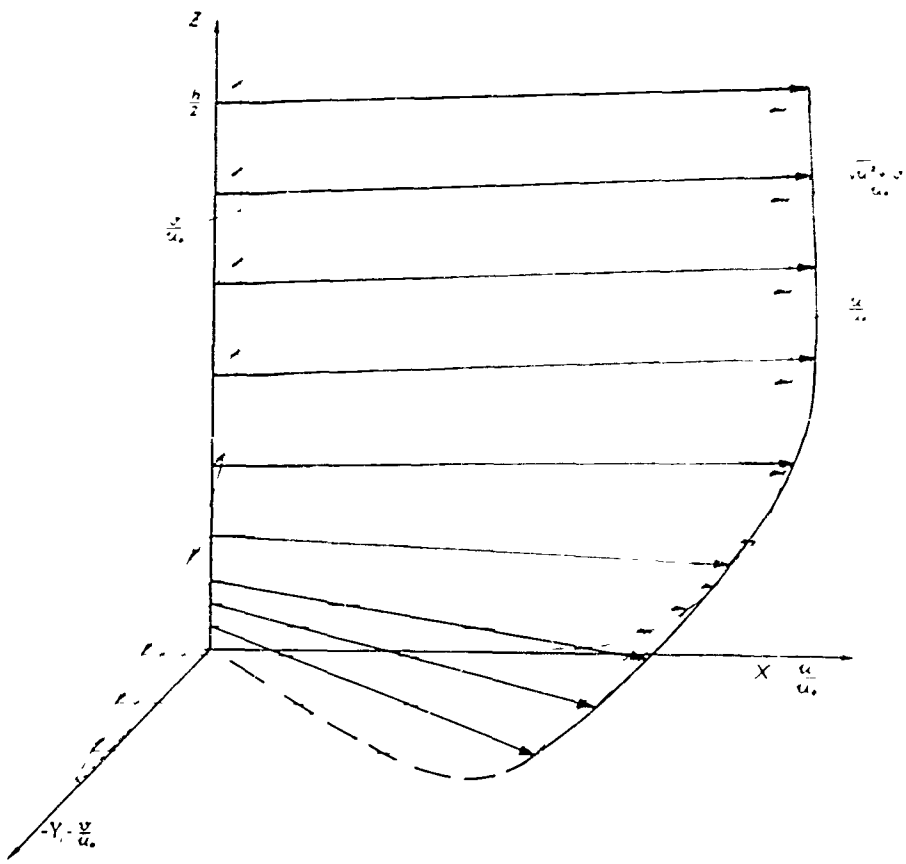

Fig. 8. Three-dimensional representation of velocity profiles in curved channel as in Fig. 7

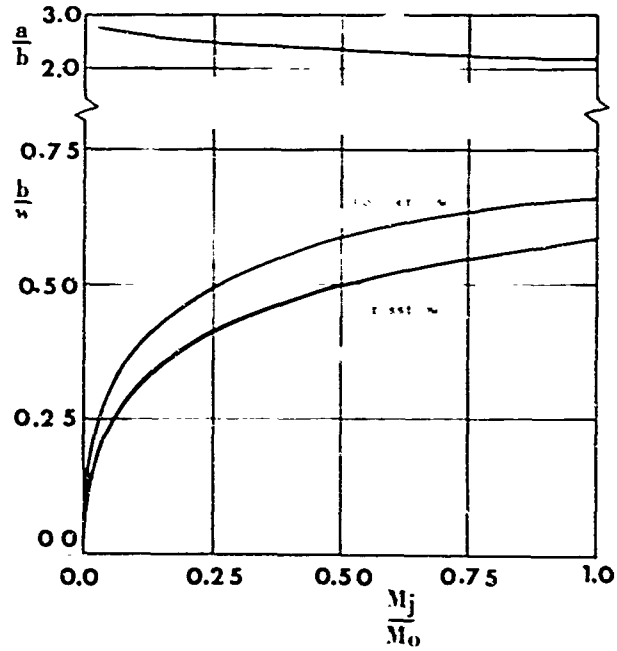

Fig. 9. Calculated values of b/w and a/b

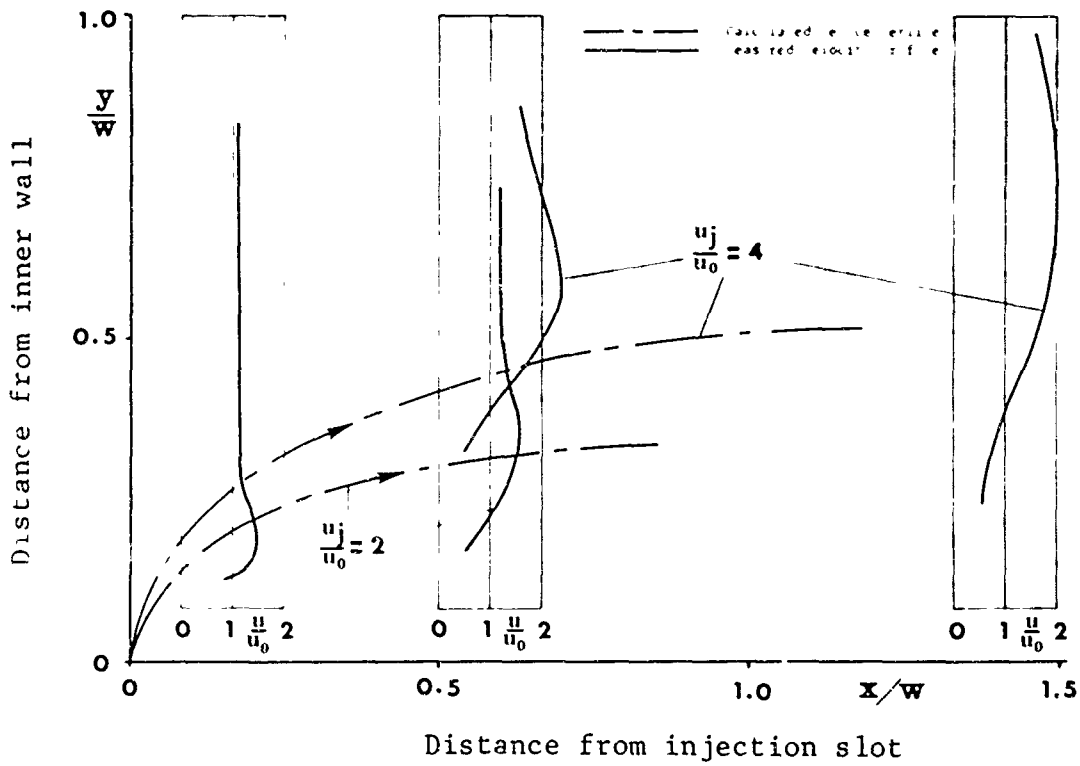

Fig. 10. Calculated injection jet flow path compared with channel velocity profiles, straight channel R = 1.0

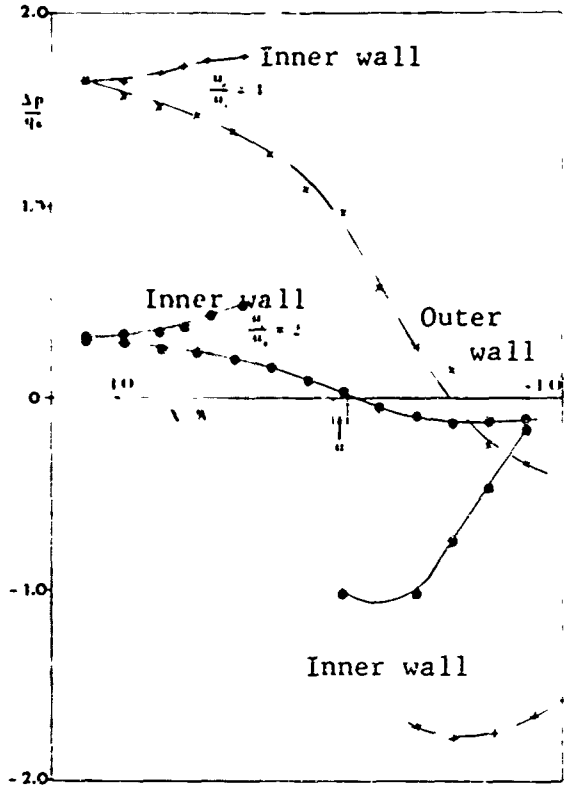

Fig. 11. Pressure distribution with injection, straight channel R = 1.0

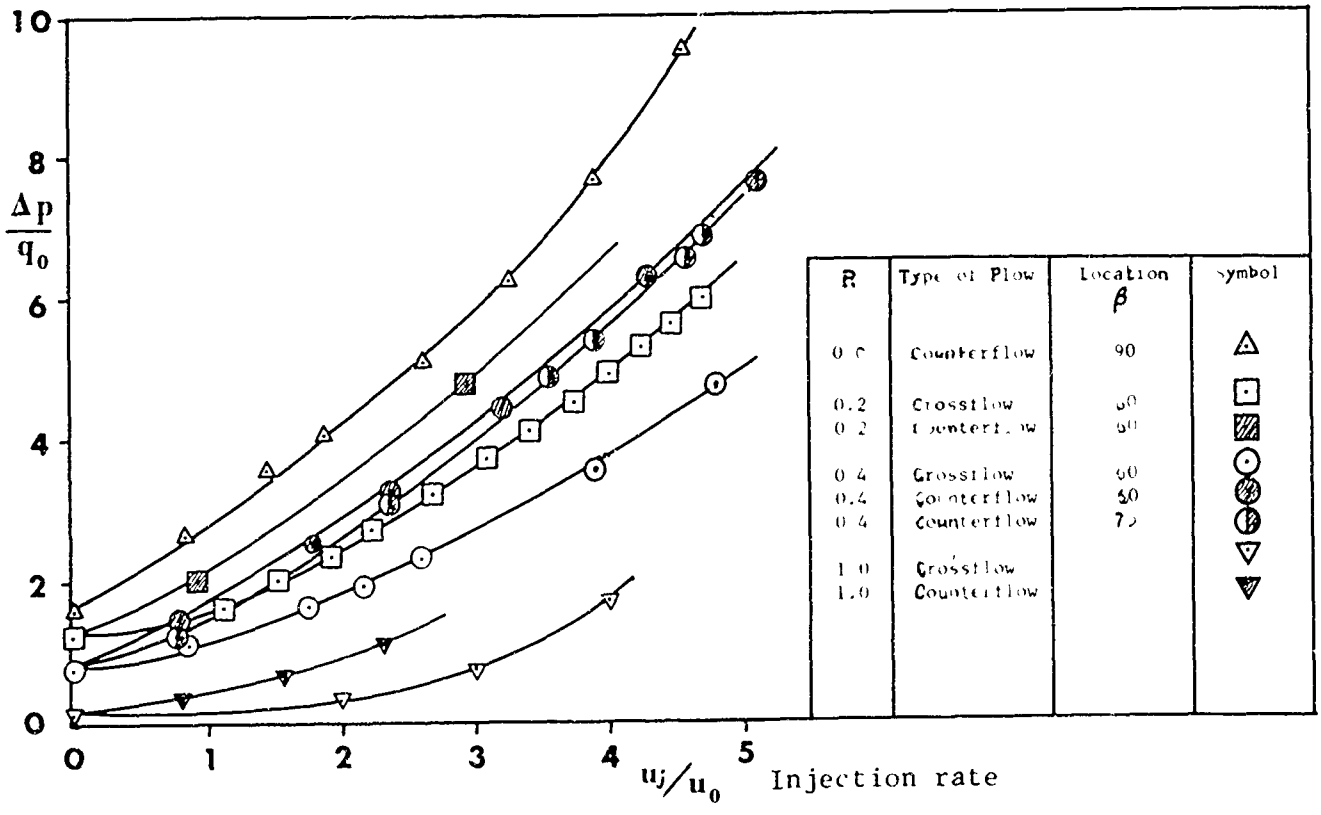

Fig. 12. Pressure drop thru channel versus injection rate for all unity aspect ratio channels

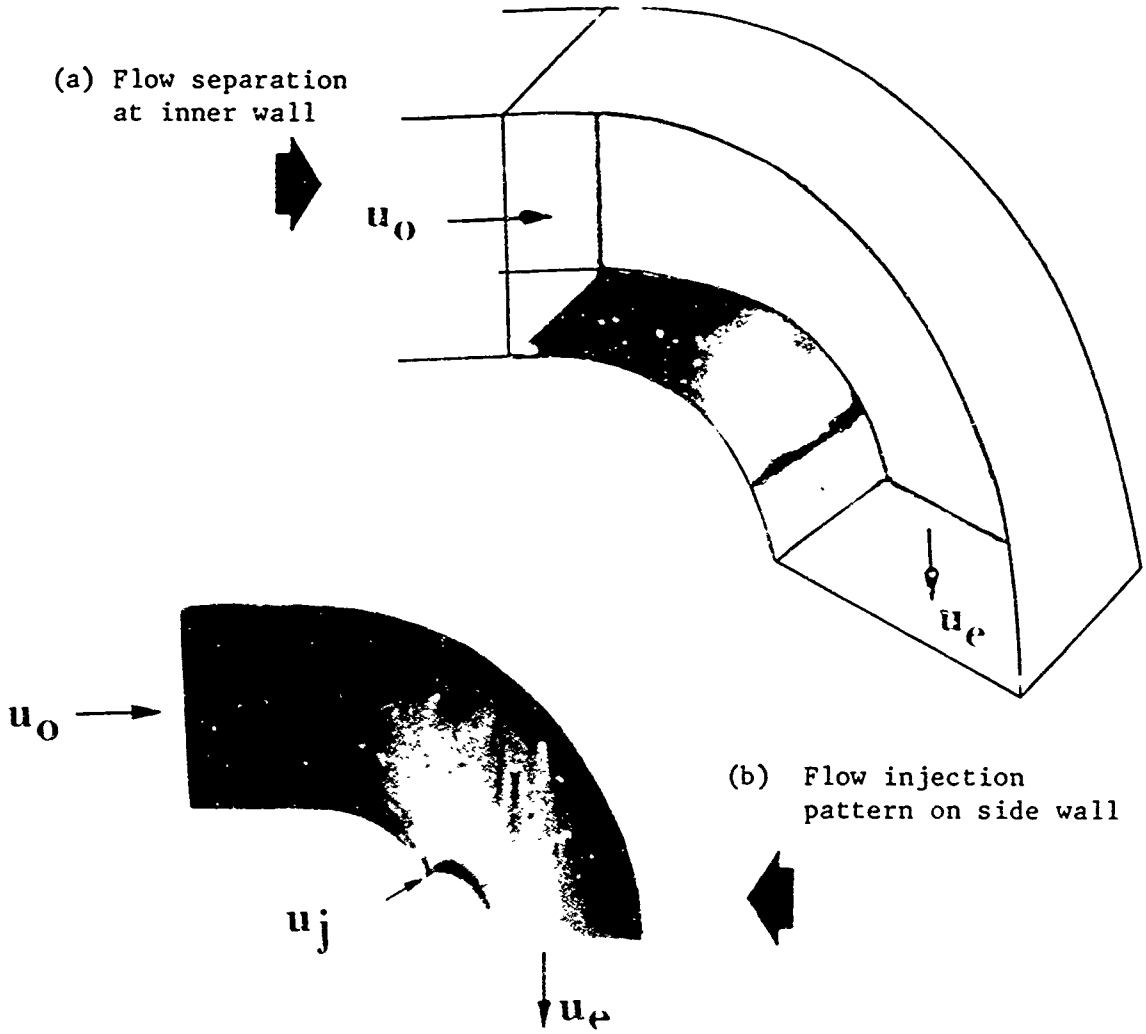

Fig. 13. Fluorescent oil photographs of wall flow patterns, channel R = 0.4

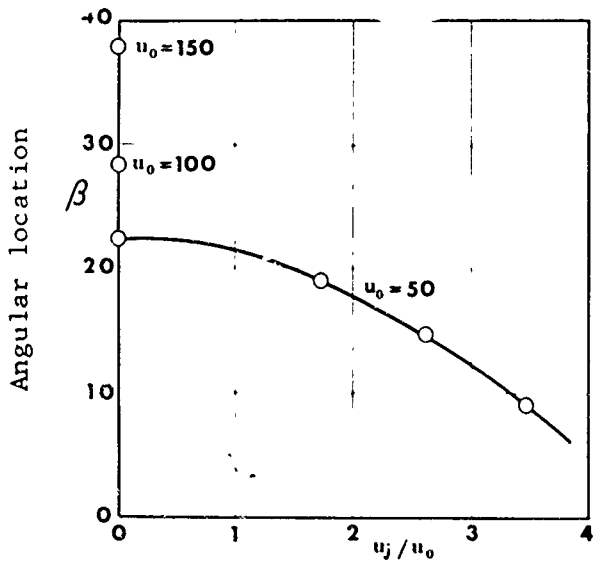

Fig. 14. Location of separation point, channel R = 0.4

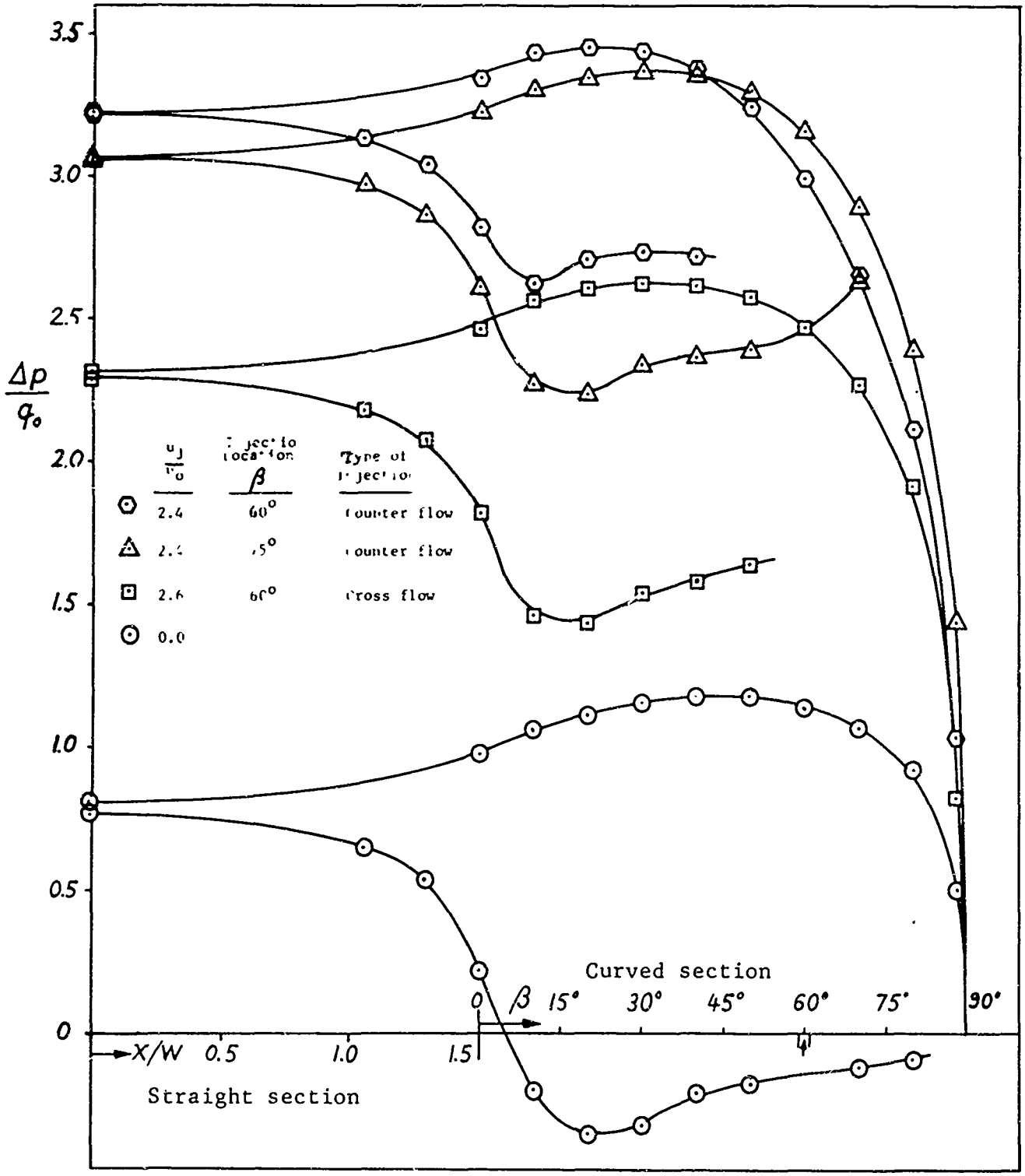

Fig. 15. Wall pressure distributions with injection, channel R = 0.4

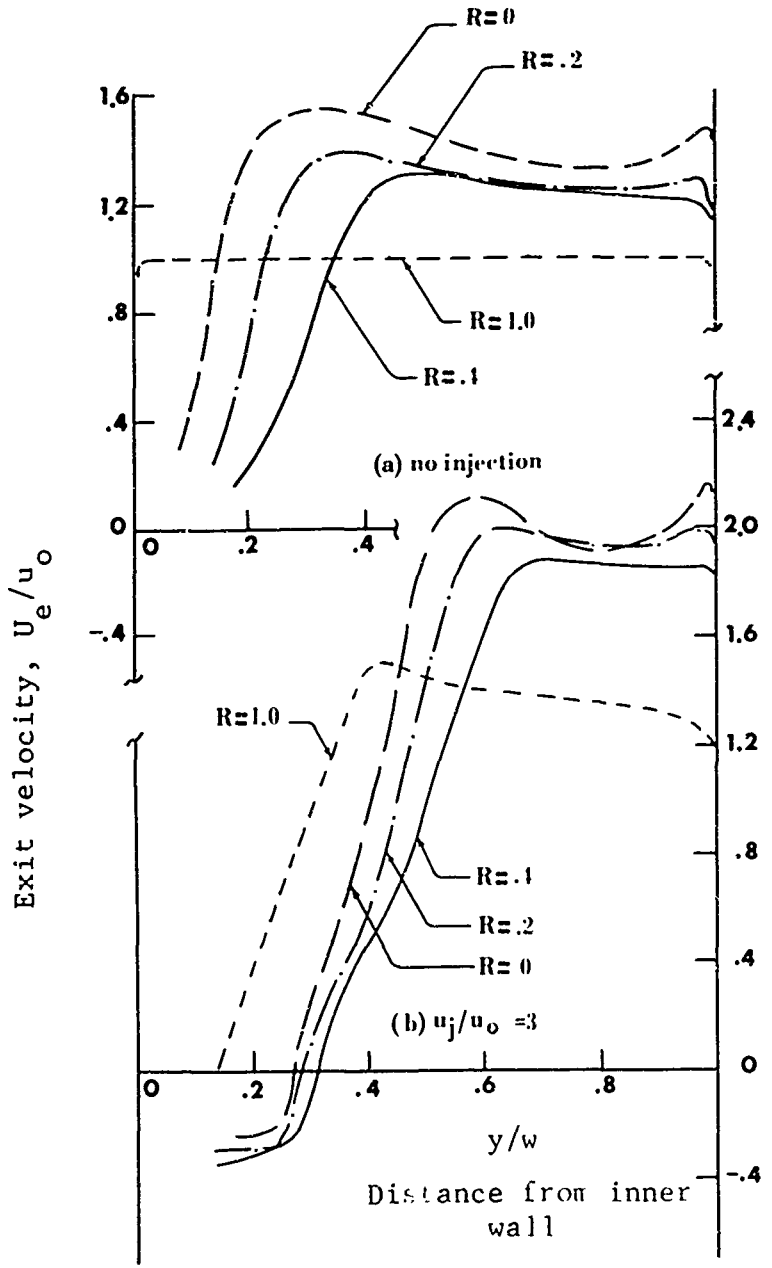

Fig. 16. Exit profiles with and without counter flow injection at $\beta = 60^o$ for all unity aspect ratio channels

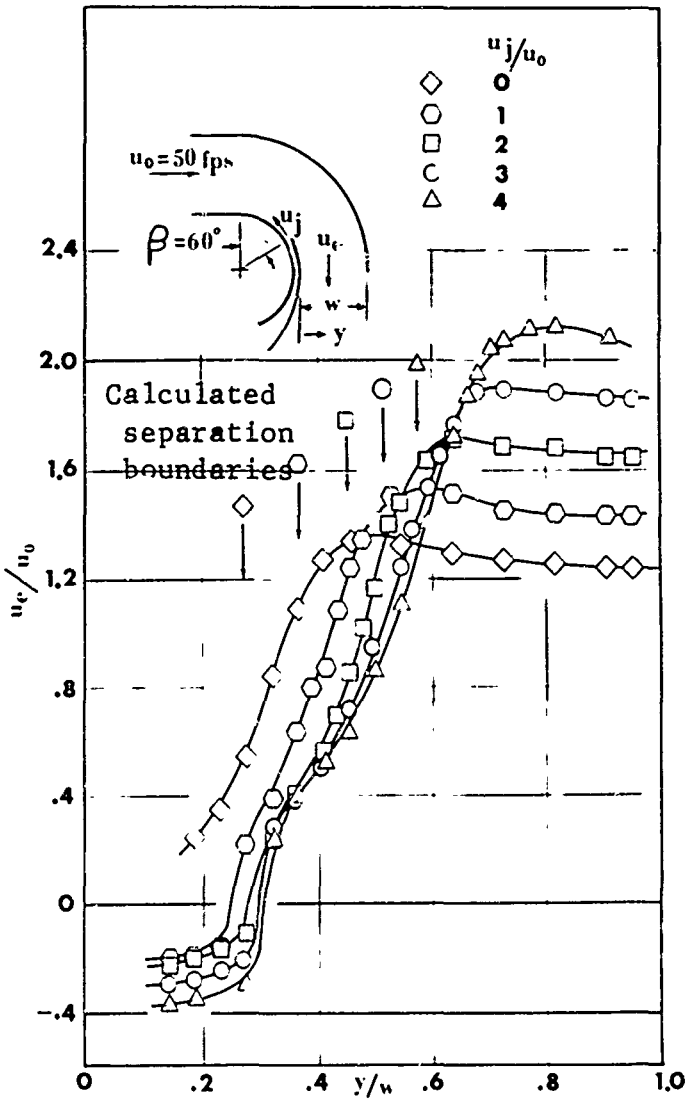

Fig. 17. Exit velocity profiles with counter flow injection at $\beta = 60^o$, channel R = 0.4

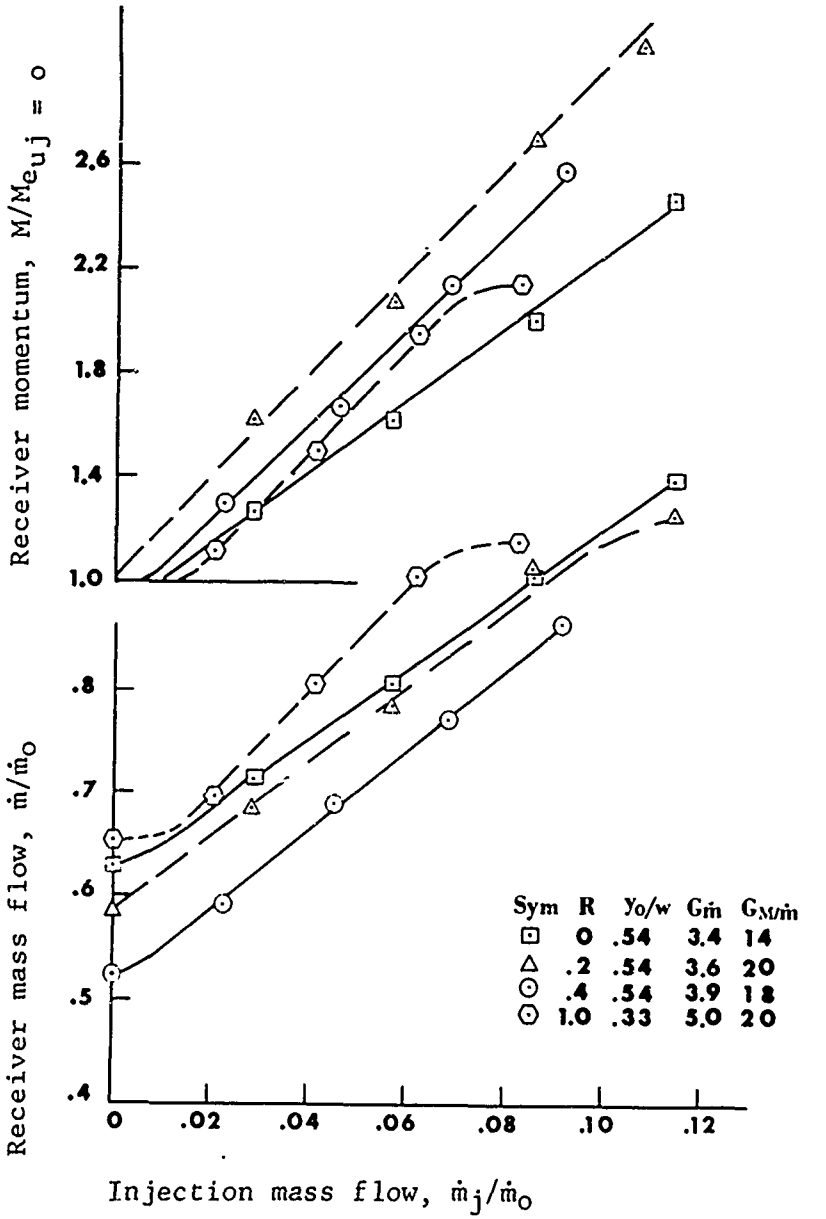

Fig. 18. Typical mass flow and momentum characteristics for aspect ratio unity channels

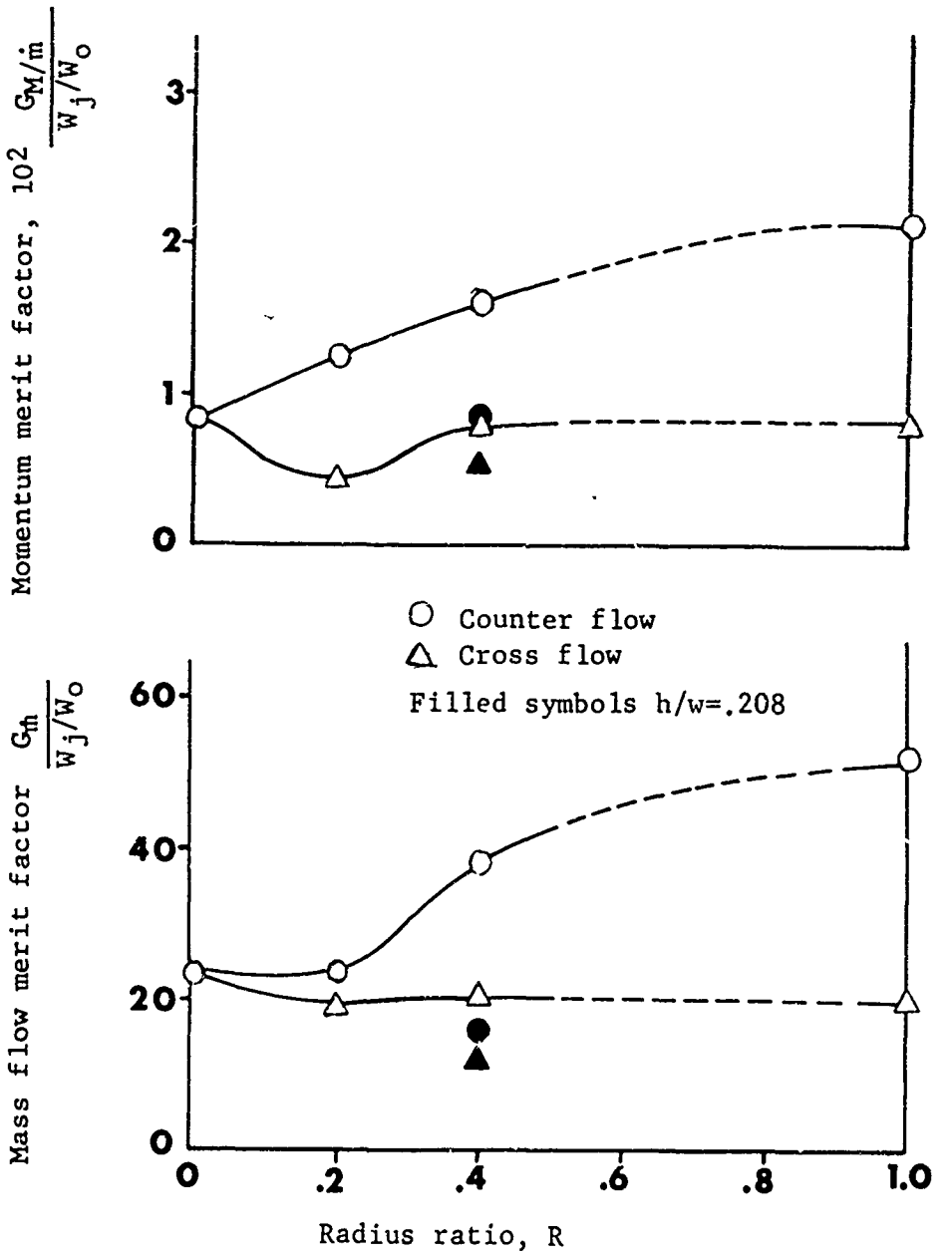

Fig. 19. Overall peak gain figure of merit comparisons

APPLICATION OF PURE FLUID LOGIC TO ON-OFF CONTROL SYSTEMS

by

D. J. Nelson

and

H. Iwata

of

The Marquardt Corporation

ABSTRACT

Digital techniques are broadly classified into: (1) arithmetic and (2) pure logic. It is noted that many control problems can be solved by using the latter technique.

Since, in general, there are alternative ways of representing the same Boolean function, the pure-logic decoding network can usually be simplified. Methods are outlined by which this can be done. In many applications, the output decoding can be restricted to two states which implies piecewise linear or on-off control. This technique was applied to a pure fluid control system. The resulting minimal logic circuit and exploratory systems synthesis are presented.

INTRODUCTION

Since the announcement in 1960 by the Harry Diamond Laboratories and Massachusetts Institute of Technology of fluid amplifying elements which have no moving parts, an almost exponential rise in interest has been created in this country and abroad. Since these devices can perform feats of logic, considerable fundamental research has been conducted in the area of pneumatic digital techniques. Work at The Marquardt Corporation has embraced both pure fluid element development and applications to aerospace propulsion system control.

Pure fluid control systems which are now emerging can be classified as either (1) analog, or (2) digital. Digital control systems can be further classified as (1) arithmetic, or (2) pure logic. A logic controller implies piecewise linear or on-off control. This

class of controllers has been used successfully for a number of years because of its inherent simplicity and economy (Reference 6). A control system combining both pure fluid logic and on-off techniques is presented.

Since there is always an interrelationship between component design and control system requirements, it is necessary that control system theory be applied early in the design stage so that realistic component specifications can be established.

A. Control System Synthesis

One of the recent applications of pure fluid control technology at The Marquardt Corporation has been to the control of the inlet spike of a supersonic ramjet engine. The basic problem can be stated: How can position information for the inlet spike servo of a supersonic ramjet engine be generated and operated on with non-electronic components and with override ability using digital techniques?

The overall control system can be represented by the simplified schematic shown in Figure 1. The position and override information is encoded in a three bit pressure pattern which is generated by three digital sensors. This pressure pattern is then decoded by a pure fluid logic network which generates one of two possible position commands. The commands are sent to an actuator. The feedback signal is compared at the summing junction with an aerodynamically generated reference position signal. The three digital sensors are: (1) an oblique shock position error sensor, (2) a buzz sensor, and (3) an unstart sensor. The two position commands are Retract and Extend. It should be noted that "buzz" is a low frequency combustion instability while unstart occurs when the inlet delivers too much air to the engine causing it to operate subcritically. When these flow conditions are sensed, override signals must be generated.

The block diagram of the spike servo with overrides is shown in Figure 2. This represents a nonlinear control problem. The preliminary control systems analysis was based on phase plane technique, since no other method of analysis seems to provide as much insight where nonlinear problems are concerned. The detailed analysis of the dynamics of the overall control system is given in Appendix A-1.

The analysis indicates that the control system is stable dependent on the presence of a damping term to negate the effects of the system transport lag. Limit cycle amplitude can be reduced to zero by eliminating the transport lag in the system.

The additional effects of coulomb damping, deadzone, and lead compensation on the basic system were studied with the aid of an analog computer. Since the emphasis in this paper is on the application of pure fluid logic to the control problem, details not pertinent to the logic problem will not be discussed.

B. Circuit Simplification

In general, it is desirable to reduce the "cost" of a particular logic circuit. "Cost" as used here refers to the general value of a function which is to be minimized. For a pure fluid logic circuit this "cost" will be a function of: (1) construction, (2) failure rate, and (3) delay time. No other factors are apparent.

1. Construction "Cost"

This "cost" will depend on the expense involved in the actual construction of the circuit.

2. Failure Rate "Cost"

Circuit failure rates can be minimized by using very reliable circuit elements or by including redundant circuit elements.

3. Delay Time "Cost"

This "cost" is the time it takes a circuit to respond to a change in the input signal and can be minimized by reducing the number of elements a signal must pass through.

An ideal design method would be one in which the absolute "cost" would be minimized automatically. Unfortunately, such a design technique does not exist for combinational logic circuits at the present time. However, there do exist several systematic simplification procedures which have been developed to reduce the complexity of any Boolean expression and hence any logic circuit. These techniques are known as the Quine Simplification Method, the Harvard Simplification Method, and the Veitch Diagram Simplification Method. These procedures are based on certain specific definitions of circuit "cost" which will now be examined from a pure fluid logic point of view. In particular, if it is assumed that delay time is of paramount importance, and that the only other factor to be taken into account is the number of components a systematic simplification procedure is available.

The assumption concerning construction "cost" assumes that there is a one-to-one correspondence between the number of switching elements and the expense of construction. This assumption is true only to a first approximation. The assumption concerning failure rate reveals that redundant circuits are not necessary. H. L. Fox has presented pure fluid failure rate data for a typical fire control system (Reference 2). Even though the rather stringent assumption of polymorphic computational operation was made, it can be seen that the assumption of nonredundant circuits is justified. The assumption concerning delay time requires that the resulting circuit be a two stage

circuit in which an input signal passes through only two gates before arriving at the output. This assumption is just what is desired since, in a "tight" pure fluid servo system, it is desirable to reduce the time delay as much as possible. For applications where the above assumptions are valid, the simplification procedures can be applied (References 3 and 5). Some hints on the possibilities of pure fluid logic simplification can be gained from a particular type of geometrical construction which is restricted to the on-off servo case. The possible combinations of N binary digits (0 or 1) correspond to the vertices of a hypercube in N dimensional space. It is the job of the logic unit to recognize the input space patterns and classify them into one of two output states according to some arbitrary rule. Examples of two and three dimensional space are shown in Figure 3. Classification corresponds to partitioning the input space into two categories. It can be seen intuitively that the simplest logic circuit will result if the logic is designed to recognize only those vertices on one side of the partitioning hyperplane. The other combinations will be recognized implicitly when the output of the logic unit switches to a binary zero. This state can be converted to a useful signal by inverting it. This, therefore, leads to a double ended output with one leg inverted. Actually, these constructions only give some intuitive insight into the problem and the real work of simplification probably would be accomplished using veitch diagram techniques since the veitch diagram method is not limited to the number of variables which are to be simplified.

Two six variable veitch diagrams are shown in Figure 4. Two diagrams are necessary in order to show the complementary conditions that exist on either side of the hyperplane in a six dimensional input space.

In this case, each vertex of the hypercube is represented by the cells in the veitch diagram. There are 2^6 such vertices. It is not the purpose of this paper to explain in detail the veitch diagram simplification procedure, but only to point out that it exists. The truth table of all possible input pressure patterns and required action is shown below.

B	U	Ss	R	E
0	0	0	0	1
0	0	1	1	0
0	1	0	0	1
0	1	1	0	1
1	0	0	0	1
1	0	1	0	1
1	1	0	0	1
1	1	1	0	1

TRUTH TABLE

The first three columns represent all the possible input pressure patterns from the digital sensor encoding section. The last two columns represent the required action to be taken by the controller. Figure 5 shows the same information but gives some insight into how much the above decoding logic can be simplified. The logical requirements of pure fluid logic gates based on the "NOR" concept require the use of an inverter, that is, the power jet of the switching element must be monostable. This fact leads to the concept of a high gain, negative resistance, analog amplifier used in a saturated mode. The TMC vortex amplifier (described in "Experimental Studies of a Proportional Vortex Fluid Amplifier") has a negative resistance characteristic and a pressure gain measured as high as 200 when designed to operate in its high gain region. The resulting decoding pure fluid logic circuit (after simplification) based on the TMC vortex amplifier is shown in Figure 6. It should be noted that an HDL flip-flop is used to convert the single-ended vortex amplifier to a double-ended output. This pressure pattern decoder unit has been successfully tested in the Marquardt Electromechanical Laboratory. It is planned to couple the pressure pattern decoder unit into the overall control system diagramed in Figure 2.

CONCLUSIONS

Even though the final choice of a controller depends on the details of a particular control problem, there are certain generalizations which can be made.

1. In general, a pure fluid on-off servo would not be considered for most applications where power availability is limited. On the other hand, in applications where the power is available (large boosters, airbreathing ramjets, etc.) the inherent short rise time of an on-off servo is attractive for applications requiring fast response.

2. For applications which require a controller to operate in an environment in which the signal-to-noise ratio is low, but where high temperature operation is also required the advantages of pulse information transmission via an on-off servo combined with the high temperature advantages of a pure fluid logic unit should be considered.

3. For systems in which an inexpensive control solution is sought, an on-off control with simple compensation is often completely adequate. Of course, as compensation requirements become quite complex, trade-off with a linear controller is often considered.

ACKNOWLEDGMENTS

This research work was conducted at The Marquardt Corporation under Contract AF 33(657)-12146.

REFERENCES

1. Brown, F. T., "Pneumatic Pulse Transmission with Bi-Stable Jet Relay Reception and Amplification," SC.D. Thesis Mass. Inst. of Tech., M.E. Dept., May 1962.

2. Fox, Harold L., "A Comparison of the Reliability of Electronic Components and Pure Fluid Amplifiers," Fluid Amplification Symposium, Vol. 1, October 1962, Sponsored by the Diamond Ordnance Fuze Laboratories.

3. McCuskey, Jr., E. J., "A Survey of Switching Circuit Theory," McGraw-Hill Book Company, Inc., 1962.

4. McDonald, D. C., "An Appraisal of Nonlinearities in Servomechanisms" Cook Tech. Rev., Vol. 2: Pg 3-13, April 1955.

5. Phister, Jr., M., "Logical Design of Digital Computers" John Wiley and Sons, Inc., 1958.

6. Thaler, George J. and Pastel, Marvin P., "Analysis and Design of Nonlinear Feedback Control Systems", McGraw-Hill Book Company, Inc., 1962.

APPENDIX A

PHASE-PLANE ANALYSIS OF DIGITAL PRESSURE PATTERN SPIKE CONTROL SYSTEM

Derivation of Trajectory Equation

For second order system with discrete nonlinearities, mathematical functions can be derived which represent the motion of the system. Simplification of Figure 2 is achieved by block diagram manipulation to combine the nonlinear element as shown in Figure 7. The nomenclature used in the following derivations is also shown in this figure. From the modified block diagram, the equation of motion is given by:

$$\tau\ddot{x} + \dot{x} = \frac{K_1 K_2 L}{B} \quad (\text{sign } \epsilon) \tag{1}$$

Taking the second derivative of the error equation and substituting into equation (1) the equation of motion can be expressed as:

$$\tau\ddot{\epsilon} + \dot{\epsilon} = - \frac{K_1 K_2 L}{B} (\text{sign } \epsilon) \tag{2}$$

Equation (2) can also be expressed as:

$$\tau \frac{d\dot{\epsilon}}{d\epsilon} = - \left[\frac{\frac{K_1 K_2 L}{B} (\text{sign } \epsilon) + \dot{\epsilon}}{\dot{\epsilon}} \right] \tag{3}$$

By substituting the identity:

$$\ddot{\epsilon} = \frac{d\dot{\epsilon}}{dt} = \left(\frac{d\dot{\epsilon}}{d\epsilon} \right) \left(\frac{d\epsilon}{dt} \right) = \frac{d\dot{\epsilon}}{d\epsilon} \dot{\epsilon}$$

Equation (3) can be integrated to yield a relationship which is suitable for display in a phase plane with coordinates ϵ and $\dot{\epsilon}$ respectively. Integration of equation (3) yields the trajectory equation:

$$- \tau \left[\frac{K_1 K_2 L}{B} (\text{sign } \epsilon) + \dot{\epsilon} - \frac{K_1 K_2 L}{B} (\text{sign } \epsilon) \ln \left\{ \frac{K_1 K_2 L}{B} \text{ sign } \epsilon + \dot{\epsilon} \right\} \right] = \epsilon + C \tag{4}$$

where c is a constant of integration evaluated at the initial conditions specified. Equation (4) defines the relationship between error and error rate during system transients.

Delayed Switching Line Equation

To determine the equation of the delayed switching line consider the system to be moving under a positive applied torque. The equation of motion as a function of time is:

$$\tau\ddot{x} + \dot{x} = \frac{K_1 K_2 L}{B} \tag{5}$$

or in phase plane notations:

$$-\tau \frac{d\dot{\epsilon}}{dt} = \left[\frac{K_1 K_2 L}{B} + \dot{\epsilon}\right]$$

Rearranging and integrating gives:

$$t = -\tau \ln\left[\frac{K_1 K_2 L}{B} + \dot{\epsilon}\right] + c \tag{6}$$

Evaluating the constant of integration c at $\dot{\epsilon} = \dot{\epsilon}_o$ and t = 0, equation (6) can now be written as:

$$t = \tau \ln\left\{\left[\frac{K_1 K_2 L}{B} + \dot{\epsilon}\right]\left[\frac{K_1 K_2 L}{B} + \dot{\epsilon}_o\right]^{-1}\right\} \tag{7}$$

Let $\dot{\epsilon}_o$ be the point where the trajectory crosses the $\dot{\epsilon}$ axis. Torque reversal now will be effective at t = T. If T is substituted into equation (7) and combined with the trajectory equation (4) an expression for the effective or delayed switching line results.

First the constant for equation (4) is evaluated at $\dot{\epsilon} = \dot{\epsilon}_o$ and $\epsilon = 0$ so that equation (4) may be written as:

$$\frac{\dot{\epsilon}_o - \dot{\epsilon}}{\frac{K_1 K_2 L}{B}} + \ln\left\{\left[1 + \frac{\dot{\epsilon}}{\frac{K_1 K_2 L}{B}}\right]\left[1 + \frac{\dot{\epsilon}_o}{\frac{K_1 K_2 L}{B}}\right]^{-1}\right\} = \frac{\epsilon}{\frac{\tau K_1 K_2 L}{B}} \tag{8}$$

Substitution of equation (7) into equation (8) results in the expression:

$$\frac{\dot{\epsilon}_o - \dot{\epsilon}}{\frac{K_1 K_2 L}{B}} + \left(-\frac{T}{\tau}\right) = \frac{\epsilon}{\frac{\tau K_1 K_2 L}{B}}$$

By eliminating $\dot{\epsilon}_o$ from equation (9) by substitution of equation (7) where t = T, an equation for the effective or delayed switching line results which is expressed as:

$$-\frac{\dot{\epsilon}}{\frac{K_1K_2L}{B}}+\left[1+\frac{\dot{\epsilon}}{\frac{K_1K_2L}{B}}\right]e^{\frac{T}{\tau}}-1-\frac{T}{\tau}=\frac{\epsilon}{\tau\frac{K_1K_2L}{B}}=-\left[1+\frac{\dot{\epsilon}}{\frac{K_1K_2L}{B}}\right]\left[1-e^{\frac{T}{\tau}}\right]\frac{T}{\tau} \quad (9)$$

or rearranging:

$$\dot{\epsilon}=-\frac{\epsilon}{\tau(1-e^{T/\tau})}-\left[\frac{K_1K_2L}{B}\right]\left[\frac{T/\tau}{1-e^{T/\tau}}+1\right] \quad (10)$$

The switching line is a straight line with a slope of $\frac{1}{-\tau(1-e^{T/\tau})}$ and a $\dot{\epsilon}$ intercept of $-\frac{K_1K_2L}{B}\left[\frac{T/\tau}{1-e^{T/\tau}}+1\right]$. When the torque is negative the $\dot{\epsilon}$ intercept is positive.

Limit Cycle Line

The system converges to a stable limit cycle and because of symmetry the magnitude of the maximum positive error will equal the magnitude of the maximum negative error. Since the maximum occurs on the ϵ axis, the constants of equation (4) can be evaluated at $\epsilon = +\epsilon_1, -\epsilon_2$ and $\dot{\epsilon} = 0$. Sign ϵ will carry the same respective signs of ϵ. Adding the two equations results in the expression:

$$(\epsilon-\epsilon_1)+(\epsilon-\epsilon_2)=-2\tau\dot{\epsilon}+\frac{\tau K_1K_2 \ln}{B}\left\{\left[1+\frac{\epsilon}{\frac{K_1K_2L}{B}}\right]\left[1-\frac{\dot{\epsilon}}{\frac{K_1K_2L}{B}}\right]^{-1}\right\}$$

and noting that $\epsilon_1 = -\epsilon_2$ the above equation can be simplified to:

$$\frac{\epsilon}{\tau\frac{K_1K_2L}{B}}=-\frac{\dot{\epsilon}}{\frac{K_1K_2L}{B}}+\tfrac{1}{2}\ln\left\{\left[1+\frac{\dot{\epsilon}}{\frac{K_1K_2L}{B}}\right]\left[1-\frac{\dot{\epsilon}}{\frac{K_1K_2L}{B}}\right]^{-1}\right\} \quad (11)$$

Equation (11) represents a curve in the phase plane which defines the condition that if torque reversal occurs at the instant the trajectory is crossing this curve, then the return trajectory will intersect the ϵ axis at a point equally distant but in the opposite direction from the origin as the previous crossing.

Maximum Limit Cycle Error Rate

Intersection of the curve represented by equation (11) and the delayed switching line (equation 10) gives the maximum value of error rate in the limit cycle. Simultaneous solution of equation (10) and (11) and denoting $\dot{\epsilon}$ as $\epsilon_{max.s.s.}$ yields:

$$\tfrac{1}{2} \ln \left\{ \left[1 + \frac{\dot{\epsilon}_{max.s.s.}}{\frac{K_1 K_2 L}{B}} \right] \left[1 - \frac{\dot{\epsilon}_{max.s.s.}}{\frac{K_1 K_2 L}{B}} \right]^{-1} \right\} =$$

$$\left[1 + \frac{\dot{\epsilon}_{max.s.s.}}{\frac{K_1 K_2 L}{B}} \right] e^{T/\tau} - 1 - \frac{T}{\tau} \qquad (12)$$

The maximum positive value error rate is equal in absolute magnitude to the maximum negative error rate.

Maximum Limit Cycle Error

The expression defining the maximum error developed during the limit cycle can be obtained by evaluating the constant of integration of equation (4) at $\dot{\epsilon} = \dot{\epsilon}_{max.s.s.}$; $\epsilon = \epsilon_{max.s.s.}$ and combining with equation (10) to eliminate ϵ. The magnitude of $\dot{\epsilon}_{max.s.s.}$ can be obtained from equation (12). The resulting expression for maximum error for $\epsilon > 0$ is:

$$\left[1 + \frac{\dot{\epsilon}_{max.s.s.}}{\frac{K_1 K_2 L}{B}} \right] \left[e - \left(\frac{\dot{\epsilon}_{max.s.s.}}{\frac{K_1 K_2 L}{B}} e^{T/\tau} \right) \right] = \qquad (13)$$

$$e - \left(\frac{\epsilon_{max.s.s.}}{\frac{\tau K_1 K_2 L}{B}} \right) e \left(e^{T/\tau} - 1 - \frac{T}{\tau} \right) \qquad (14)$$

Equation (14) can be further simplified by taking the log of the equation:

$$\ln\left[1+\frac{\dot{\epsilon}_{max.s.s.}}{\frac{K_1K_2L}{B}}\right]=\frac{\dot{\epsilon}_{max.s.s.}}{\frac{K_1K_2L}{B}}e^{T/\tau}-\frac{\epsilon_{max.s.s.}}{\tau\frac{K_1K_2L}{B}}+e^{T/\tau}-1-\frac{T}{\tau} \quad (15)$$

For $\epsilon < 0$ the sign of $\dot{\epsilon}_{max.s.s.}$ and $\epsilon_{max.s.s.}$ will be negative.

Limit Cycle Period

The period of a limit cycle can be derived by evaluating equation (6) between the limits of $-\epsilon_{max.s.s.}$ and $+\epsilon_{max.s.s.}$ which give the VALUE for $\frac{1}{2}$ the limit cycle period P. Therefore, the limit cycle period can be expressed as:

$$P = 2\tau \ln\left\{\left[1+\frac{\dot{\epsilon}_{max.s.s.}}{\frac{K_1K_2L}{B}}\right]\left[1-\frac{\dot{\epsilon}_{max.s.s.}}{\frac{K_1K_2L}{B}}\right]^{-1}\right\} \quad (16)$$

The predicted spike control system phase portrait and steady state frequency characteristics are shown in Figures 8 and 9 respectively.

The existence of a stable limit cycle is dependent on the presence of a damping term to negate the effect of the system transport lag. This can be seen by analyzing the points of intersection of the trajectory of a pure inertia load and the switching line in the first and third quadrants. The switching line is orientated relative to the coordinate axis with a positive slope of 1/T. The trajectory of an inertia load with no damping is a parabola. The intersections of the trajectory with the switching line occur at a large absolute value of error rate at each successive intersection such that the trajectory diverges, thus indicating system instability.

If damping is present, the trajectory converges or diverges, dependent on initial conditions, to a limit cycle which is represented by the intersection of the switching line with the limit cycle curve shown in Figure 8. If torque reversal occurs before crossing the limit cycle curve, the trajectory will converge, and if the switching occurs after crossing the limit cycle curve, the trajectory will diverge. In either case, the trajectory will approach a stable limit cycle as shown in Figure 8.

SPIKE POSITION CONTROLLER USING A DIGITAL PRESSURE PATTERN DECODER

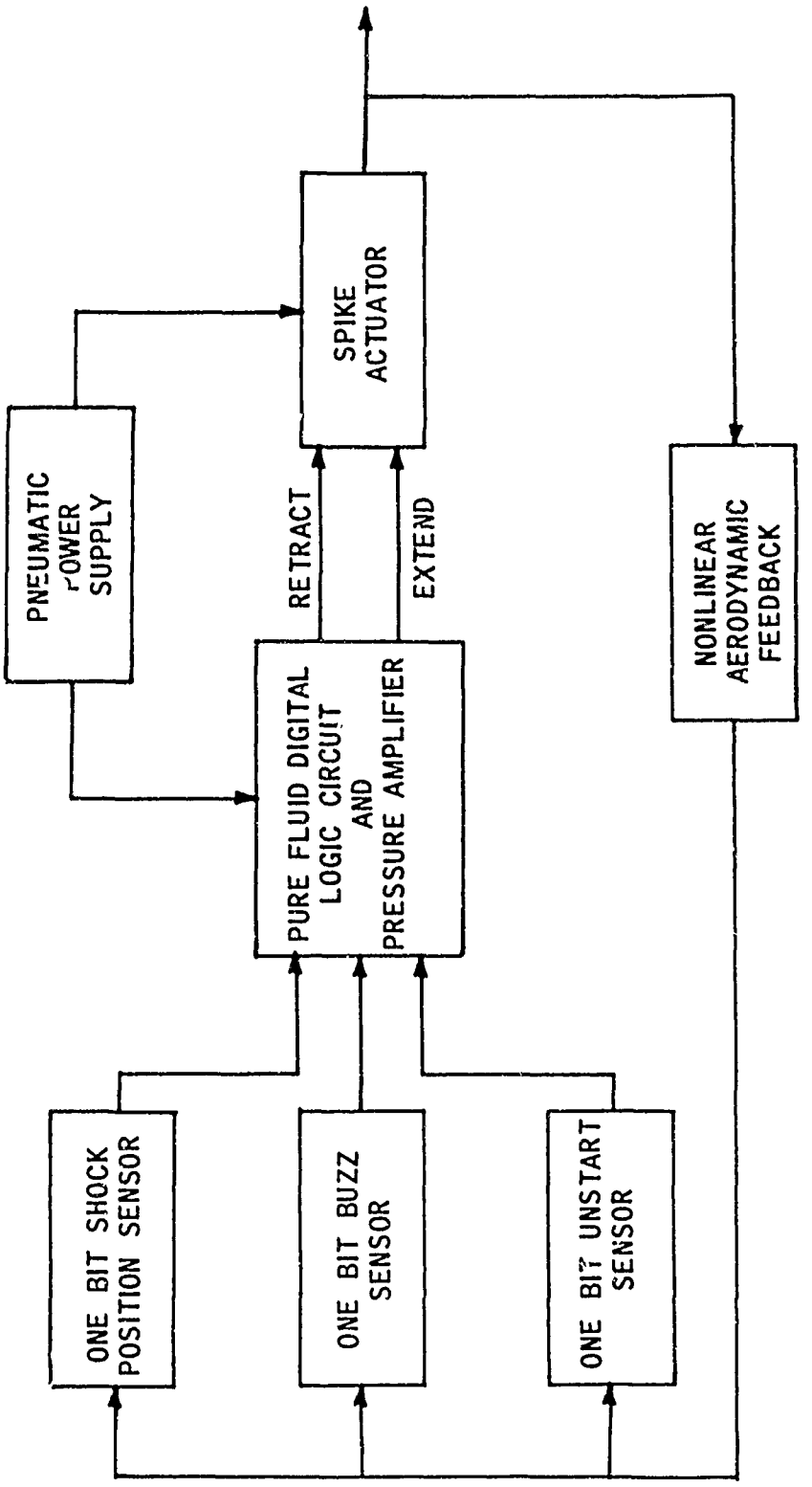

FIGURE 1

DIGITAL PRESSURE PATTERN SPIKE CONTROLLER
BLOCK DIAGRAM

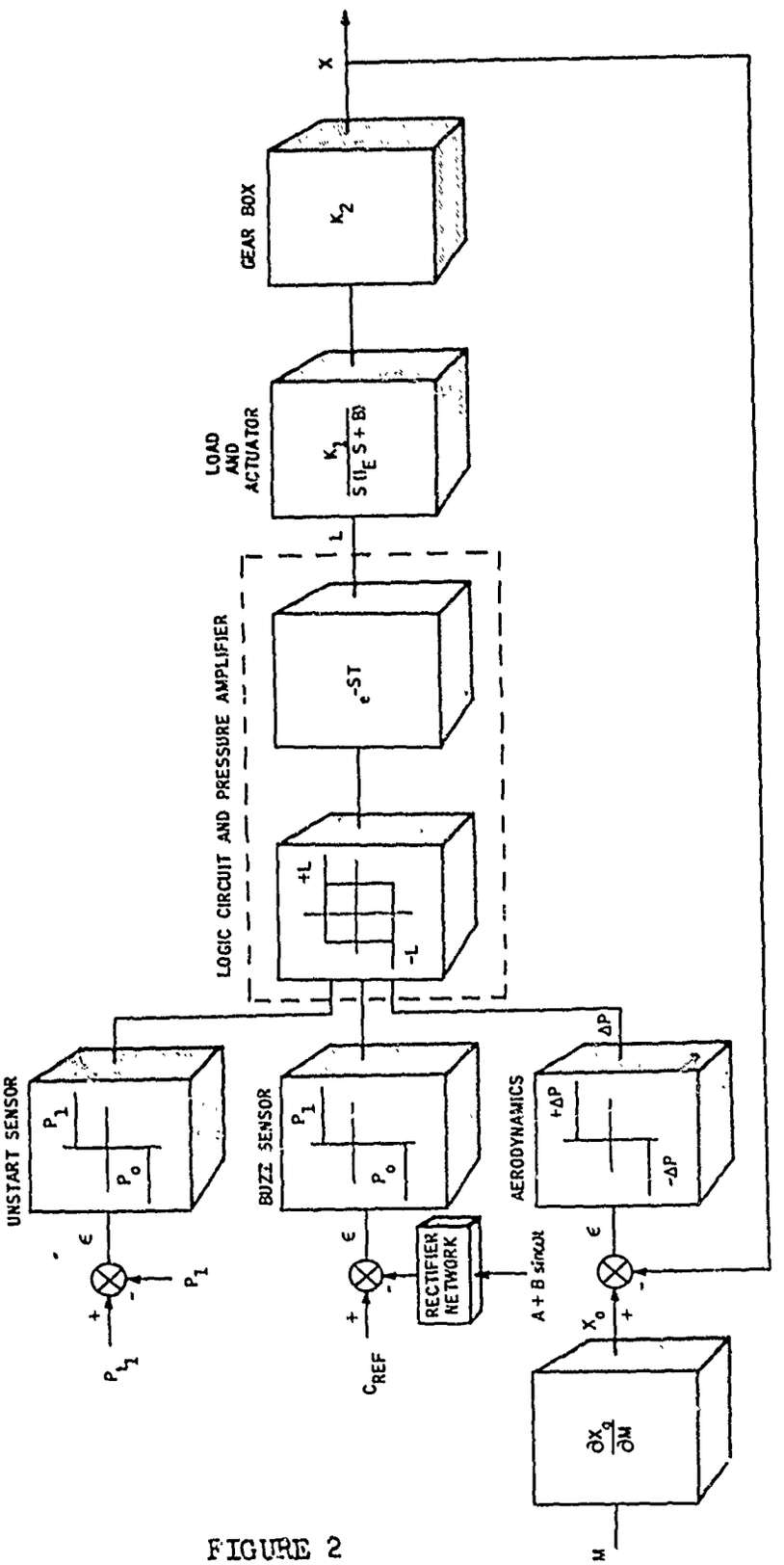

FIGURE 2

SIMPLIFICATION WITH HYPERPLANES

TWO-DIMENSIONAL INPUT SPACE

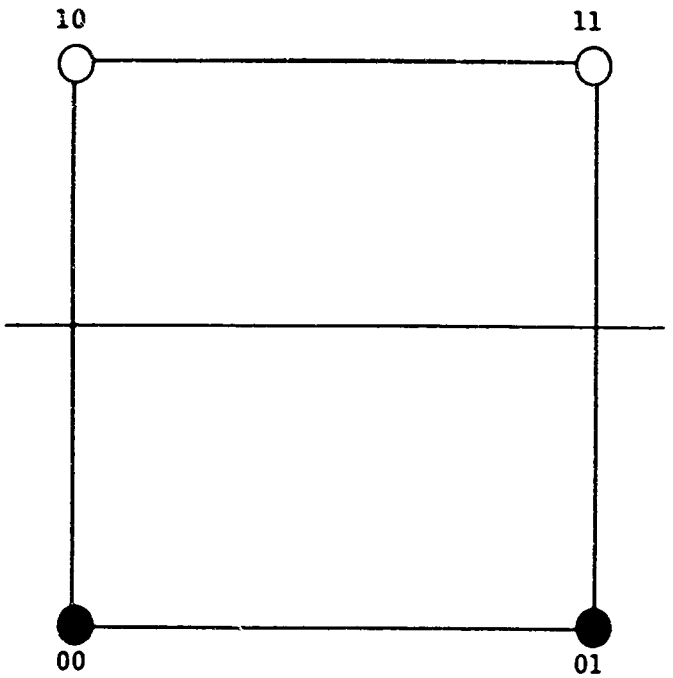

THREE-DIMENSIONAL INPUT SPACE

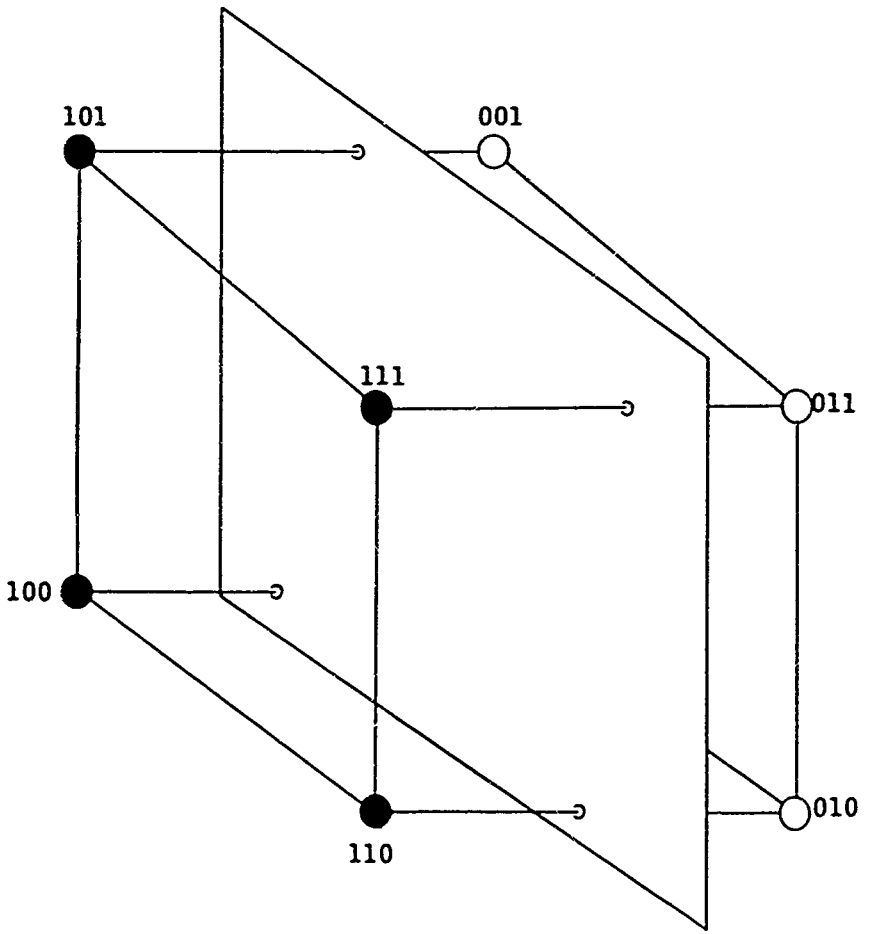

FIGURE 3

BINARY INPUT PATTERNS	ARBITRARY CLASSIFICATION
00	1
01	1
10	0
11	0

BINARY INPUT PATTERNS	ARBITRARY CLASSIFICATION
000	0
001	0
010	0
011	0
100	1
101	1
110	1
111	1

VEITCH DIAGRAM SIMPLIFICATION

SIX-DIMENSIONAL INPUT SPACE

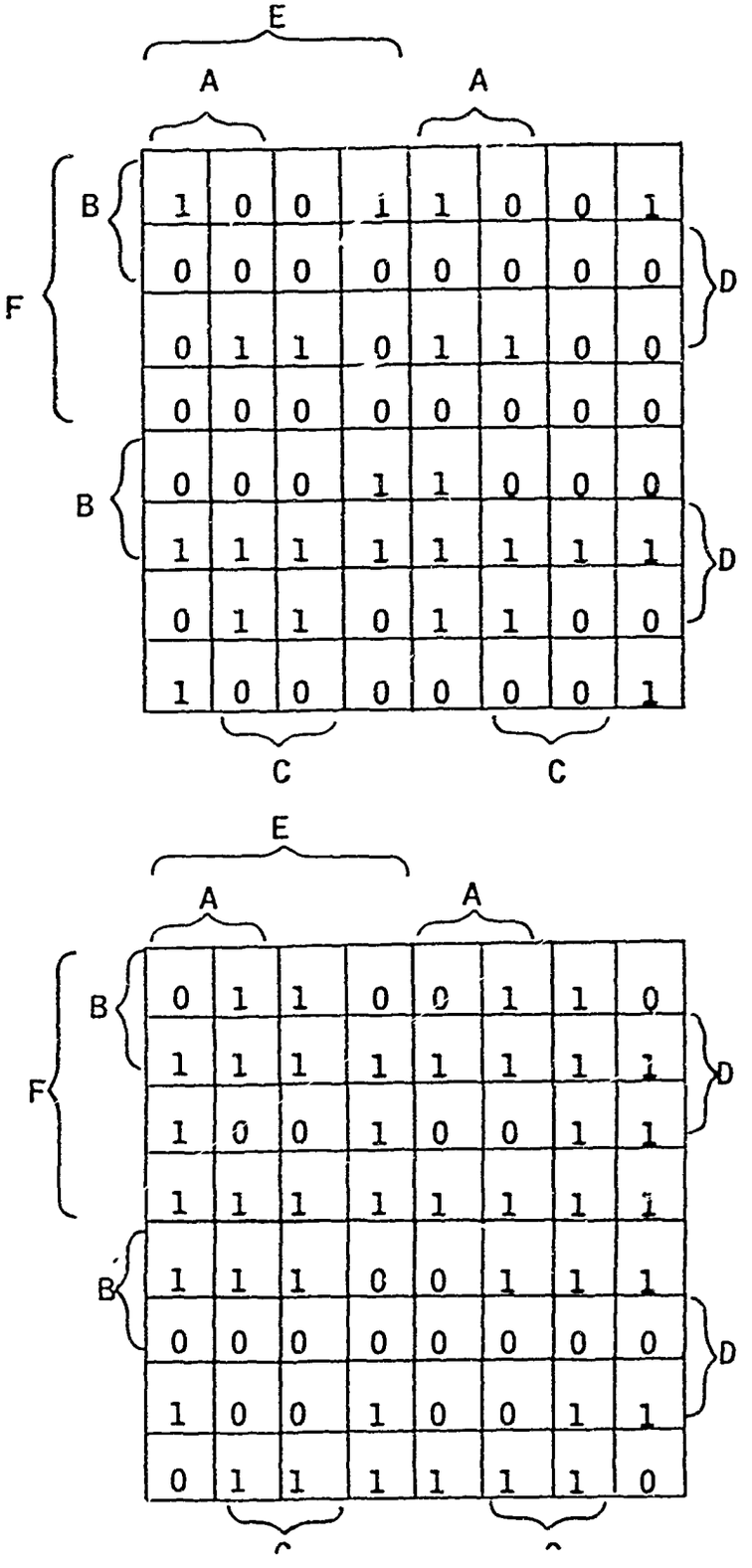

FIGURE 4

BINARY N-CUBE WITH PARTITIONING HYPERPLANE

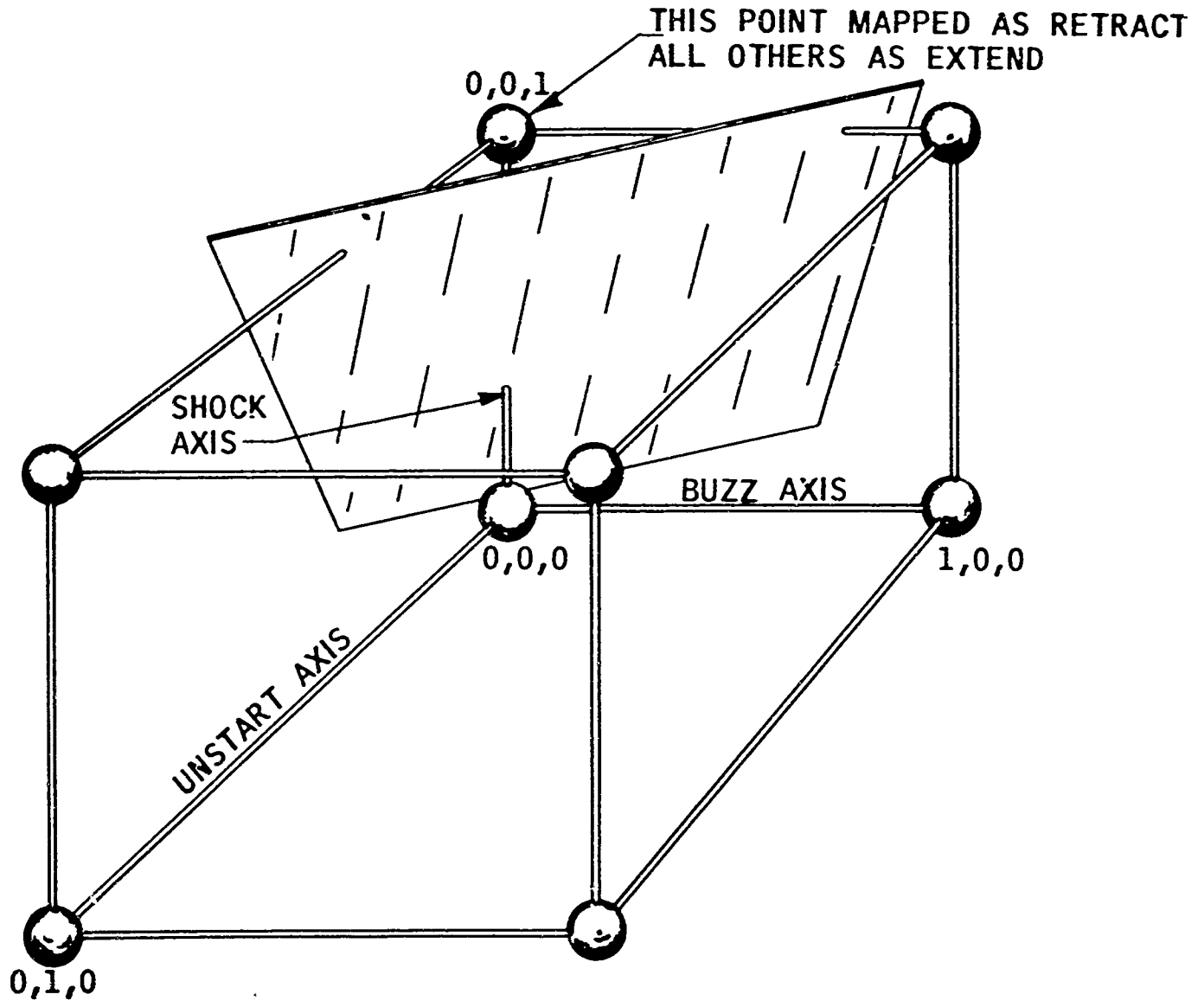

FIGURE 5

PURE FLUID PRESSURE PATTERN DECODER

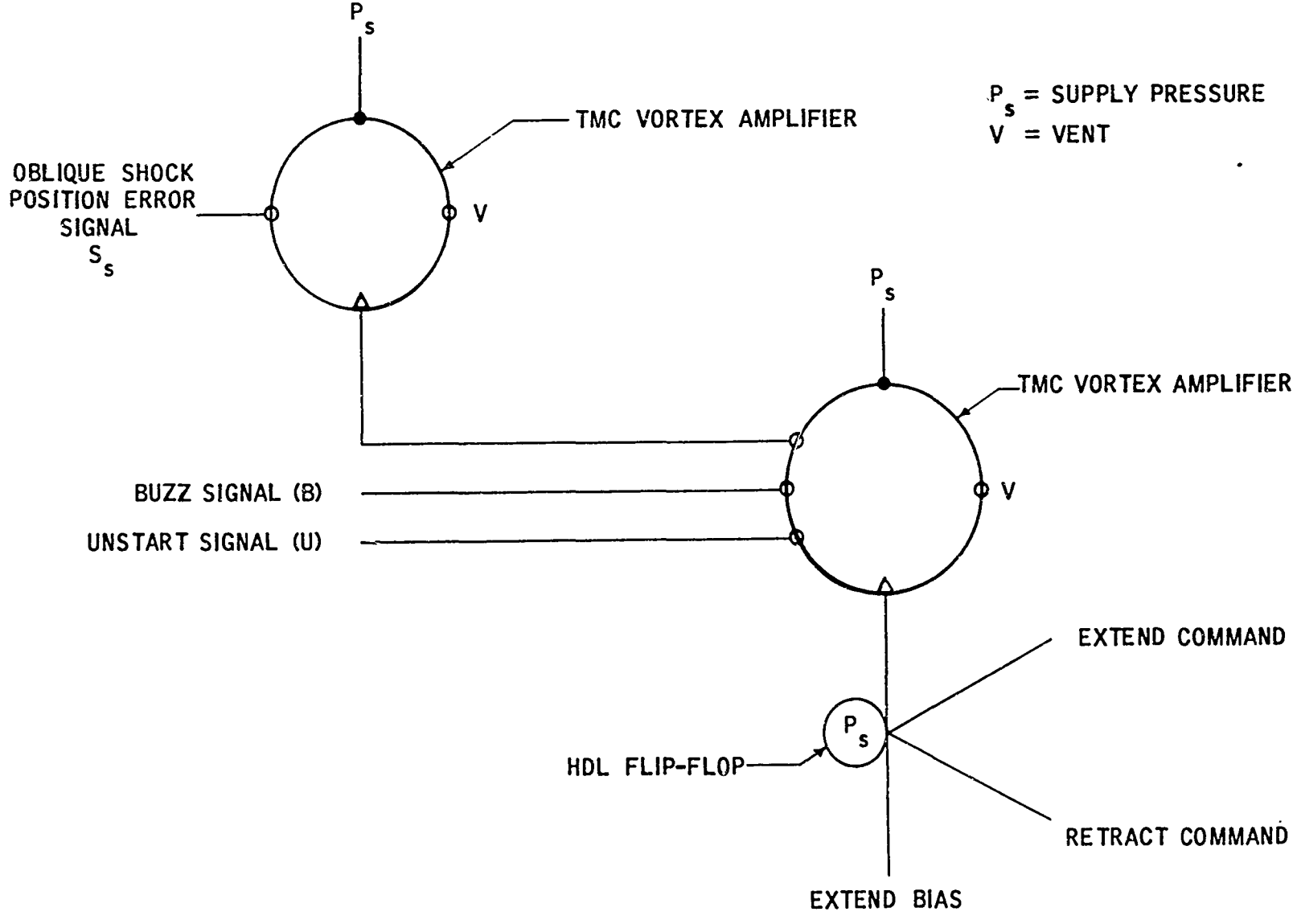

FIGURE 6

MODIFIED PRESSURE PATTERN SPIKE CONTROLLER BLOCK DIAGRAM

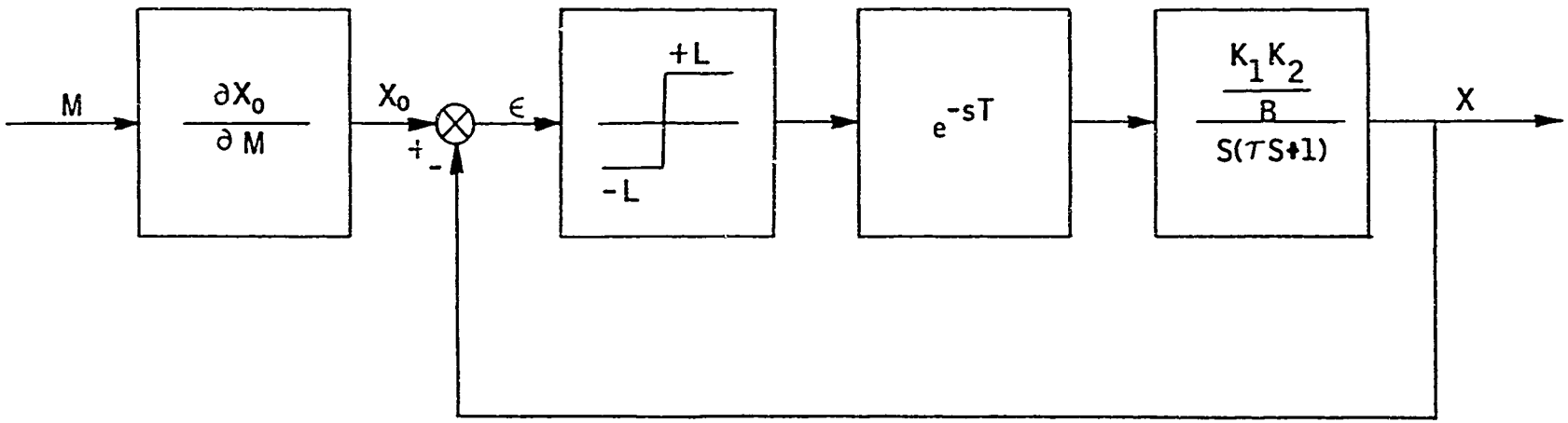

FIGURE 7

ϵ = ERROR SIGNAL

$\dot{\epsilon} = \frac{d}{dt}$ = ERROR RATE

τ = I/B

B = DAMPING COEFFICIENCT

I = EFFECTIVE SYSTEM INERTIA

K_1 = ACTUATOR TORQUE COEFFICIENT

K_2 = GEAR BOX GAIN COEFFICIENT

L = ΔP APPLIED TO ACTUATOR

M = MACH NUMBER

T = SIGNAL TRANSPORT TIME DELAY

X = SPIKE POSITION

X_o = SPIKE REFERENCE POSITION

SPIKE CONTROL SYSTEM PHASE PORTRAIT

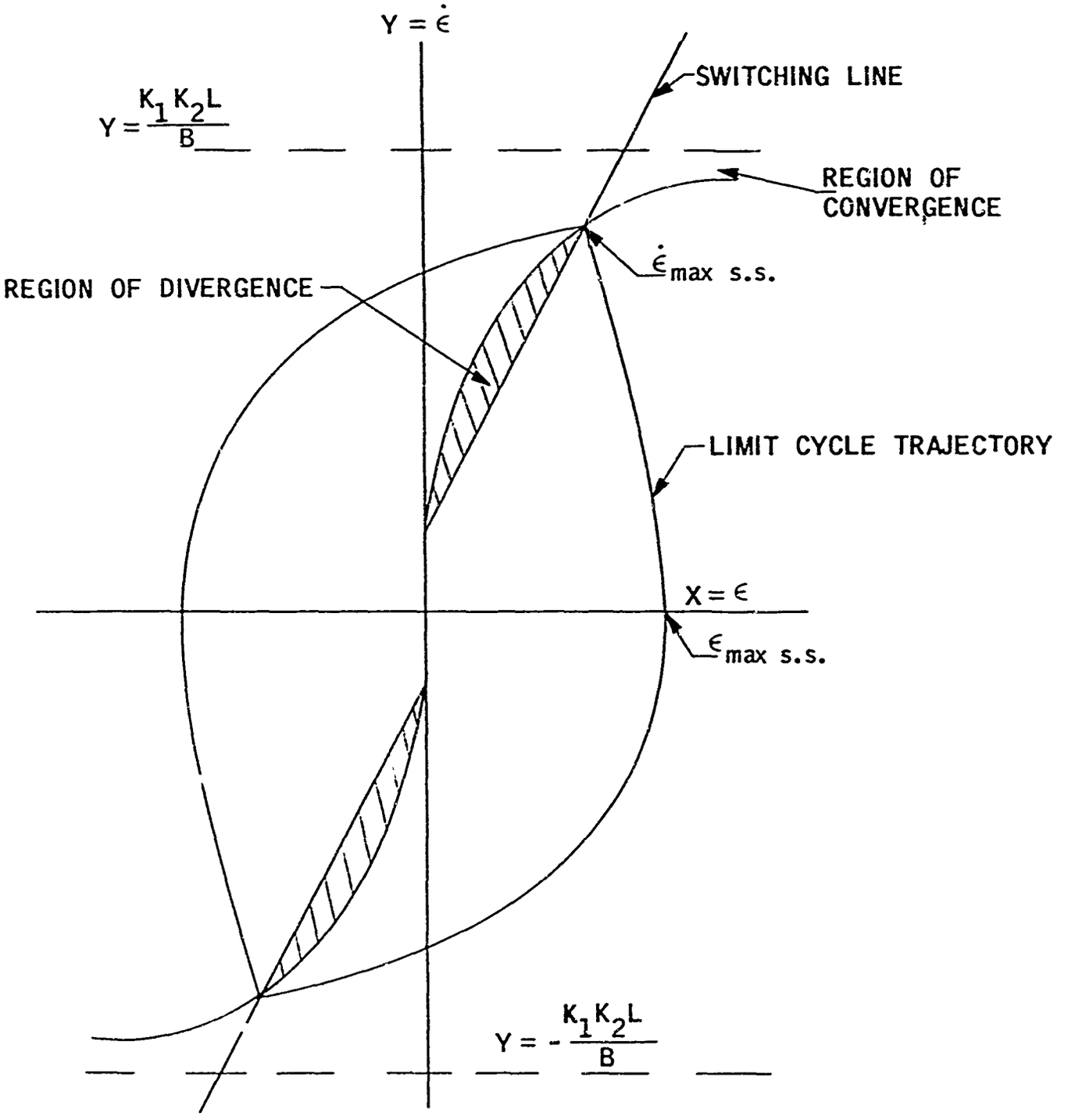

FIGURE 8

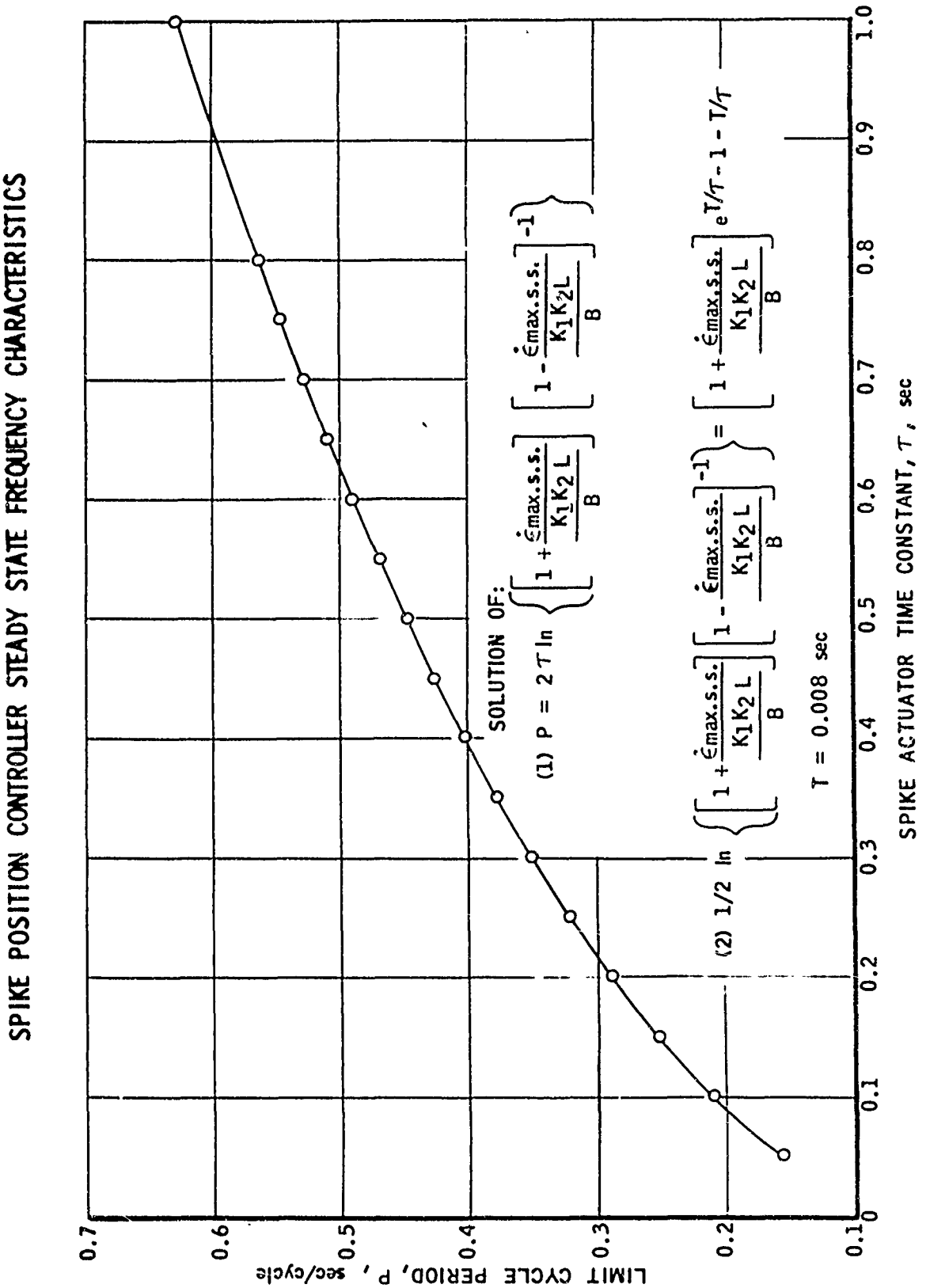
SPIKE POSITION CONTROLLER STEADY STATE FREQUENCY CHARACTERISTICS
LIMIT CYCLE PERIOD, P, sec/cycle
SPIKE ACTUATOR TIME CONSTANT, T, sec
SOLUTION OF:
(1) $P = 2\tau \ln \left\{ \left[1 + \frac{\dot{\epsilon}_{max.s.s.}}{\frac{K_1 K_2 L}{B}} \right] \left[1 - \frac{\dot{\epsilon}_{max.s.s.}}{\frac{K_1 K_2 L}{B}} \right]^{-1} \right\}$
(2) $1/2 \ln \left\{ \left[1 + \frac{\dot{\epsilon}_{max.s.s.}}{\frac{K_1 K_2 L}{B}} \right] \left[1 - \frac{\dot{\epsilon}_{max.s.s.}}{\frac{K_1 K_2 L}{B}} \right]^{-1} \right\} = \left[1 + \frac{\dot{\epsilon}_{max.s.s.}}{\frac{K_1 K_2 L}{B}} \right] e^{T/\tau} - 1 - T/\tau$
T = 0.008 sec
0.7
0.6
0.5
0.4
0.3
0.2
0.1
0
0.1
0.2
0.3
0.4
0.5
0.6
0.7
0.8
0.9
1.0

FIGURE 9

A Fluid Encoding System

by

Dr. Charles K. Taft and James N. Wilson

Case Institute of Technology

INTRODUCTION

Pure fluid amplifiers have great potential advantages for feedback control systems. Simplicity, low cost, ruggedness, no moving parts, small size are just a few of these advantages. In order to evaluate the feasibility of pure fluid amplifiers as control elements, a complete incremental digital control system is presently being developed at Case Institute of Technology.

Figure 1 shows a block diagram of the proposed system. The system will receive fluid flow pulses in either the plus or minus input lines of a bidirectional counter C. Each pulse directs the system to change the controlled variable θ by one increment or quanta. The position of the controlled variable is detected by a direction sensitive pulse generator or quantizer Q. This device feeds back a fluid pulse whenever the controlled variable takes on values equal intervals apart. The pulses are fed to the minus or plus inputs of the counter depending on whether the controlled variable is increasing or decreasing. The state of the counter is the algebraic difference

between the number of input and feedback pulses. This state is the quantized system error which is then converted to an analog signal by a digital-to analog converter D/A. The converter output is amplified by the power amplifier P to deliver power to an actuator A. The actuator then moves the load L to reduce the state of the counter to zero.

This system is a basic type of digital control which can be used to control any variable capable of representation by a direction sensitive pulse train. If a direction sensitive pulse generator could be developed which would accept a mechanical input rotation, the system could control any variable which can be expressed as a mechanical rotation. Thus, the design of a quantizer becomes an important part of the overall control system design. This paper describes the encoder design and development.

QUANTIZER LOGIC

A quantizer can be mechanized photoelectrically, electromagnetically or electromechanically by means of a rotating disc which interrupts a light beam, or shunts lines of magnetic flux or commutates electrical current.[1] The logical circuitry used to produce the quantizer output is essentially the same for these three approaches. The basic form is used in the fluid quantizer developed. The photoelectric quantizer operates as follows: A disc is attached to the angular rotation to be

quantized. The disc has a series of evenly spaced transparent and opaque zones around its circumference. The circumferential width of the opaque and transparent zones at a fixed radius are equal, as shown in Figure 2. Two or more pairs of photocells and lamps are located at the zone radius. The photocells and the lights are located on opposite sides of the disc so that the transparent zones allow the light beam to reach the photocells. The opaque zone prevents the light from reaching the photocells. The relative position of the two photocells and lights is adjusted so that one photocell just begins to receive light when the other cell is half way between two dark regions. This is illustrated by rotating the disc at a constant speed and observing the voltage output from the photocells. The resulting wave form of the two voltages is shown in Figs. 3a and 3b. If the photocells are located correctly, the two square waves should be 90° out of phase.

If one photocell output voltage is differentiated, the resulting pulses can be used to detect the transparent to opaque zone transitions. These pulses then indicate when the controlled variable (in this case angular rotation) has taken on particular values. However, it is also desirable to distinguish between clockwise and counter clockwise rotation. That is, it is desirable to direct the pulses into one line when the rotation is clockwise and into another line for counter clockwise rotation. Figure 3 indicates how to perform this process. Call the positive pulse generated by differentiating V_A (the voltage from photo-

cell A), α_A and the negative pulse β_A. Notice that when the disc is rotating counter clockwise β_A occurs when V_B is off and α_A occurs when V_B is on. For clockwise rotation α_A occurs when V_B is on and β_A occurs when V_B is off. Thus, using Boolean notation,

$$CW = \alpha_A \cdot V_B + \beta_A \cdot \bar{V}_B$$

$$CCW = \beta_A \cdot V_B + \alpha_A \cdot \bar{V}_B$$

The wave forms from photocells A and B, shown in Figs. 3a and 3b, are for an arbitrary but constant angular rotation. The Boolean equations derived are valid for any rotational speed. Thus, the direction sensing portion of the quantizer can be mechanized by implementing the given Boolean equations with electronic logic elements. Since, in the project described herein, it is desired to produce a fluid quantizer, the logical circuitry is mechanized using pure fluid devices.

PURE FLUID QUANTIZER

In order to minimize power consumption in the computational circuits of the pure fluid control system, low pressure air (1-2 psig) is used.

Quantizer Disc

The principle of the disc with alternate opaque and transparent zones interrupting the light received by photocells appeared to be a satisfactory concept to use in the design of

a pure fluid quantizer. A slotted disc is used to interrupt the flow between a supply nozzle and a receiver nozzle. The slots correspond to the transparent zones in the photoelectric quantizer disc. The nozzles would play the role of light source and receivers the role of photocells. In this way, a pure fluid quantizer is mechanized, as shown in Figure 4.

Two such nozzle sets are located on opposite sides of the disc. The supply nozzles in each set are pressurized with air. A plenum chamber slightly upstream from each nozzle maintains a fairly constant supply pressure P_S. The receiver output flow depends upon:

a. the net area of flow communication between supply and receiver nozzle. The flow area depends in turn upon the net angular rotation of the encoding disc.

b. the relative distance between supply and receiver nozzles and the encoding disc. To recover maximum flow, the distance between supply and receiver nozzles should be less than 6 nozzles widths, in accordance with results reported by Albertson[2] for a free jet. Increasing the distance between either receiver nozzle and the encoding disc tends to increase the leakage area to surroundings.

c. the width of the receiver nozzle. The wider the nozzle, the more flow captured. However, there is an upper limit on the width of the receiver

nozzle to preserve good definition near a transition zone. It is noted that presence of one edge of the disc slot near the edge of the supply nozzle provides an adjacent wall to which the jet may attach. The influence of a slot near a transition zone could increase or decrease the receiver flow dependent upon which side of the transition zone the slot edge is.

d. the receiver pressure which in turn depends on the load being driven. Figs. 5 through 8 show the normalized flow pressure load characteristics of the receiver for various geometries.

It is apparent that the recovery characteristics are most affected by the width of the receiver nozzle. The width of the quantizing disc and spacing between nozzles have only secondary effects. There does appear to be a slight increase in recovered flow for the closer nozzle spacing.

The slots in the quantizing disc should have the shape as shown in Figure 9a. As the disc turns, the supply nozzle should be uncovered in as short an angular distance as possible. This means that the nozzle included angle should be small relative to slot included angle. Figure 9b shows the ideal receiver flow at a fixed receiver pressure for various ratios of nozzle to slot angle. The smaller this ratio the better the definition at a transition point.

The radial length of both supply and receiver nozzles is to some degree arbitrary and can be designed to meet the flow requirements of subsequent circuitry.

PNEUMATIC DIRECTION SENSING CIRCUIT

A previous section described the logical approach for determining direction of rotation using the photoelectric quantizer. It is noted that a pulse indicating a change in output voltage of one photocell is gated logically with the voltage level of the opposite photocell. In order to eliminate a one "quanta" hysteresis, the pulses indicating both the OFF to ON and ON to OFF voltage changes on one photocell must be used. In other words, the output voltage of the photocell must be differentiated.

One means of obtaining the equivalent of a derivative of a fluid flow or flow transition signal using pure fluid devices is as follows: Consider a bistable element in which one control port is flow biased before a flow level is admitted to the supply port. The bias flow causes the initially unstable supply flow to reattach to the wall dictated by the bias. A portion of the supply flow may be delayed in time and admitted to the opposite control port. (The time delay may be achieved by either a length of tubing or another bistable element). When the flow in the opposite control port reaches a value sufficiently large to overcome the bias flow, the supply jet

is switched to the opposite wall. In this way a flow pulse is generated from a step in flow. The time duration of the flow pulse is related to both the delay time and the switching characteristics of the bistable element. This scheme provides a means of generating a flow pulse for a positive step in control flow obtained from the quantizer receiver. The pulse forming circuit is pre ented in Figure 10 which shows the entire direction sensing circuit.

This method may be employed to generate transition pulses. Let Q_A be the flow signal from receiver A, and α_A be the generated transition pulse. In order to generate a β_A pulse, a flow level which is present when Q_A is OFF and absent when Q_A is ON is required.

A second supply receiver set spaced exactly one slot width circumferentially from the set A would provide the necessary complementary flow level. Practically, this is a poor approach, for the spacing of each nozzle becomes critical and could lead to erroneous information due to tolerances in the disc slots and relative spacing of the nozzles. A more practical scheme is to use a single input active NOR gate, which acts as an inverter. If Q_A is present, the active NOR supply jet is switched to the OR output. In the absence of Q_A, the supply jet delivers pressure to the NOR output. Thus, each output of the NOR gate can be shaped to form α_A and β_A transition flow pulses using the circuit described previously.

The use of a NOR gate for generating Q_A and its complement has several advantages over using a second supply-receiver set to provide the complementary flow:

a. The flow Q_A need only be sufficient to switch the NOR gate. The NOR gate provides one stage of amplification and, consequently, the required receiver output flow and pressure is considerably less (approximately a factor of 10) than that required to generate α_A and β_A pulses of similar strength using Q_A directly in the pulse forming circuit. This permits an increase in resolution of the encoding disc since the supply nozzles may have smaller width.

b. The need of an extra supply receiver nozzle set to generate the complementary flows is eliminated.

c. When the NOR gate output flows are used as supply flows to the pulse forming circuits, the resulting α_A and β_A pulses have much steeper initial slope than otherwise obtainable with the Q_A flow used directly. This is quite important at very low angular rotation near a transition point. The slope of the Q_A flow versus time curve increases with increasing angular velocity. If a NOR gate is eliminated, the α_A pulse before cut off has essentially the same slope as the Q_A flow. The α_A (or β_A) pulse generated without the use of the NOR gate varies both in amplitude and duration.

It is desirable from an operational viewpoint that the α_A and β_A pulses which must drive subsequent circuitry have essentially the same amplitude and time duration.

In using a NOR gate, a transition pulse is generated only after the NOR supply jet switches from one output to the other. The pulse forming circuits are therefore supplied with essentially a constant flow. Hence, the α_A and β_A flow pulses have constant amplitude and a time duration determined by the dynamics of the pulse forming circuit.

Since there is some freedom in selecting the amplitude and duration of the transition pulses, this permits selecting a desired relationship to obtain maximum speed of operation of subsequent circuitry.

d. The use of a NOR gate to provide the complementary flow signal eliminates the possibility of generating erroneous pulses for sufficiently small oscillations near a quanta point. This is made clear by considering the case in which an extra supply receiver set provides the complementary flow. Call this flow Q_C.

It is entirely possible that, due to inaccurate nozzle spacing or unequal slot widths, there will be a finite amount of overlap or underlap between the Q_C and Q_A flow signal.

Assume, for clarity, that the ideal output wave forms are rectangular and an oscillation amplitude of less than one-half slot width occurs. For this case, the Q_B level remains a constant value. Hence, a change in Q_A gated with the Q_B level generates a pulse indicating one direction of rotation. Similarly, for a change in Q_C (complement of Q_A) with the same Q_B level, the opposite direction of rotation is indicated. For either overlap or underlap of the Q_A and Q_C signals, it is possible that the disc oscillates with an amplitude sufficient only to intersect one side of the hysteresis region and return followed by a reentrance. This would generate either two α_A or two β_A pulses in succession. A bidirectional counter recording the pulses would register a net change in direction of two quanta while actually there is no change.

This problem does not exist when a NOR gate provides the complementary flow signal. This is accomplished by the hysteresis in the input characteristic of the NOR gate, as shown in Figure 11. It is impossible to generate two α_A pulses in succession without generating an intermediate β_A pulse. In other words, for an oscillation about a quanta point, a switch to the OR output (generating an α_A pulse) must be followed by a return to the

NOR output (generating a β_A pulse) before a re-switch to the OR output can take place.

The equations describing direction of rotation given previously are:

$$CW = \alpha_A \cdot Q_A + \beta_A \cdot \overline{Q}_B$$

$$CCW = \alpha_A \cdot \overline{Q}_B + \beta_A \cdot Q_B$$

It is noted that the complement of Q_B flow is required. A NOR gate provides the required complement, thereby reducing the output flow pressure requirement of the B receiver nozzle.

The α_A and β_A pulses can be gated with the appropriate Q_B levels by means of a bistable logic element. For purposes of discussion, consider the problem of gating the α_A pulse only. The α_A pulse is fed to the supply port of a bistable element while one control port is prebiased by the Q_B flow signal and the other by its complement. Since the bias levels are present before the α_A pulse arrives at the supply port, the pulse will be steered to the output dictated by the bias. One output indicates CW rotation and the other CCW rotation in accordance with the above equations.

A similar scheme is used for gating the β_A pulse (see Figure 10).

This method of gating is essentially passive in nature and, consequently, has no dynamics other than the transport lag through the element.

In order to fulfill the equations for direction sensing, the appropriate output signals from the gating elements must be connected by a logical OR gate. Tuo dual input NOR gates are used to logically sum the gated α_A and β_A pulses for each direction of rotation. The OR output of each gate is fed to the appropriate input channels of a bidirectional counter.

SPEED OF OPERATION

In order to predict the ultimate speed of operation of the complete encoding system, the dynamics of the individual components must be considered.

Consider first the NOR gate as used to invert the Q_A and Q_B flow levels. Figure 12 shows a curve of switching time versus the ratio of control flow to supply flow for a NOR gate designed at Case. (Here the switching time is defined to be the elapsed time between application of a step in control flow until the OR output reaches 90% of the final value.) Also shown are the reattachment times for the same element. (The reattachment time is defined to be the elapsed time between removal of the control signal until the NOR output reaches 90% of the final value.)

Although limited data is presented for this particular element, the general characteristics are the same as those observed on other elements and also observed by Johnson.[3] The important point is that the switching time decreases as the ratio of control flow to supply flow increases. For a given ratio of control flow to supply flow, the switching time decreases as the supply flow increases. This has also been observed by Johnson[3] and Comparin[4] et al and is predicted by analytical studies at Case.[5] Because the product of switching time and control flow to switch tends to be constant, it appears that a certain critical amount of fluid must be injected into the separation bubble before switching occurs.

Expressed mathematically,

$$\int_0^{T_s} Q_c(t)\, dt \geq A$$

where $Q_c(t)$ = control flow

T_s = switching time

A = a constant determined by the geometry of the element and the supply flow.

Another point to be noticed is that the reattachment time, although somewhat erratic, tends to be constant and decreases as the supply flow increases.

Consider now the receiver nozzle is driving the NOR gate. Assume also that the receiver output flow has the wave form shown in Figure 13. For very low frequencies, the NOR gate is switched by a relatively low receiver flow Q_A. As the disc speed is increased, the slope of Q_A increases. In addition, NOR element switching occurs at a higher level of Q_A. However, the time to switch decreases. Since the NOR element switching flow increases in magnitude with increasing frequency, the angle of α_A and β_A pulse location shifts slightly with speed. The ultimate speed, of course, is reached when the area under the Q_A curve for one cycle becomes less than constant A noted above.

This reasoning can be extended to the case in which the transition pulses (α_A and β_A) are used to drive subsequent circuitry such as a bidirectional counter. Dependent upon the amplitude of the flow into the pulse forming circuit and the dynamics of the circuit, the α_A and β_A pulses will have a fixed amplitude and duration. This in turn limits the frequency at which tney are capable of driving other dynamic elements.

CONCLUSIONS

The feasibility of a pure fluid quantizer has been demonstrated by the design described in this paper. The speed of operation of the quantizer and its direction sensing circuits will depend primarily on the following factors:

1. The maximum amount of flow that the disc receiver can deliver to the NOR element.
2. The reattachment time of the NOR element.
3. The quantizer slot width which will determine the amount of fluid delivered to the receiver at any speed.
4. The transition pulse amplitude and width.

The logical design of a pure fluid digital circuit has been demonstrated proceeding from a logical requirement to the finished fluid circuit design. The use of logical NOR element in the circuit prevents the possible generation of erroneous pulses for disc oscillations near a transition point.

The bistable element is used as an "AND" gate which eliminates the switching time of an active gate. Thus, the unique characteristics of pure fluid elements are used in the logical circuit design.

The versatility of fluid logic elements has also been demonstrated. It is noted that only two basic elements, namely a NOR gate and a flipflop, are required to implement all logical functions.

REFERENCES

1. Susskind, A. K., "Analog - Digital Conversion Techniques," Wiley and Technology Press, 1957.
2. Albertson et al, "The Diffusion of Submerged Jets," ASCE Proceedings, Vol. 74, No. 10, Dec. 1948.
3. Johnson, R. P., "Dynamic Studies of Turbulent Reattachment Fluid Amplifiers," MS Thesis University of Pittsburgh, 1963.
4. Comparin, R. A. et al, "On the Limitations and Special Effects in Fluid Jet Amplifiers," ASME Symposium on Fluid Jet Control Devices, November 1962.
5. Progress Report No. 7, to Harry Diamond Laboratories, Contract DA-49-186-AMC-79(D), "A Fluid Encoding System," April 1964.

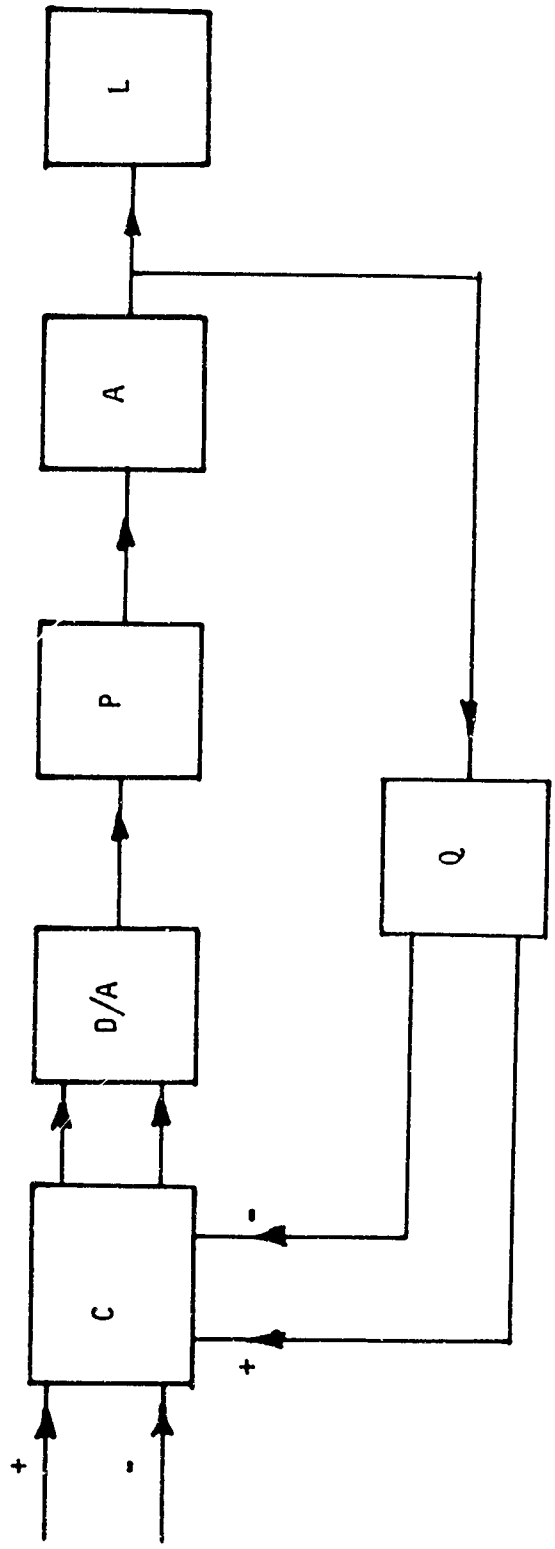

Figure 1 Schematic of Pure Fluid Digital Control System

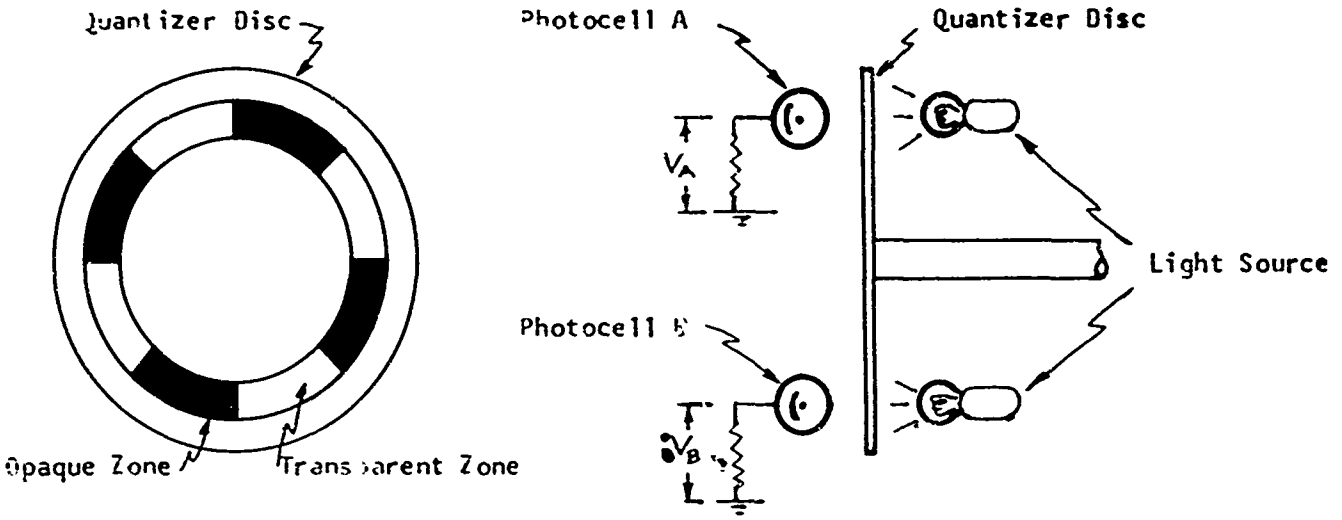

Figure 2 Photoelectric Quantizer

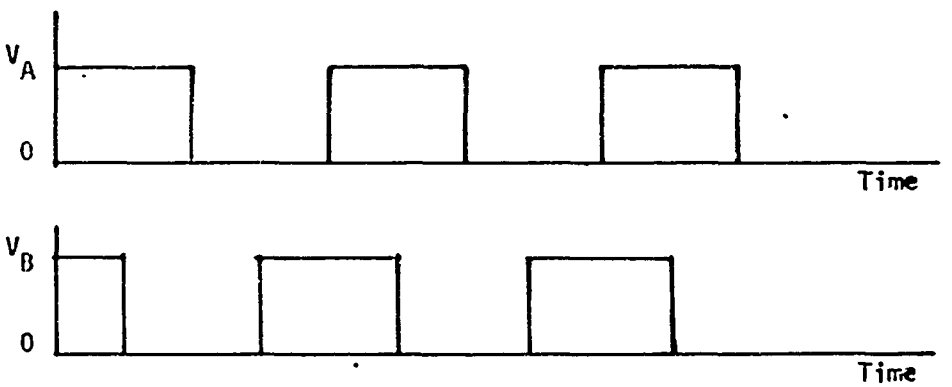

Figure 3(a) Photocell Output Voltage - CW Rotation

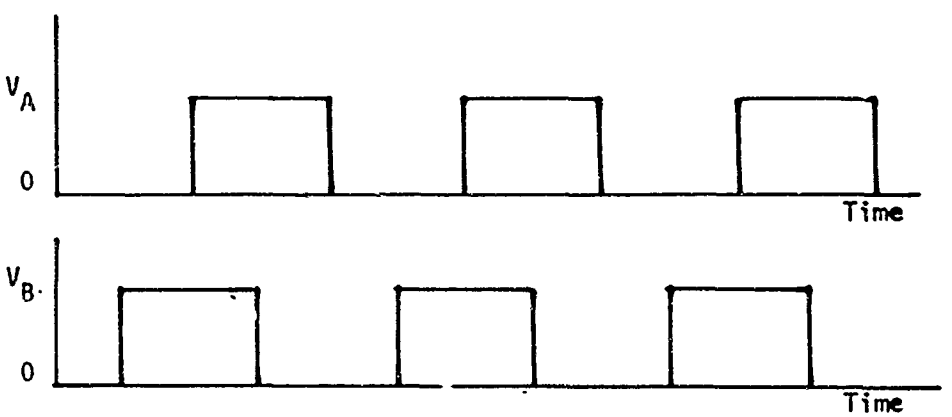

Figure 3(b) Photocell Output Voltage - CCW Rotation

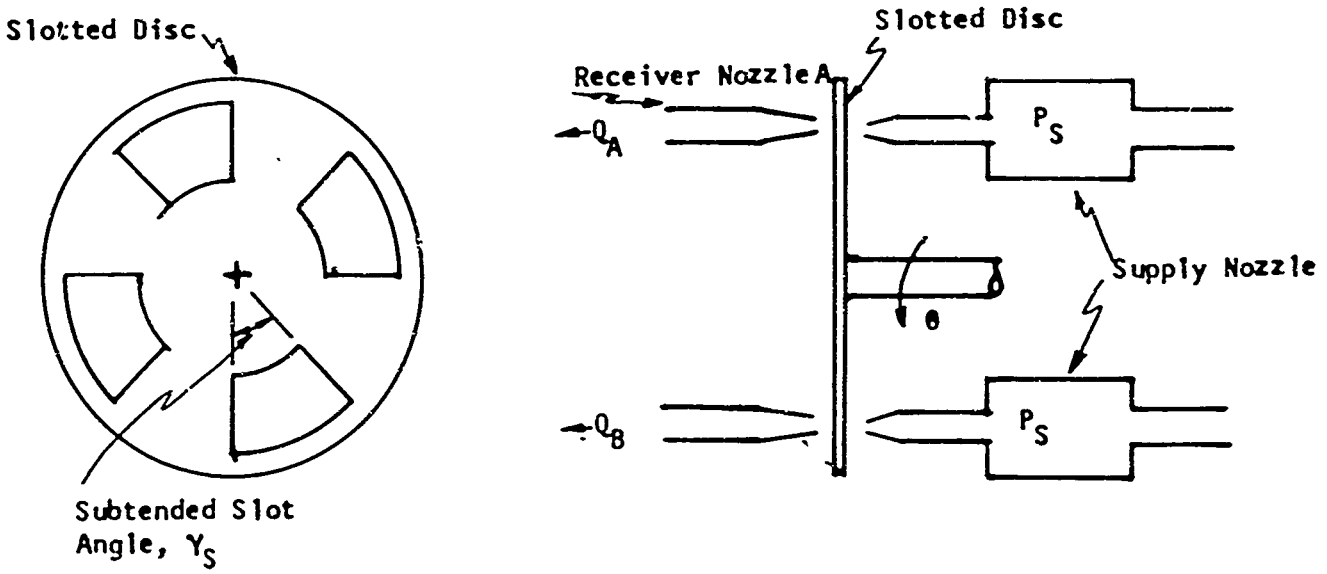

Figure 4(a) Pure Fluid Quantizer

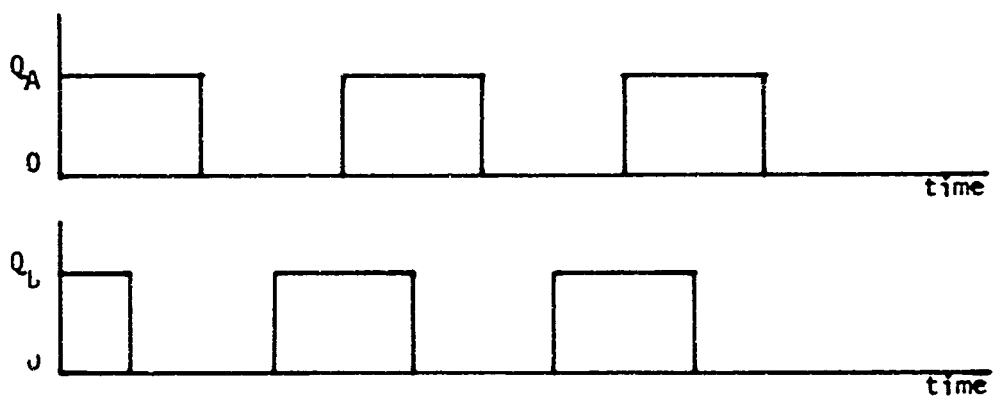

Figure 4(b) Receiver Output Flow - CW Rotation

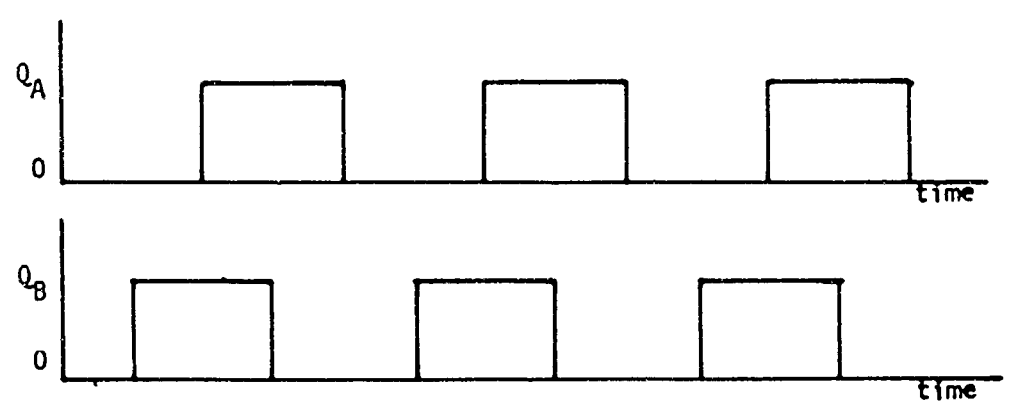

Figure 4(c) Receiver Output Flow - CCW Rotation

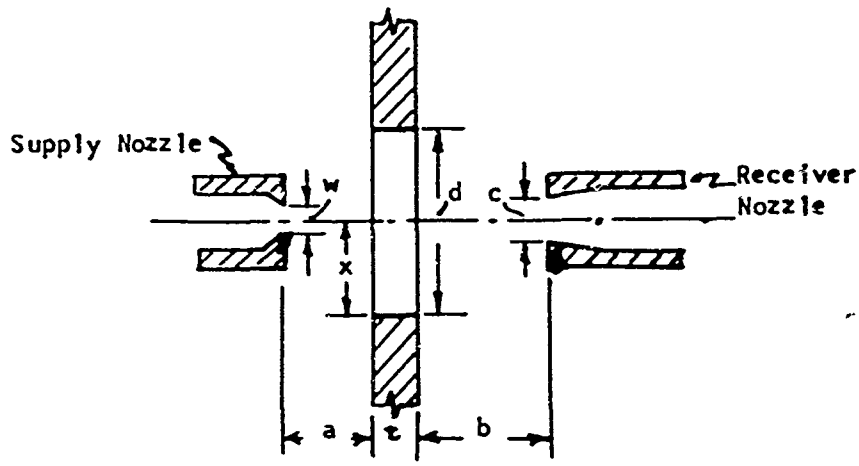

a = 1w
b = 1w
c = 1w
d = 4w
t = 2w
x = 2w
w = .015"

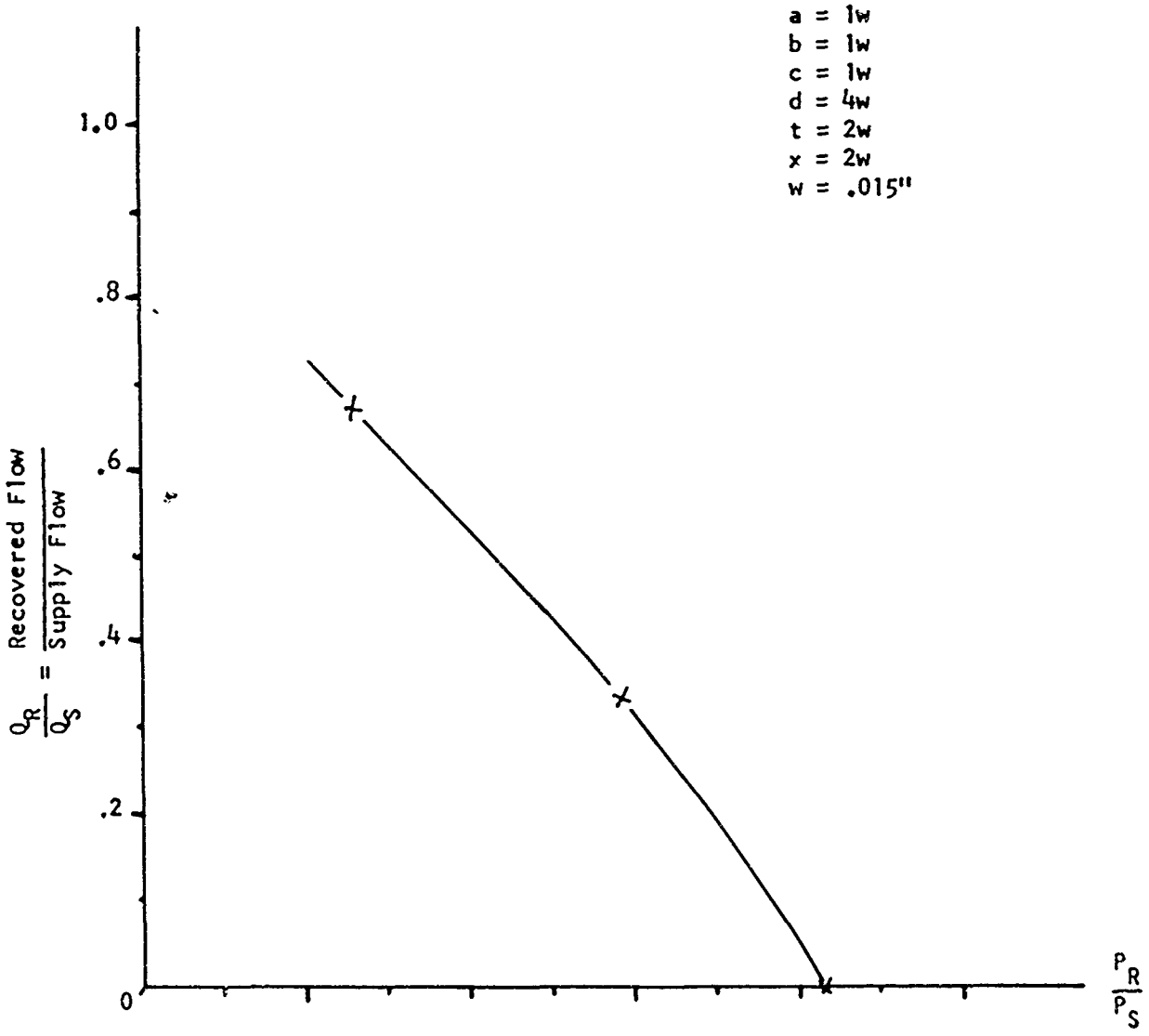

Receiver Flow-Pressure Characteristics

Figure 5

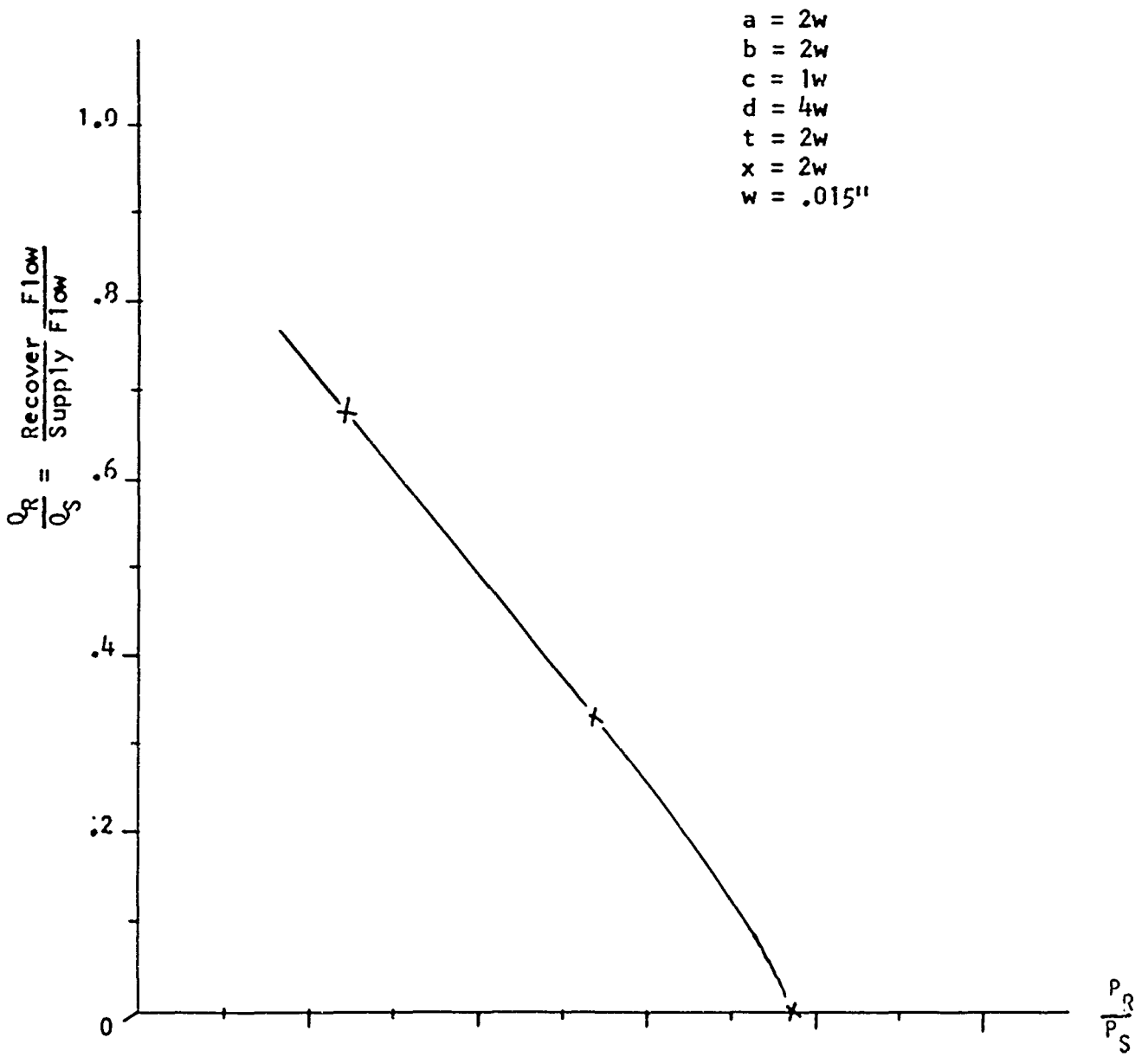

Figure 6 Receiver Flow-Pressure Characteristics

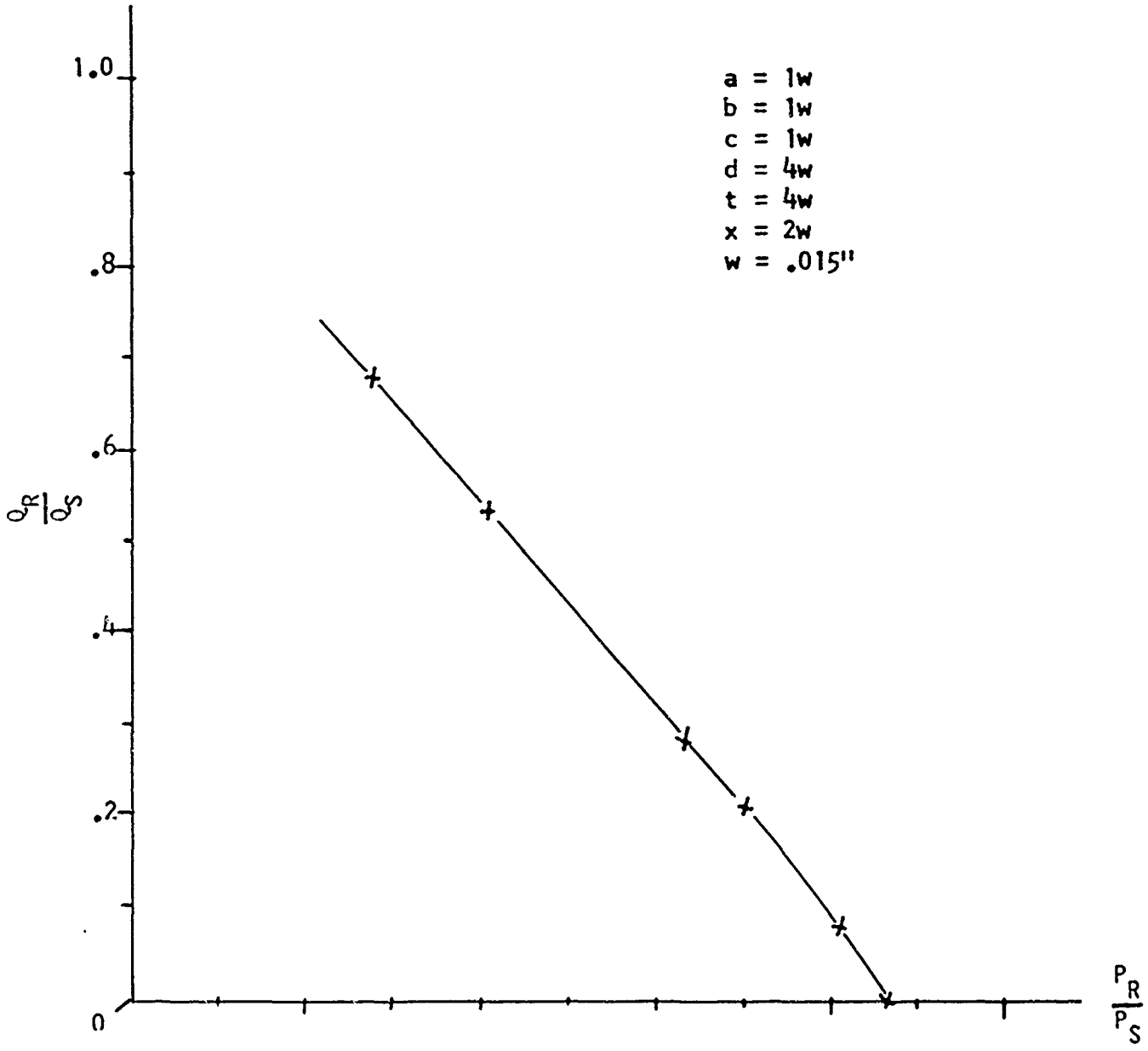

Figure 7 Receiver Flow-Pressure Characteristics

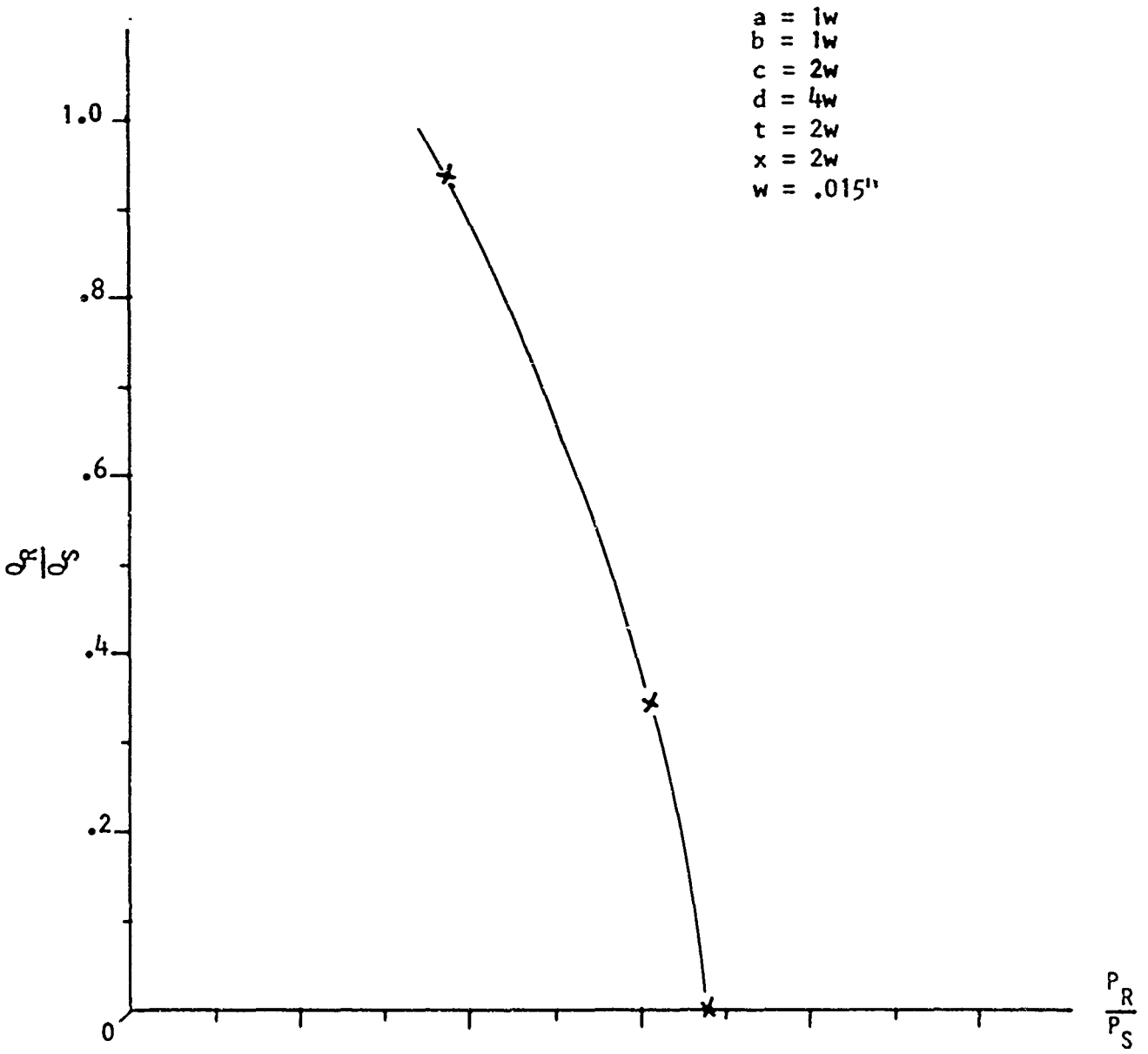

Figure 8 Receiver Flow-Pressure Characteristics

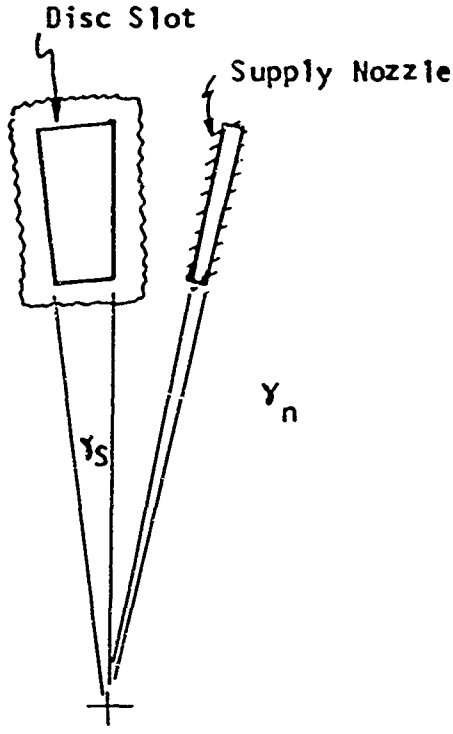

Figure 9(a) Desired Shapes of Disc Slot and Supply Nozzle

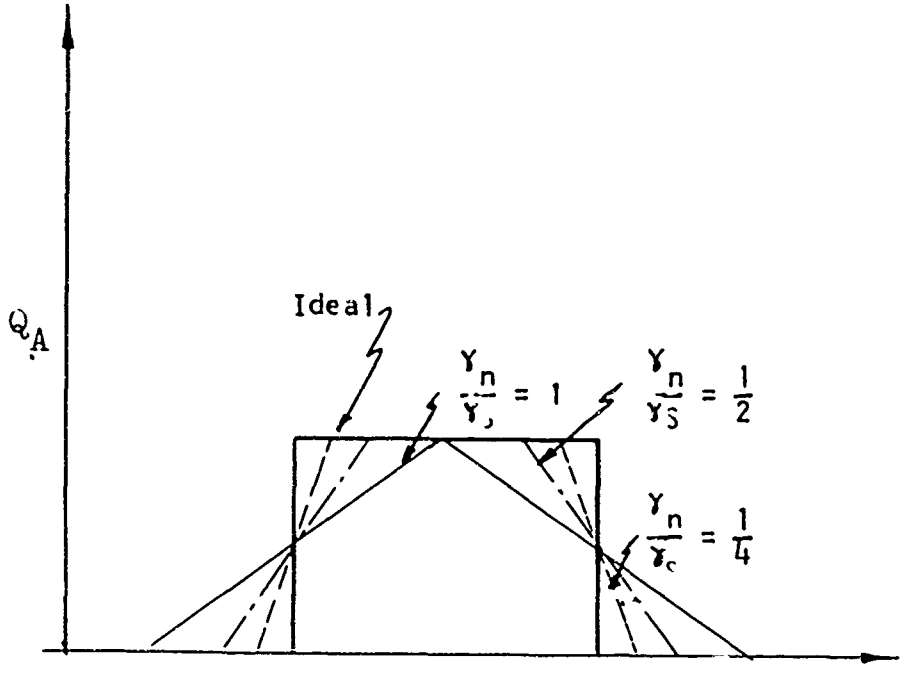

Figure 9(b) Plot of Q_A vs θ with $\frac{Y_n}{Y_S}$ as Parameter

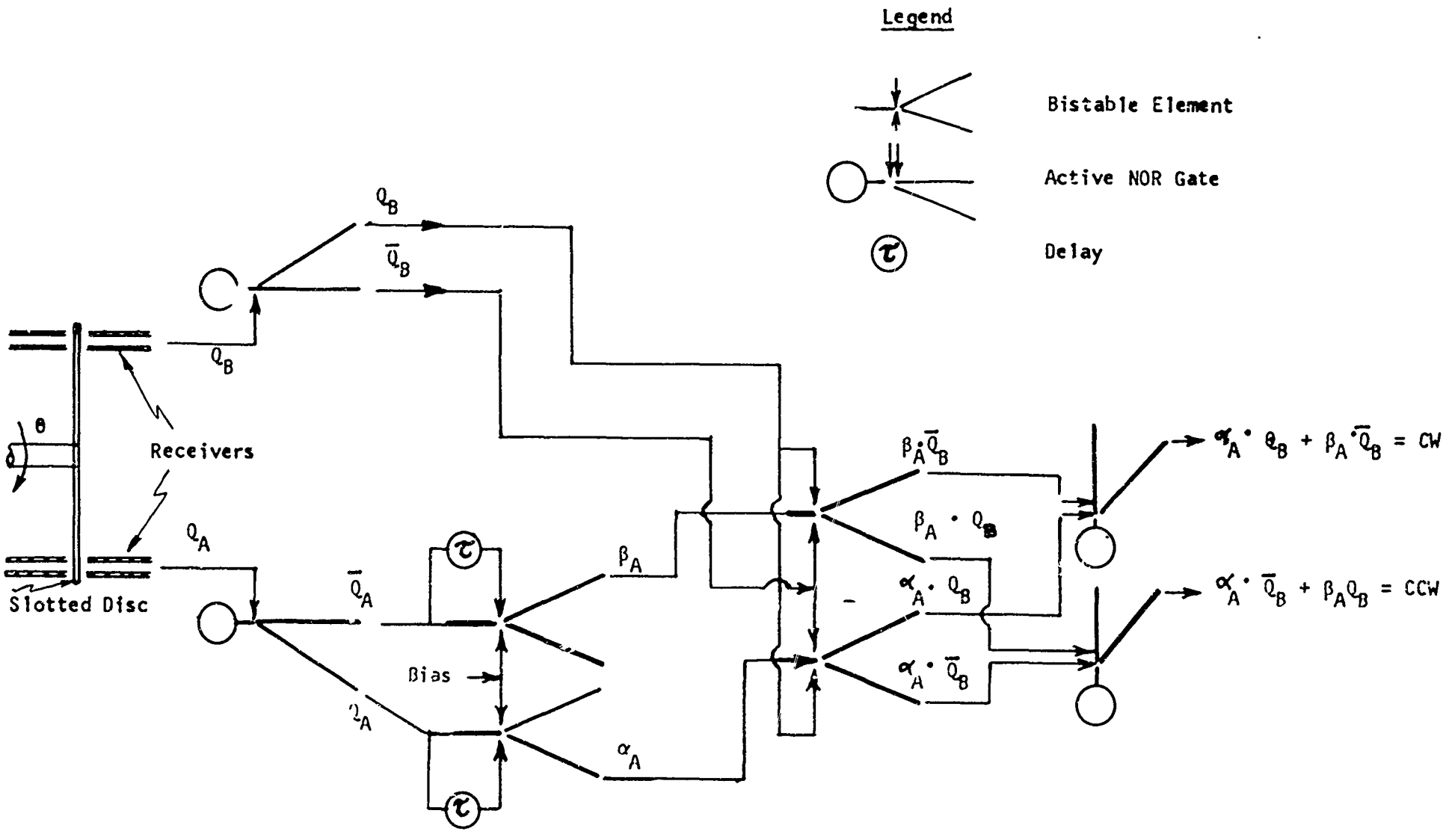

Figure 10 Schematic Diagram of Entire Direction Sensing Circuit

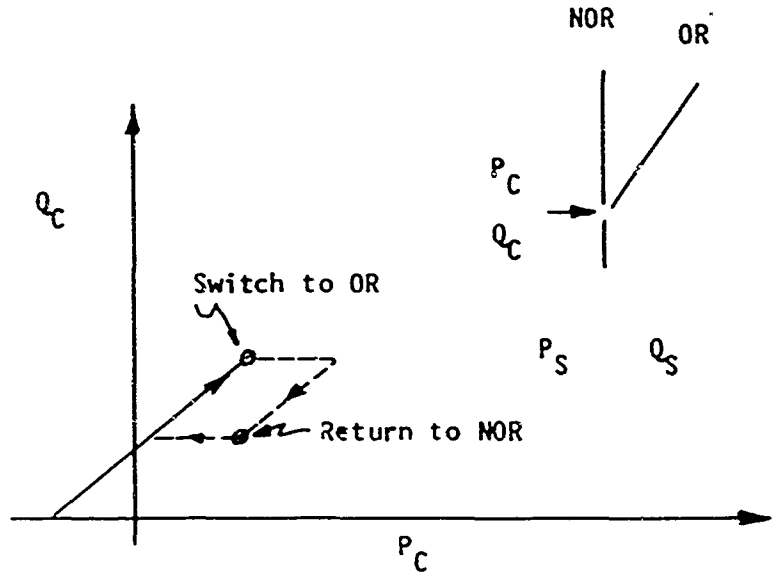

Figure 11 Input Characteristic of NOR Gate Showing Hysteresis

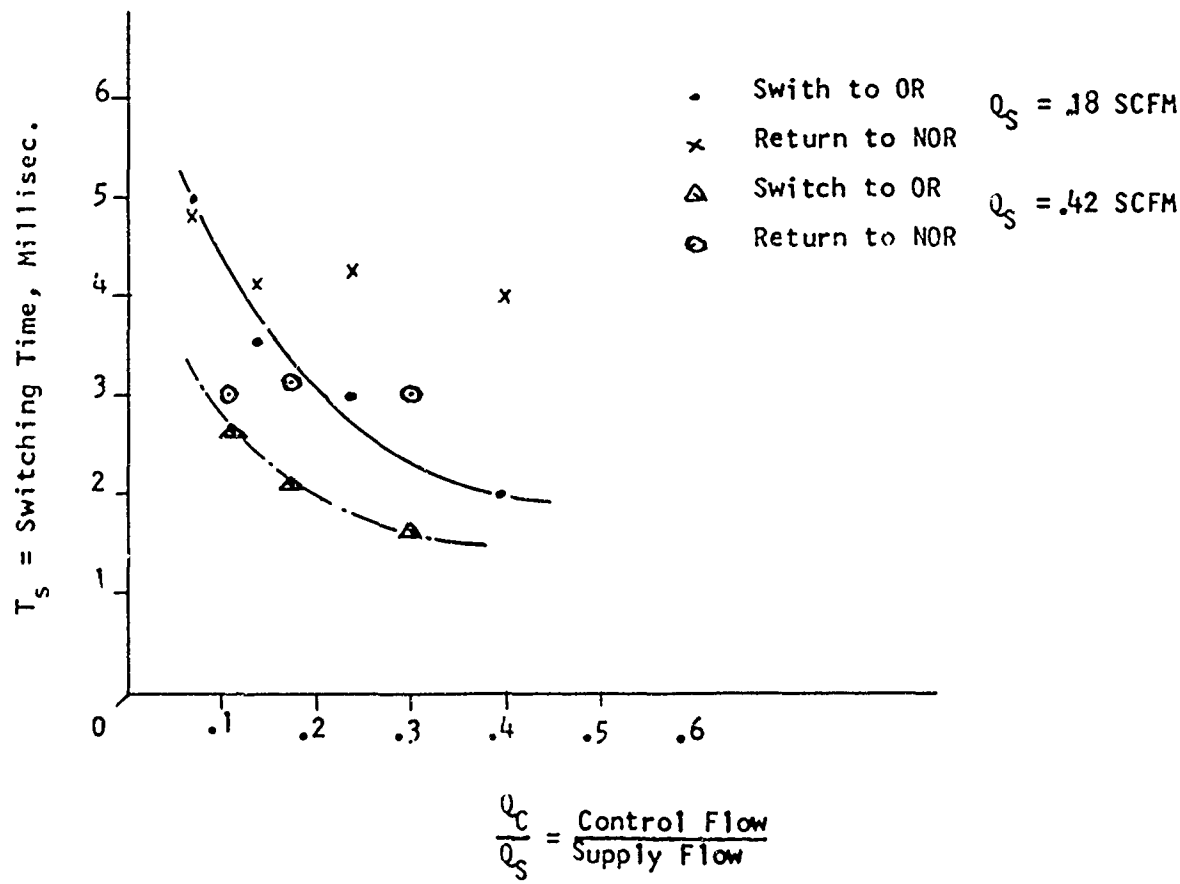

Figure 12 Switching Characteristics of NOR Gate

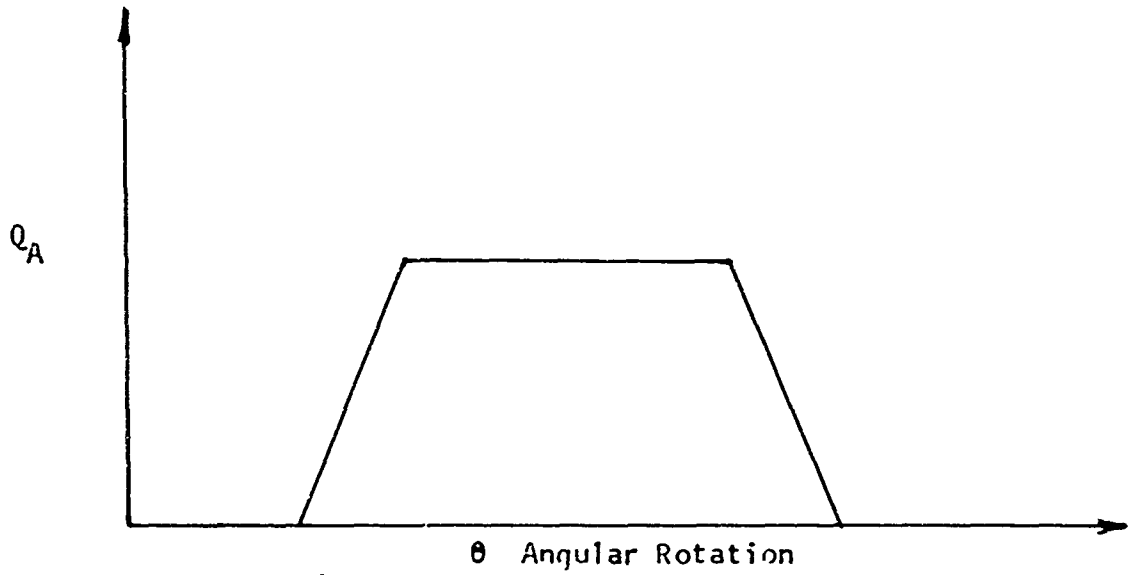

Figure 13(a) Q_A vs Angular Rotation

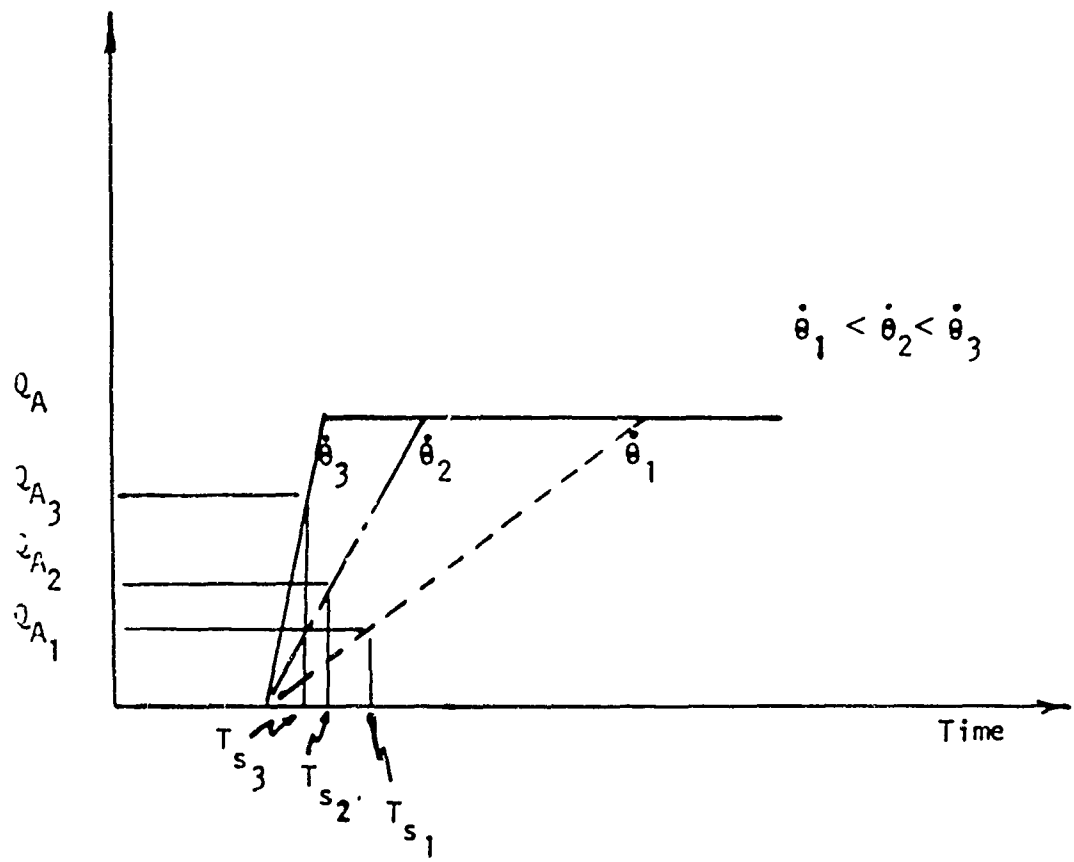

Figure 13(b) Q_A vs Time Showing Change in Switching Flow Level For Angular Velocities ($\dot{\theta}$)

THRUST VECTOR CONTROL

USING A BLEED OFF-REINJECTION DEVICE

C. PAVLIN

1. INTRODUCTION

During the past years, a sudden change in rocket guidance policy has occurred with a more and more marked tendency towards a purely aerodynamic vectoring through direct action on the propulsive gaseous jet.

The main advantages generally put forward in support of this method are suppression of gimbaled nozzles ; increased rigidity of structures, allowing to lighten them ; suppression of coupling between the nozzle and the rocket motions ; flexibility of use ; quickness of response, allowing to reduce the overall needs in vectoring, all these advantages being likely to lead to a favourable weight balance.

Liquid injection piloting has essentially been investigated so far, on account of easiness of development, but it is generally recognized that this can only be a step towards the injection of hot gases, permitting to obtain markedly higher performances, both in vectoring intensity (20 % vectoring is currently reached without appreciable gain drop) and in consumption (twice as economical as the best reactive liquids)

BERTIN & Co. on its part, has long advocated this piloting procedure The theoretical and experimental work that followed the development of jet deviators on jet engine, at S.N.E.C.M.A. by J. BERTIN and his assistants, was carried on, without interruption since 1956. It consisted in determining the effect of all the parameters taking part in the phenomena of interaction of a supersonic jet with a gaseous control jet. It evidenced a gain of approximately 2,5 to 3 between the momentum of the injected gas and the lateral thrust obtained. The results arrived at were the subject of a number of published papers. It is therefore easy now to choose, in each case of application the most favourable injection pattern.(ref. 1 to 4)

Nevertheless, apart from the technological problems raised by the adaptation of deviators fed with hot gases on a nozzle, the problem of generation and mass-flow control of the injected gas remains to be solved. The apparently most attractive solution consists in a direct bleed-off of the combustion gases of the rocket.

A first way is to bleed-off the gas from the combustion chamber. The valving of these gases must then be obtained mechanically under severe temperature and pressure conditions.

Another way consists in combining an aerodynamic valving and a bleeding This allows to do away with every moving part in contact with the hot gas and therefore to increase the reliability of the whole assembly.

BERTIN & Co. recommends a bleed off re-injection device with aerodynamic control, arranged on the diverging part of the nozzle.

This device is closely related to fluid amplifiers and may consequently take advantage of the progress lately made in this field.

2 - DESCRIPTION OF THE DEVICE. (fig. 1)

The hot gas is bled off from the nozzle through a by-pass into which the gas entering at high speed regains pressure. It is then reinjected crosswise to the main flow in order to take advantage of the amplification effect of the momentum thus obtained.

The flow rate control is effected at the by-pass inlet station by means of an auxiliary gaseous jet. The whole assembly therefore represents one channel of a conventional fluid amplifier. It however appreciably differs from it in practice on account of its destination.

The requirements relating to the by-pass.

1º) When there is no flow in the by-pass, the flow in the nozzle should be as little disturbed as possible. This implies that no part of the by-pass should protrude in the flow, which would immediately give rise to a recompression shock and a drag.

2º) The re-compression should be as high as possible, for re-injection to take place with as great a momentum as possible. As the gas is usually supersonic at the inlet, this calls for a re-compression profile similar to that of

supersonic air intakes. The problems set by these air intakes must then be solved ; they are made even more complicated on account of the fact that the by-pass intake is at a marked angle with the direction of the flow, and that is leading edge receives the boundary layer of the main flow.

3º) The by-pass inlet and exhaust must be sufficiently far away from each other in order that the foot of the compression oblique shock limiting the separation caused by reinjection stays downstream of the intake. If it were not so, re-injection would disturb bleed-off.

Requirements relating to mass-flow control.

1º) The control efficiency is measured by the momentum gain which may be reached through the use of this bleed-off re-injection device with respect to that which the controlling jet would have if it were injected directly into the nozzle. This gain must be as high as possible.

2º) The controlling jet isolates two areas of the by-pass.

a) An upstream part the average static pressure of which is equal to that of the main flow at the by-pass intake station.

b) A downstream part, in which no fluid flows as a rule, and which consequently is at the static pressure of the main flow at the re-injection station.

It can be understood that the mass-flow control will be the more efficient as the pressure difference between both parts is smaller. But, on the other hand, the by-pass may only start if there is a sufficient difference of static pressure between the intake and the exhaust. Therefore, a compromise is necessary.

3º) Control may consist either in gradually starting a normally stopped by-pass, or in gradually stopping a normally started by-pass. Occasionally it may be necessary to combine the above mentioned means if the by-pass is normally partially fed.

3 - EXPERIMENTAL STUDY

An experimental study of a bleeding device on a supersonic divergent has been effected by BERTIN and Co., under a contract awarded by "Direction des Recherches et Moyens d'Essais". It has been carried out by means of a two-dimensional model. The first results obtained are presented below.

3.1 - Description of the model.

3.1.1 - Stream.

The test stream is a two dimensional half nozzle. The upper part is so profiled as to achieve a uniform Mach number equal to 2,32 in the terminal section. The plane lower part materializes the centre plane of a symmetrical nozzle.

The test stream dimensions are :

5,4	x	5	cm	at the throat
12	x	5	cm	in the exhaust plane.

The lateral faces are constituted by strioscopy glasses. A compressor maintains a generating pressure of about 1000 mm of mercury (1,30 atm.).

3.1.2 - The model

The by-pass is provided on the plane lower part of the stream. It is limited by a leading edge rounded at its connection with the stream and a downstream edge formed by a movable beak the upper face of which is the prolongation of the plane of the stream, and the lower face is streamlined.

This assembly forms a diffuser the intake of which is supersonic and the exhaust is subsonic and which has an intermediate throat that can be adjusted between 0 and 10 mm through displacing the beak.

This by-pass is connected to a vacuum plant through a flowmeter and a hand operated regulator valve.

The control mechanism consists in a blowing slot provided in the leading

edge of the by-pass and directed against the flow. It is connected to a high pressure generator through a flowmeter and a throttle valve.

Two other suction circuits which have proved necessary during the experiment have also been provided with a flowmeter and adjusting devices.

3.1.3 - Measurements.

In addition to the generating pressure P_{io} of the flow and to the pressures corresponding to the various flowmeters, measurements are made of the distribution of static pressures prevailing in the stream, on the lower face and at various points of the by-pass, among which the throat. The recovery pressure P'_o of the by-passed flow is measured in a rather large size capacity provided at the exhaust of the subsonic section fo the diffuser.

3.1.4 - Visualization

The plant is supplemented by a strioscopy bed allowing to visualize the flow in the by-pass and that of the stream in the vicinity of the intake.

3.2 - Tests.

3.2.1.- Influence of the by-pass on the main flow.

At the by-pass intake, the Mach number in the nozzle of origin is 1,8.

When the by-pass is completely closed by means of the valve located on the suction, the main flow separates at the by-pass intake and reattaches at the beak tip. An expansion fan is observed which is limited by a slight shock on the leading edge, showing that the flow slightly changes its direction towards the by-pass before separating, Similarly, an expansion fan is visible at the stream reattachement on the beak. It is due to the small angle that the flow must form at that place to become parallel to the axis again. (photo 1)

The static pressure recordings show that the presence of the by-pass introduces no appreciable disturbance into the flow.

3.2.2 - Starting of the by-pass.

a) Operating conditions.

In order to arrive at the by-pass axis, the main flow must undergo a 16º deflection. The detailed study of the expansion profile in that zone shows that the theoretical Mach number at the by-pass intake is 2,42, which corresponds along the wall, to a pressure of approximatively 65 mm of mercury.

b) Effective operation.

Experience shows that whichever pressure level is maintained in the capacity, the by-pass is never completely started. An appreciable separation occurs on the leading edge of the by-pass. The flow rate in the by-pass does not exceed 30 % of the theoritical flowrate. (photo 2)

c) How to obtain a correct starting ?

One condition for the startin to be possible is that there be generated on the leading edge, the pressure level corresponding to Prandtl-Meyer's expansion. This was achieved by suction through holes provided on the leading edge.

The suction quantity needed to prevent separation (qc_1) substantially corresponds to that defining the displacement thickness of the boundary layer.

3.2.3 - Pressure recovery.

a) Theoretical value.

The elimination of the boundary layer is not the only necessary condition required for starting the by-pass. In the case of a fixed geometry, the throat must not be too small. In order that there be no choking effect at intake, the throat must be such that it will allow flow rate to pass at intake even assuming a normal shock would arise there. With the model conditions, this leads to a contraction ratio between the intake and the throat :

$$\frac{e}{e_c} \leqslant 1{,}83$$

Under these conditions, the recovery level cannot exceed 67,5 %

$$\frac{P'_o}{P_{io}} \leqslant 0{,}576$$

b) Effective operation

As a result of the disturbances created at the suction holes in the leading edge, the flow is uniform neither in Mach number, nor in direction at intake. A shock attaches to the beak tip and is reflected on the opposite wall from where it goes as far as the throat. Moreover, the flow must reascend a positive pressure gradient, which makes the boundary layer instable. slight separation is usually observed in the supersonic diffuser. (photo 3)

It is possible to reduce its effect by providing a boundary layer suction in that zone (flow rate qc_2). (photo 4)

Towards the inside of the nozzle, this suction may be obtained automatically through the beak by providing holes there, according to a technique used for the automatic starting of supersonic air intakes (ref. 5)

Nothing then forbids to take as the theoritical section at the throat the section of which corresponds to the sonic throat since the risks of intake stopping are eliminated.

c) Flow rate versus pressure curves.

When all precautions have been taken regarding the by-pass starting, it is found that the maximum pressure recovery which may be obtained does not exceed 62 %.

The flow rate vs pressure curves show an optimum taking place around a flow rate equal to 50 % of the maximum theoretical flow rate with a pressure level equal to 50 % of the generating pressure.

The curves obtained are very similar to those given by some fluid amplifiers published by W.A. BOOTHE ref (6) which we reproduce, fig. 5.

3.2.4 -- Efficiency of the control flowing.

The suction on the leading edge of the by-pass already provides a control means since it allows to increase flow rate from 30 % to 60 % of its maximum theoretical value. There remained to be tested the efficiency of the blowing as it had been provided.

a) Theoretical value of the gain. (fig. 2)

If it is admitted that the by-pass is wholly started with a constant Mach number equal to 2,42 at the intake, a maximum value of the gain momentum may be determined by writing that the controlling jet isolates two regions where the static pressure that exist within the main flow respectively at intake and at exhaust

$$\frac{qv}{R} = p_1 - p_2 \qquad (1)$$

q, flow rate per unity of length

$$e = R(\cos \alpha + \sin \lambda)$$

$$qv = \frac{e}{\cos \alpha + \sin \lambda} (p_1 - p_2) \qquad (2)$$

The momentum of the reinjected fluid depends on its re-compression level and on how expansion is guided.

Assuming only sonic injection is made :

$$QV\ (air) = (1{,}27\ P'_o - p_2) \frac{P_o}{P'_o} e_c \qquad (3)$$

Let us admit for more simplicity, that the control jet is injected with the generating pressure P'. The gain may then be written as :

$$G = \frac{Q\,V}{q\,v} = \frac{(1{,}27 - \frac{p_2}{p'_o})\ (\cos\alpha + \sin\lambda)}{(\frac{p_1}{p_o} - \frac{p_2}{p_o})\ \frac{e}{e_c}} \qquad (4)$$

Applied to the experimental case, this formula gives :

$$G = 8{,}2$$

b) Effective gain.

Without suction, the flow rate in the by-pass is of the order of 30 % of the theoretical flow rate which considerably reduces the interest of blowing. The actual gain, measured under these conditions, does not exceed 2.

It is moreover found that the control jet which remains quite coherent throughout the crossing of the separated zone, disperses when coming in contact with the sound flow. A fraction of this jet is then swallowed into the by-pass the flow rate of which is therfore never zero. The gain decreases as the blowing flow rate is increased. This phenomenon of dispersion of the secondary jet is currently observed in the case of jet deviation by gas injection. It limits the penetration to a value smaller than that which direct application of formula (1) would give. For example, for a sonic injection at $M = 3$, in a direction perpendicular to the flow, it is experimentally found that all upstream phenomena are identical to those given by a physical obstacle of a height equal to $\frac{2}{3}$ of the calculated penetration. Jet photographs show that the secondary jet disperses before having taken the direction of the deflected jet.

c) Efficiency of control by suction.

The suction quantity necessary to avoid jet stream separation at the by-pass intake depends on the development of the boundary layer and

not on the by-pass flow rates. The flow rate gain increases when more fluid is bled off. It also increases when it is passed on from a two-dimensional geometry to a revolution symmetry, since the relative dimensions of the by-pass are different for a same fraction of bled off main fluid.

In our tests, the flow rate for suction is also approximately 2.

3.2.5 - Influence of bleed off on the main stream.

The bled off flow rate, in our tests, is of the rate of 5 to 10 % of the main flow rate. The disturbances created in the nozzle are insignificant as shown in figure 6 . The only marked disturbance is caused by the re-injection, at the end of the stream, of flow rate qc_2, which however, amounts only a small fraction of the total bled off flow rate (less thar 10 %). This clearly shows that the bleed off does not practically modify the nozzle thrust whereas re-injection is efficient to create a lateral thrust.

4 - DISCUSSION OF PERFORMANCES - COMPARISON WITH FLUID AMPLIFIERS.

Bleed off and re-injection in a supersonic divergent may be considered as the final power stage of a fluid amplification chain. Performances may therefore be analysed on the basis of the conventional amplifiers.

4.1 - Pressure re-compression level.

It has been seen that it was possible to reach values comparable to those provided by the best conventional models. It is to be noted besides, that seeking to obtain a high pressure ratio is not a prime importance for, beyond a certain value of the pressure necessary for a sonic re-injection, the fluid momentum hardly varies any more. This observation may allow, in particular, to blunt the sharp downstream edge of the by-pass the behaviour of which in hot gases might become critical.

4.2 - Momentum gain.

It has been seen that this gain is the most accurate characteristic to qualify this type of amplifier. It should be noted that, subject to an injection at a sufficiently high pressure, it is, owing to its definition, fairly close to the flow rate gain. Its value is rather small in the case of our tests, and this is partly due to the necessity of placing all the by-pass back from the main flow when it is not started. It may, however, be hoped that present performances will be improved, if the values currently reached in similar devices are taken into account. To this end, the optimum position of the control blow will have to be found out. We may be led to modify the shape of the by-pass intake to draw nearer to those usually adopted for fluid amplifiers. Anyhow, where a final stage of an amplifier chain is concerned, it is not compulsory that the gain be very high. It seems that the 3 to 10 range is quite sufficient for the applications.

5 - DESIGN OF A PILOTING CHAIN.

Based on such a device, a complete pneumatic chain is conceivable, from a pneumatic signal, which may, for instance, be provided by an appropriate detection device.

Without going into the details of such a chain, we may consider the interconnection system between stages at the level of the power stage.

The procedure for the control of flow rate in the by-pass may be either pure blowing or pure section, or a combination of both, depending on the pressure levels prevailing at intake and at exhaust, and on the Mach number, in way of the intake.

As an example we are giving the manner of adjusting the control flow rate in each case, from fluid amplifiers of a conventional type. (fig. 8)

When these flow rates must be maintained throughout all the time during which the by-pass is closed, it is of interest, if the mass of gas to be stored is to be reduced, to tandem connect two hot stages, the first one being assumed to be controlled by blowing.

Figure 8a Normally started by pass jet controlled, by means of a not gas first stage.

Figure 8b Normally stopped by pass suction controlled, by means of a hot gas first stage, through a vortex amplifier.

Figure 8c Normally stopped by pass suction controlled through another type of vortex amplifier.

Figure 8d Partially started by pass controlled by both blowing and sucking through a vortex amplifier driven by a proportional amplifier.

Acknowledgements.

We gratefully thank "Direction des Recherches et Moyens d'Essais" (DRME) for permission to publish this paper.

We also acknowledge help and advice received from ONERA during the experimental part of this investigation.

BIBLIOGRAPHY

1) J. BERTIN, M. KADOSCH, R. MARCHAL, F. PARIS.

"MECANISME DE LA DEVIATION DES JETS PROPULSIFS"

Comptes rendus de l'Academie des Sciences, Paris, 16 mai 1955.

2) M. KADOSCH - Thesis, 5 janvier 1957.

"Mécanisme de la déviation des jets propulsifs"

nº B.S.T. 124, a : publication Scientifique et Technique du Ministère de l'Air, at :
"Service de Documentation et d'Information Technique, 2, avenue de la Porte d'Issy
PARIS (15è)

3) Gérard DUPUICHS. Thesis, 25 février 1961

"Action d'un jet transversal à un écoulement supersonique"

Publication Scientifique et Technique du Ministère de l'Air n9 396.
(same address as in reference 2)

4) Gérard DUPUICHS.

"Les performances du pilotage par injection fluide secondaire en atmosphère raréfiée"
Published in : Technique et Science Aéronautique et Spatiale, 3,1963 and in :
3 rd European Spatial Symposium STUTTGART (May 1963)

5) An experimental study of perforated intake diffusers at a Mach of 2,50
J.H.T. WU September 1960 UTIA report nº 69

6) Performance evaluation of a high-pressure Recovery Bistable fluid amplifier.
W.A. BOOTHE Fluid jet control devices
ASME Symposium on fluid jet control devices Nov. 1962

TEST ASSEMBLY

Figure 1

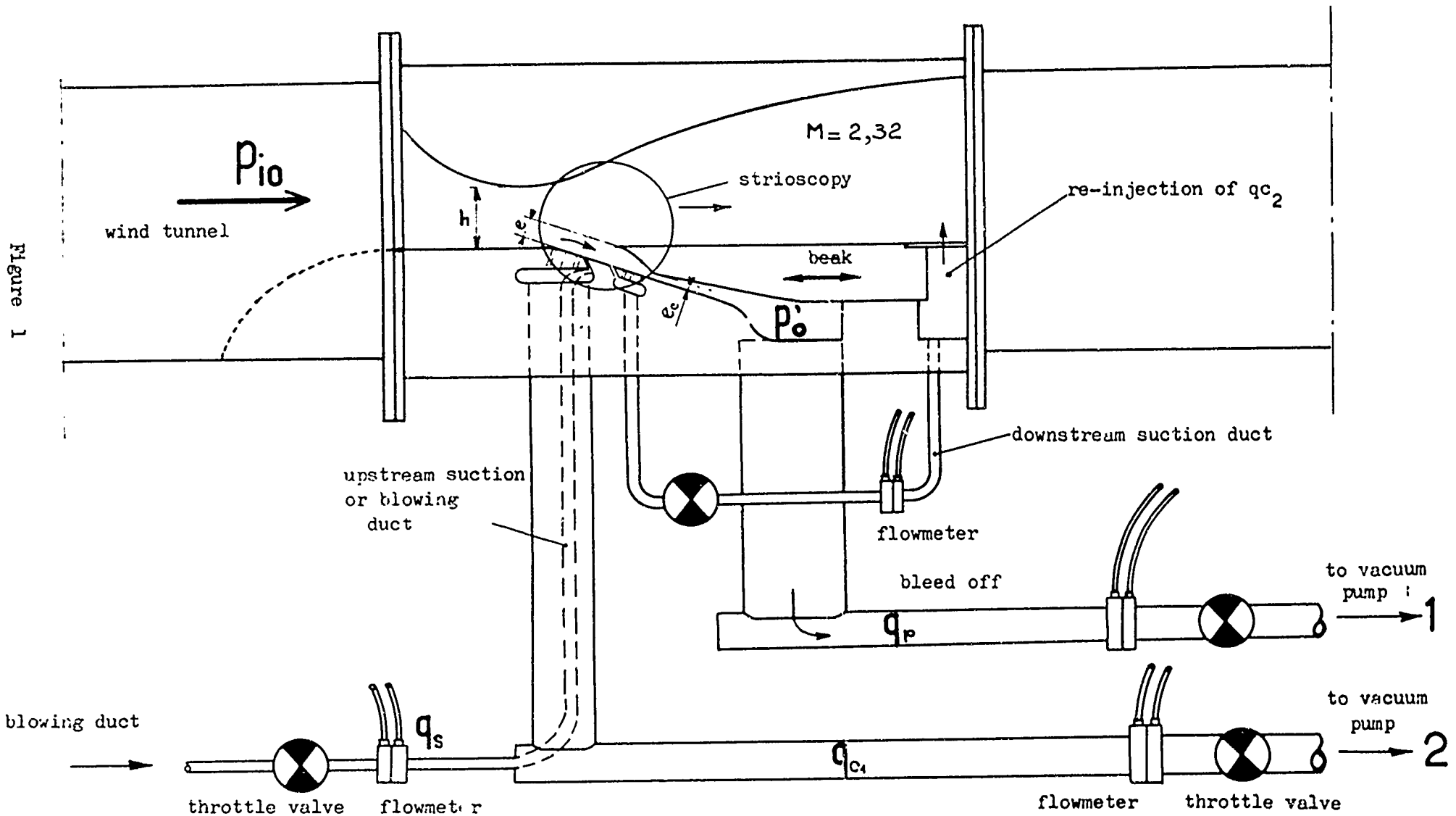

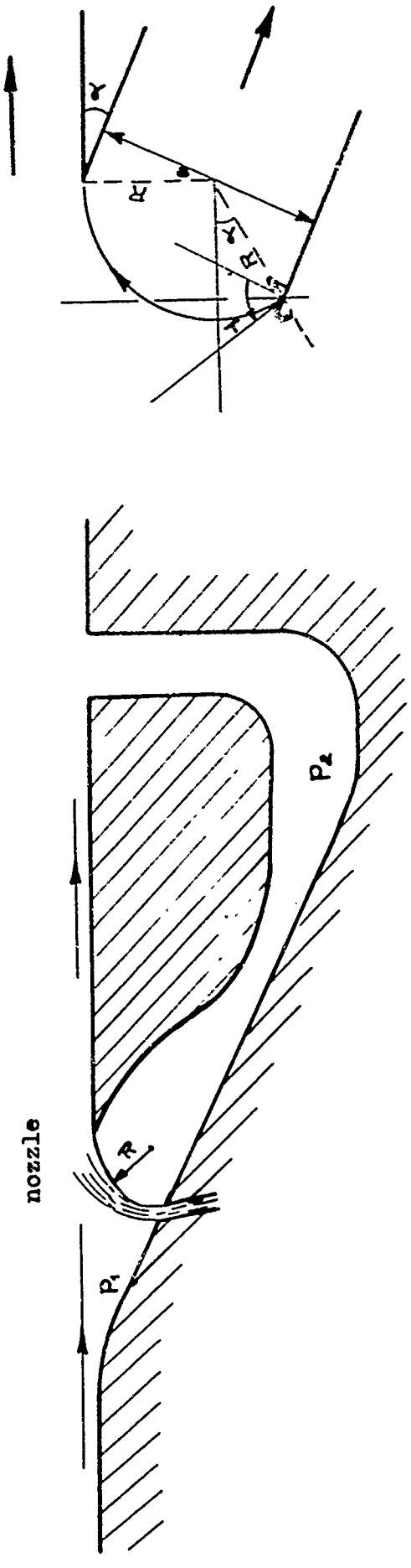

Figure 2

OPERATION WITHOUT UPSTREAM SUCTION

Pressure vs mass flow rate curves

q_e : theorical mass flow rate of a fully started by-pass

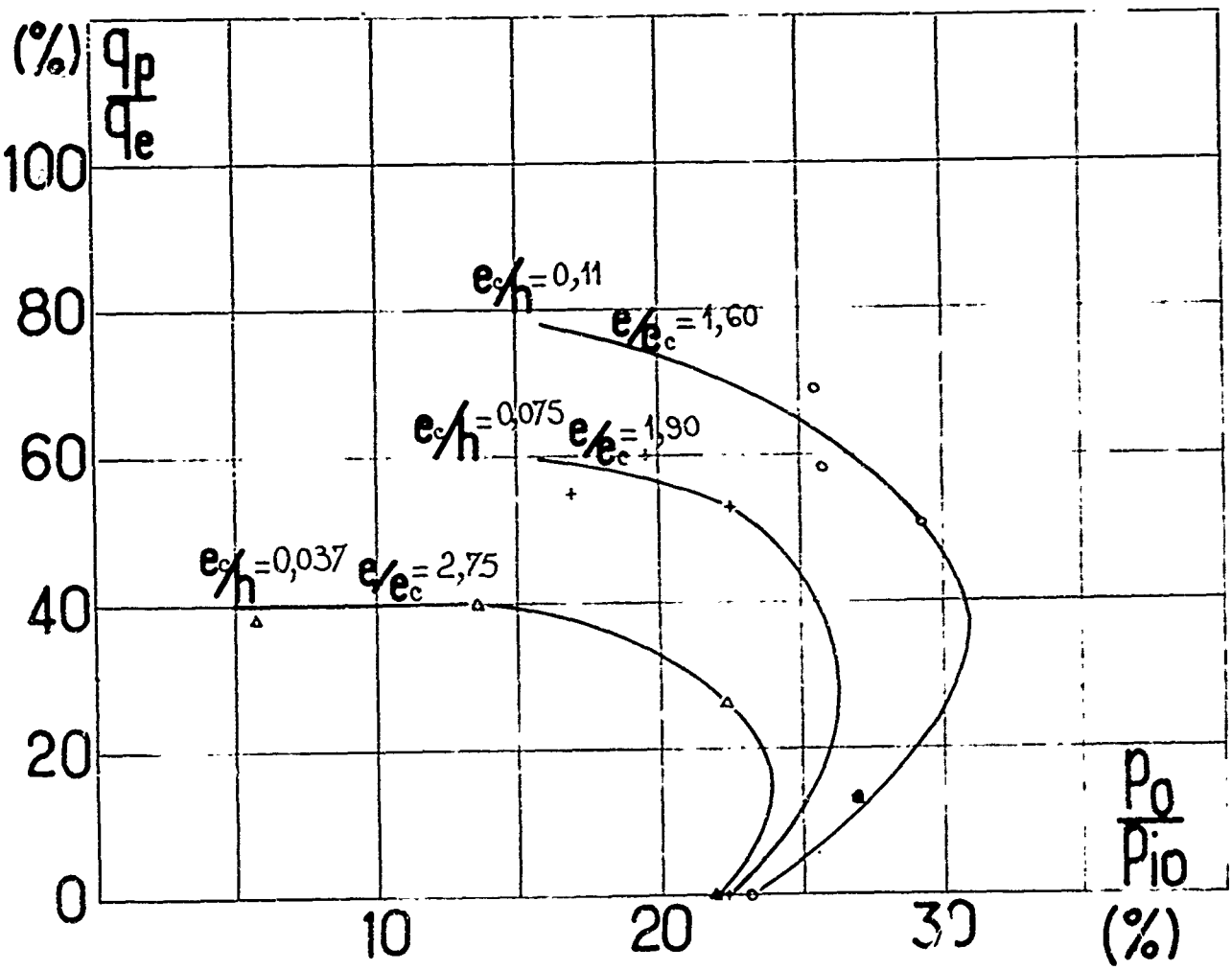

Figure 3

PRESSURE VS MASS FLOW RATE

for different $\frac{e}{e_c}$

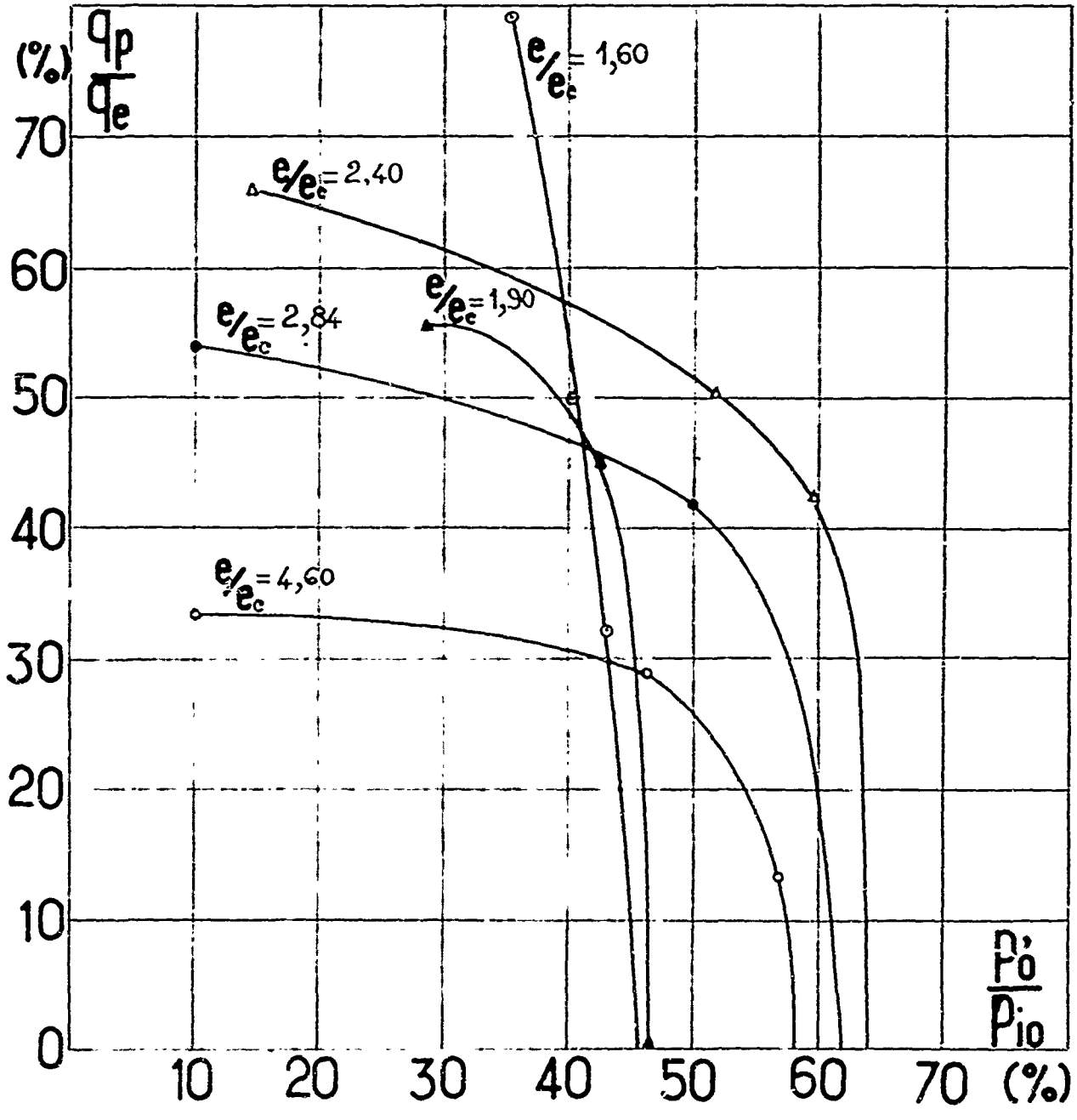

Figure 4

PRESSURE RECOVERY

A comparison with some results obtained

with fluid amplifiers

BERTIN ——

W.A. BOOTHE
- B - subsonic
- C - supersonic
- D - more supersonic
- E - still more supersonic
- F - highest pressure ratio tested

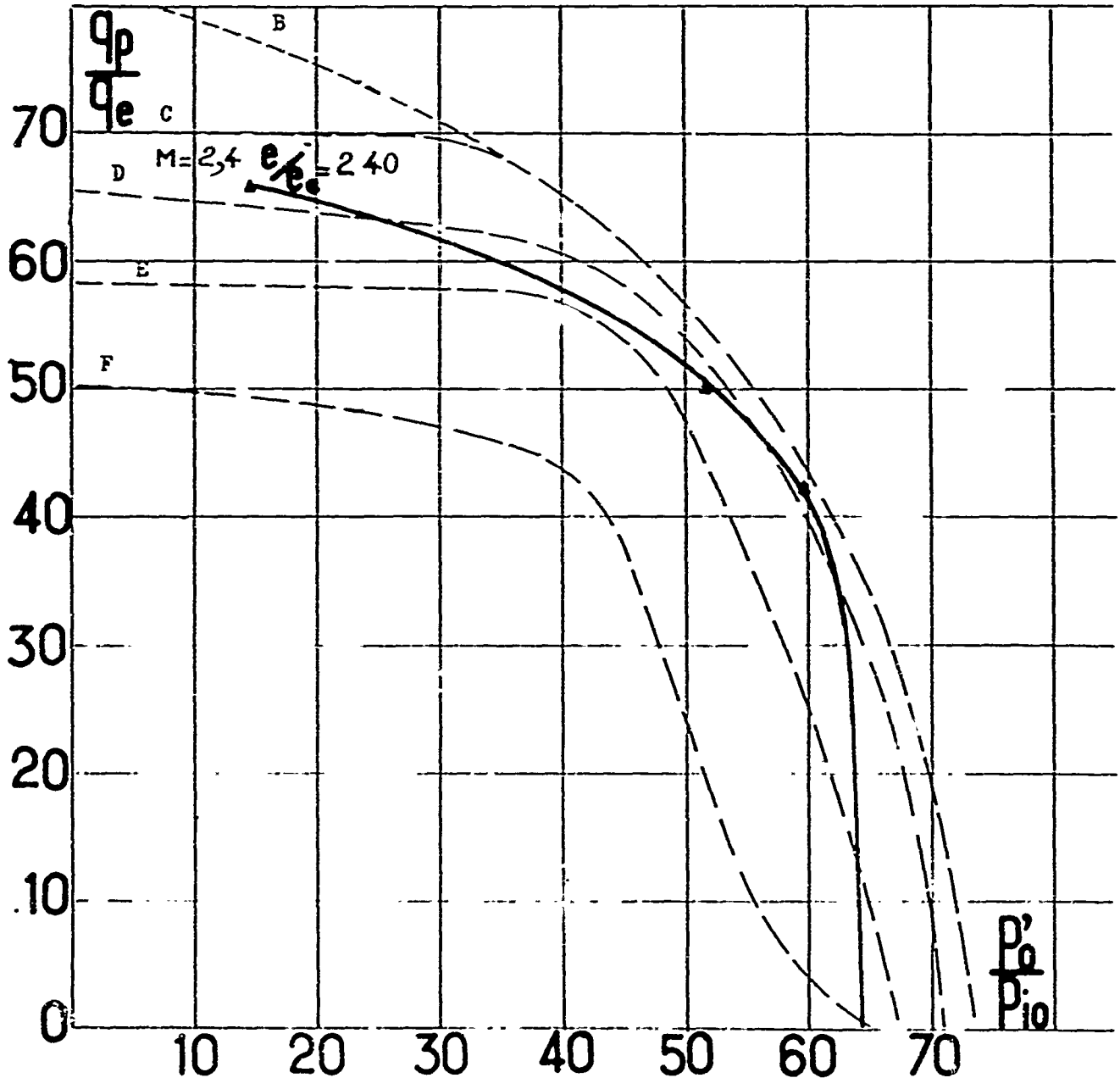

Figure 5

STATIC PRESSURE PROFILES

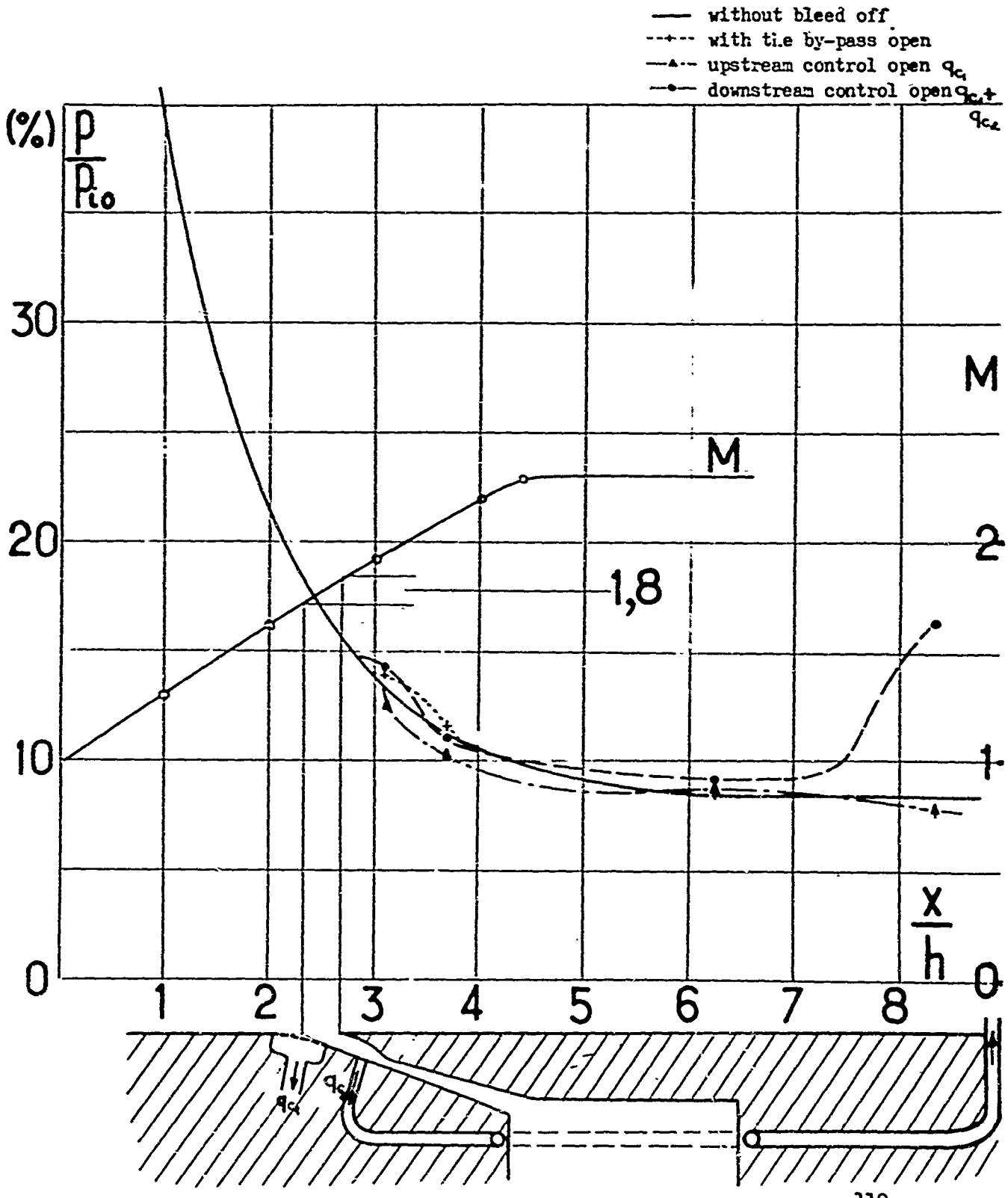

Figure 6

STREAM PHOTOGRAPHS

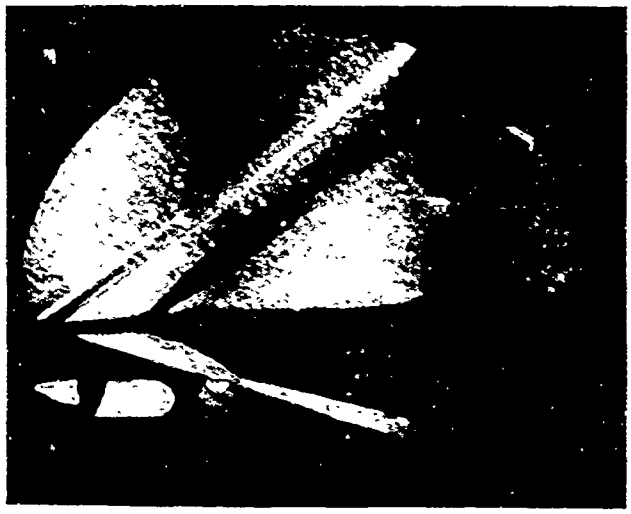

Stream without bleed off

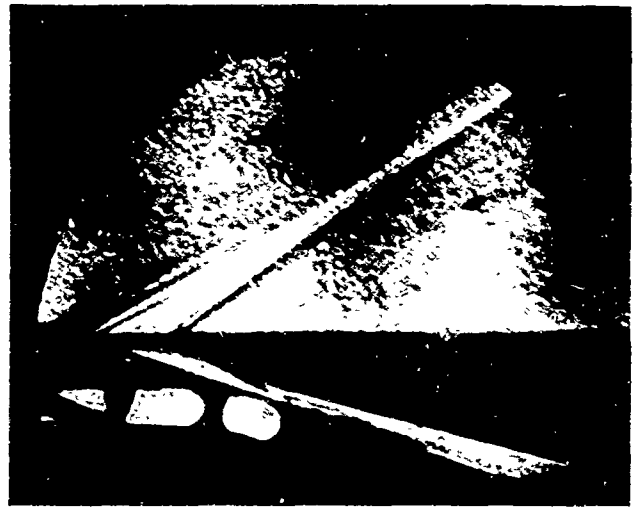

By-pass open without control suction

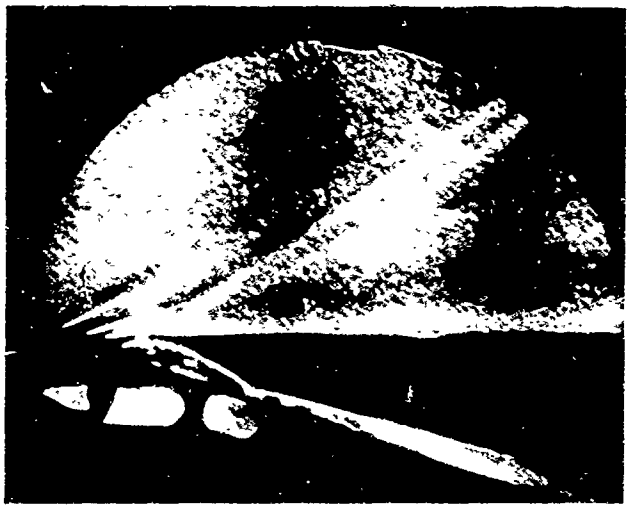

3

Upstream control suction operating

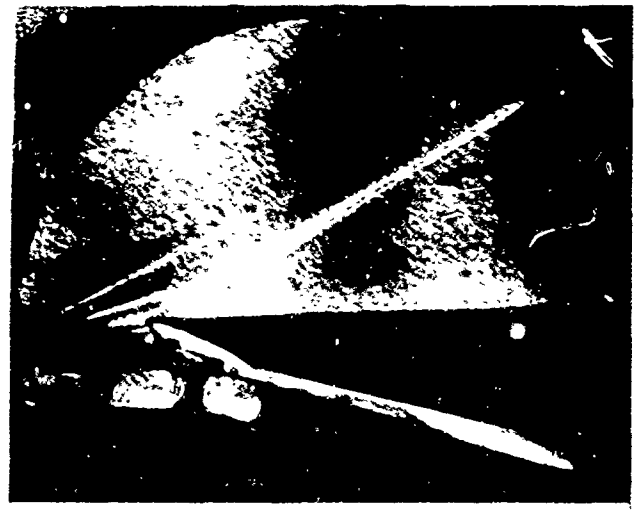

4

Downstream control suction operating

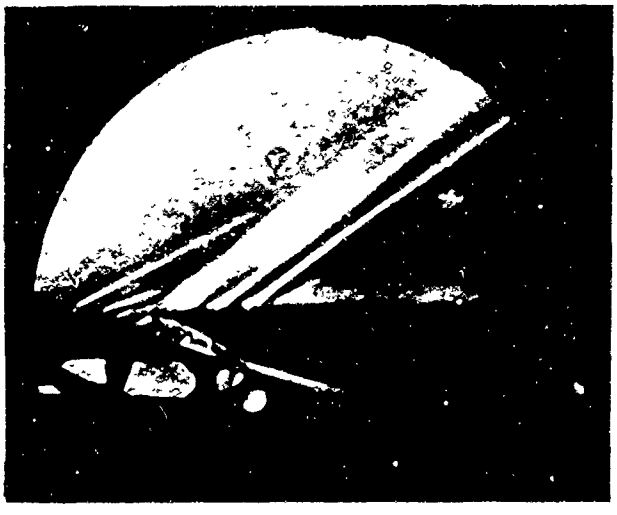

5

Influence of beak perforation

6

Bleed off control by blowing

Figure 7

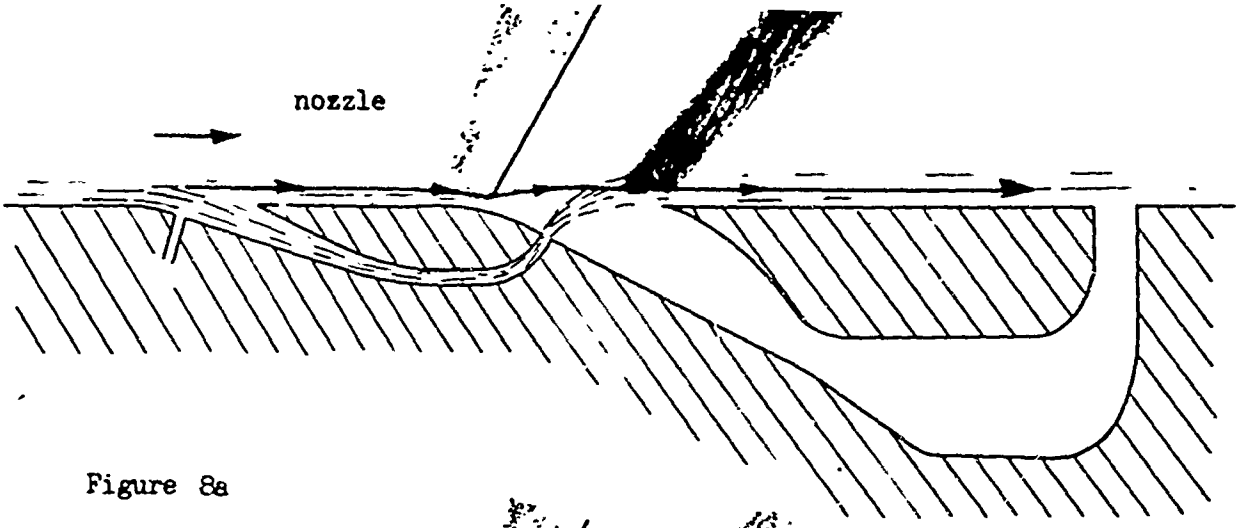

Figure 8a

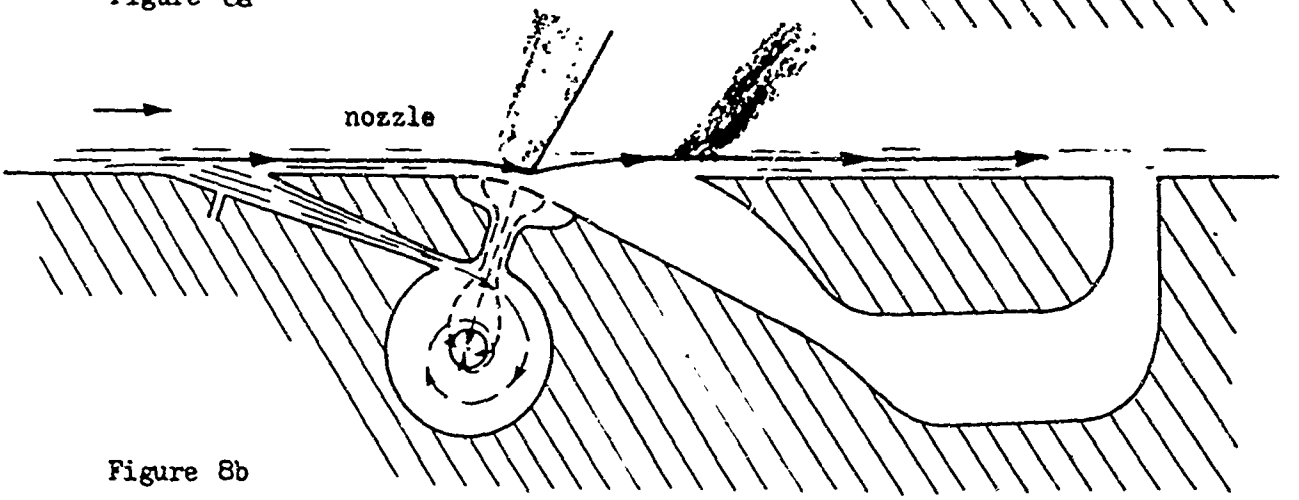

Figure 8b

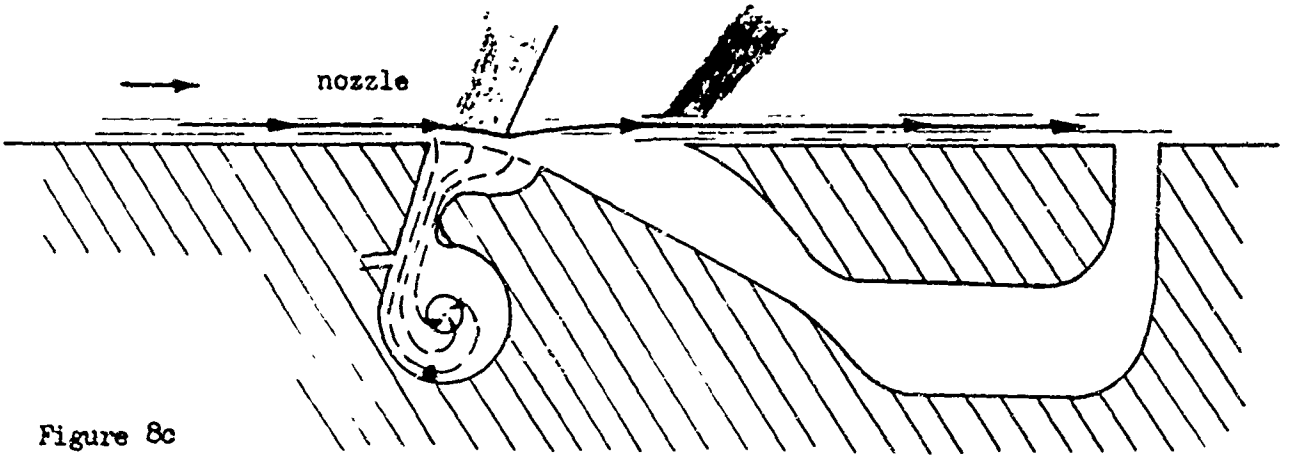

Figure 8c

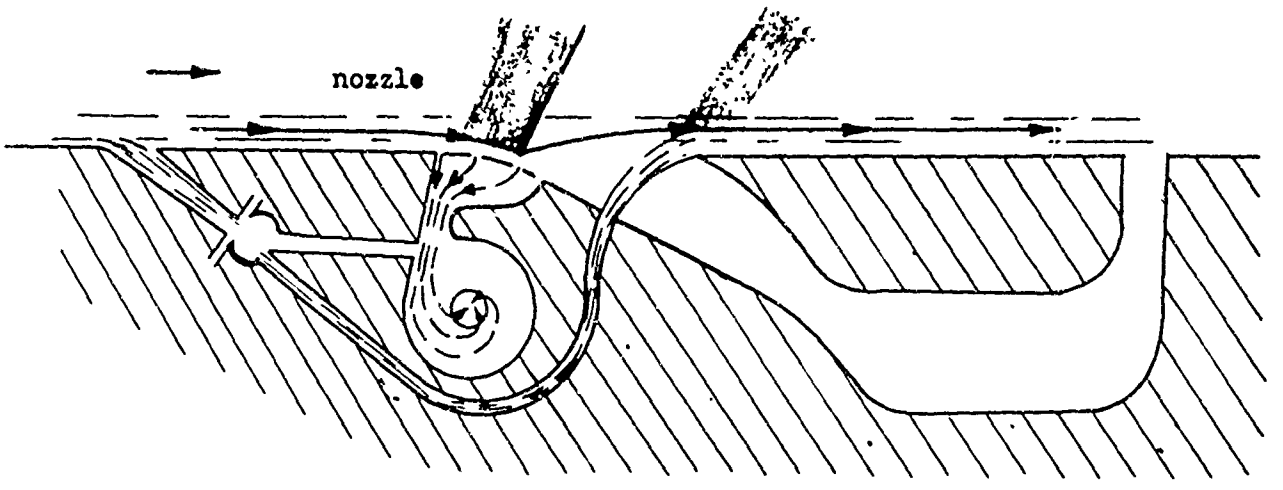

Figure 8d

Figure 8

HARRY DIAMOND LABORATORIES
WASHINGTON 25, D.C.

SUPERSONIC FLUID AMPLIFICATION WITH VARIOUS EXPANSION RATIO NOZZLES

by

Allen B. Holmes
and
John E. Foxwell, Jr.

NOMENCLATURE

A_e	power-jet nozzle exit area
A^*	power-jet nozzle throat area
D	diameter of output channel
K	specific heat ratio
L	output duct length
M	Mach number
M_e	power-jet exit Mach number
P	free stream static pressure
P_b	boundary layer static pressure
P_a	ambient pressure
P_e	power-jet exit static pressure
P_{cl}	left control-jet static pressure
P_{cr}	right control-jet static pressure
P_{pj}	power-jet total pressure
P_s	boundary layer static separation pressure
Q_c	control-jet flow
Q_{pj}	power-jet flow
ϵ	expansion ratio A_e/A^*

ABSTRACT

The design and performance of high pressure supersonic fluid amplifier devices is discussed. A single amplifier design is evaluated using conical power nozzles with expansion ratios of 5, 10, 15, 20, and 25. All experiments were performed using air as the flowing medium.

The effect of expansion ratio on the input pressure level is determined, and an analysis for predicting the operating pressure level for various expansion ratio nozzles is presented. The predominant effects of pressure loading and friction loading are presented. Flow switching at input pressures in excess of 1000 psia with sea-level atmospheric air control signals is discussed. Output thrust measurements are noted and estimates of the kinetic energy losses due to the ducting of high-velocity gases are given.

1. INTRODUCTION

The control of a fluid by the use of fluid amplification can be accomplished by either a digital or a proportional output response from a given input signal.

Proportional control is achieved when the output response is a function of the momentum of the control signal. As the momentum of the control signal is increased (i.e., an increase in pressure and/or flow), the angle of deflection of the output stream increases until all flow issues from one output. A digital control unit uses the entrainment characteristics of the output stream and the influence of the boundary wall to deliver a bistable output response when a predetermined control signal level is reached. There is no response from the unit when the control signal is less than the required amount and increases in the control signal after the unit has responded have no effect on the output flow. Through digital control it is possible for the output response to remain constant even after the control signal is removed. This paper is concerned solely with fluid amplifiers which deliver a digital output response.

In the field of rocketry there has been a long and thorough search for more efficient and effective means to control the flight path of a missile (ref. 1). Fluid amplification offers the possibility of using hot propellant gases for missile attitude control with no moving mechanical parts in contact with the hot gas stream. Figure 1a illustrates one application of a digital fluid amplifier for use as a missile attitude control device. With actuators A and B closed, the flow from the hot gas generator is equally divided between output A and output B. When actuator A is open (Figure 1b), air is entrained into the unit and the hot gas flow exits entirely from output B.

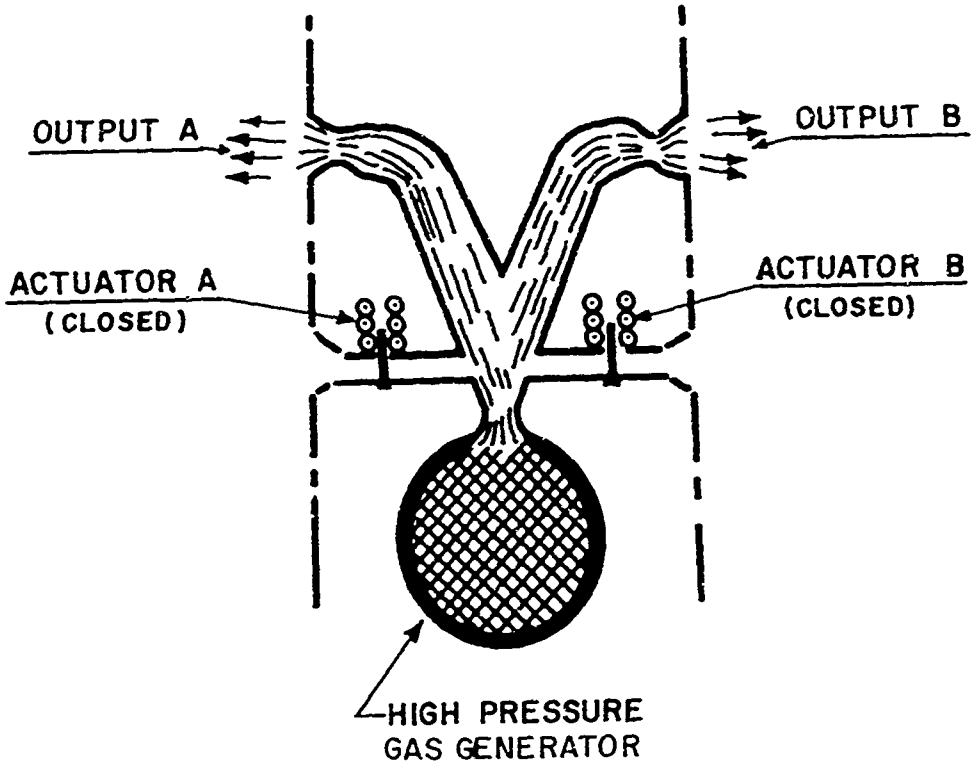

a

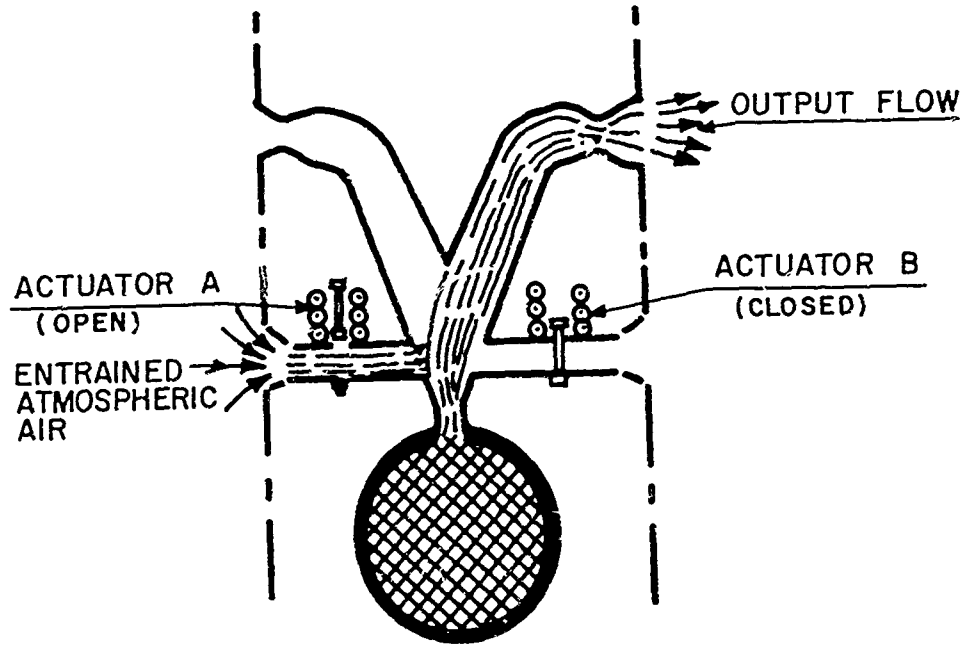

b

Figure 1. Fluid amplifier reaction-jet control system.

2. AMPLIFIER DESIGN

Figures 2 and 3 illustrate a typical fluid amplifier configuration. The unit consists of an adapter, a conical power nozzle insert, and an amplifier housing. Five conical nozzle inserts with expansion ratios of 5, 10, 15, 20, and 25 were designed to be interchangeable with a single amplifier housing. The nozzle inserts were pinned and soldered to the adapter. A later design improvement combined the nozzle and adapter into a single piece. The amplifier housing was counterbored to allow for alignment of the nozzle with the housing piece. The nozzle and the housing were held together with four screws. The output channels in the amplifier housing were also counterbored to allow the output ducting (Figure 4) to be properly aligned with respect to the output channels. The output ducting was formed from commercially available copper tubing.

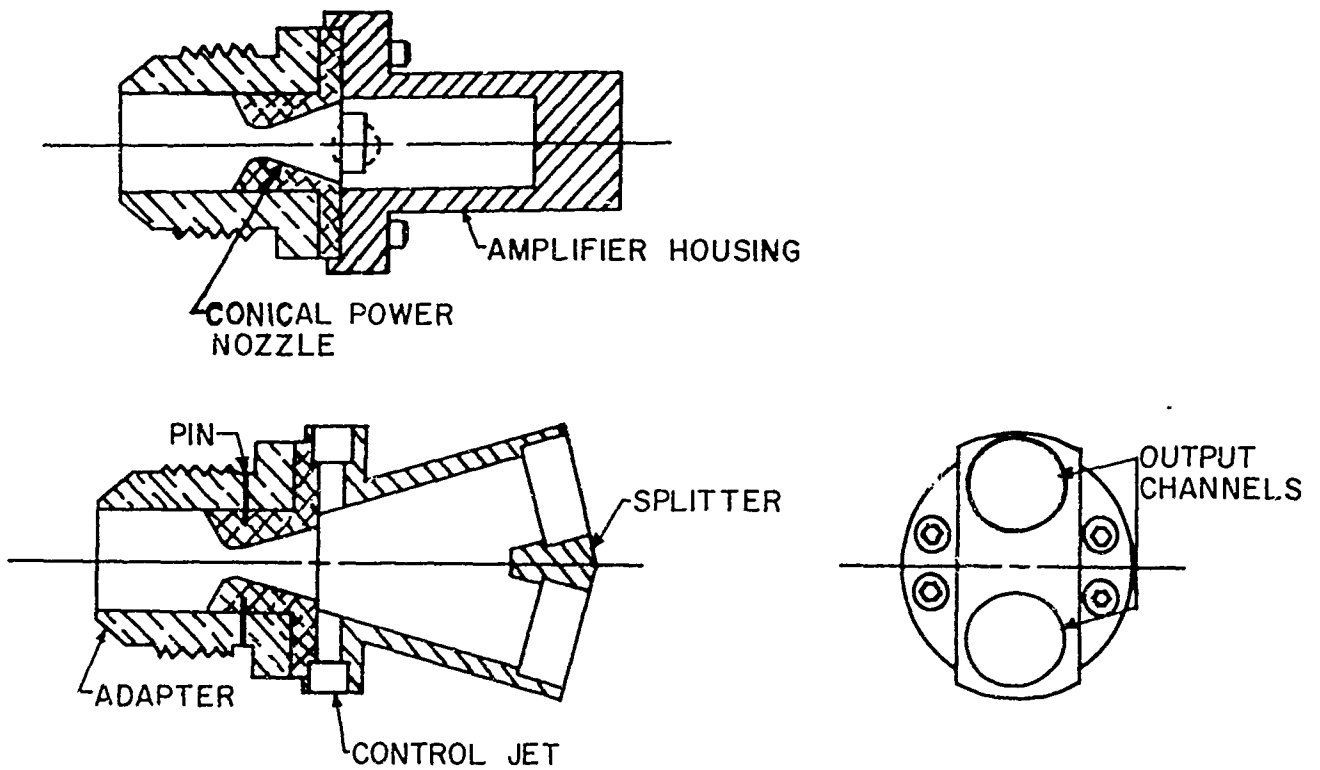

Figure 2. Basic fluid amplifier design.

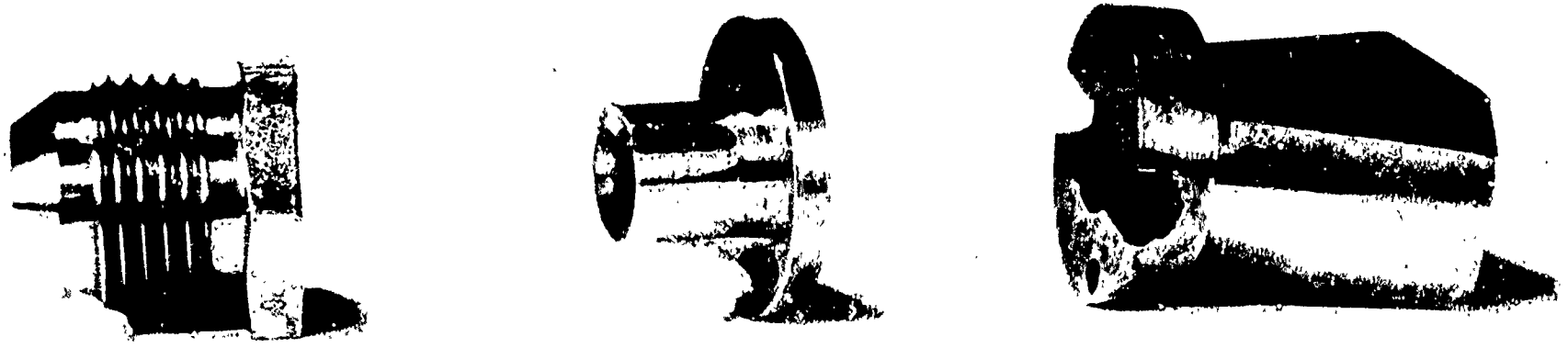

Figure 3. Basic fluid amplifier parts assembly.

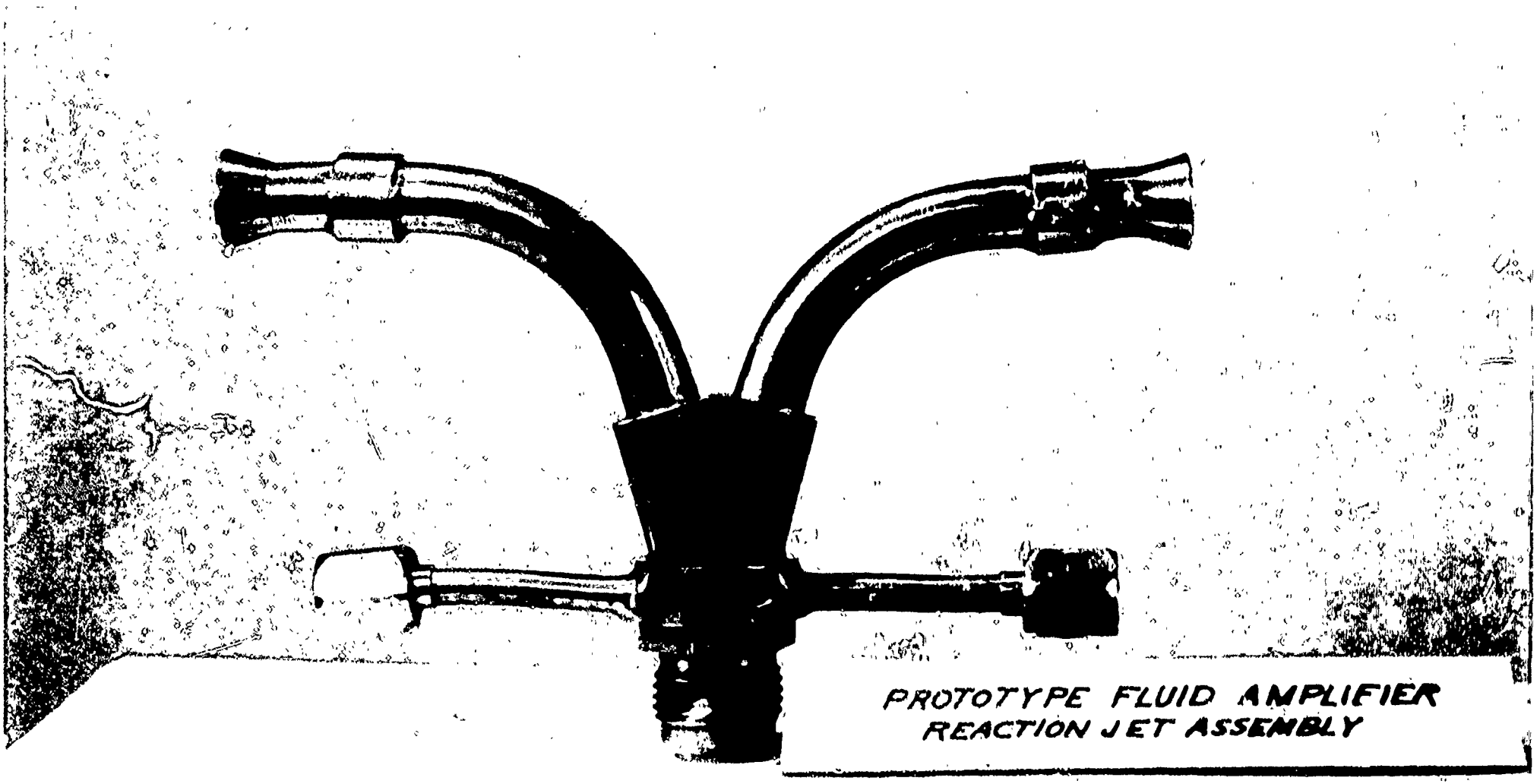

Figure 4. Basic fluid amplifier assembly with output ducting.

3. EXPERIMENTAL OBJECTIVES

Tests were made with the following objectives.

1. To determine the control-jet pressures and mass flow rates required to switch the output flow of the amplifier with a continuous control-jet signal.

2. To determine the power-jet pressure required to enable the power-jet flow to symmetrically re-attach downstream of the control ports.

3. To compare the experimental results with those obtained through the application of theories on turbulent boundary layers and flow separation.

4. To measure the actual thrust output of the units at various input pressures with control-jet pressures not exceeding 14.7 psia.

5. To determine the predominant effects of amplifier output ducting.

4. PRINCIPLE OF OPERATION

4.1 Pressure Regimes

The operation of the amplifier tested may be divided into three regimes:

REGIME I: Overexpanded power-jet with jet separation;
REGIME II: Overexpanded power-jet without jet separation;
REGIME III: Overexpanded power-jet with symmetric wall attachment.

In regime I, when the flow is overexpanded with jet separation, the flow leaving the power-jet nozzle is inherently unstable. A relatively large amount of control flow is required to establish a stable flow in either of the two output ducts. The additional flow is accounted for by assuming that the supply flow is insufficient to fill the power-jet nozzle. As a result, the flow separates from the wall. This separated region allows part of the control flow to pass around the power-jet close to the wall without mixing with it and consequently without giving up its momentum to the power jet.

In regime II, the supply pressure is sufficient to fill the nozzle, but insufficient to cause symmetrical reattachment to the wall downstream of the control ports. This range of supply pressure will enable the flow to be fully established in either output duct without the aid of a continuous control signal. In this regime the amount of control flow necessary to switch the power jet flow is an order of magnitude less than that required for switching in regime I, because there is no leak of control flow around the fully expanded stream. The switcing mechanism is discussed in more detail later.

In regime III, the supply pressure has increased to values where the flow leaving the power-jet nozzle is underexpanded. This causes the flow to remain completely attached to the diffuser walls of the amplifier past the region of the control ports, and produces equal exit flows from the output ducts in the absence of control flow. In this regime, a greater amount of control flow is necessary to obtain a response from the unit, as compared to regime II.

4.2 Boundary Layer Separation

The major parameters determining the location of the separated boundary layers are:

(1) free stream Mach number M,
(2) boundary layer separation pressure P_s, relative to the free stream static pressure P, and
(3) amplifier exhaust pressure P_a.

Starting with a power-jet pressure corresponding to regime III, a reduction in power-jet pressure will cause the separation point to move upstream. This flow separation phenomenon results from the action of the back pressure upon the boundary layer due to the flow being in the direction of a positive pressure gradient. As the power-jet pressure P_{pj} is reduced, the ratio of the power jet exit pressure P_e to the exhaust pressure P_a decreases. An increase in P_a cannot propagate itself into the high-velocity core of the power-jet flow outside the boundary layer, because the flow is supersonic. However, the pressure P_a can propagate itself upstream through the boundary layer surrounding the power-jet flow. This is possible because there is a velocity gradient from zero at the wall to supersonic values inside the jet stream. This velocity gradient produces a region where the velocity of the fluid is subsonic and allows pressure disturbances to propagate upstream. If the pressure ratio of P_e/P_a is sufficiently high, P_e/P_a = 0.4 to 0.5 (ref. 2), the jet will detach from the wall of the unit.

It is possible to predict the approximate power-jet pressure P_{pj} that will initiate the separation of the turbulent boundary layer in regime II (Figure 5). This approximation is dependent upon the following assumptions.

1. The flow upstream of the nozzle separation point is isentropic.
2. The separation pressure ratio P_e/P_s is a function of the power-jet nozzle Mach number, and hence a function of the expansion ratio (ref. 3).
3. The separation static pressure P_s is dependent upon the geometry of the interaction region of the amplifier housing and can be considered as a constant for the various expansion ratio nozzles under examination.

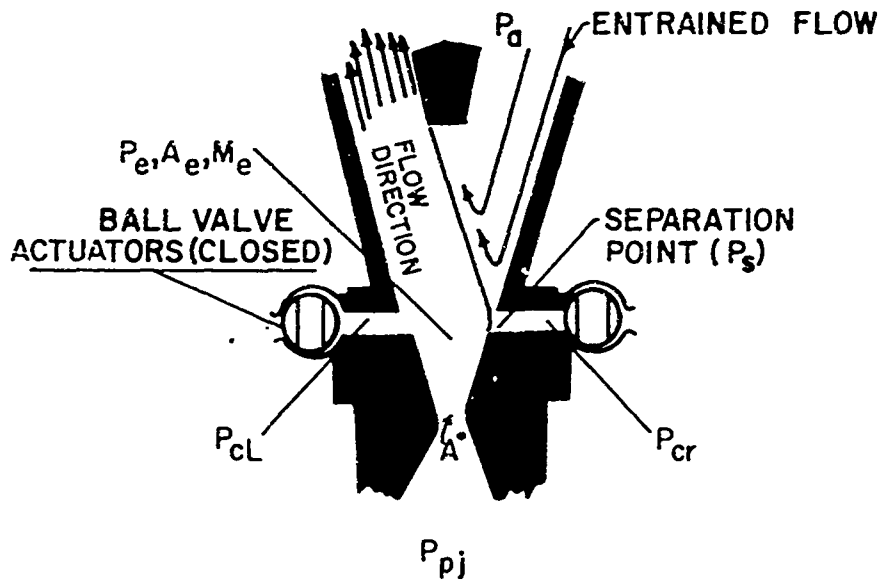

Figure 5. Overexpanded power-jet nozzle with flow separation occurring at the nozzle exit plane.

Isentropic flow calculations from the fluid amplifier experimental data determined the power-jet pressure at which initial turbulent boundary layer separation occurred in regime II (Figure 6). The theoretical treatment giving the best agreement with the fluid amplifier experimental data appears to be that of G. E. Gadd, reference 4 (Figure 6). At the higher expansion ratios in Figure 6, Gadd's theory fails to give a good approximation of the fluid amplifier experimental data; however, published experimental data on separation pressure ratios at Mach numbers ranging from 3 to 5 give a better agreement with the fluid amplifier data (ref. 3).

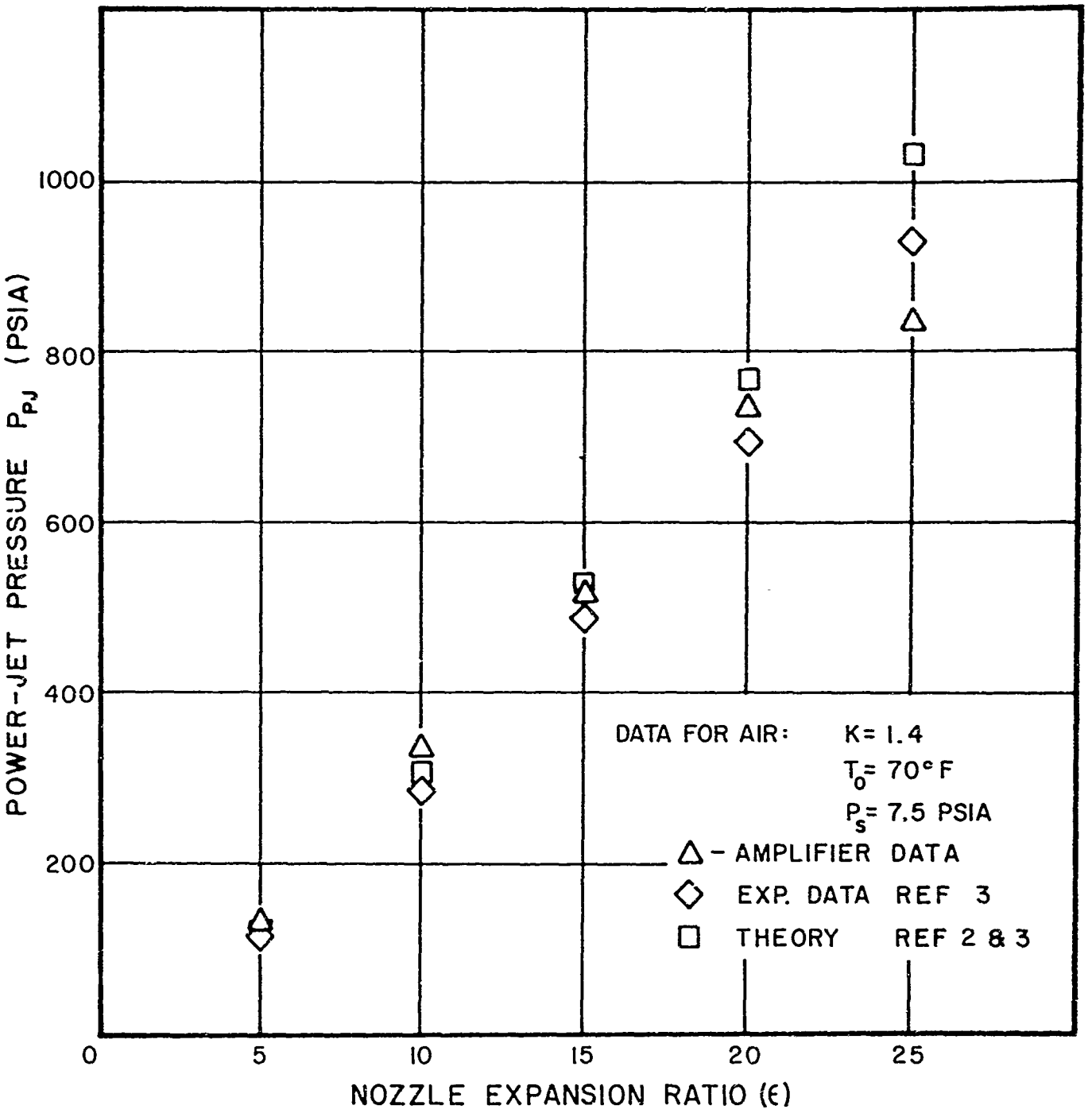

Figure 6. Power-jet pressure required to initiate regime II flow separation.

5. EFFECT OF POWER-JET PRESSURE

As the power-jet pressure is increased, the indicated control-jet pressure in both controls decreases until flow is fully established in the nozzle. The three flow regimes are illustrated for a

power-jet expansion ratio equal to 15 (Figure 7). These curves were generated by recording the pressure measured in each control nozzle as the power jet pressure was increased. It should be noted that

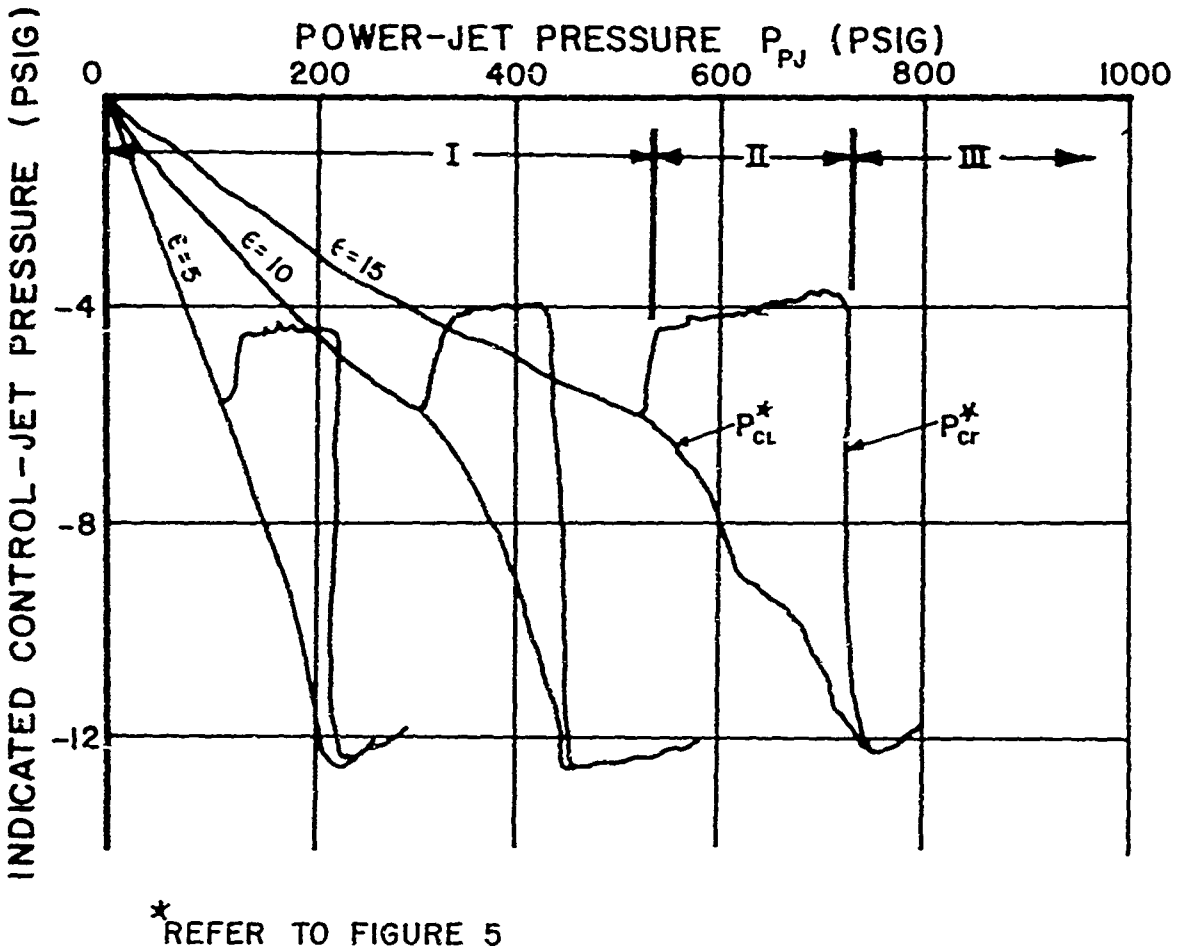

Figure 7. A summary of the indicated control-jet pressures recorded as a function of power-jet pressure for $\epsilon = 5$, 10, and 15.

the indicated control-jet pressures were measured by using the control nozzles as static pressure taps. The accuracy of these measurements is estimated to be ±1 psi. However, since the same configuration was used for each test, the curves do illustrate the relative changes in control-jet static pressures for each of the three regimes.

Flow separation in the power-nozzle (Figure 8) produces a random oscillation of the output flow. A further increase in the power-jet pressure causes the nozzle to flow full, thus moving the separation point to the nozzle exit plane (Figure 9). Since the

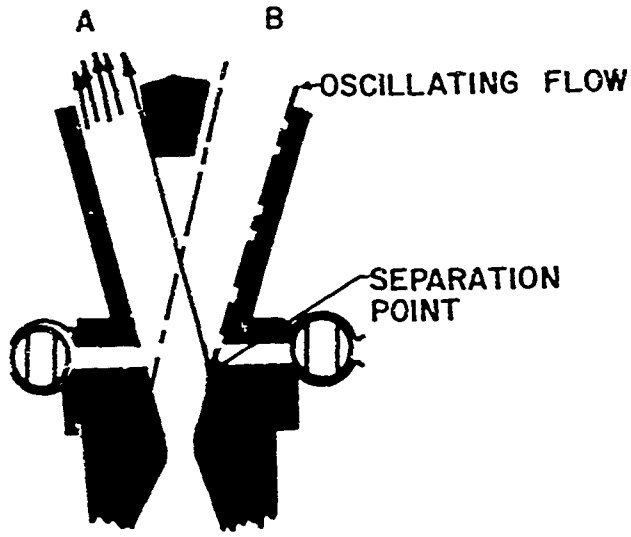

Figure 8. Regime I - Flow with an overexpanded power-jet.

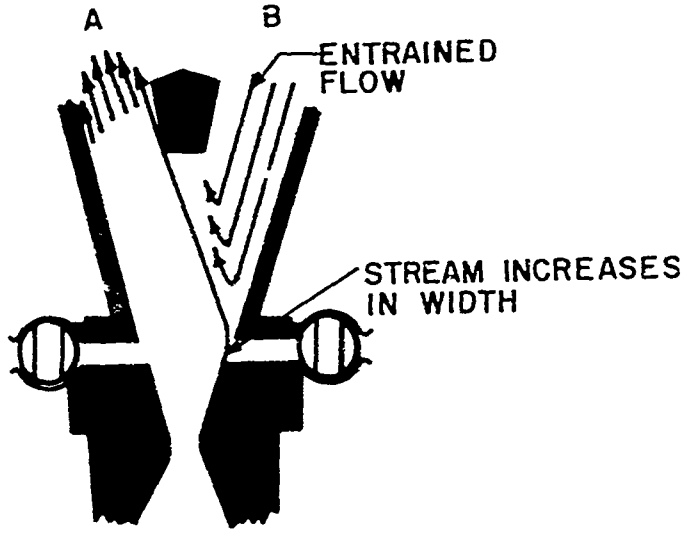

Figure 9. Regime II - Flow with an overexpanded power nozzle without jet separation.

walls of the interaction region limit the entrainment of the power-jet stream, a low pressure is developed at the output of the nozzle. The power-jet stream tends to entrain an equal amount of fluid on either side. Any small perturbation or misalignment will cause an

asymmetrical distribution of the output flow. This will restrict the area available for the entrainment of counter flow through a single output (Figure 9). This flow restriction causes the pressure drop in the boundary layer between the wall and the power-jet stream. The pressure difference forces the stream to the side with the lowest pressure. This regenerative action further decreases the area available for entrainment, causing the power-jet stream to be locked to the wall. Figure 7 illustrates this pressure unbalance in regime II. As the stream attaches to a single wall, the static pressure measured in the closed control port (P_{c1}) drops off rapidly, while the pressure in the opposite control port (P_{cr}) increases.

As the power-jet pressure is increased while operating in regime II, the free stream static pressure rises. The pressure ratio P/P_{pj} is constant for any specific location in the power nozzle. Increasing the power-jet pressure causes the power jet stream to continue to expand down stream of the nozzle exit plane. These gas particles are accelerated radially and, because of their inertia, are displaced from their equilibrium positions, causing an increase in the width of the exhaust stream (Figure 9).

As the power-jet pressure is raised, the stream continues to increase in width until it hits the wall downstream of the control port (Figure 10).

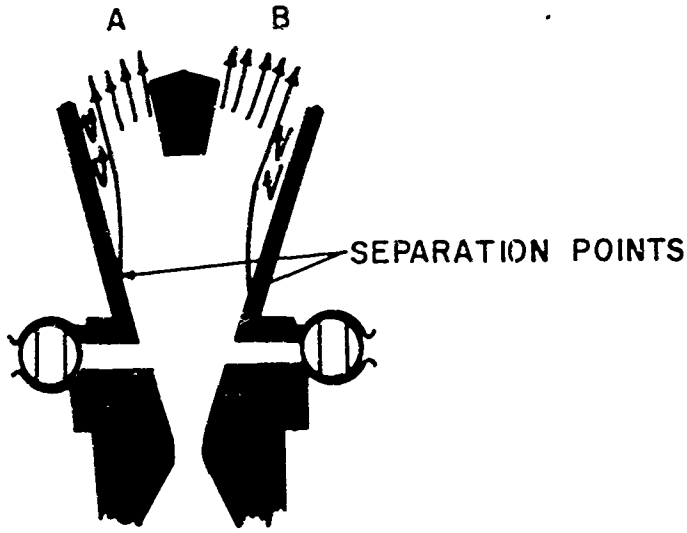

Figure 10. Regime III - Underexpanded power-jet flow with symmetrical reattachment.

Under these conditions, the flow is equally distributed between outputs A and B. Referring to Figure 7, this flow condition is characterized by the abrupt drop in P_{cr} where P_{c1} becomes approximately equal to P_{cr}.

The relative control-jet flow rates and pressures required to switch the flow from output A to output B, or output B to output A for regimes I, II, and III are indicated in Figures 11 and 12.

6. LOADING

Basically, there are two types of loading: pressure loading and friction loading. Pressure loading occurs when there is a back pressure at the amplifier outputs. Friction loading is attributed to the external plumbing required to channel the outputs of the amplifier to a desired location.

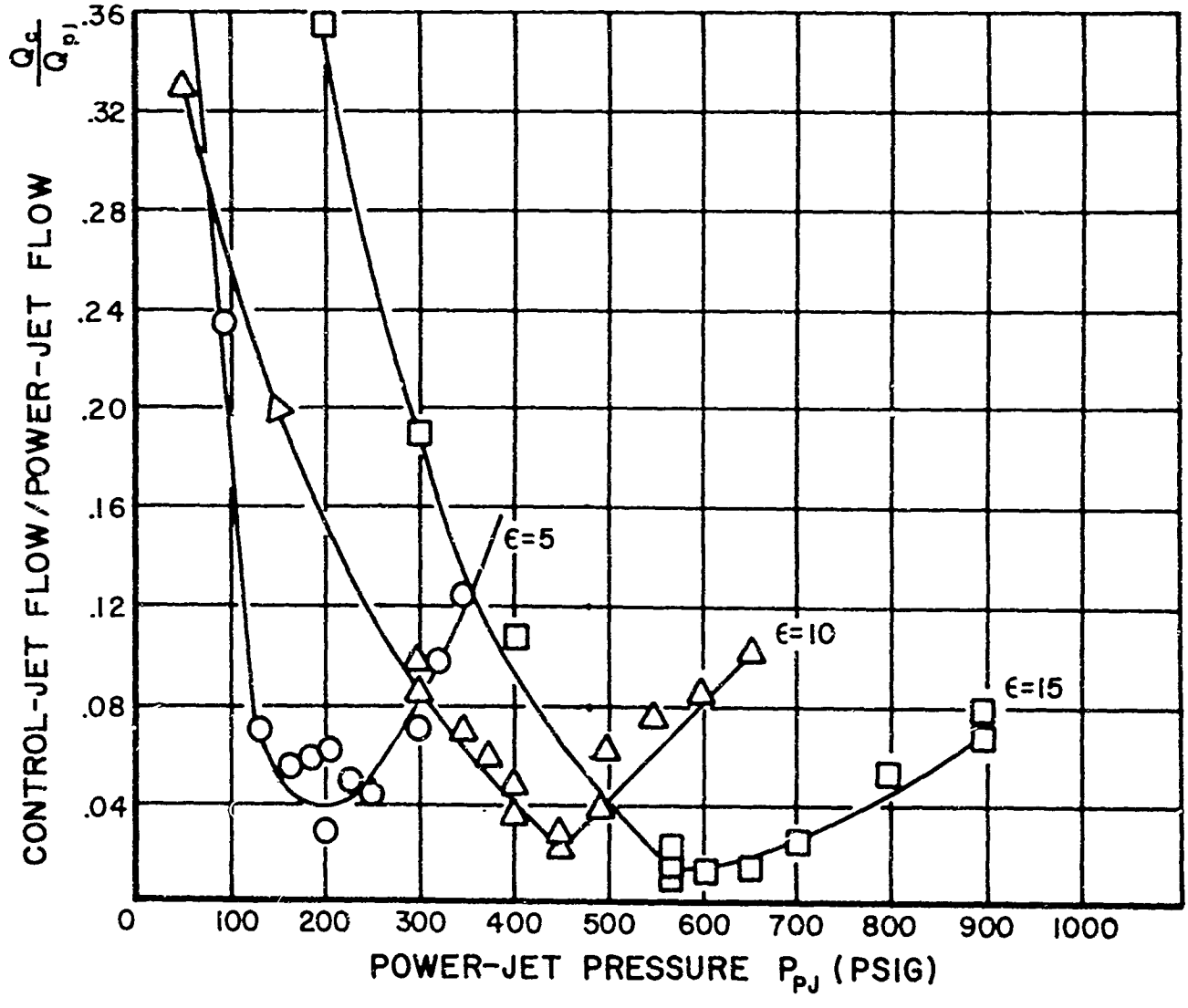

Figure 11. Control-jet flow ratios required to switch the output flow.

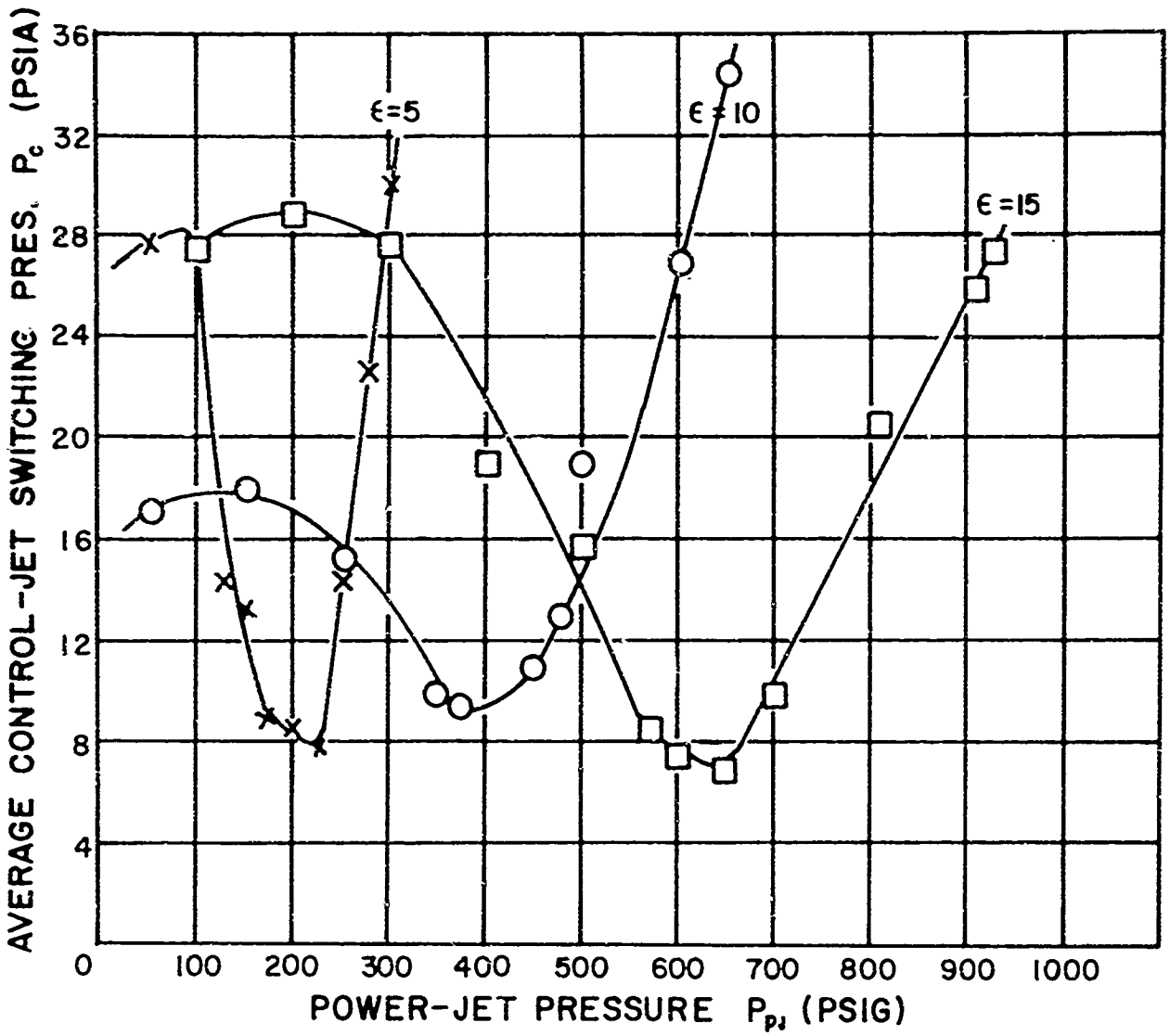

Figure 12. Average control-jet pressures required to switch the output flow.

At the present time the experimental test rig cannot be used for testing under variable back-pressure conditions. The effects of variable ambient back-pressure loading are of extreme importance in the design of a supersonic fluid amplifier. Since no tests have been run to this date (Jan. 1964), certain basic assumptions must be made. For a given set of conditions on P_{pj}, A_e/A^*, and P_s, a reduction of P_a, the ambient back pressure, manifests itself esentially the same way as an increase in P_{pj}. The pressure ratio P_s/P_e determines the separation point in the interaction region. In regime II, P_s is always less than P_a. Therefore, a reduction in P_a will cause the stream to expand into the interaction region and separate at the nozzle exit at a lower value of input power-jet pressure. This

produces a downward shift in the operating range defined approximately by regime II. An exact theoretical determination of the operating range of regime II is impossible at present because there is no accurate method of theoretically determining the separation pressure P_s in the interaction region.

Friction loading manifests itself in the form of a rise in the boundary layer static pressure. Various lengths of constant area ducting were symmetrically attached to outputs A and B. As the ducts were increased in length from 1 to about 15 diameters, the control flow required to switch the stream from output A to B was reduced. Ducting lengths from 15 to 18 diameters were sufficient to cause enough feedback through the boundary layer to produce an oscillating power-jet flow. The frequency was estimated at 1 to 3 cps, depending upon the duct length. At lengths greater than about 18 diameters total capture of the flow in any single output duct was impossible, regardless of the level of the control signal.

It is possible to explain these phenomena, if a few basic assumptions are made.

(a) The flow is one-dimensional.
(b) Steady flow is present throughout the system.
(c) There is neither heat exchange nor external shaft work.
(d) The duct is of constant area.

If the flow entering the amplifier is initially supersonic, the frictional effects will decrease the stream velocity and Mach number and increase the enthalpy and static pressure of the stream. The fluid is travelling in the direction of a positive pressure gradient because the mean velocity of the stream is diminishing. The fluid particles in the boundary layer are decelerated not only by the viscous forces acting upon them, but also by the positive pressure gradient. The retarding influences thicken the boundary layer in the direction of flow, subjecting some of the fluid particles in the boundary layer to a positive pressure gradient. This positive pressure gradient forces the fluid in a direction opposite to that of the main stream flow (Figure 13).

The reversed flow causes the static pressure in the boundary layer at the interaction region to rise as the duct length is increased. At some critical length the boundary layer static pressure reaches a value sufficient to separate the stream from the wall and cause the main stream to switch to output B. As output B fills with fluid, the boundary layer static pressure rises as it did in output A. The rate of static pressure rise is determined by the diameter and length of the duct. The boundary layer static pres-

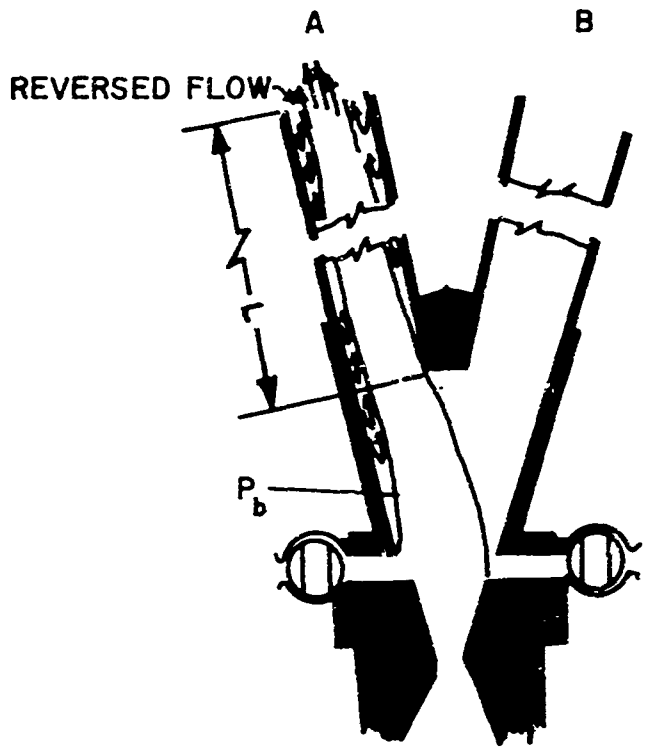

Figure 13. Assumed flow diagram of an amplifier under conditions of extreme friction loading.

sure in output B is soon sufficient to switch the main stream back to its original position in output A. Under these loading conditions, the total power-jet flow has been observed to oscillate between outputs A and B without the application of an external control signal.

At a length of about 18 diameters, the ducts were essentially choked. This meant that the flow was subsonic somewhere in the duct. It was assumed that the duct was now long enough to cause the normal shock to stand at the duct inlet (Figure 14). Under these conditions, a flooding of the interaction region was observed and the units became completely inoperative.

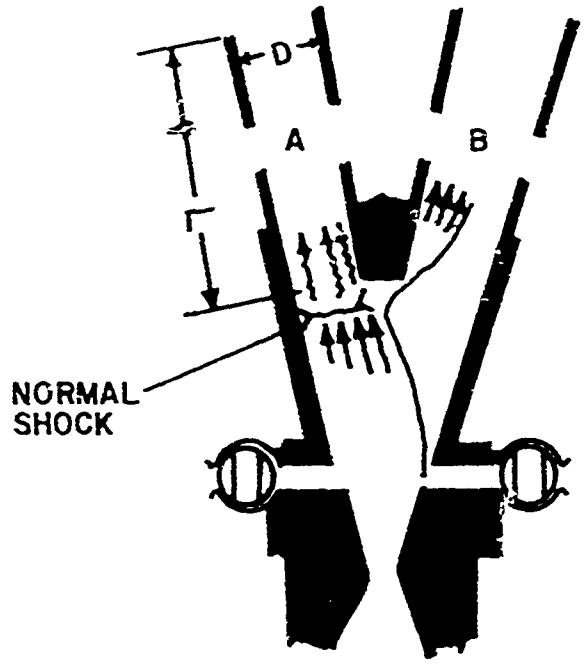

Figure 14. Possible normal shock location under choked conditions.

7. THRUST MEASUREMENTS

Two additional units with expansion ratios of 20 and 25 were made and tests were conducted on all five units to determine the amount of reactive thrust available at the output nozzles of a fluid amplifier device with ducting, the operating range of the amplifier with atmospheric control signals, and the performance changes due to ducting.

The amplifiers were installed on a thrust stand, as seen in Figure 15. The control-jet signals were obtained by opening two opposing $\frac{1}{2}$ in. ball valves. The input flow to the ball valves came directly from ambient atmospheric air. Force measurements were made with a load cell and fed into the y-axis of an x-y recorder. Power-jet pressures were plotted on the x-axis.

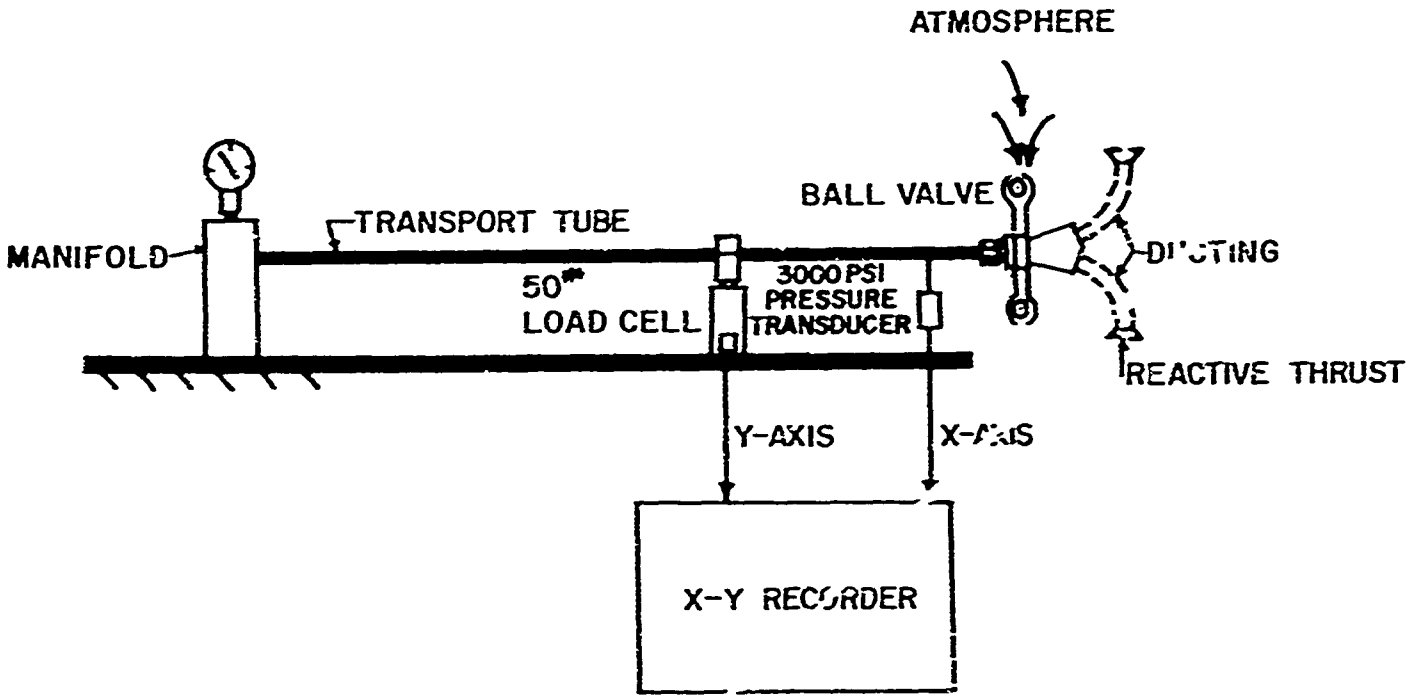

Figure 15. Experimental test rig for amplifier thrust measurements.

Figure 16 illustrates the typical output thrust data obtained with an expansion ratio of 25. During the tests, the input pressure was increased at a constant rate, while the ball valves were alternately opened and closed. These tests were performed both with and without output ducting. The operating pressure range was noted for each condition. The operating range of these amplifiers is defined as the range of input pressures that produces a linear change of output thrust from either of the two output nozzles. A decrease in the slope of the thrust line (a to b) indicates that a portion of the flow is leaking by the splitter and causing a reaction force opposing that of the flowing output nozzle. Over the range (c to d) only a portion of the flow is being switched. All units tested indicated a small amount of bias ($b > b'$), developing from minute symmetry variances in the amplifier housing.

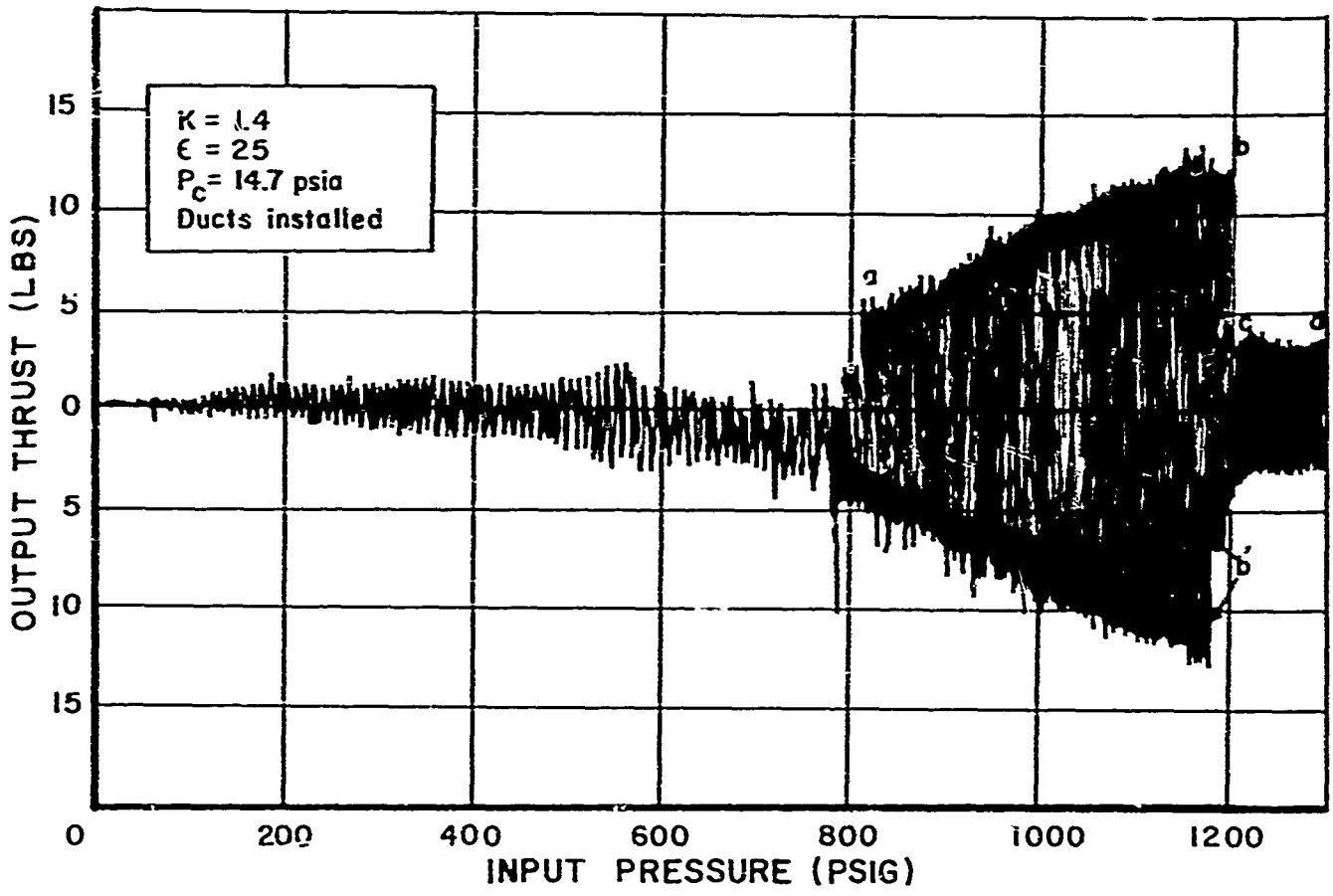

Figure 16. Sample output thrust data for $\epsilon = 25$, indicating the range of operating pressures with ducting installed.

In Figure 17 it may be noted that large changes in operating pressure range result from the addition of output ducting. This may be attributed to the rise in the boundary layer pressure P_b (Figure 13) and a reduction of P_s caused by the addition of ducting.

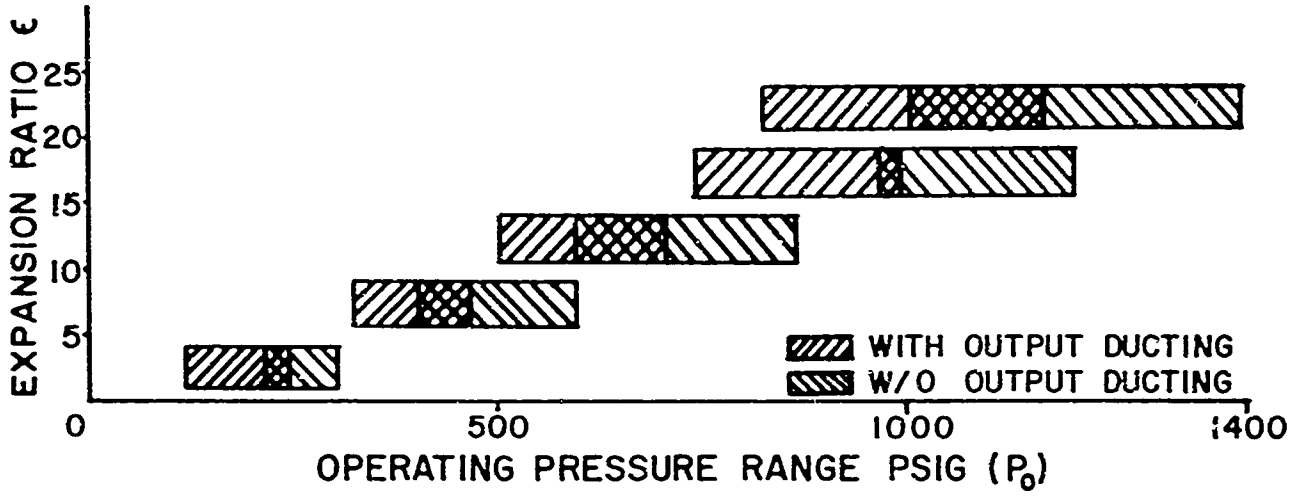

Figure 17. Change in operating pressure range due to nozzle expansion ratio and output ducting.

Direct measurements of the average output thrust over given ranges of pressure (a to b in Figure 16) were made by measuring the peak-to-peak values of thrust and dividing by 2. All units tested indicated about a 25 to 35 percent loss of thrust compared with the isentropic thrust calculated for the same power nozzle exhausting to a back pressure of 14.7 psia.

8. SUMMARY OF RESULTS

(1) Operation in regime I required from 5 to 10 times more control energy than in regimes II and III. Switching in regime I is very unstable and is not recommended.

(2) Switching in regime II is bistable, and the units do not require a continuous control signal in this range. The units operate in regime II at a control-jet mass flow to power-jet mass flow ratio of less than 5 percent and at control-jet pressures of less than 14.7 psia.

(3) Switching in regime III is tristable. The units required a continuous control-jet signal in this range to hold the power-jet flow in either of the two outputs. With zero control-jet signal, the flow was split equally between outputs A and B.

(4) The units operated over a relatively wide range of input pressures. The operating ranges are significantly reduced by the impedance of the output ducting. Output thrust efficiencies ranging from 65 to 75 percent were realized.

9. CONCLUSIONS

The units exhibited many characteristics that make them applicable to a pure reaction jet or secondary fluid injection system. An analytical determination of the power-jet supply pressure that initiates regime II operation is possible when the separation pressure P_s is assumed. A certain minimum pressure ratio between the power-jet nozzle exit static pressure and the local separation pressure P_s must be satisfied; however, a theoretical determination of this separation pressure is very difficult, because it is a function of the entrainment characteristics of the power-jet stream which are, in turn, primarily dependent upon the internal geometry of the amplifier housing.

It should be noted that nozzle expansion ratio and duct length were the only geometrical variable investigated. Changes in the internal amplifier geometry, such as splitter location and setback, will also influence the operation of the amplifiers.

10. REFERENCES

1. Warren, R. W., Barclay, R. G., and Holmes, A. B. "Application of Fluid Amplification to Rocketry", Fourth Joint Army-Navy-Air Force-NASA-ARPA Liquid Propulsion Sympsoium, pp. 131-145, 1962.

2. Pushkin, V. S. "Some Properties of Supersonic Flow", NASA TT-F-79.

3. Arens, M. and Spiegler, E. "Shock-Induced Boundary Layer Separation in Overexpanded Conical Exhaust Nozzles", AIAA Journal, Vol. 1, No. 3, pp. 579, 1963.

4. Gadd, G. E. "Interactions Between Wholly Laminar or Wholly Turbulent Boundary Layers and Shock Waves Strong Enough to Cause Separation", Journal of the Aeronautical Sciences, Vol. 20, No. 11, pp. 729-739, 1953.

HARRY DIAMOND LABORATORIES
WASHINGTON 25, D.C.

HIGH-SPEED SCHLIEREN CINEMATOGRAPHY

by

Kenji Toda

ABSTRACT

High-speed schlieren motion pictures have been taken for use in the visualization of flow transients in fluid elements.

A WF3 Fastax camera (using 16-mm film), an E.G.& G. Type 501 high-speed stroboscope, and an FX-12 xenon flash lamp are used to produce high-speed motion pictures at speeds of over 8000 frames per second. The high-speed stroboscope was modified to optimize its operation with the WF3 camera. The modification to the stroboscope not only improved its general performance but also increased the maximum flash rate to better than 10,000 per second.

1. INTRODUCTION

High-speed cinematography is the taking of motion pictures at frame rates of several hundred to several million per second. By taking pictures at a rate many times faster than the normal projection speed, an ultra-slow-motion film is produced magnifying both space and time, thus enabling the study of fast motion.

The HDL schlieren system (fig. 1 & 2), which has been described in an earlier paper (ref 1), has as part of its recording facility a high-speed camera and a stroboscopic light source. This equipment is used to photograph the transients of compressible, subsonic fluid flows in fluid elements of small dimensions.

2. LIGHT SOURCE

The light source used for the high-speed schlieren movies is an FX-12 xenon flash lamp (ref 2). This lamp, when driven by an E.G.& G. Type 501 stroboscope and a matching transformer, is capable of flashes of 1μs duration and peak light output of 10^6cp. Its small size (1-mm by $\frac{1}{4}$ in.) makes it ideal for the schlieren system; its pulse of short duration and high intensity make it well suited for high-speed movies. Its only limitation is in the running time per operation, since this is what determines the number of frames in a given run and hence the length of viewing time of the projected film.

The lamp is rated for a maximum of 30 watt-seconds per operation, where watt-seconds (WS) = $CV^2fT/2$, and C = capacitance across the lamp in microfarads; V = voltage on capacitor in kilovolts; f = frequency in cycles per second; and T = running time in seconds.

The stroboscope charging voltage is 8000-v with a choice of discharge capacitance of 0.01, 0.02, or 0.04μf. Calculating on the basis of f = 8000fps, V = 8-kv, C = 0.02μf, and WS = 30, T = 0.006 sec. This would profuce a total of 48 frames, and when projected at a rate of 16fps, would yield a total viewing time of 3 sec.

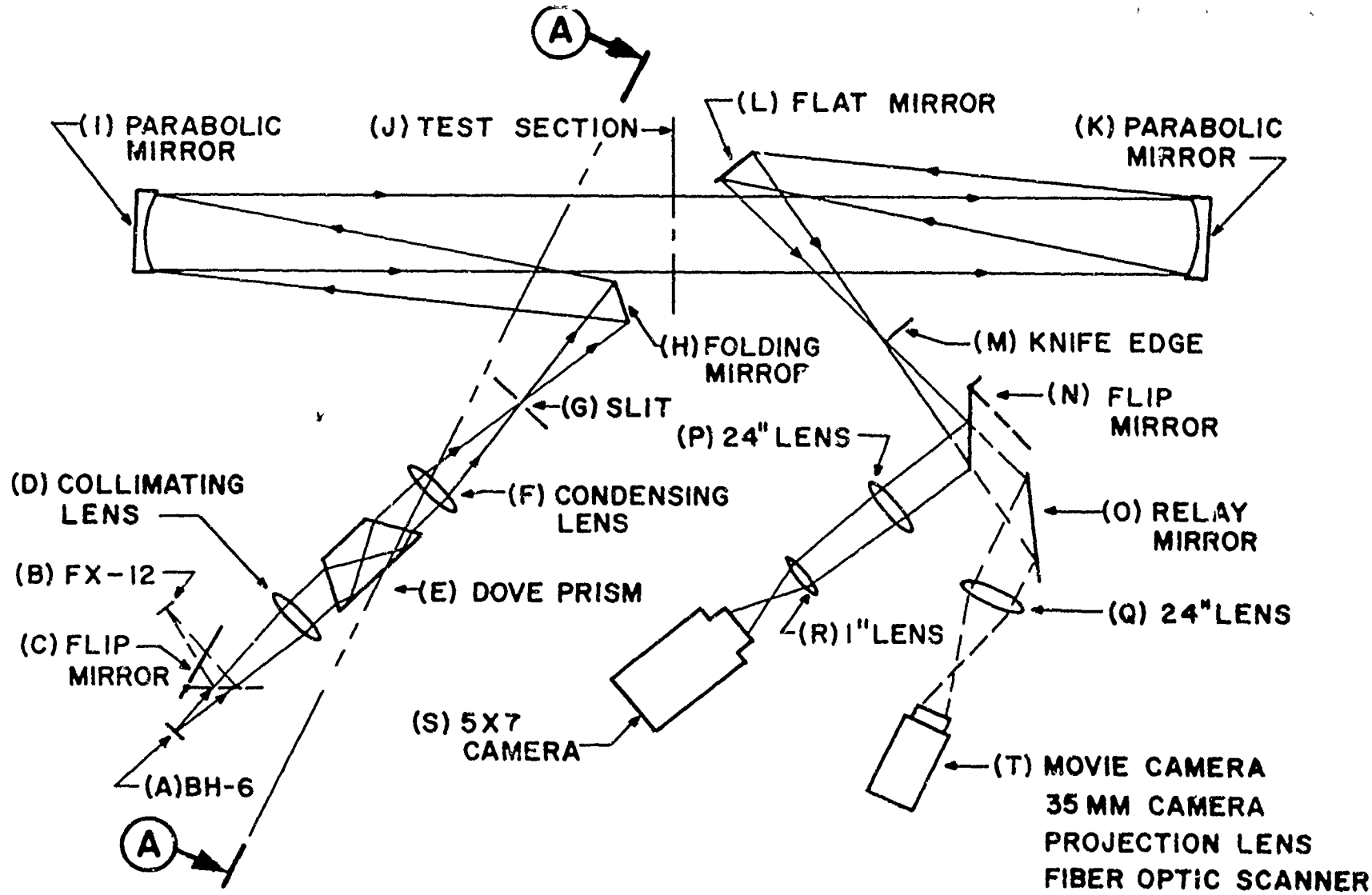

Figure 1. Schematic of HDL schlieren system. (See Figure 2 for photograph of actual system to the right of section A-A).

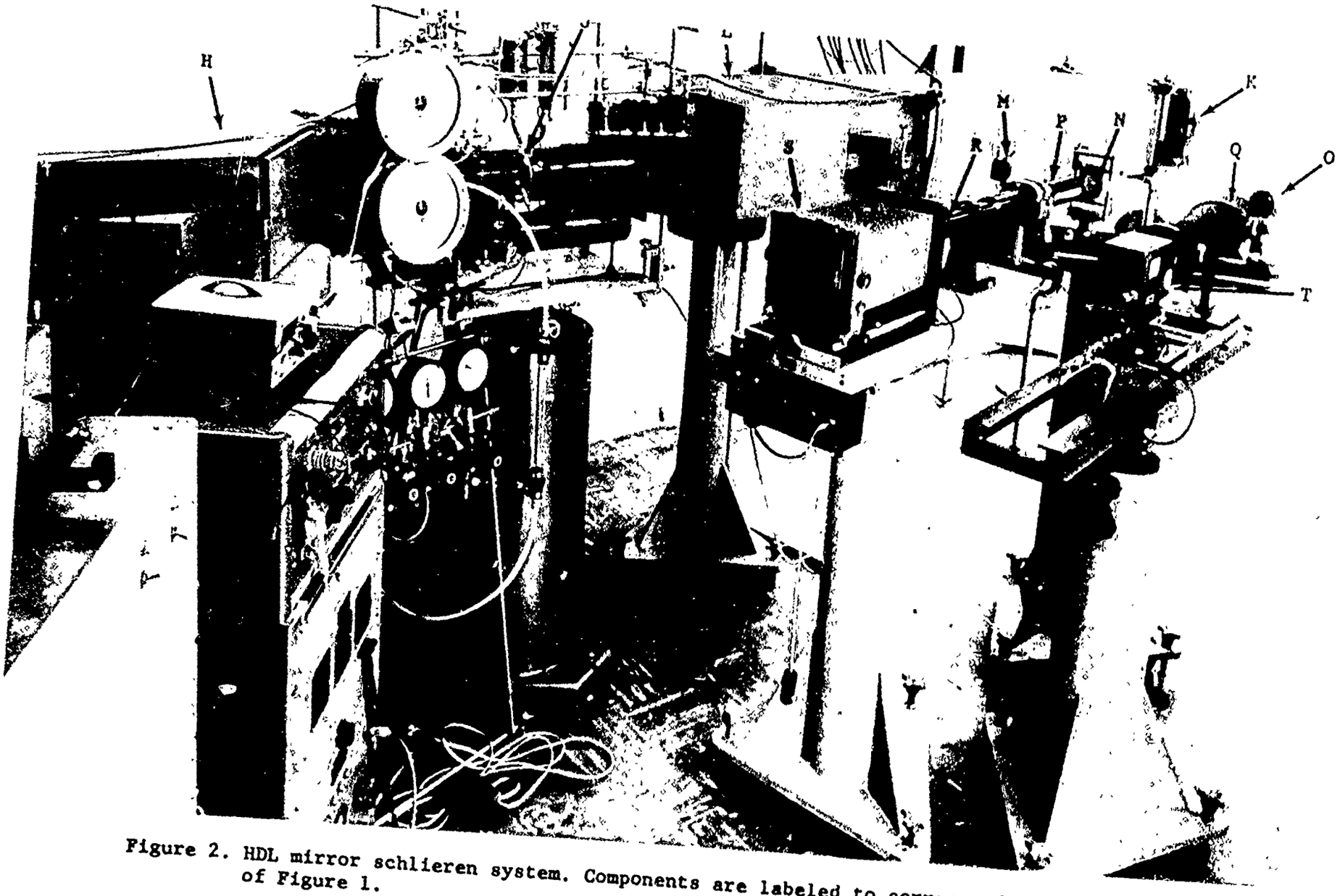

Figure 2. HDL mirror schlieren system. Components are labeled to correspond to schematic of Figure 1.

To increase the projection time, the lamp was operated to produce a minimum of 80 frames; although, this corresponds to approximately 56 WS, this caused no apparent damage to the lamp.

3. LAMP CIRCUIT

The high-speed stroboscope, which consists of a power supply, modulator, and timer unit, was used to flash the lamp. The power supply employs a conventional full-wave bridge rectifier with a thermal overload circuit breaker in the transformer that opens the circuit if excessive direct current is drawn from the power supply.

The modulator unit, which supplies current pulses to the lamp, consists of a hydrogen thyratron switch tube and a trigger amplifier that fires the thyratron. The reluctance pickup of the camera is connected to the input of the trigger amplifier to synchronize the camera with the stroboscope.

The timer unit comprises (1) a lamp delay, which allows the camera to reach operating speed before the lamp is started; (2) a lamp running-time switch, which determines the length of time the lamp will be operated (this is necessary to prevent damage from overheating), and (3) an event delay which produces a trigger signal for filming at the desired time.

Figure 3 is a schematic of the modified circuit. The changes involve C_1, the filter capacitor, and CH_2, the charging inductance, and insertion of a current-limiting resistor R_2. C_1 was increased from 12 to 125μf; this eliminated a serious droop in the output voltage waveform. CH_2 was replaced with a hand-made choke, whose size and value ($\approx$ 30 mh) were experimentally determined in the laboratory, to increase the high-frequency response of the circuit. R_2 (50 ohms, 100-w) was inserted for circuit protection and to prevent the thermal overload circuit breaker from opening.

Figures 4a and 4b are oscillograms of the voltage (upper trace) and light (bottom trace) output before and after modification to the 501. The first few pulses of the output voltage are always less than full amplitude because of the time constant of the resonant charging circuit.

As can be seen in the oscillograms, the high-frequency response of the stroboscope has been increased to more than 8000 cps. Of equal importance is the marked improvement in the uniformity of light output; this is particularly important if any quantitative work is anticipated. Slight modifications in light intensities (as little as 5%) are not only noticeable and annoying, but can lead to a misinterpretation of the results when viewing the projected film.

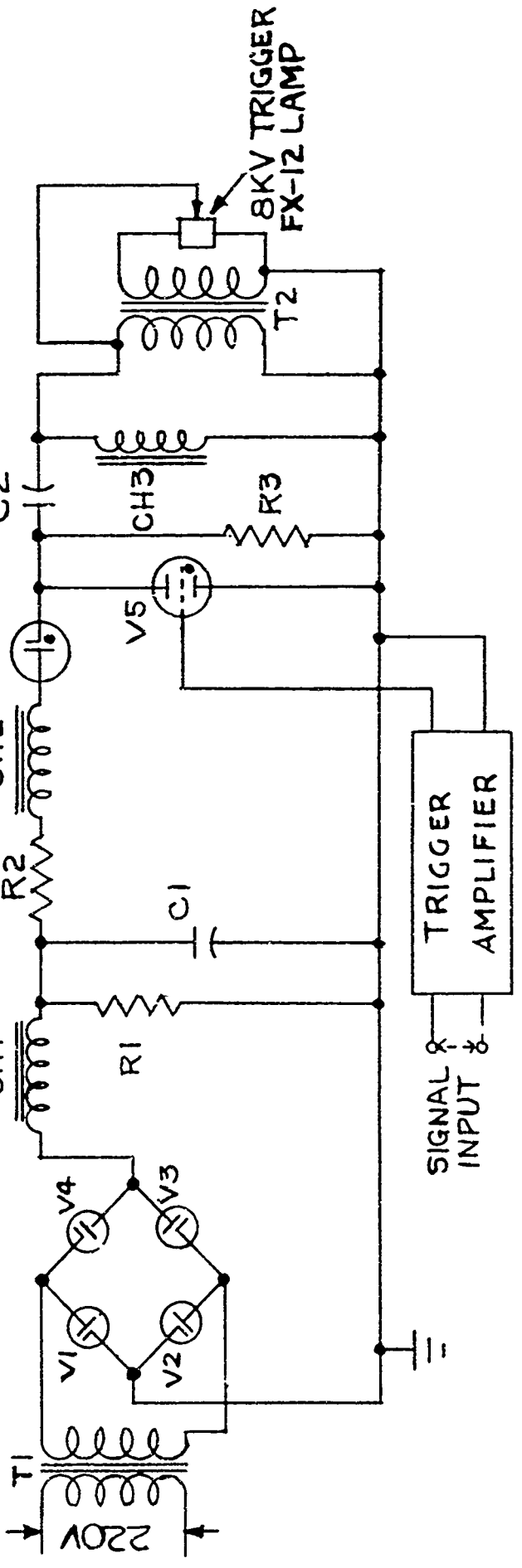

Figure 3. Schematic diagram of modified portion of the 501 circuit.

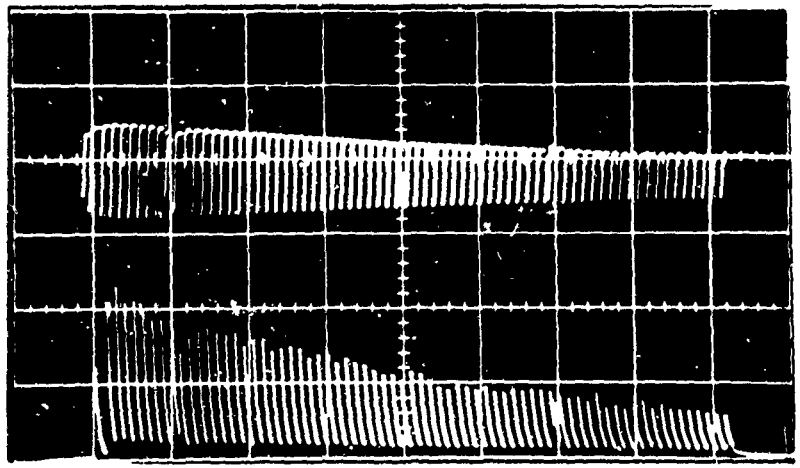

Frequency: 4 kc Sweep: 2 msec/cm

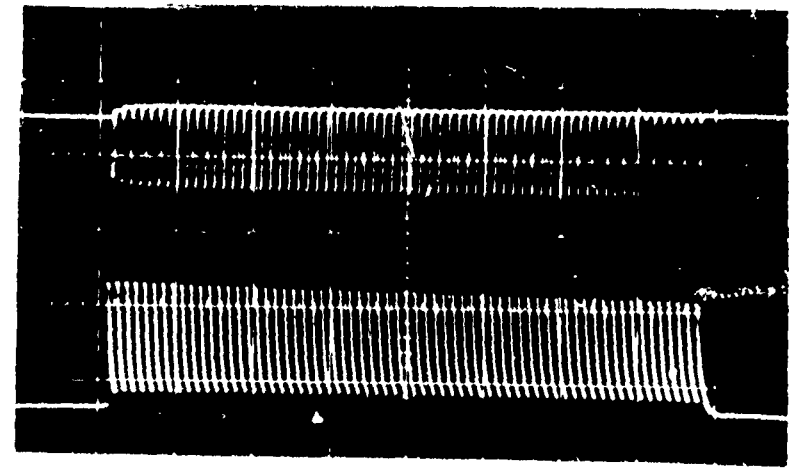

Frequency: 4 kc Sweep: 2 msec/cm

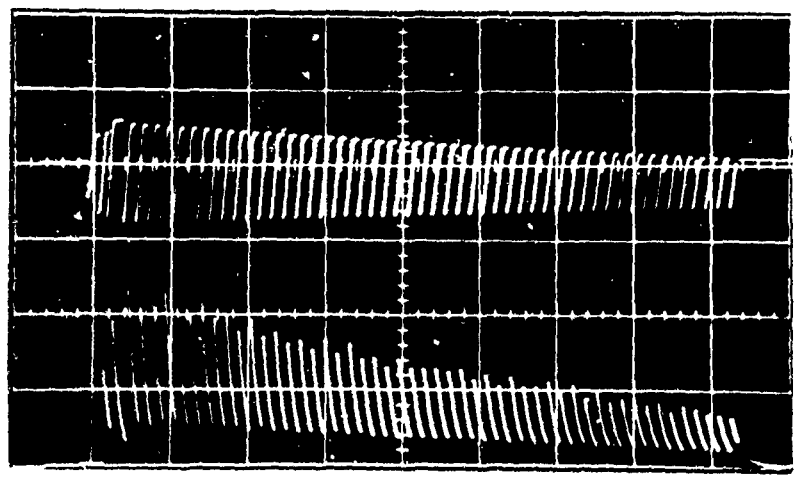

Frequency: 6 kc Sweep: 1 msec/cm

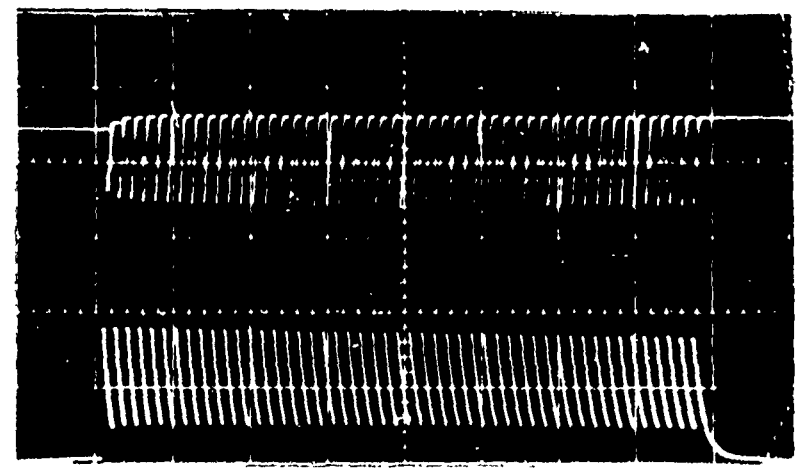

Frequency: 6 kc Sweep: 1 msec/cm

Figure 4a. Oscillograms of the 501 voltage output and the FX-12 light output.

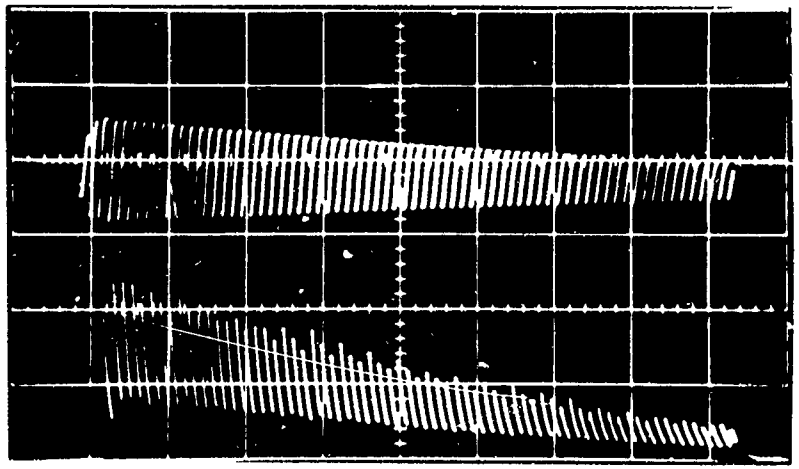

Frequency: 8 kc Sweep: 1 msec/cm

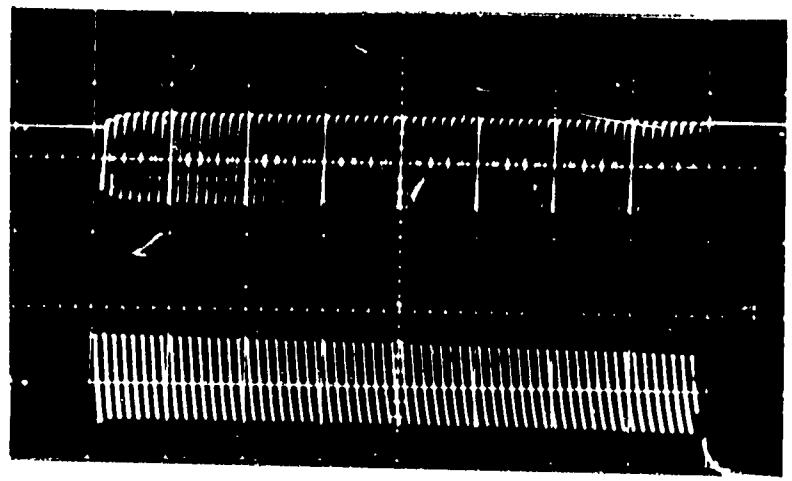

Frequency: 8 kc Sweep: 1 msec/cm

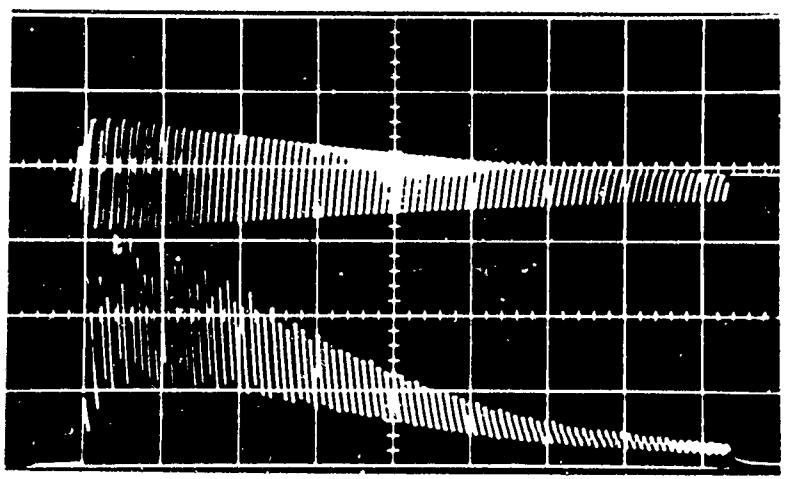

Frequency: 10 kc Sweep: 1 sec/cm

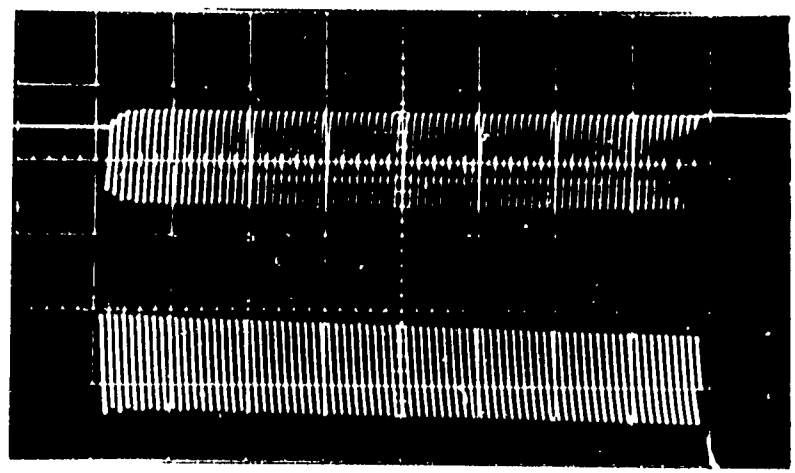

Frequency: 10 kc Sweep: 1 msec/cm

Figure 4b. Oscillograms of the 501 voltage output and the FX-12 light output.

4. HIGH-SPEED CAMERA

The high-speed camera used with the schlieren system is a model WF3 (16-mm) Fastax. This camera is equipped with a rotating prism that has two functions -- to perform the shutter operation and to move the image in synchronism with the film to minimize blur. Inasmuch as the exposure time is determined by the flash duration of the lamp, the prism was removed from the camera to improve the spatial resolution of the image.

A calibrated 1000-cps timing light is focused on one edge of the film producing small exposed areas separated by equal time intervals. These timing marks are used to compute the framing rate of the camera and the interframe interval of the film.

The camera is equipped with a reluctance pickup (see fig. 5) which, upon the passage of a sprocket tooth, generates a signal. This signal is used to operate the stroboscope, which flashes the lamp in synchronism with the camera.

The operating speed of the camera is determined by the voltage level of the power supplied to the camera motors. (See fig. 6 for typical voltage speed curve.) When operating at its maximum speed of 8000 frames per second, a 100-ft roll of 16-mm film will be exhausted in 0.75 sec. The useful running time at top speed is a little over 0.25 sec, since the camera requires approximately 0.5 sec to attain its operational speed.

5. TYPICAL OPERATION

Figure 7 is a block diagram of the instrumentation used in a high-speed schlieren movie sequence. This particular sequence was of the switching of a bistable element from a pulse input.

The starting switch initiates the camera control and stroboscope simultaneously. The lamp delay allows the camera to reach the proper operating speed, then a relay is activated that triggers the pneumatic pulse generator (fig. 8). The generated pulse, which switches the bistable element, is measured by a pressure transducer, whose output is, in turn, monitored on an oscilloscope.

The reluctance pickup signals of the camera are transmitted to an AND circuit whose output is connected to the stroboscope. The relay that triggered the pulse generator also triggers the oscilloscope and a one-shot variable-delay, gating circuit. When the AND circuit receives the signals from the reluctance pickup simultaneously with the "gate" signal, the stroboscope flashes the lamp for the duration of the gate. The lamp output is measured by a phototube and is recorded on the oscilloscope.

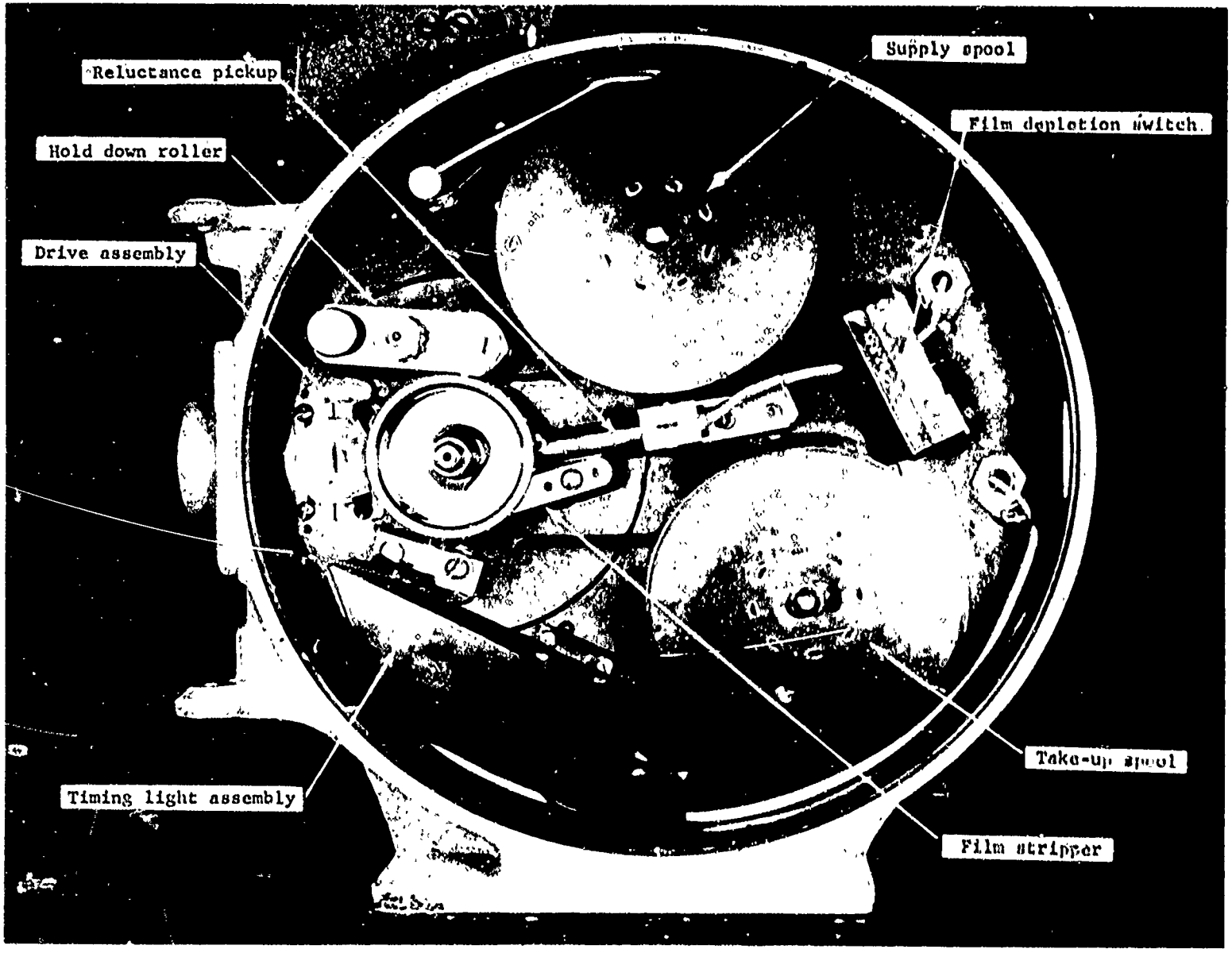

Figure 5. The WF3 Fastax camera with a reluctance pickup.
(The rotating prism has been removed).

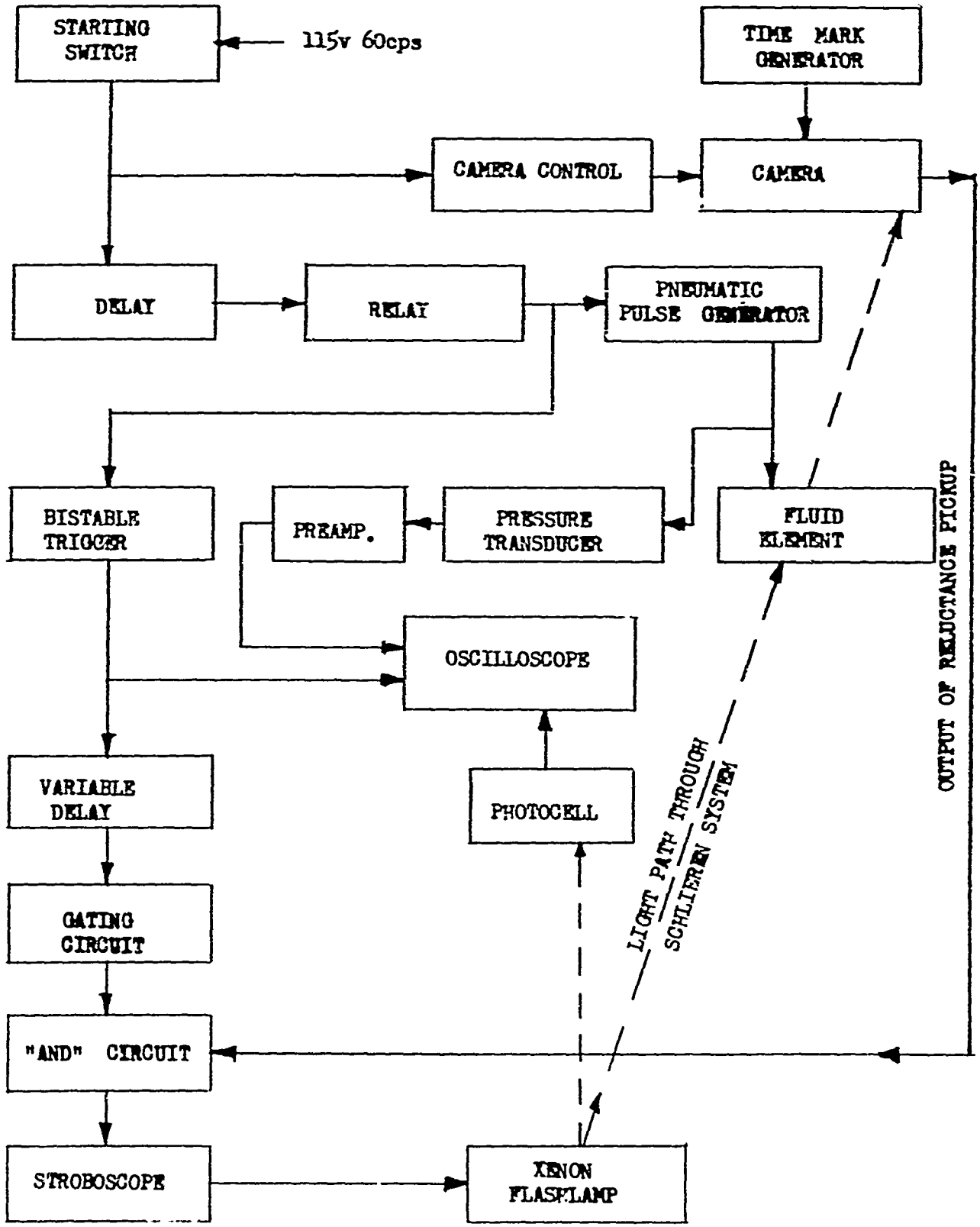

Figure 6. Block diagram of instrumentation for high speed schlieren movie of the pulse switching of a bistable fluid amplifier.

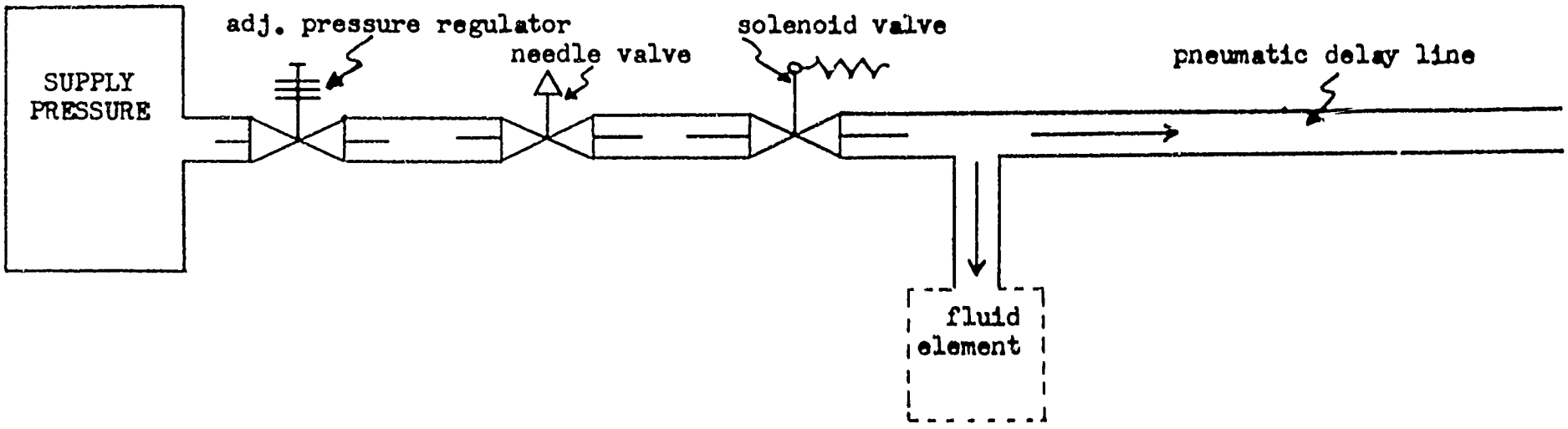

Figure 7. Schematic of pneumatic pulse generator.

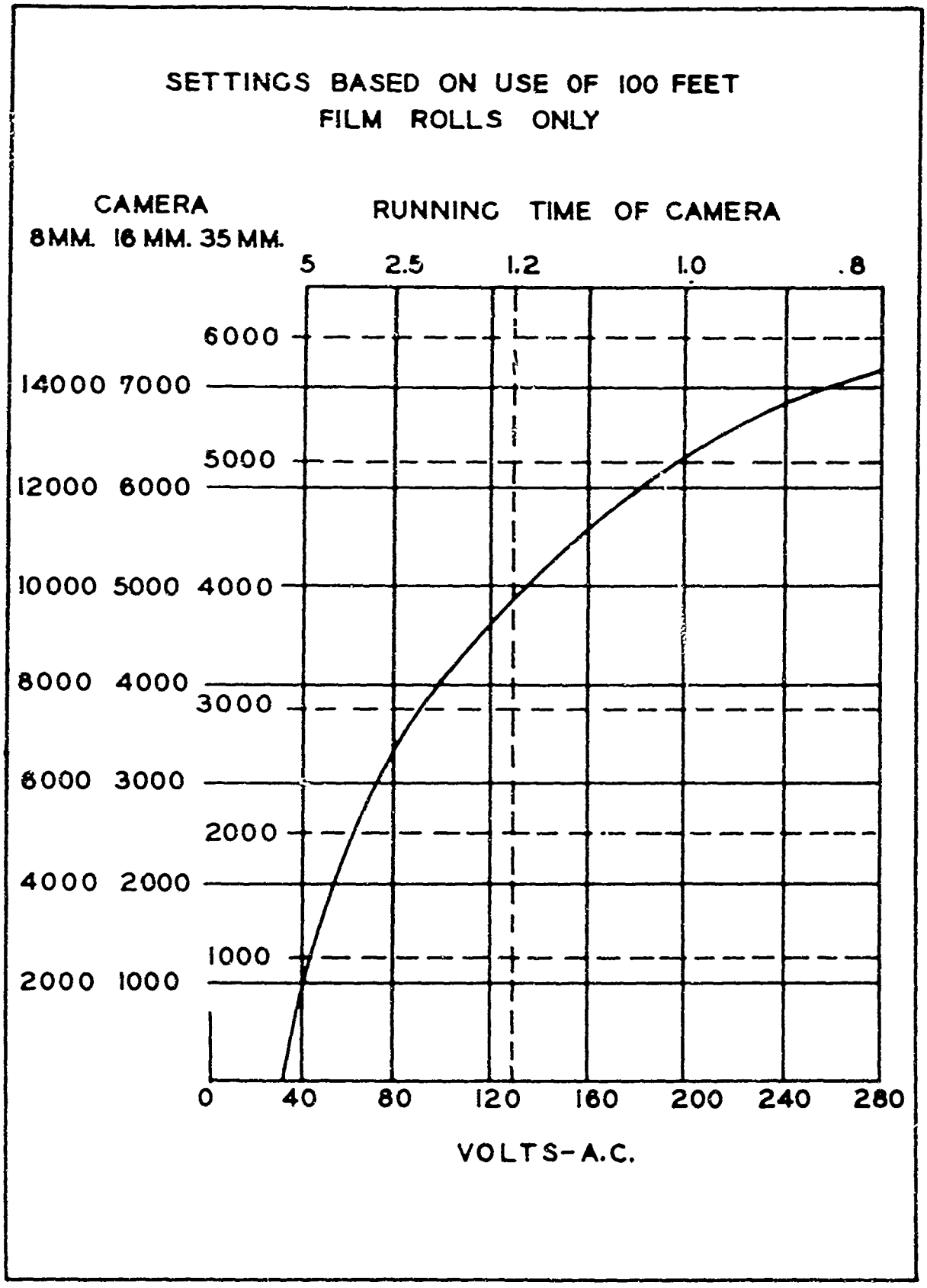

Figure 8. Graph of camera speed as a function of voltage. (Reprint from Fastax instruction book).

6. STRIP-PRINT

Figures 9 and 10 show strip prints of the pulse switching of a bistable fluid element. Note that in figure 9 the first timing mark is seen in frame number 16 and the second in frame number 24 so that there is slightly more than eight frames between timing marks. Thus, the frame rate is slighcly greater than 8000 frames per second.

The first frame in each row is numbered so that each frame can be identified with a corresponding light signal on the oscillogram. The dark protrusions in the upper left and right corners of figure 10 are small probes, which emit a small flow of helium to aid in flow visualization. Note that in frames 22-23 the helium in the right channel has changed its direction before there is any appreciable shifting of the power stream, indicating that the switch is preceded by a pressure wave. One should be careful not to misinterpret the schlieren image, keeping in mind that it is a density gradient representation of the flow rather than the flow itself.

The strip prints are useful supplements to the projected movie film but a proper appreciation of motion cannot be perceived by viewing the strip prints alone. Often faint density gradients show up as motion when projected as a movie but prove difficult to detect when viewed frame by frame.

Figure 11 is a strip print of a pressure pulse expanding through a nozzle. The frame rate for this sequence, as measured between the timing marks, is a little better than 8000 per second. Since the duration of the entire sequence is less than 2ms, or less than 16 frames, the projection time (at 16 fr/sec) would be less than 1 sec. In this case a frame-by-frame study would be more practical.

7. STRETCH-PRINT

At times the equipment available will not permit adequate time resolution of a given event. This is due to an excessive interframe interval that may cause loss of information between pictures. Inadequate time resolution can also result in such brief coverage that the limited number of frames available will not provide sufficient viewing time upon projection.

To increase the projected viewing time, stretch or freeze prints can be made by reproducing each frame several times in succession. This lengthens the viewing time by the number of times each frame has been repeated.

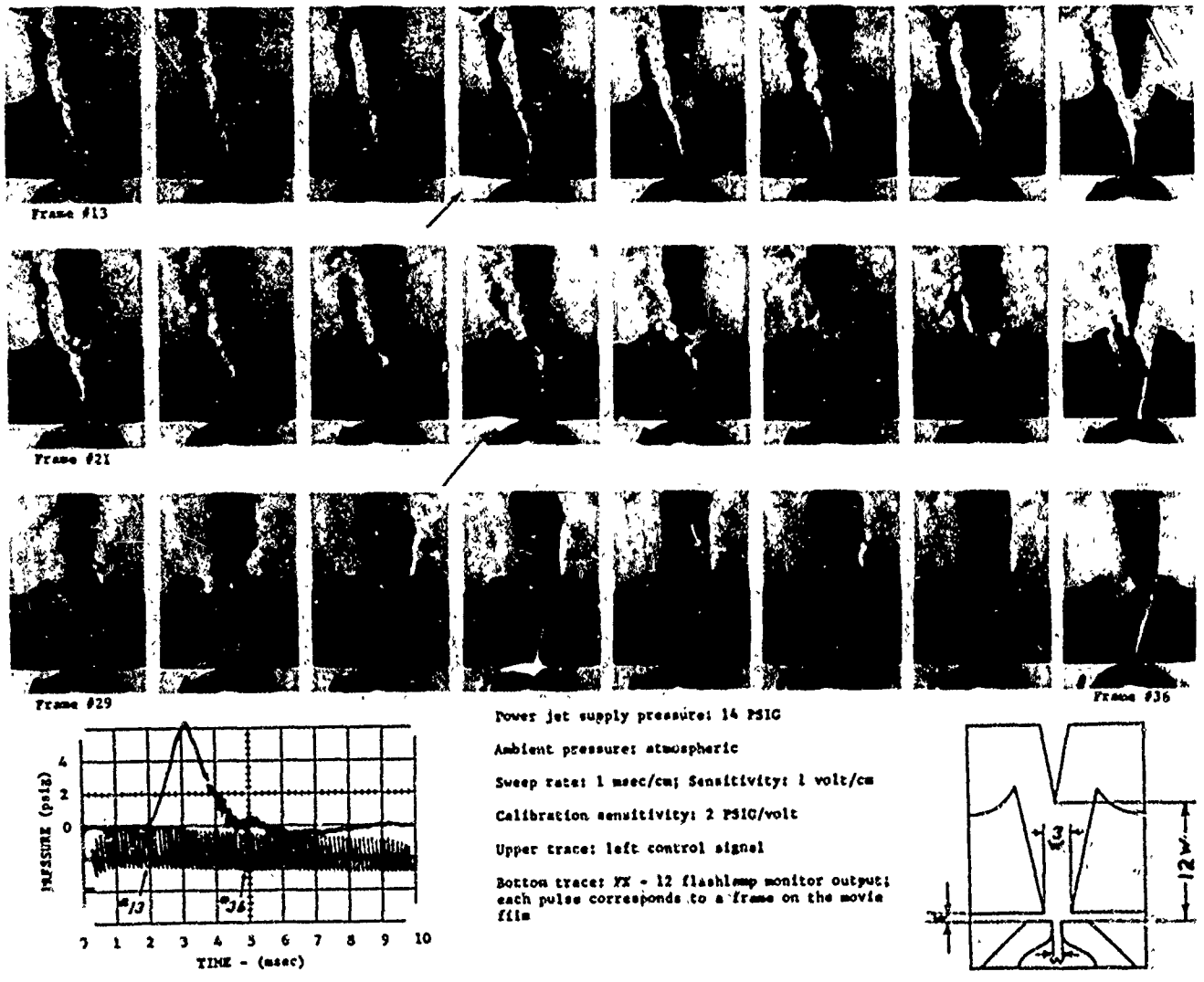

Figure 9. Strip prints of the pulse switching of a bistable fluid amplifier.

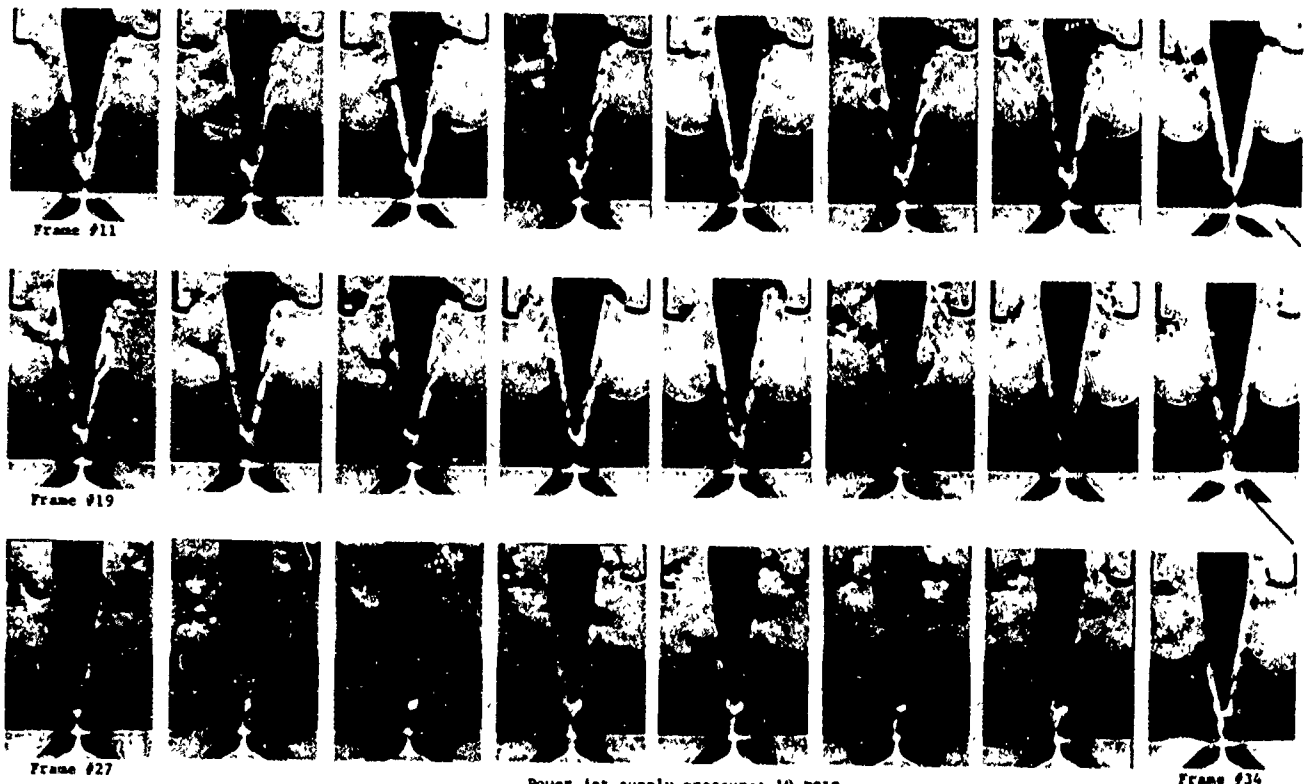

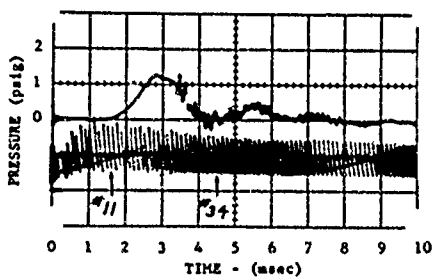

Power jet supply pressure: 10 PSIG

Ambient pressure: atmospheric

Sweep rate: 1 msec/cm; Sensitivity: 0.5 volt/cm

Calibration sensitivity: 2 PSIG/volt

Upper trace: left control signal

Bottom trace: FX - 12 flashlamp monitor output; each pulse corresponds to a frame on the movie film

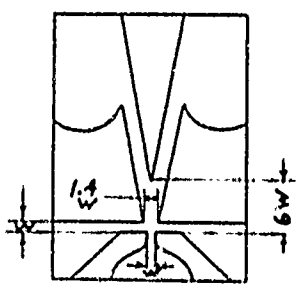

Figure 10. Strip prints of the pulse switching of a bistable fluid amplifier.

Figure 11. Strip print of pressure pulse expanding through a nozzle.

8. FILM

The film speed requirements are not as severe as some of the other requirements of high-speed schlieren photography. The amount of light available at the film can be varied by changing the source slit width (see fig. 1). This will permit more or less light to pass through the system, but, of course, will also change the schlieren sensitivity. Although for qualitative visualization the slit width is not critical, the slit width settings should be calibrated for exposure purposes.

Two types of film, suitable for high-speed work, are Eastman Kodak's Plus-X Reversal and Tri-X Negative. The Plus-X Reversal is a fine grain, slow speed (ASA 50) film and used whenever possible because of its superior resolution. The Tri-X Negative is a grainier, but faster speed (ASA 320) film which permits lower light levels to be used and thus longer filming sequences.

The choice of the proper film must be determined experimentally because of the failure of the reciprocity law due to the high light intensities involved. In some instances it is possible to recover film speed by prolonging the development period (ref.4) and by using fresh developer for each operation.

9. CONCLUSION

High-speed schlieren cinematography can be used for visualization of transients of subsonic fluid flows. There are two common methods used to analyze the film: (1) a visual or qualitative analysis of the projected film, and (2) a frame-by-frame inspection for quantitative measurements of deflection, velocity, deformation, etc.

With a rotating-prism type camera, the time resolution is limited by the maximum available speed of the camera. Even for subsonic transients, there appears to be a need for better time resolutions than that available with this type camera. Certainly, for sonic and supersonic transients, ultra-high-speed cameras, the problems become increasingly greater, particularly those associated with illumination and synchronization.

Some preliminary work has been done here at HDL with a turbine-driven rotating mirror-type camera. The camera is capable of producing 78 frames at a rate in excess of 400,000 per second. Acceptable exposures have been obtained with Plus-X film at speeds of over 200,000 frames per second.

REFERENCES

(1) J.R. Keto, "Fluid Amplification - 2. Flow Visualization - Compressible Fluids," DOFL Report, TR-1041, Aug 1962.

(2) H.E. Edgerton and P.Y. Cathou, "Xenon Flash of Small Size," Review of Sc. Inst., Vol. 27, No. 10, 821-825, Oct 1956.

(3) H.E. Edgerton, "Theory and Application of Electronic Flash," E.G.& G., Inc.

(4) C. Wyckof, "Exposure Reciprocity Effects on Several Photographic Films," E.G.& G. Tech Memo, No. B-289, Sept 1960.

ACKNOWLEDGMENT

Acknowledgment is made of the efforts of Jorma R. Keto in the development of the circuits described and in supervision of this project.

Four Fluid Amplifier Controlled Medical Devices

Kenneth Woodward*, George Mon*, James Joyce*, Henry Straub*
and Timothy Barila**

INTRODUCTION

The fluid amplifier provides a solution for certain design problems associated with modern military medicine. The military requires its medical equipment to possess not only a reliability and life compatible with its proposed use, but sufficient ruggedness to withstand the rigors of logistics and operation in the field. The equipment must be lightweight. Pneumatically powered devices should be able to tolerate fairly high degrees of contamination in the power fluids without malfunctioning. Repeated autoclaving of appropriate portions of the apparatus should not degrade its function.

Where fluid amplifiers are used, these requirements are generously satisfied. By reducing the number of moving parts involved, logistics problems are simplified and manufacturing cost reduced.

In illustration, this paper describes a pressure-limited respirator, a volume-limited respirator, an external cardiac compressor, and a blood pump all utilizing fluid amplifiers for control and designed primarily for Army medicine.

*Harry Diamond Laboratories, Washington, D. C. 20438
**Walter Reed Army Institute of Research, Washington, D. C. 20012

THE BINARY FLUID AMPLIFIER

Bistable fluid amplifiers are used in all equipment described herein. Figure 1 shows a bistable amplifier used to control the gas flows in a pressure-limited respirator. Gas from the power orifice is caused to flow into one of two receivers. If the gas is initially caused to flow into the left receiver, a flow of air from the left control orifice sufficient to satisfy the entraining requirements of the power stream causes the power stream to switch and flow into the right receiver. The switching of the power stream from right to left receiver is accomplished in the same manner. Bistable amplifiers can be produced with memory, nonmemory, and reset characteristics.

The amplifier can be made by engraving or etching the configuration in a solid block and is therefore extremely rugged. In the absence of the inertia associated with moving parts, the response of the amplifiers to control flows is rapid. Reliability and manufacturing costs are both favorably influenced by the absence of moving mechanical parts. The four medical devices discussed illustrate these advantages. It is to be emphasized that these devices are in various stages of development.

A PRESSURE-LIMITED RESPIRATOR

The bistable fluid amplifier has been applied to the control of the pressure-limited respirator shown in figure 1. This respirator has no moving parts and functions both as an assistor and controller with the change from one function to the other taking place automatically. The respirator can not produce pressures in the face mask greater than a predetermined maximum. Pressures in the face mask are

transmitted to the left amplifier control orifice through the feedback line shown. The power stream switches from left to right receiver when the predetermined face mask pressure has been reached. Switching to the face mask recurs when the pressures in the feedback line have dropped to some desired negative pressure.

Because of its size and weight, the respirator can be attached directly to the face mask. Its final size will approach that of a small matchbox. It can be molded entirely out of a suitable plastic and be produced inexpensively enough to be owned by a patient, and used at home under a physician's direction, eliminating trips to the hospital or office, and assuring more nearly optimal treatment of their chronic respiratory disease.

Animal tests on the early prototypes demonstrated flows from 3 to 9 ℓ/min, cycling rates from 15 to 50 cpm, and pressures from -4 to +18 cm H_2O. Input oxygen pressures under the most demanding conditions did not exceed 2 psig with flows of 25 ℓ/min. It is expected that these characteristics will require some adjustment for clinical application. It is also possible that individual models for the child and the adult may be necessary.

A VOLUME-LIMITED RESPIRATOR

Figure 2 shows a volume-limited respirator controlled by a fluid amplifier. It, too, functions either as an assistor or controller, with mode transition occurring automatically. In the control mode, it is volume limited with a maximum pressure safety limit. It can be made to be pressure limited after relatively minor design changes.

The adoption of fluid amplification to the control of this device has reduced the number of moving parts to a piston, a bellows, two excursion triggers with springs, a rubber flapper, and an inspiration trigger piston.

Power requirements in the final design are expected to be comparable to those of similar equipment using commercially available pneumatic parts. Maximum air flows of 0.6 cfm at pressures not in excess of 35 psig satisfy the most severe load anticipated for the device. The most severe load is associated with a pulmonary circuit compliance of 0.010 $\ell/(\text{cm } H_2O)$ combined with a resistance of $20(\text{cm } H_2O)/\ell/\text{sec}$ calibrated at a flow of 1/2 ℓ/sec.

Presently its tidal volume is variable between 300 and 1000 cc with cycling rates from 6 to 60 cpm, the lower tidal volume being associated with the higher cycling rate and vice versa. If desired, these output characteristics can be suitably altered by appropriate design changes.

EXTERNAL CARDIAC COMPRESSOR

A first prototype of an external cardiac compressor controlled by a fluid amplifier is shown in figure 3. It has only three moving parts - a piston with an integral excursion control rod, an excursion limit trigger, and a spring. Functionally the device has one new aspect not present in commercial models. Prior to the onset of assistance to the subject, an estimate is made of the desired chest deflection, and the ram excursion control on the device is set accordingly. Then the operator increases the air pressure to the ram

until the ram begins to move up and down rythmically. At this point the compressor is functioning properly. It is not possible for the operator to accidentally cause chest deflections greater than the preset value by the application of excess air pressure. Once the compressor has been started, the operator need only check it to insure that the ram is moving up and down. No measurement of displacement or force is necessary. The inability to cause unwanted rib-cage deflections is a decided advantage for a cardiac compressor.

The frequency of compression tends to increase as the ram excursion decreases. This parallels the human situation. However, a separate frequency control is provided for selecting a desired frequency.

The ram is capable of a 3-in. maximum and 1/2-in. minimum excursion. Maximum cycling rates are variable from 30 cpm (3-in. excursion) to 120 cpm or more (1/2-in. excursion). Maximum power requirements are 2.5 cfm of air flow at 30-psig pressure. This pressure corresponds to a 100-lb ram force.

A FLUID AMPLIFIER HEART PUMP

The Army Artificial Heart Pump (figure 4) which uses a fluid amplifier was reported to the symposium in 1962. Included in the proceedings for that year is a description of the general functional characteristics of the pump. Its performance has since been improved. It is being developed by the Army to support the wounded soldier, but its application to civilian medicine is perhaps greater.

Several hundred animal tests of various sorts have been completed with generally encouraging results. The Walter Reed Army

Institute of Research has determined that animals perfused by the pump in total heart-lung bypass procedures for 2 hours survive while animals perfused by the roller pump all die, everything else in the blood circuit remaining the same. Indiana University has established that the resistance of both the systemic and pulmonary circulations were significantly less for pulsatile than for nonpulsatile flow. Renal blood flow was also found to be much greater for pulsatile flow than for nonpulsatile flow when the pressures were maintained at the same level in both groups. The pulsatile flows were provided by the Army pump. It is believed that the pulsed flows from this pump closely resemble those from the heart since the rise time of the pulse is very rapid due to the fast switching time of the fluid amplifier. It is not suggested that pulsed flow only from the Army pump can produce the results cited.

Criticism received thus far suggests that the flows from the pump might be slightly low for certain clinical applications, and that there are too many controls for easy operation. The flow has been increased through design modification effected in the latest model. Only two controls are now considered necessary to operate the pump. The weight of the model shown in figure 4 is 6 lb.

One pump with ball valves has been operating for 14 months producing a $3\frac{1}{2}$-ℓ/min water flow at 450-mm-Hg pressure. After 6 months, a natural rubber ventricle was replaced by one made of silastic, not because it was worn out, but because oil in the power air had created a sticky coating on the exterior of the ventricle.

This affected control. A second pump with a silastic ventricle and bicuspid valves has been running under the same flow conditions for 10 months. Occasionally the pumps are adjusted (about once a week) to compensate for oil and debris in the power stream. These accumulate in the controls. However the accumulation is never great enough to stop pump operation.

DISCUSSION

Fluid amplification has been successfully applied to two types of respirators, an external cardiac compressor, and a heart pump. It has been found to provide a satisfactory solution both functionally and from the packaging viewpoint. The heart pumps have been operating continuously under severe loads for a peiod of about a year (and these pumps are still operating), which emphasizes the extreme reliabilities and lives that can be expected of devices controlled by fluid amplifiers. The source of power for these pumps has been ordinary shop air, and in spite of the significant amounts of foreign material in the supply, the pumps continue to function reliably.

The elimination of moving parts not only accomplishes dramatic increases in reliability and life, but significantly decreases the manufacturing cost and increases environmental ruggedness of the items.

It is not suggested that all of the items have been thoroughly tested, but with the exception of the heart pump, the functional design of the devices do not deviate greatly from existing commercial designs. Consequently it is not expected that functional characteristics will create problems. The heart pump, however, has significant functional

deviations from existing designs. The medical evaluations of the pump to date are encouraging.

Fluid amplification is also being considered as a means of control for an internal heart transplant. Using the principles of design of the Army Heart pump (assuming tests prove these principles are compatible with the human requirements for pumping blood) packaging for internal use would be a relatively easy task. The life of the pumps as suggested by existing test results encourages this application. The fact that the ultimate design would require at most a single external control for occasional adjustment and a simple power supply supports this application from the viewpoint of the user.

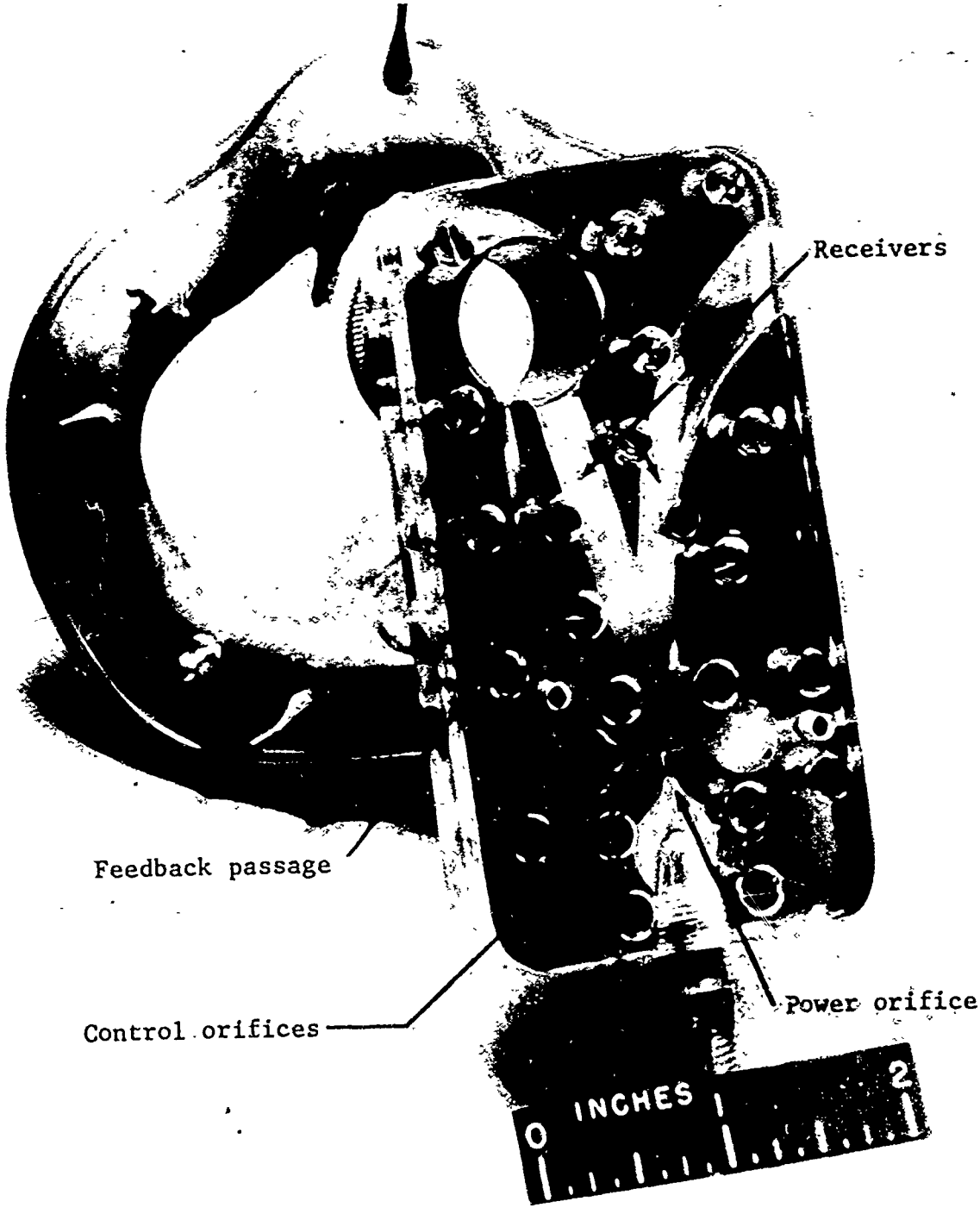

Figure 1. Pressure-limited fluid amplifier respirator.

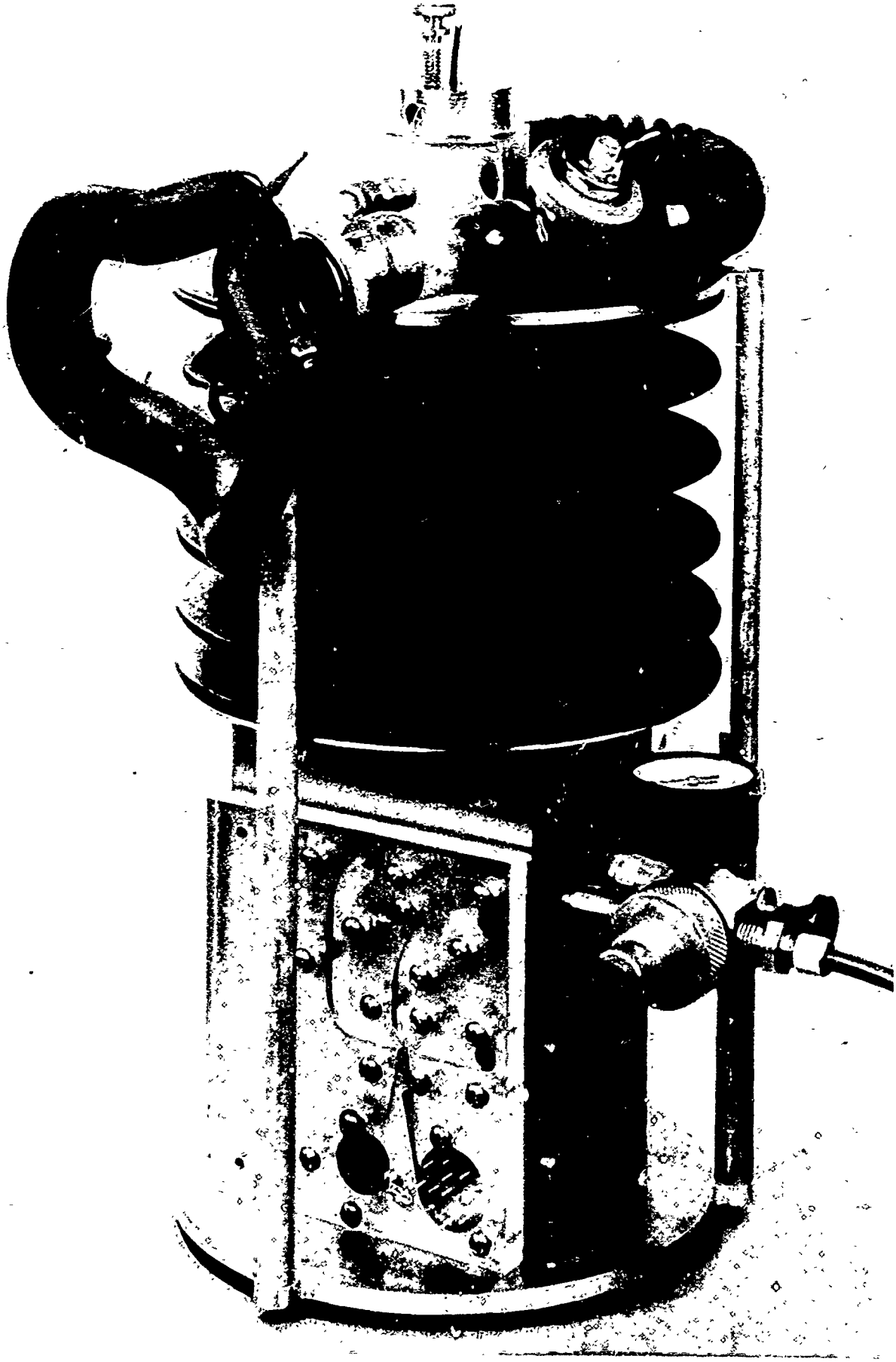

Figure 2. Volume-limited fluid amplifier respirator.

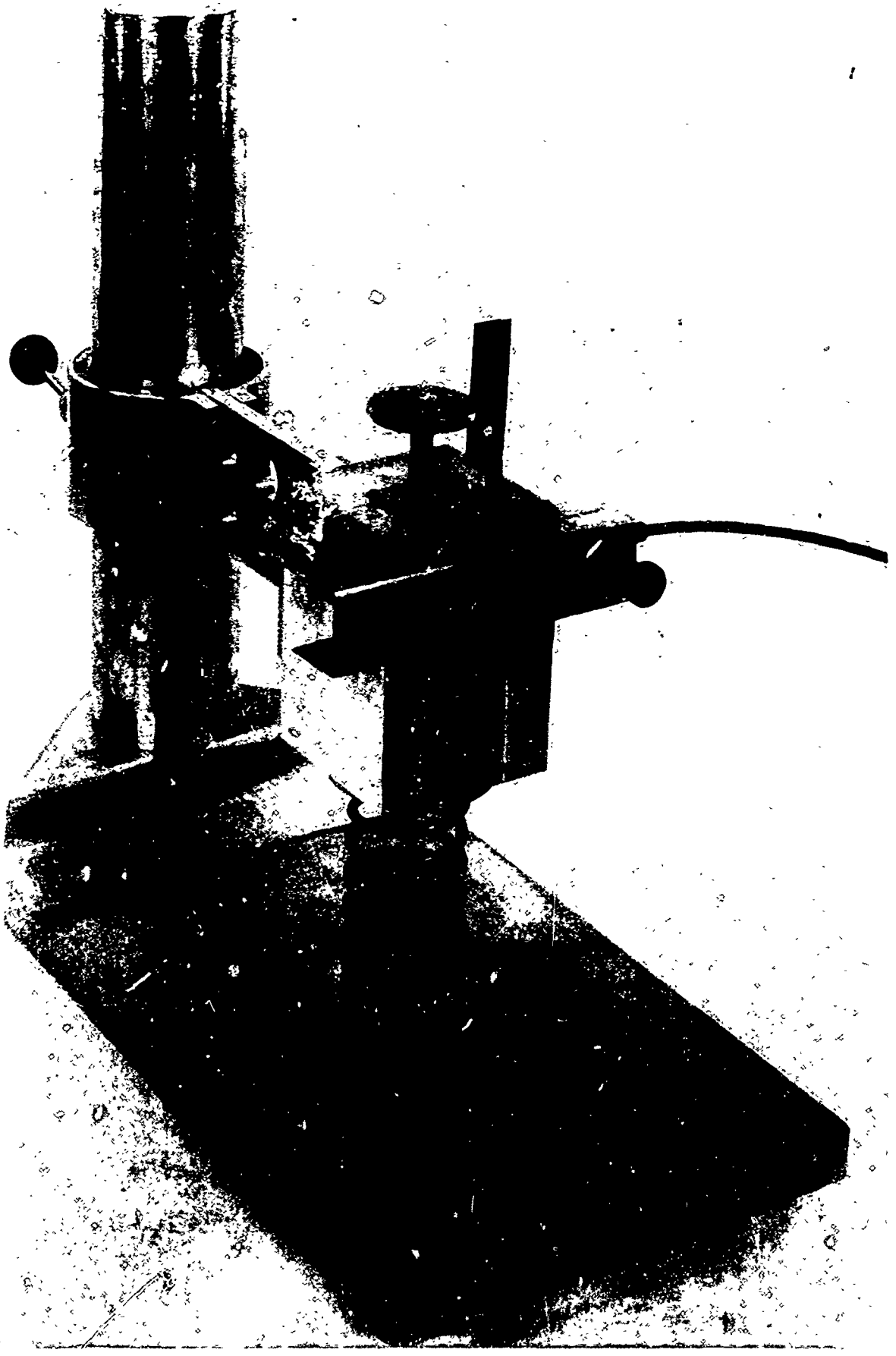

Figure 3. External cardiac compressor.

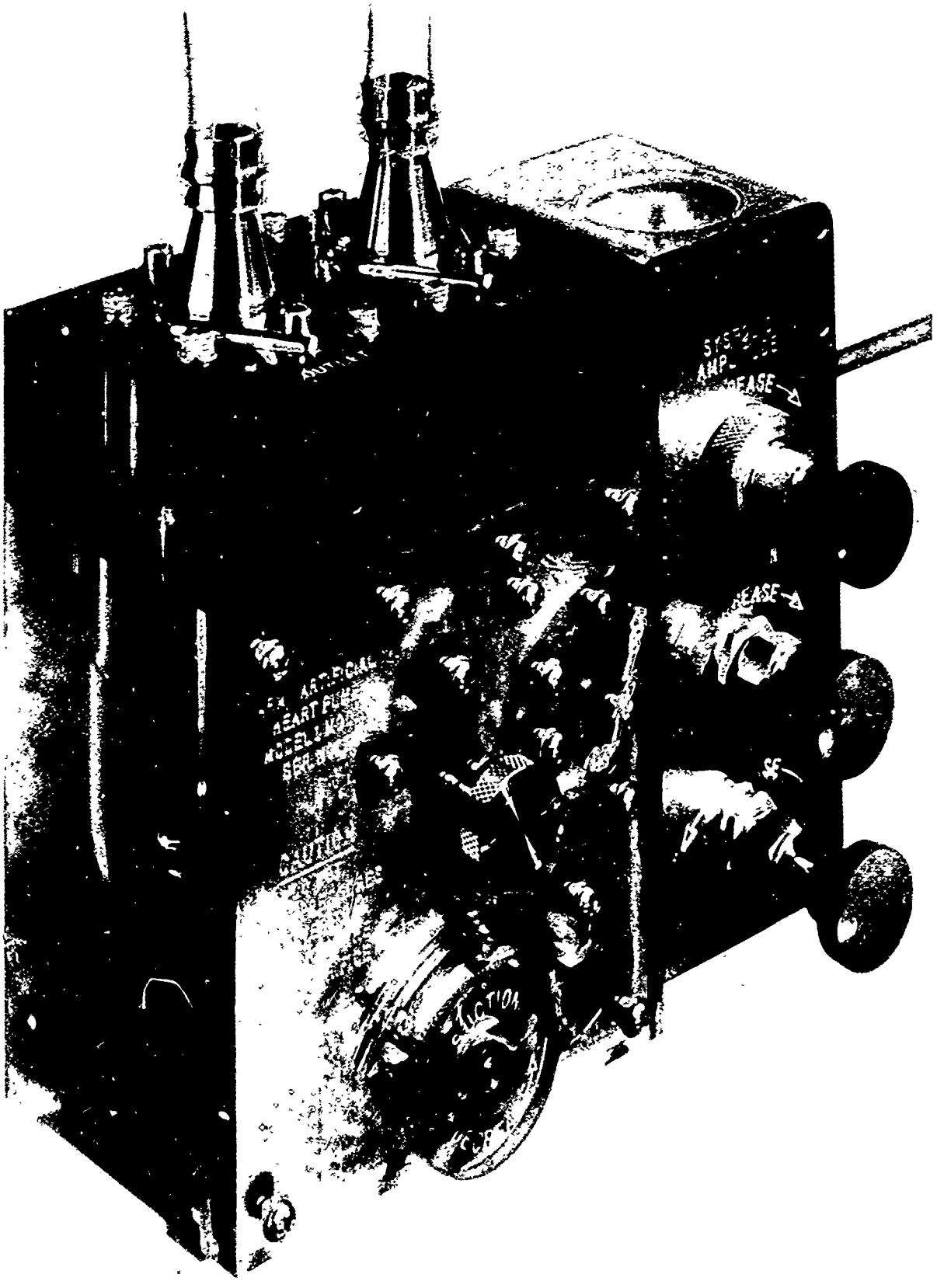

Figure 4. Army artificial heart pump.

CRANFIELD

DEPARTMENT OF PRODUCTION AND INDUSTRIAL ADMINISTRATION.

FLUID UNITS OF THE BALL VALVE TYPE AND THEIR APPLICATION TO THE CONTROL OF A MACHINE TOOL.

C.J. Charnley B.Sc., M.S.I.T. - Part I

R.E. Bidgood D.A.E., Grad.I.Mech.E. - Part II

Summary. The paper begins with a review of experimental work done at Cranfield into the characteristics and behaviour of ball valve switching devices and indicates the scope of the present investigations which are being sponsored by the Department of Scientific and Industrial Research.

Part II of the paper deals with the design and fabrication of a fluid logic control system for application to a step controlled grinding machine which is used for research at the College.

PART I.

Introduction.

The investigations leading to the applications outlined in this paper began as a student thesis (1) into fluid logic devices and their potential application to the control of machine tools. At the end of the thesis a report was prepared (2) on the basis of which a research grant for further investigation was awarded by the Department of Scientific and Industrial Research: the present paper outlines some of the work now proceeding with the aid of this contract..

From the findings of the review it was considered that the ball valve unit was likely to prove most suitable for application in the immediate future and it was decided to concentrate the research on this type of unit. Pure fluid units were kept in mind for application at a later stage when more research had been carried out into their behaviour and limitations.

Several models of the basic unit were constructed in perspex (see Plate I) and tests were conducted to determine the parameters governing their operation. The models illustrated used 3/32" (2.3 mm) diameter ball bearings, with variable switch path lengths, variable external resistances and supply pressures from 5 - 20 lb/in.^{2} gauge.

Some of the configurations used are shown schematically in fig. 1 with typical amplitude response curves illustrated on graphs I and II. The response curves shown do, in fact, give the circuit response times since the output pressure of the device was measured: the ball switch time was a negligible proportion of the circuit time constant. As might be expected a reduction in circuit resistance and capacitance as a result of miniaturisation, can lead to significant reduction in response time.

Limitations of the device are governed by the speed of sound within the circuit and the power output available, although in general it is felt that for most applications only small power outputs will be required, as the output signals can always be fed into some type of power amplifier. It would appear from preliminary investigations that tolerances of $\pm$ .001" (.025 mm) on most dimensions will be sufficient and that, provided reasonable care is taken with the air supply, small amounts of dirt or oil in the supply will not affect the operation. The main problem would appear to be that of obtaining an air tight seal between the ball and its seating.

Turning to the applications it was felt that there were four main areas where further research would be of value:-

1. Amplification of the output signals from the devices from pneumatic to higher power pneumatic, pneumatic to hydraulic, and pneumatic to electric.

2. Replacement of present methods of electro-pneumatic step control by completely pneumatic circuits.

3. Universal sequence control including the design of pneumatic limit switches, and an investigation of the problem of impedance matching complex circuits.

4. Investigation of tape input systems with pneumatic reading heads, for application to sequence controlled machine tools, and the development of continuously controlled systems.

The second application listed refers in particular to the methods used in cylindrical grinding operations. A considerable effort has been made at the College (3) to produce machined ground components to increasingly close tolerances on a production basis. As far as grinding is concerned the position has now been reached, with existing equipment, that a batch of 40 components can be produced to within $\pm$ 15 x 10^{-6} in. on a two minute time cycle.

The techniques and equipment used to obtain this degree of control are shown in fig II. The system operates on a closed loop basis with intermittent feedback at the pre-set tolerance bands. Measurement is by an air gauge (4) on the component during machining which is the best place to give optimum overall control. The recorder does not operate in the control loop, but is fitted to enable a continuous record to be kept of the operation and as a check on the performance of the control system. The control element converts the pneumatic signal into an electrical signal which is used to perform the required sequential logic operations and which in turn initiate the various rates of feed and finally withdraw the grinding wheel, in the operating sequence as illustrated in fig. III. The feed drive is by hydraulic cylinder and leadscrew, hence another conversion is required from the electrical output signal of the controller to a hydraulic signal.

The research undertaken to achieve a similar degree of control using fluid logic units is described in the second part of this paper.

PART II

Introduction.

This part of the paper is particularly concerned with the application of the Kearfott ball valve to a step controlled grinding machine and is an account of the difficulties experienced and practical results obtained.

During the research programme on the ball valve it was decided that after the initial evaluation some attempt should be made to design a proximity switch to enable direct application to machine tools. Figure 4 shows a simple proximity switch on which original tests were conducted; the ball will remain in the position shown until the restriction caused by the decrease in gap between the micrometer and orifice is large enough to switch the ball. When this occurs the pressure in line B will rise and give an output A variation of this circuit is the basic switch of the control system for the grinding machine. This particular set up would trigger repeatedly within a tolerance band of ± .0001".

Reasons why the step controlled machine was chosen have already been discussed and it has been shown that a case for control by fluid logic exists for this particular application.

The Studer Grinding Machine.

One of the first steps when designing the control was to write down all the basic operations as follows:-

a) Press the wheelhead fast traverse button; the wheelhead moves to a pre-set zero position.

b) Switch on the table traverse and the grinding wheel; the wheelhead coarse feed starts at the end of the table stroke.

c) The measuring apparatus signals that the required first size is reached and fine feed starts at the end of the stroke.

d) The measuring apparatus signals required second size and fine feed stops at end of the stroke.

e) Final size is acquired and the wheelhead retracts at the end of the stroke.

By minimising the above operations it was possible to construct a block diagram of the control system translated into logical terms; this is shown in figure 5. The next step was to interpret the block diagram in terms of the necessary ball valve units required to operate the machine; this is shown in figure 6. From the figure shown, when the fast traverse button A is pressed, air flows through units B and C and actuates the pneumatic ram; this will traverse the fast feed towards the work piece until the pre-set position is reached and unit B is triggered.

The grinding wheel is now started and the table traverse button E is pressed. This puts an input pulse into unit C and prevents any further operation of the fast traverse. Unit F is also triggered and allows a full supply pressure through to the coarse feed ram. The coarse feed will only operate at the end of each stroke, when unit H is triggered by limit switches at the extremities of the table. Grinding of the workpiece continues under coarse feed until a pulse from the limit switch signals a pre-set size; this triggers unit I and shuts off the coarse feed at the end of a stroke. Simultaneously units L and K are triggered which bring the fine feed into operation. The operation of this unit is similar to the coarse feed and again the machine continues cutting on a fine feed until a second pre-set size is reached and unit N is triggered. This cuts off the fine feed and a period of "spark-out" or dwell occurs until first size is reached and pressure is supplied to unit O.

Unit O is a bi-stable unit. When pressure is fed to the unit the ball remains in the position shown and low pressure results at output. However, when a signal from the limit switch at the end of the stroke is fed into the unit, the ball triggers and gives a high pressure at output, thus retracting the wheelhead on fast traverse. The ball will remain in the triggered position until the fast traverse button is pressed for a new cycle of operations.

The complete system for the control of the machine would require 12 small ball valve units, three high accuracy limit switches, one air measuring gauge and a small selection of on/off valves.

The advantages of this system are obviously largely economic as the expected failure rate is somewhat less than that of the present system. Also if plug-in connections are used between the units the system will be extremely easy to maintain.

The success or failure of such a system depends entirely on the repeatability and sensitivity of the high accuracy limit switches and therefore it was this part of the problem that has been tackled first.

Limit switches.

Fig. 7 shows the diagrammatic layout of the design chosen for the limit switches. This system was manufactured and tested, with and without the ten to one gain amplifier, for sensitivity and repeatability.

The most essential part of this subsystem is the air gauging unit and it is the sensitivity of this unit that ultimately determines the repeatability of the limit switch. One disadvantage of this arrangement is that the more sensitive it is the longer the time constant for a given pressure readout.

The performance of an air gauging system can be shown to be represented by:-

$$\frac{P_3 - P_a}{P - P_a} = \frac{1}{1 + \chi \frac{P_3}{P}\left(\frac{P_3 - P_a}{P - P_a}\right)\left(\frac{g}{cl}\right)^2}$$

where pressure values of P_3, P_1 P_a etc., are given in fig. 8. Now the sensitivity of the unit can be maximised by increasing the value of which can be shown to be =

$$16\frac{\beta^2}{\alpha^2}\cdot\frac{(D/d)^2}{(d_2/d)^4}\cdot\frac{C_g^2}{C^2}\cdot\frac{[1-(d_2/d_1)^4]}{[1-16(P/d)^2(g/d)^2(\frac{d}{d_1})^4]}$$

As β, α, C_g, C are sensibly constant for a particular configuration the main factors are D/d and d_2/d By increasing D/d and d_2/d the sensitivity can be increased considerably, however experience has shown that the D/d ratio cannot practically be increased above 2.

A series of control and measuring orifices were tested over a range of pressures to obtain the best results between $\frac{P_3-P_a}{P-P_a}$ = 0.3 -.85. A microvalve measuring head was also tested but the resultant sensitivity was poor and therefore rejected. The combination which produced the most satisfactory and sensitive results was using a .014" dia. control orifice with .125" dia. measuring orifice, D = 0.250 and supply pressure 5 lb/in^2. The performance curve for this unit is shown on graph (3) and shows an average sensitivity of $0.786\frac{P_3-P_a}{P-P_a}$ per thousandth of an inch. The problem of realising the full supply pressure at zero gap was increased when this configuration was used, due to the difficulty of arranging the measuring orifice normal to the face of the calliper gauge. It was for this reason that no units were tested to obtain higher sensitivity.

Having obtained a highly sensitive air gauging system a suitable ball valve was designed It was decided to design a ball valve with a maximum pressure gain of 4, where pressure gain has been defined as the ratio of the output amplitude achieved to the pressure required to achieve it. It can be shown (5) that the static gain of a monostable unit is given by

$$G_2 = \frac{A}{A_{S_2}}\cdot\frac{R_i/R_o}{[1+R_i/R_o]}$$

where A = area of bore

A_{S2} = area of seat shown

Ri = input resistance

Ro = output resistance

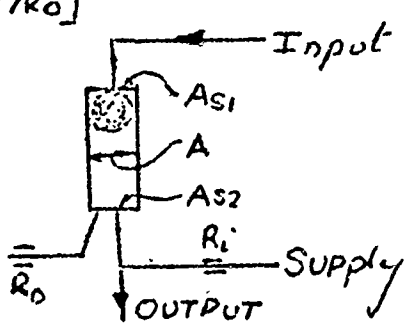

Now it was decided that a value R_i/R_o of not greater than 10 would be ideal, as when this increases then the circuit time constants increase. Now using the fact that the ratio of $G_1/G_2 \leq 1$ where $G_1 = AS_1/A \cdot R_i/R_o$ and also the fact that the bore diameter was to be 3/32" the respective seat areas were calculated.

A curve gain of maximum gain versus Ri/Ro is given on gr h (4) and shows the comparison between theoretical and practical results.

The rig already shown in fig. (7) was set up to test the repeatability with the designed air gauge and ball valve. This was done by simulating the grinding process by means of a motor driven micrometer screw, set to reduce the air gauge gap at grinding speed. The output from the final size limit switch was fed into a transducer, which in turn disengaged the motor drive at the switched condition. by this method it was possible to test the limit switch for the repeatability, by setting a pre-set gap (or size) at which the ball valve would trigger and cut off the drive, allowing the ball to switch, and repeating the process several hundred times. From the results obtained from the initial tests it was decided that an amplifier between the air gauge and ball valve would be necessary to produce a higher repeatability. The actual type used is a ten to one nozzle type amplifier. A summary of a series of tests is given on Table II with a schematic layout of the test rig in fig. 9. A histogram of the best results achieved is also shown on graph (5). This shows that the maximum tolerance band for a hundred readings was 10×10^{-6}in., the mean 0.7×10^{-6}in. and standard deviation 2×10^{-6}in.

Discussion and Conclusion.

There is a restricted but extremely important area of machine tool control that can be tackled using fluid logic devices. At first sight it may appear that the switching frequencies claimed are not very high, especially when compared with other published values; but the prime aim has been to obtain high positional switching accuracies. The frequency of operation required is set by the characteristics of the machine tool and machining operations; for relatively unsophisticated control units using only a few elements, high speed of operation is not particularly important. At this stage it is considered that miniaturisation will lead to sufficiently high speeds of operation to handle the applications envisaged in this report. It is felt at Cranfield that the immediate uses are in some cases only piecemeal applications where conventional techniques are not good enough, but at a later stage the ball valve and also the pure fluid unit could be integrated into the complete sequence control of a machine tool. There are many machine tools where the ball valve could be used quite easily with punched tape input, such as straight line milling and large radius contour grinding. These projects will be undertaken at Cranfield in the near future.

One important conclusion from the paper is, now that a method of switching is possible to a high degree of accuracy, then the problem of designing limit stops for machine tool slideways is reduced.

It is regretted that actual test results of the performance of the grinding machine are not available to be published at the symposium, but at the time of print the laboratory staff have not yet received all the parts necessary to fit to the machine. It is however, intended to issue a further paper at a later date with the machine tests results included.

Acknowledgements.

The authors would like to acknowledge Professor Loxham, Head of the Department of Production and Industrial Administration and the Department of Scientific and Inudstrial Research for help with this report.

References.

1. Bidgood R.E. — A technical assessment of fluid logic devices and their application to machine tools. (Student thesis 1963, College of Aeronautics).

2. C.J. Charnley and R.E. Bidgood — Fluid logic devices. A review. College of Aeronautics note H and P no. 1.

3. C.J. Charnley — The principles and application of size control in engineering manufacture. National Physical Laboratory Conference April 1962.

4. Evans J.C. — February 1957 I.P.E. Journal. The pneumatic gauging technique and its application to dimensional measurement.

5. Bidgood R.E. — An approximate assessment of the static and dynamic performance of the Kearfott Ball valve.

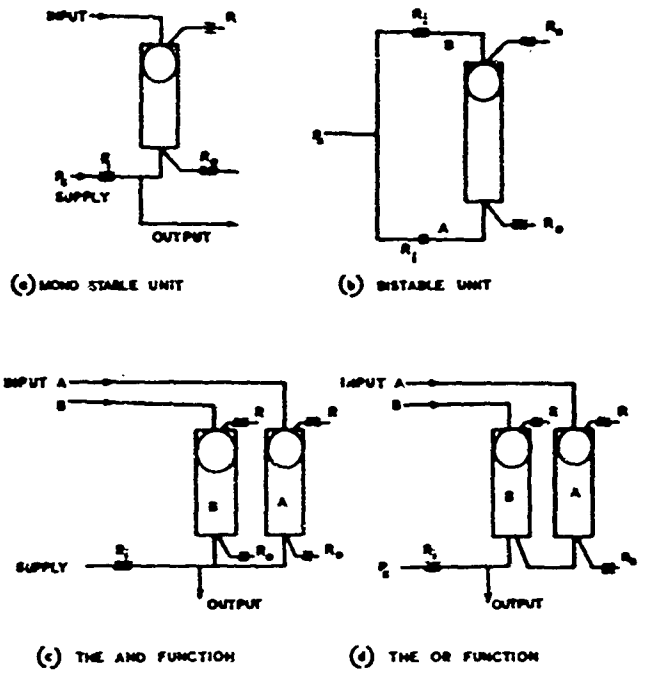

FIG.1 BALL VALVE CONFIGURATIONS.

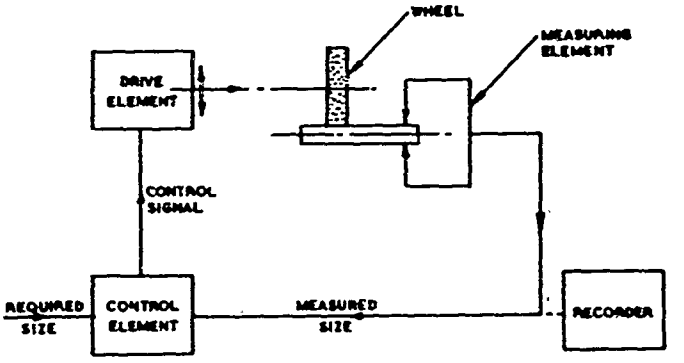

FIG.2. CLOSED LOOP SYSTEM.

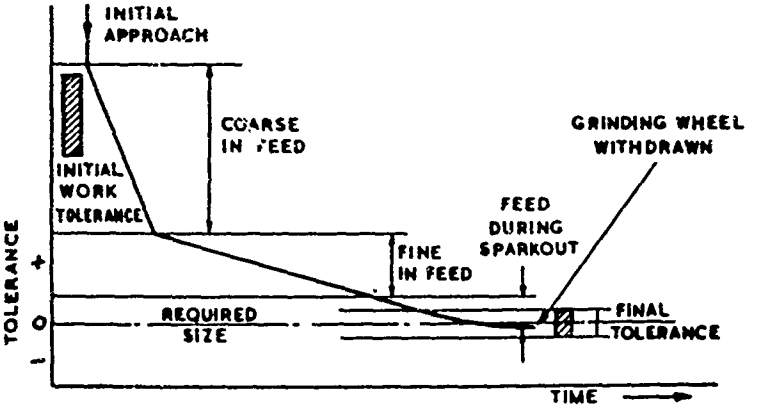

FIG.3. AUTOMATIC OPERATING PROCEDURE

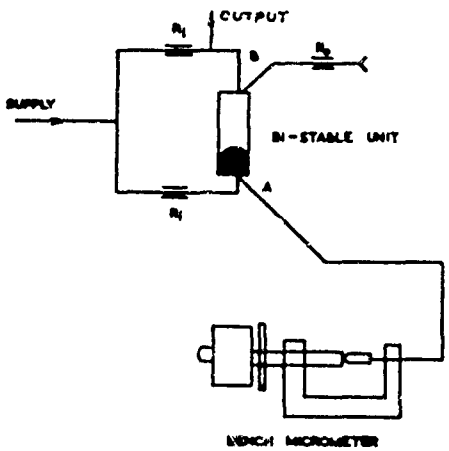

FIG. 4. LABORATORY SET UP OF A PROXIMITY SWITCH.

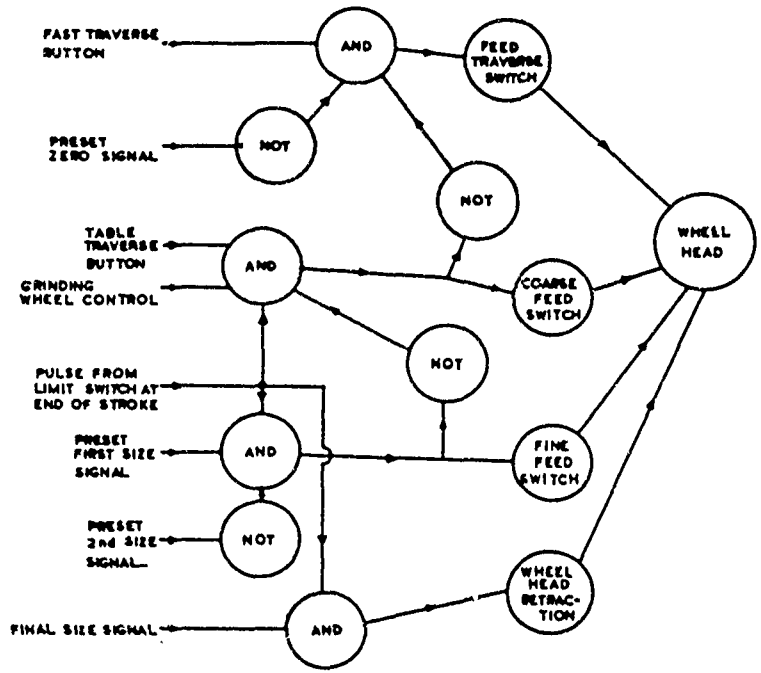

FIG. 5. LOGIC CIRCUIT FOR CONTROL OF THE STUDER CYLINDRICAL GRINDING MACHINE.

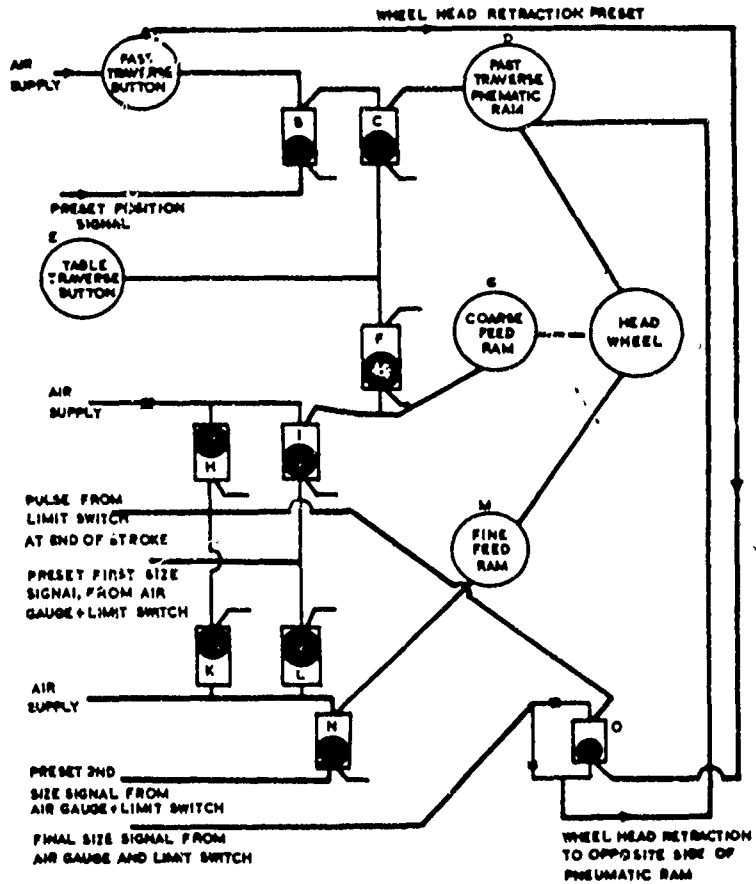

FIG. 6.

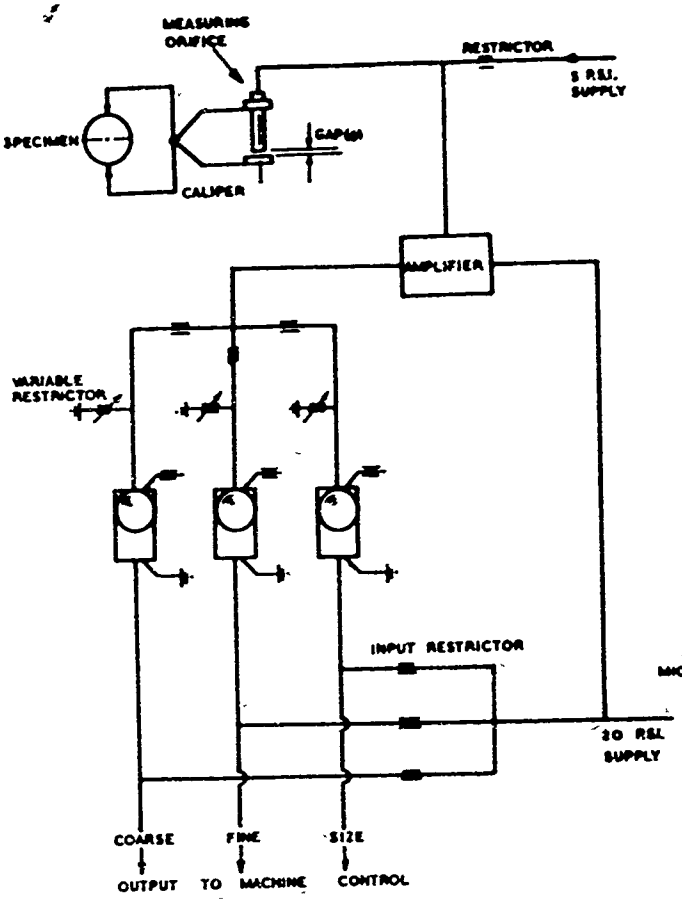

FIG.7. HIGH ACCURACY LIMIT SWITCH.

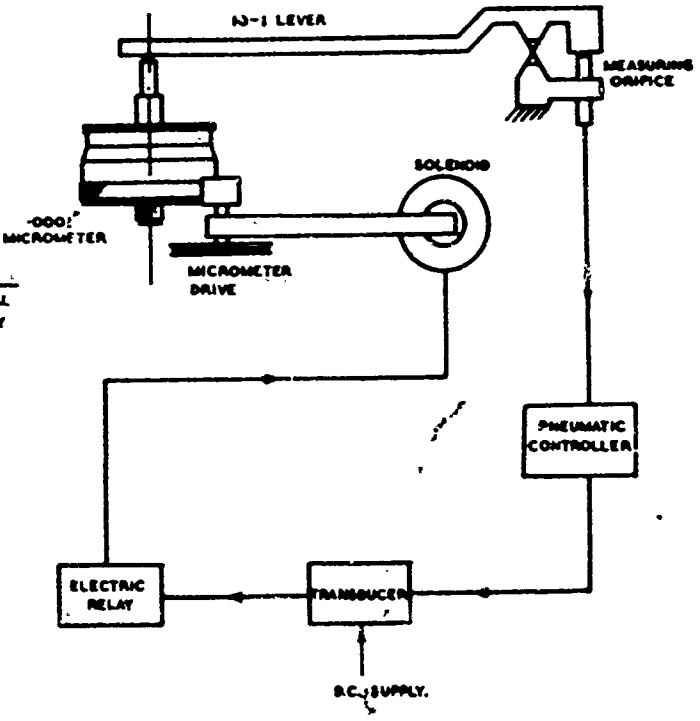

FIG.9. LABORATORY TEST RIG.

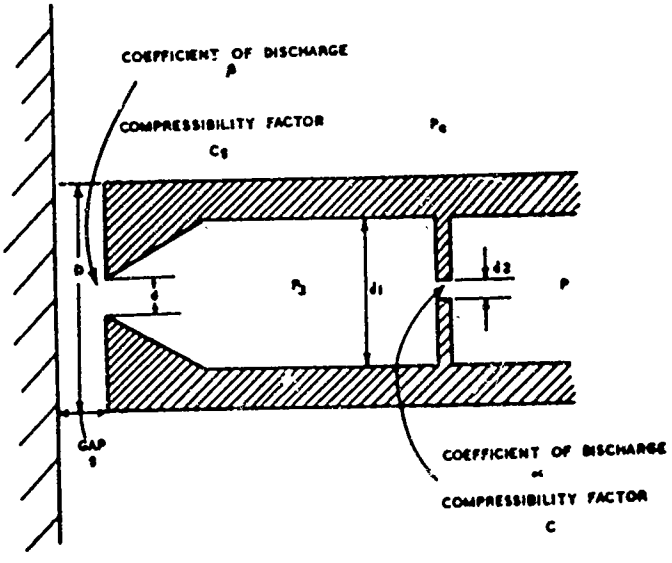

FIG.8. AIR GAUGING SYSTEM.

NOMINAL DIAMETER OF SPECIMENS = 0·9993 IN.
TABLE SPEED = 3 FT/MIN
WORK SPEED = 400 REV/MIN
AMOUNT OF MATERIAL REMOVED FROM DIAMETER = 0·0005 IN.
COARSE INFEED = 0 00013 IN AT 0·001 IN/MIN
FINE INFEED = 0·0003 IN. AT 0·0004 IN/MIN
SPARK OUT = 0·00007 IN.

PIECE NO.	VARIATION IN SIZE INCHES x 10^{-6}	
	BATCH A	BATCH B
1	0	+5
2	0	+5
3	0	0
4	+5	+10
5	+10	-10
6	+5	+15
7	+5	+15
8	+10	-15
9	-5	0
10	-5	0
11	0	0
12	-5	+15
13	0	-15
14	+10	-10
15	+5	+10
16	0	-5
17	-5	+10
18	0	+5
19	+10	-10
20	-10	-15

ROUNDNESS ERRORS: 5-8 x 10^{-6} IN.
SURFACE FINISH: 1 TO 1·2 x 10^{-6} IN. C.L.A. VALUE
STANDARD DEVIATION: ±8 x 10^{-6} IN.

TABLE I.

CONTROL ORIFICE	MEASURING ORIFICE	SUPPLY PRESSURE TO AIR GAUGE	SUPPLY PRESSURE TO UNIT	AMPLIFIER YES / NO	TOLERANCE BAND	MEAN FROM NOMINAL	STANDARD DEVIATION FROM MEAN
INS	INS	lb / IN^2	lb / IN^2		10^{-6}	10^{-6}	10^{-6}
014	·125	5	20	YES	10	0·7	2
·014	·125	5	20	NO	40	4·5	4·7
2" x ·026 CAPILLARY	·125	5	20	YES	15	8·25	3·27
0·14	·125	5	20	YES	—	2·25	6·26
0·14	·125	10	20	YES	—	5·2	7·8
0·14	·070	5	20	YES	10	2·45	6·7
0·14	·070	5	20	NO	55	4·05	2·89
0·14	·070	15	20	YES	40	8·55	11·1
0·14	0·70	15	15	YES	40	3·05	9·55
0·14	·070	15	20	NO	60	0·4	10·34

TABLE II

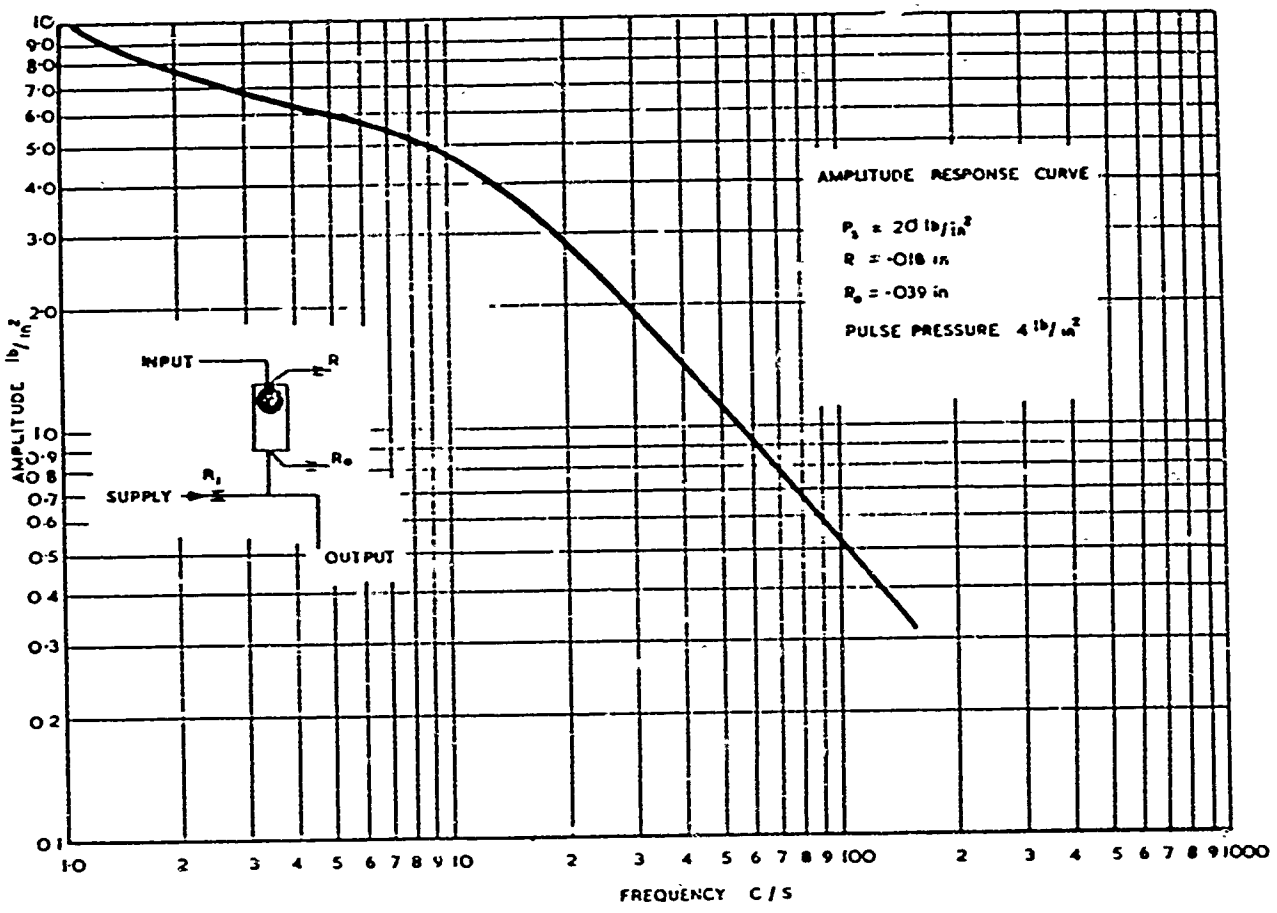

GRAPH 1. FORCED SWITCHING MONOSTABLE UNIT

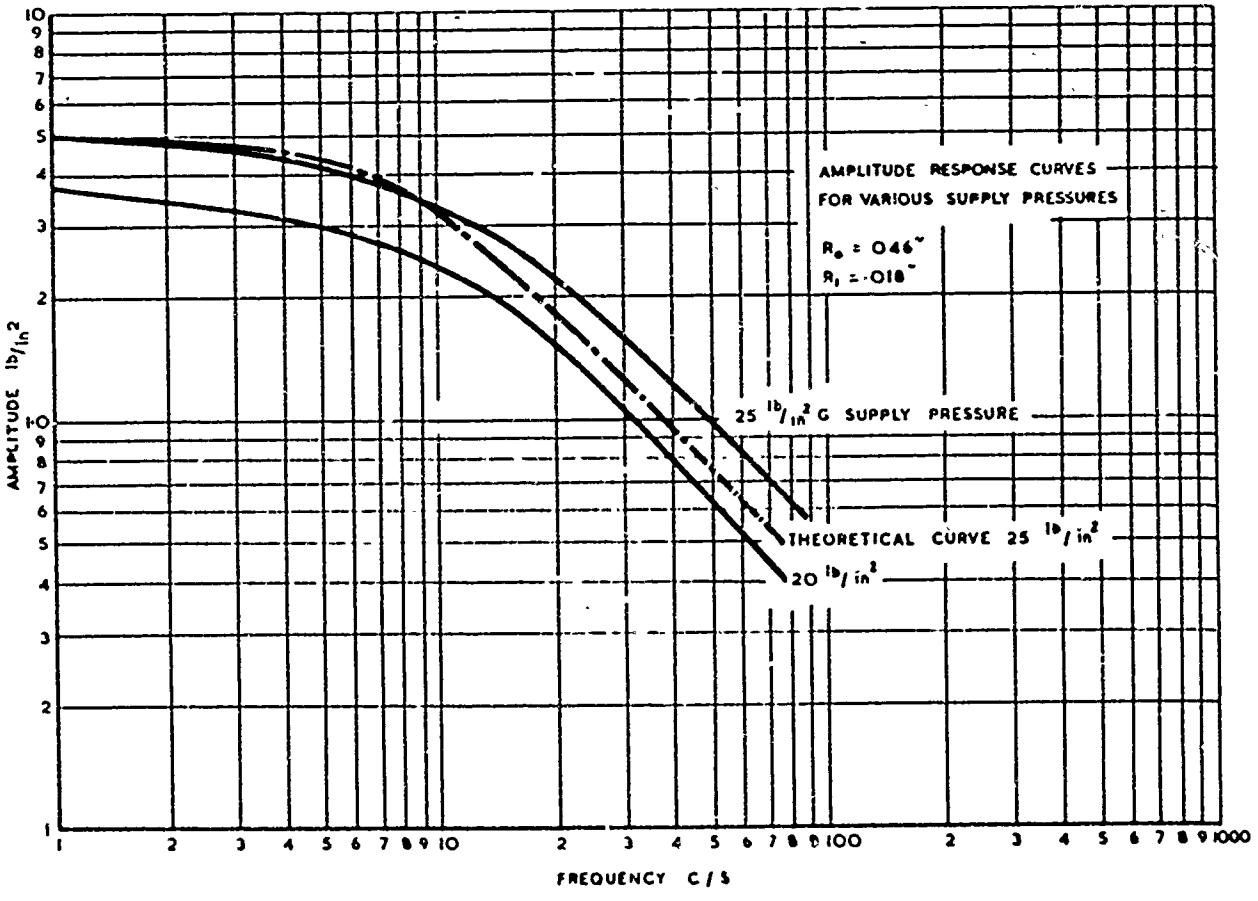

GRAPH II FORCED SWITCHING BI-STABLE UNIT.

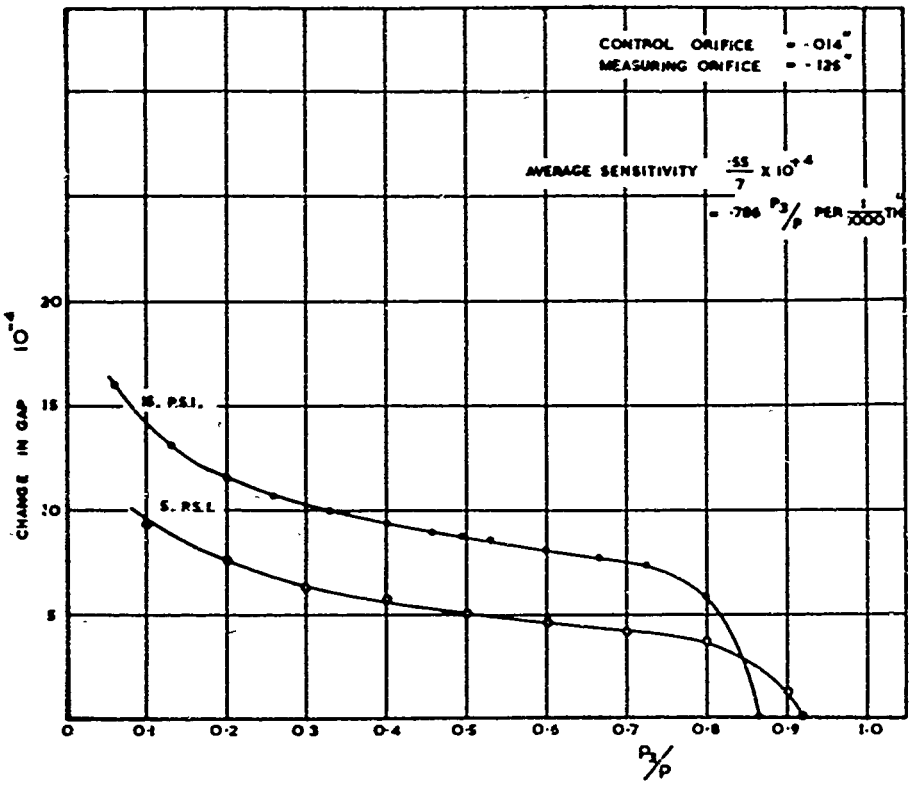

GRAPH III CURVE OF VARIATION IN BACK PRESSURE FOR CHANGE IN GAP

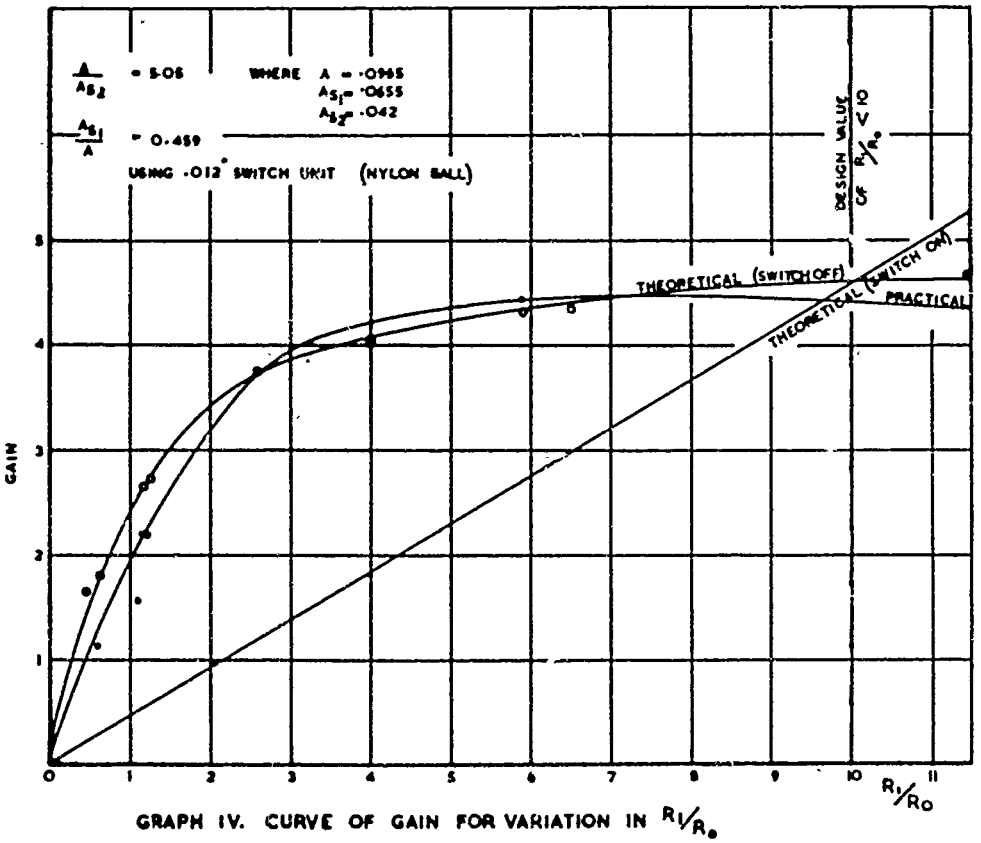

GRAPH IV. CURVE OF GAIN FOR VARIATION IN R_1/R_o

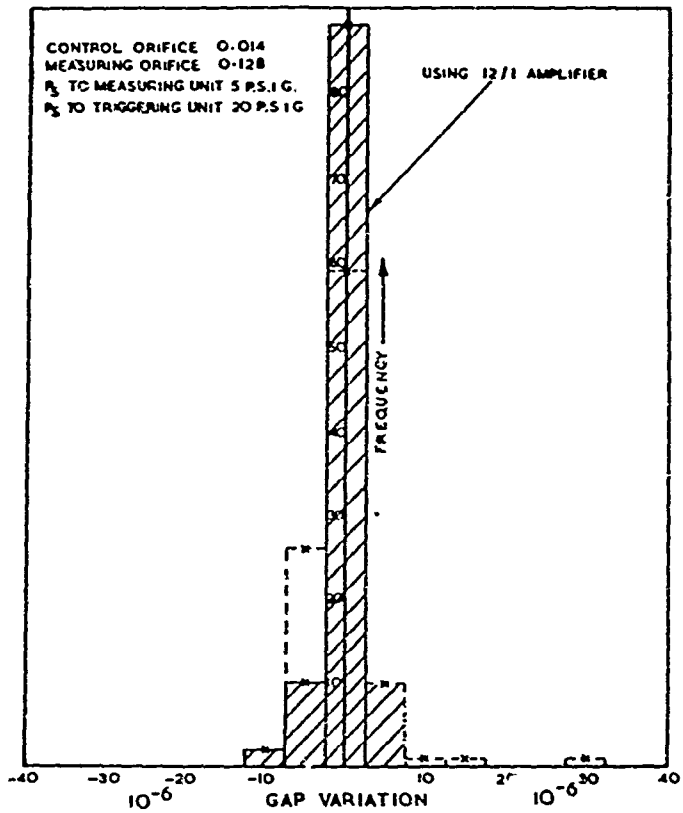

GRAPH V DISTRIBUTION OF REPEATABILITY TEST RESULTS

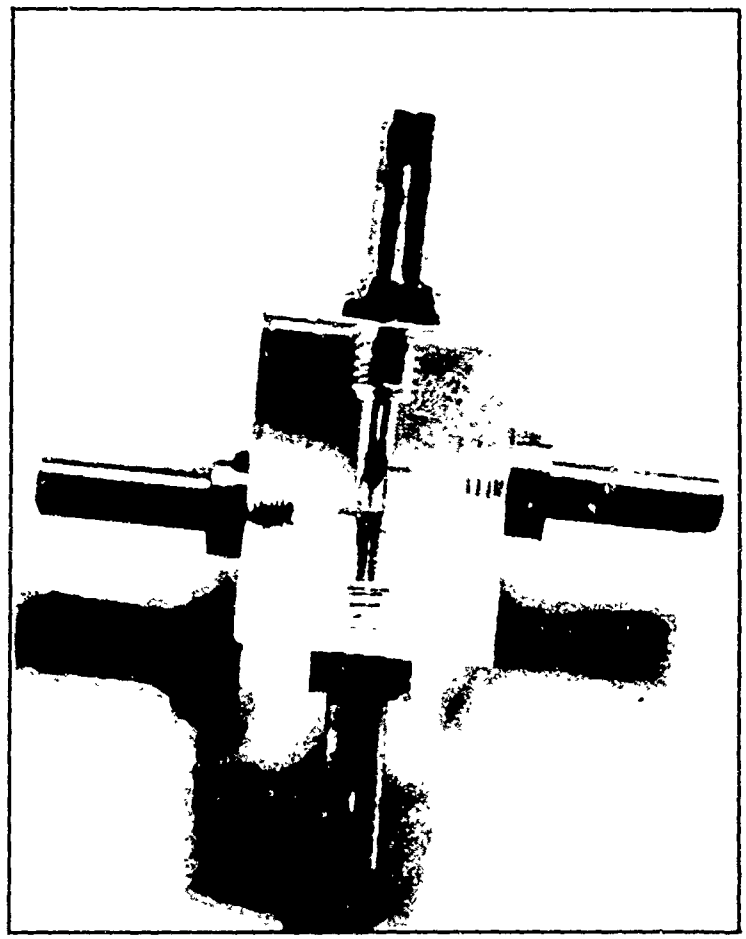

PLATE 1 BI-STABLE UNIT

Symposium Attendees' List

The College of Aeronautics Cranfield, Bletchley, Buckinghamshire England	C. J. Charnley R. E. Bidgood
Aerophysics Company 17 Dupont Circle Washington 6, D. C.	Dr. Gabriel D. Boehler
Air Force Aero Propulsion Laboratory Research and Technology Division Air Force Systems Command United States Air Force Wright-Patterson Air Force Base, Ohio 45433	Charles E. Bentz 2/Lt Stephen J. Przybylko
Air Force Avionics Laboratory Research and Technology Division Air Force Systems Command Wright-Patterson Air Force Base, Ohio 45433	Seth A. Young Ronald Ringo
Air Force Flight Dynamics Laboratory Air Force Systems Command United States Air Force Wright-Patterson Air Force Base, Ohio 45433	James F. Hall (AFFDL-FDCI) Harry Snowball(AFFDL-FDCI
Air Force Weapons Laboratory Research and Technology Division Air Force Systems Command United States Air Force Kirtland Air Force Base, New Mexico	Capt Charles V. Fada WLDCL 2/Lt William R. Cowherd WLC 2/Lt James K. Morrow WLDN-2
Airtronics, Inc. River Road Bethesda, Maryland	Robert Eidson
University of Alabama College of Engineering Department of Engineering Mechanics P. O. Box 6204 University, Alabama 35486	Dr. Harold R. Henry Dr. James D. Matheny
American Bosch Arma Corporation Springfield 7 Massachusetts	Charles F. Cartledge

Applied Physics Laboratory John Hopkins University 8621 Georgia Ave. Silver Spring, Md	Tom Rankin
Ampex Corporation 934 Charter Street Redwood City, California	Gerald Elsbach
University of Arkansas Technology Campus P. O. Box 3017 Little Rock, Arkansas	Paul C. McLeod
Auburn University School of Engineering Auburn, Alabama	Cornelius Shih
Automatic Controls Division Barber-Colman Company 1300 Rock Street Rockford, Illinois	Irving C. Erickson
Avco-Radiation Lab. 201 Lowell Street Wilmington, Mass	L. Fusegni R. Coulombre
Aviation Electric Ltd P. O. Box 2140, St. Laurent Montreal 9, P. Q, Canada	William F. Hayes Hugh A. Raymond
Bailey Meter Company Wickliffe Ohio, 44092	V. J. Melville J. A. Danvic
Barry Controls Division of Barry Wright Corporation 700 Pleasant Street Watertown 72, Massachusetts	Richard D. Cavanaugh
Battelle Memorial Institute 505 King Avenue Columbus, Ohio	Raymond E. Hess

Beckman Instruments, Inc.
Scientific & Process Instruments Division
2500 Harbor Boulevard,
Fullerton, California

Jerry E. Rochte

Bell Telphone Laboratories, Inc.
Murray Hill
New Jersey 07971

A. Zinnes
F. L. Howland

The Bendix Corporation
Friez Instrument Division
Baltimore 4, Maryland

P. D. Evanoff
Dr. Frederick K. Davey

The Bendix Corporation
Bendix Products Aerospace Division
South Bend 20, Indiana

G. R. Howland
R. M. Salemka
D. J. Schaffer

The Bendix Corporation
Research Laboratories Division
ATTN: L. B. Taplin, Dynamic Controls Dept.
Southfield, Michigan

Endre A. Mayer (Author)
Paul Maker (Author)
L. B. Taplin
C. B. Sung
K. W. Dowling

Societe Bertin & Co.
35 Rue Auguste Buisson
La Garenne Colombes (Seine)

M. Kadosch
C. Plavin

Mechanical Engineering Dept.
The University of Birmingham
Birmingham, 15, England

K. Foster

Boonshaft and Fuchs Inc.
Hatboro Industrial Park
Hatboro, Penssylvania

J. C. Boonshaft

Bowles Engineering Corporation
9347 Fraser Street
Silver Spring, Md

R. Bowles
E. Dexter
P. Bauer
R. Humphrey
F. Manion
E. Metzger
C. DiCamillo
E. Sowers
R. Jones
J. Colston
W. O'Neill
M. Schweiger
S. D. Wills

Bowmar Instrument Corporation
8000 Bluffton Road
Fort Wayne, Indiana

Howard P. Barry, Jr.

Bowmar (Local Office):
9 Lincoln Ave., P. O. Box 31
Rutherford, N. J.

F. Jack Hartley

University of Bridgeport University Avenue Bridgeport, Connecticut	Willard P. Berggren
Brown Engineering Company, Inc. P. O. Drawer 917 Huntsville, Alabama	Wayne Vaught
University of California Lawrence Radiation Laboratory P. O. Box 808 Livermore, California	George I. Boyadjieff
Carnegie Institute of Technology Schenley Park Pittsburgh 13, Pennsylvania	John A. Brighton
Case Institute of Technology University Circle Cleveland 6, Ohio	Dr. Charles K. Taft James N. Wilson Ralph Turnquist Peter Orner Albert Weiss Phillip Koerper Isaac Greber
Caterpillar Tractor Co. Controls & Fluid Mechanics Division Peoria, Illinois 61611	W. H. Belke, Div. Manager
Catholic University of America Mechanical Engineering Department 620 Michigan Avenue, N. E. Washington, D. C.	Dr. Paul Chang William Kelnhofer
Chandler Evans Corporation Charter Oak Boulevard West Hartford 1, Connecticut	A. M. Wright Jay I. Black
Chrysler Corporation Missile Division P. O. Box 2628 Detroit 31, Michigan	Richard T. Cronin
The Cincinnati Milling Machine Co. Marburg Avenue Cincinnati 9, Ohio U.S.A. 45209	Mr. Graham A. Parker

Clarkson College Pottsdam, N. Y.	Gerald Schrader
Controls Company of America 2450 North 32nd Street Milwaukee 45, Wisconsin	R. W. Sloane
Controls & Fluid Mechanics Division Caterpillar Tractor Company Peoria, Illinois	Fred D. Proksch
Cornell Aeronautical Laboratory, Inc. Of Cornell University P. O. Box 235 Buffalo, New York, 14221	F. Dell"Amico O. F. Giombini
Corning Glass Works Electronic Research Laboratory 3800 Electronics Dr. Raleigh N. C. 27604	W. F. Gesell Lawrence W. Langley
Corning Glass Works Corning Bradford Plant, Bradford, Penna	Robert W. Van Tilburg Whitney L. Cochran Robert H. Bellman Richard A. O'Brien
Control Engineering 330 West 42nd Street, New York, N. Y.	Edward J. Kompass
Curtiss-Wright Corporation Curtiss Division Caldwell, New Jersey	J. H. Sheets
Cutler-Hammer Airborne Instruments Laboratory Melville, Long Island, New York	Dr. Berthold Zarwyn
Delavan Manufacturing Company Grand Avenue and Fourth St. West Des Moines, Iowa	Roger W. Tate Richard L. Wilcox
Department of the Army Bureau of Ships Washington 25, D. C.	Marvin D. Martin Code 632 Arthur Chaikin " 341
Department of the Navy Office of Naval Research Washington, D. C. 20360	Stanley W. Doroff ONR:438:YSH

Department of the Navy U. S. Naval Ordnance Test Station China Lake, California 93557	L. Kielman R. Gilbertson
Design Penton Building Cleveland, Ohio 44113	Melvin E. Long
Douglas Aircraft Co. Santa Monica, California	H. W. Lenczyk
Duke University College of Engineering Durham, North Carolina	C. M. Harman, Ph. D.
Dupont E. I. Du Pont De Nemours & Co 1309 Noble Street Philadelphia 23, Pa	Dr. Gerd W. Michel
Dupont E. I. Du Pont De Nemours & Co, Incorporated Wilmington, Delaware 19898 Engineering Department	Dominick Gigliotti Van D. Sherrill
Emerson Electric of St. Louis Electronics and Space Division 8100 Florissant Ave. St. Louis 36, Mo	Harry D. Nelgner John F. Hynes
Engineering Research Swift & Company Packers & Exchange Ave. Chicago, Illinois	Paul Lucas
University of Florida Chemical Engineering Dept. Gainesville, Florida	Frank P. May
Ford Instrument Co. 31-10 Thomsen Ave. Long Island City 1, New York	John Woodruff
The Foxboro Company Neponset Avenue Foxboro, Mass.	Dr. Frederick D. Ezekiel

Francis Associates Inc. Consulting Engineers Barnabas Road Marion, Mass 02738	Samuel A. Francis Thayer Francis
The Franklin Institute Electrical Engineering Division Philadelphia 3, Pa	C. W. Hargens K. C. Tsui C. A. Belsterling
General Dynamics P. O. Box 748 Fort Worth 1, Texas	W. M. Rowell
General Dynamics/ Astronautics Kearney Villa Road San Diego, California, MZ 528-30	J. E. Stumm
General Electric Company One River Road Schenectady, New York 12305	W. A. Boothe Dr. J. N. Shinn C. G. Ringwall W. T. Rauch
General Electric Company Missile and Armament Department Lakeside Avenue Burlington, Vermont	Richard Ziemba
General Kinetics Incorporated 2611 Shirlington Road Arlington, Va	Alfred E. Roberts, Jr.
General Precision Inc. Aerospace Group (Kearfott) 808 - 17th St. N. W. Washington 6, D. C.	Dr. Albertus E. Schmidlin
The Geotechnical Corporation 3401 Shiloh Road Garland, Texas	Charles J. Grimland Robert F. McMurray
Giannini Controls Corporation Astromechanics Research Division 179 Lancaster Ave. Malvern, Pennsylvania	Howard A. Curtiss Melvin B. Zisfein Otto G. Feil David J. Liquornik
Goodyear Aerospace Corporation Akron 15, Ohio	Edward W. McGraw
GM Engineering Staff General Motors Corporation General Motors Technical Center Warren, Michigan	George R. Smith Jerome B. York

Holley Carburetor Company Automotive and Aviation Accessories 11955 E. Nine Mile Road Warren, Michigan	Edward K. Ranke Paul M. Douglas
Honeywell Regulator Co. Aeronautical Division, ATTN: R. W. Mueller 2600 Ridgway Road Minneapolis 40, Minnesota	N. McQueen E. G. Zoerb R. J. Reilly F. A. Moynihan N. C. Sher R. A. Evans E. G. Johnson J. H. Lindahl J. W. Franks
Honeywell Minneapolis-Honeywell Regulator Co. Aeronautical Division 13350 U. S. Highway 19, St. Petersburg, Florida	Dr. I. H. Rubaii Thomas Anspach
Honeywell Minneapolis-Honeywell Regulator Co. California Ordnance Center 1200 East San Bernardino Road West Covina, California	Rubein Tucker
Honeywell Ordnance Division 600 North 2nd Street Hopkins, Minnesota	Erick Tromburg
Hydraulic Research and Manufacturing Co. 2835 North Naomi Street Burbank, California	L. F. Griffith
Hydro-Aire Division 3000 Winona Ave. Burbank, Calif.	Dr. J. S. Anderson William H. Gibson
IBM Boardman Road Poughkeepsie, New York	Vladimir Nejeschled
IBM Electric Typewriter Division Lexington, Kentucky 40507	William F. Voit, Jr.

IBM General Products Division Development Laboratory P. O. Box 6 Endicott, New York 13764	Robert R. Schaffer Tom Saghafi R. E. Norwood
IBM Research Laboratory Saumerstrasse 4 Ruschlikon Zh, Switzerland	H. H. Glaettli H. R. Mueller
IIT Research Institute Technology Center 10 W. 35th Street Chicago 16, Illinois	Dennis W. Prosser Michael J. Fisher Roy Kamo
University of Illinois Department of Theoretical and Applied Mechanics College of Engineering 212 Talbot Laboratory Urbana, Illinois	Professor J. M. Robertson
Institute for Defense Analyses 1666 Connecticut Avenue, N. W. Washington 9, D. C.	W. E. Bradley
Johnson Service Company 507 East Michigan Street Milwaukee 1, Wisconsin	Bjorn G. Bjornson Thomas J. Lechner Paul H. Sorenson Harris M. Sullivan
Kenett Corporation P. O. Box 55 275 Needhma St. Newton, Mass. 02164	Julius Kendall
Kollsman Instrument Corporation 80-08 45th Ave. Elmhurst 73, New York	George Leon Bleckman
The Library of Congress Reference Department Science and Technology Division Washington D. C. 20540	I. Bruce Blankenhorn
Lockheed Missiles & Space Company Huntsville Research & Engineering Center P. O. Box 1103 West Station Huntsville, Alabama	Kenneth M. Alder

LTV Vought Aeronautics Division P. O. Box 5907 Dallas, Texas 75222	Jess N. Beberstein
Lycoming Division of Avco Corporation Stratford, Connecticut	Mel Feinstein
University of Maine Boardman Hall Mechanical Engineering Department Orono, Maine	Robert A. Comparin
Marlboro Research Corporation Box 144, Maspeth 78 Long Island, New York	Leonard Weiss
The Marquardt Corporation 16555 Saticoy Street Van Nuys, California	B. A. Otsap D. J. Nelson W. H. Henley
Martin Company Orlando Division Orlando, Florida	E. F. Richards W. L. Matthes
University of Maryland College of Engineering College Park, Md	Allen A. Bowers Donald S. Gross Phillip W. Eckles
Maryland University Institute for Fluid Dynamics and Applied Mathematics College Park, Md	Professor S. I. Pai Professor John Weske
Massachusetts Institute of Technology Department of Mechanical Engineering Cambridge 39, Mass.	F. T. Brown S. Y. Lee K. N. Reid
Mattel, Inc. Toymakers 5150 Rosecrans Avenue Hawthorne, California	H. N. Unfried
The University of Michigan College of Engineering Department of Mechanical Engineering Ann Arbor, Michigan	Professor Arthur Hansen Charles Perry
Milwaukee School of Engineering Fluid Power Institute 1025 N. Milwaukee St. Technology Park Milwaukee 1, Wisconsin	Russel W. Henke
Moog Servocontrols, Inc. Electro Hydraulic Servomechanisms Proner Airport, East Aurora, New York	Kenneth D. Garnjost

Moore Products Co. Spring House, Pa	Robert B. Adams David B. Kirk
NASA Automatic Control Section Mail Stop 350 Langley Field Hampton, Virginia	Harry Fuller H. D. Garner
NASA National Aeronautics and Space Administration George C. Marshall Space Flight Center Huntsville, Alabama	William T. White Jerry A. Peoples
NASA National Aeronautics and Space Administration Lewis Research Center 21000 Brookpark Road Cleveland 35, Ohio	Kirby W. Hiller
National Cash Register Co. Dayton Ohio	Douglas Clancy
National Research Council Ottawa 2 Canada	J. W. Tanney
National Water Lift Company A Division of Pneumodynamics Corporation 2220 Palmer Ave. Kalamazoo, Michigan	Ted R. Scarff
The University of Nebraska Department of Engineering Mechanics Lincoln 8, Nebraska	Dr. Turgut Sarpkaya
Neptune Meter Company Neptune Research Laboratory Wallingford, Connecticut	Richard Y. Pei
C. A. Norgren Co Manufacturers of Pneumatic Products 3400 South Elati Street Englewood, Colorado	A. W. Dewberry
North American Aviation, Inc. Los Angeles Division ATTN: K. Snider, D/280-147 International Airport Los Angeles, California 90009	Gordon R. Toomey

Northern Research and Engineering Corporations 219 Vassar Street Cambridge 39, Mass	J. E. Smith Dr. A. D. Carmichael
Office of Naval Research Washington 25, D. C.	Dr. L. N. Morscher, Code 492
Office of the Commander British Navy Staff Main Navy Building, P. O. Box 165 Benjamin Franklin Station, Washington, D. C.	A. C. Law, Scientific Adviser
Oklahoma State University School of Mechanical Engineering Stillwater, Oklahoma, 74075	Dr. Glen Zumwalt
Pegann Air Inc. P. O. Box 3497 Glendale 1, California	Ralph J. Havens
The Pennsylvania State University 213 Mechanical Engineering Bldg. University Park, Pennsylvania, 16802	D. P. Margolis J. C. Tamulis R. G. Cunningham
Philco Corporation M 250-20 Aeronutronic Division Ford Road Newport Beach, California	Tetsuo Nakamura Warren F. Kaufman
Pitney-Bowes Inc. Walnut and Pacific Streets Stamford, Connecticut	Dr. George T. Croft Brooks Lyman,
Pratt & Whitney Aircraft Division of United Aircraft Corporation 400 Main Street, East Hartford, Connecticut	William Gardner
RADIO Corporation of America Defense Electronic Products Camden 2, New Jersey	Herman Knoll

Ranco Incorporated Ranco Research Columbus, Ohio	S. S. Fineblum
Rocketdyne Dyanmic Control Group North American Aviation 6633 Canoga Ave. Canoga Park, California	S. V. Gunn Sherwood E. Milleman Charles Margion
Rutgers, The State University College of Engineering Department of Mechanical Engineering University Heights Campus New Brunswick, New Jersey 08903	R. H. Page W. G. Hill, Jr.
Sandia Corporation Sandia Base Albuquerque, N. M. 87115	George V. Lemmon Samuel B. Martin, Jr. Robert P. Stromberg Thomas H. Martin
The Sheffield Corporation Dayton 1, Ohio	Carl Goth
The Singer Company 400 East Main Street Denville New Jersey Cnetral Research Laboratory	Shen Ling
A. O. Smith Corporation P. O. Box 584 Milwaukee, Wisconsin	Alfred Rynning
South Eastern Editor Design News 1819 John F. Kennedy Boulevard Philadelphia, Pennsylvania	Margaret Maas
Spark Plug The Electronic Division of General Motors Engineering Building P. O. Box 1002 Flint 1, Michigan	Kenneth G. Leslie
Sperry Rand Research Center North Road (Rt 117) Sudbury, Massachusetts	Dr. Robin E. Esch
Sperry Utah Co. Salt Lake City, Utah	F. R. Goldschmied H. L. Fox R. L. Blosser

Supramar AG Lucerne/Switzerland U.S. Office: 1300 Connecticut Ave. N. W. Suite 301 Washington 6, D. C. 20036	W. H. G. Fitzgerald
Tapco-Roanoke Laboratories Thompson Ramo Wooldridge Inc. Rocky Mount, Virginia	Walter M. Evans Robert J. Anderson
Taylor Instrument Companies 95 Ames St., Rochester 1, N. Y.	Dr. Paul F. Pagerey Howard R. Jaquith
Technik Incorporated 50 Jericho Turnpike Jericho, New York	Melvin Zaid Howard Jaslow
Tulane University Department of Mechanical Engineering New Orleans, La 70118	Larry N. Pearce H. F. Hrubecky
Union College Mechanical Engineering Schenectady 8, New York	Prof. Joseph Modrey Prof. W. Aubrey
United Aircraft Corp. Hamilton Standard Div. Windsor Locks, Connecticut	F. Richard Emmons Aldo Peracchio
United Aircraft Corporation Research Laboratories East Hartford 8, Connecticut	Robert E. Olson Thomas J. Mueller David P. Miller C. Edward Kepler A. W. Blackman
United Kingdom Scientific Mission British Embassy 3100 Massachusetts Ave. N. W. Washington 8, D. C.	Harry K. Bourne
Univac Division of Sperry Rand Corp. P. O. Box 500 Blue Bell, Pa	M. Jacoby E. R. Phillips T. D. Reader Dr. T. F. Chen T. A. Shock R. S. Gluskin

U. S. Army Frankford Arsenal Philadelphia, Pa	Robert A. Shaffer Frank Luke
U. S. Army Limited War Laboratory Aberdeen Proving Ground Maryland 21005	Col Joseph T. Brown 023969 Cap Don M. Stotser 069370
Hq. U. S. Army Materiel Command	E. M. Graham
Hqs. U. S. Army Materiel Command Development Division R&D Dir. ATTN: AMCRD-DS Washington 25, D. C.	Harold Jersin Bob Hall Ed Sedlak Walt Morowski Roger Ragowski Gil Rosenberg
Hq. U. S. Army Materiel Command Research Division, R & D Directorate ATTN: Major Walter T. Kerttula Washington 25, D. C.	Major W. Kerttula
Headquarters U. S. Army Missile Command AMSMI-RGC Redstone Arsenal, Alabama 35809	J. C. Dunaway V. H. Ayre W. A. Griffith T. G. Wetheral
U. S. Army Transportation Research Command Manned Aircraft Fort Eustis, Virginia	George Fosdick
United States Atomic Energy Commission Washington 25, D. C.	Frank C. Legler Div. of Reactor Development
U. S. Naval Ordnance Laboratory White Oak Silver Spring, Maryland	David L. Blanchard Norman Czajkowski
U. S. Naval Ordnance Test Station Pasadena Annex 3202 E. Foothill Blvd. Pasadena 8, California	J. T. Bartling J. D. Brooks

United States Navy Marine Engineering Laboratory Annapolis, Maryland - 21402	Mr. Donald R. Laster Mr. Guy Johnson
U. S. Patent Office Patent Group 430 Commerce Building Washington 25, D. C.	Martin P. Hoffman Ronald L. Panitch Leo Smilow
U. S. Patent Office Group 360 Washington 25, D. C.	Samuel Scott
United States Army Picatinny Arsenal Office of the Commanding Officer Dover, New Jersey, 07801	George Demitrack Alexander Janushevich Ib. Berg Frederick Soechting Paul Sadlon William Lehman
Van Schwartz and Associates, Inc. Specialists in Research & Developm 2250 Western Federal Bldg. Denver, Colorado	Zolly C. Van Schwartz
Vickers Incorporated Division of Sperry Rand Corporation Administrative and Enineering Center Detroit 32, Michigan	A. H. Delmege R. R. Reinke
Vickers Incorporated Crooks and Maple Road Troy Michigan	W. Hunley
Washington Technological Associates, Inc. 979 Rolling Ave. Rockville, Md	Walter G. Wadey
Wayfield Research and Development Company 225 Liberty Ave.. West Islip, Long Island,New York, 11795	David J. Wayfield
Wayne State University College of Engineering Department of Engineering Mechanics Detroit 2, Michigan	Professor C. C. Perry

The Weatherhead Company 300 East 131st Street Cleveland 8, Ohio	Gene Bahniuk
Western Electric Aerospace Division Mail Stop 496 Box 746 Baltimore Md, 21203	John C. Mentzell
Westinghouse Electric Corporation Research and Development Center Pittsburgh 35, Pa Beulah Rd, Churchill Boro Pittsburgh 35, Penna.	L. R. Allen W. O. Osbon
Weston-Borg-Warner 7500 Tyrone Ave. Van Nuys; California	William Frantz Donald W. Irwin
University of Wichita School of Engineering Department of Aeronautical Engineering Wichita 8, Kansas	David B. Howes
Mechanical Engineering Department College of Engineering The University of Wisconsin Madison 6, Wisconsin	John Bollinger
Fluid Logic Control Systems 456 Riverside Dr. New York 27, N. Y. 10027	Raymond N. Auger
Stanford Research Institute Controls Systems Laboratory Menlo Park, California	John J. Eige
Whittaker Controls and Guidance 9601 Canoga Ave. Chatsworth, California	R. Denker

DISTRIBUTION

Office of the Dir. of Defense
Research and Engineering
The Pentagon, Washington 25, D. C.
Attn: Tech Library (Rm 3C128)

Director
Advanced Research Projects Agency
Washington 25, D. C.
Attn: Fred A. Koether

C. A. Lejonhud
D.C.N.C. (Development)
Op-07T8
The Pentagon (Rm5E621)
Washington 25, D. C.

Director, Army Research Office
Office, Chief of R & D
Washington 25, D. C.
Attn: Library

Department of the Army
Office of the Chief of R & D
Washington 25, D. C.
Attn: Chief, Combat Material Div.

Director, Special Weapons
Office of the Chief of R & D
Department of the Army
Washington 25, D. C.

Department of the Army
Office, Chief of R & D
Physical Science Div
Washington 25, D. C.
Attn: Dr. R. B. Watson

Commanding General
Army Materiel Command
Washington 25, D. C.
Attn: R & D Directorate, AMCRD-RS-CM
AMCRD-DE-MI
AMCRD-DE-N
AMCRD-RS, Major W. Kerttula

Commanding General
Army Munitions Command
Dover, New Jersey
Attn: Technical Library

Commanding Officer
U.S. Army Munitions Command
Frankford Arsenal
Philadelphia 37, Pennsylvania
Attn: Library, 0270

Commanding Officer
Aberdeen Proving Ground, Md.
Attn: J. A. Tolen

Commanding Officer
U.S. Army Limited War Lab.
Aberdeen Proving Ground, Md.
Attn: Lt. Col. J. T. Brown

Commanding Officer
Picatinny Arsenal
Dover, New Jersey
Attn: Tech Library (3 cps)
SMUPA-VA6

Commanding Officer
U.S. Army Biological Lab
Fort Detrick
Frederick, Maryland

Commanding General
U.S. Army Engineer Research & Dev Lab.
Fort Belvoir, Virginia
Attn: Tech Library
Attn: Office of Patents, R. Lucke

Army Security Agency
Arlington Hall Station
Arlington 12, Virginia
Attn: OACS DEV (OBJ-Div)

Commanding Officer
Army Research Office - Durham
Box CM - Duke Station
Durham, N. C.

DISTRIBUTION (Continued)

Commanding Officer
Artillery Combat Dev Agency
Fort Sill, Okla.

Redstone Scientific Info Center
U.S. Army Missile Command
Redstone Arsenal, Alabama
Attn: Chief, Document Section
(10 copies)

Commanding General
U. S. Army Missile Command
Redstone Arsenal, Alabama
Attn: Charles Schriener
Bldg 7446

Commanding General
U.S. Army Weapons Command
Technical Information Branch
Rock Island, Ill.

Commanding Officer
U.S. Army Weapons Command
Springfield Armory
Springfield, Mass.
Attn. TIU

Commanding Officer
U.S. Army Materials Research Agency
Watertown Arsenal
Watertown 72, Mass.
Attn: Tech Info Center

Commanding General
White Sands Missile Range
White Sands, New Mexico
Attn: Tech Library

Army Mathematics Research Center
University of Wisconsin
Madison 6, Wisconsin
Attn: Librarian

Commanding Officer
Watervliet Arsenal
Watervliet, New York
Attn: Tech Library B-C

Department of the Navy
Bureau of Naval Weapons
Washington 25, D. C.
Attn: S. J. Gorman, RRRE-31

Director
U.S. Naval Research Laboratory
Washington 25, D. C.
Attn: Code 2027

Office of Naval Research
Washington 25, D. C.
Attn: Code 492, Dr. Morscher

Department of the Navy
Chief, Bureau of Ships
Washington 25, D. C.
Attn: Code 210L, 442, 632

Commander
U.S. Naval Ordnance Laboratory
Corona, Calif.
Attn: Tech Library

Commander
Naval Ordnance Laboratory
White Oak, Silver Spring, Maryland
Attn: B. Gilbert

Commander
U.S. Naval Ordnance Test Station
China Lake, Calif.
Attn: Tech Library

Commandant
U.S. Marine Corps
Washington 25, D. C.
Attn: Code A04F

DDC Headquarters
Cameron Station, Bldg 5
5010 Duke Street
Alexandria, Virginia
Attn: TISIA (20 copies)

Mr Pervy Griffin
CIA Headquarters
Langley, Virginia
143-7671

Aeronautical Systems Division
Wright-Patterson AFB, Ohio
Attn: ASRMOD (Mr. M. Shorr)
Attn: ASRMC-ZO (Mr. Wible)

Aeronautical Systems Division
Avionics Laboratory
Wright Patterson AFB, Ohio
Attn: ASRNG-1

Aeronautical Systems Division
Propulsion Laboratory
Wright Patterson AFB, Ohio
Attn: ASRMP-1 (Mr. Bentz)

Air Force Special Weapons Center
Kirtland Air Force Base
Albuquerque, New Mexico
Attn: Tech Library - SW01

Commander
Air Proving Ground Center
Eglin AFB, Florida
Attn: Library APGC(PGAPI)

Commander
Edwards Air Force Base, Calif.
Attn: M. Jones AFTTC (FTOOT)

Sandia Corporation
Sandia Base
Albuquerque, New Mexico
Attn: Tech Library

U.S. Atomic Energy Commission
Space Nuclear Propulsion Office
Washington 25, D. C.
Attn: F. C. Schwenk

U.S. Atomic Energy Commission
Washington 25, D. C.
Attn: Library

Oak Ridge National Lab
P.O. Box Y
Oak Ridge, Tennessee
Attn: Technical Library Y-12

Los Alamos Scientific Laboratory
P.O. Box 1663
Los Alamos, New Mexico
Attn: Reports Librarian

Marshall Space Flight Center
Huntsville, Alabama
Attn: Roy Currie (R-ASTR-TN)
Attn: Dr. Walter P. Krause

Scientific & Technical Info Facility
P.O. Box 5700
Bethesda, Maryland
Attn: NASA Representative
(S-AK/DL)-A366

National Aeronautics & Space Agency
Lewis Research Center
Cleveland 35, Ohio
Attn: K. Hiller

Library of Congress
Science & Technology Div.
Washington 25, D. C.

National Bureau of Standards
Washington 25, D. C.
Attn: Chief, Sec. 14.01

National Bureau of Standards
Boulder, Colorado
Attn: Tech Library

Patent Office
Washington 25, D. C.
Attn: Scientific Library
Acquisitions, Rm 1886-C
Attn: Group 220, R. Stahl
Attn: Group 360, W. O'Dea
Attn: Group 370, R. Nilson
Attn: Group 430, M. Hoffman
Attn: Miss Steddom

Armour Research Foundation of
Illinois Inst. of Tech.
Chicago 16, Illinois
Attn: George I. Jacobi
10 W. 35th Street

Franklin Institute of the State of Pennsylvania
Philadelphia 5, Pennsylvania
Attn: C. W. Hargens, Tech Dir
Attn: Charles A. Belsterling

Johns Hopkins University
Applied Physics Lab
8621 Georgia Avenue
Silver Spring, Maryland
Attn: Tech Library (2 copies)

University of Maryland
College Park, Maryland
Attn: W. Sherwood, College of Aero Engineering
Attn: Dr. Donald S. Gross, Director,Wind Tunnel
Attn: Dr. S. Pai

University of Southern California
University Park
Los Angeles 7, California
Attn: Library

University of California
Engineering Library
405 Hilgard Avenue
Los Angeles 24, California
Attn: Mr. J. Tallman

Cornell Aeronautical Laboratories
P.O. Box 235
Buffalo, New York
Attn: Librarian

New York University
Engineering Library
University Heights
Bronx 53, New York

Arizona State University
Measurement Engr. Lab. Library
Engineering Center
Tempe, Arizona

University of Minnesota
St. Anthony Falls Hydraulic Lab
Mississippi River at 3rd Ave S. E.
Minneapolis, Minnesota 55414

Purdue University
Mechanical Engineering Library
Mechanical Engineering Building
West Lafayette, Indiana

Wichita State University
Documents Department
Wichita 8, Kansas
Attn: Library

Johnson Service Company
507 East Michigan Street
Milwaukee 1, Wisconsin
Attn: Thomas J. Lechner

Purdue University
West Lafayette, Indiana
Attn: Librarian

Carnegie Institute of Technology
Pittsburgh, Pennsylvania
Attn: Technical Library
Attn: Dr. E. M. Williams

University of California
Engineering Library
Berkeley 4, California

Cornell University
Ithaca, New York
Attn: Dr. Ed Resler, Jr.

Engineering Societies Library
345 East 47th Street
New York 17, New York

Illinois Institute of Technology
Research Institute
10 West 35th Street
Chicago, Illinois
Attn: Mr. Roy Kamo

Worcester Polytechnic Institute
Worcester, Massachusetts 01609
Attn: Library

DISTRIBUTION (Continued)

Mass. Inst. of Technology
Dept of Mech. Engineering
Cambridge, Mass.
Attn: J. L. Shearer - B
Rm 3-453

Manhattan College
Riverdale 71, New York
Attn: Technical Library

Fairleigh Dickenson University
Teaneck, New Jersey
Attn: Engineering Library

University of Michigan
Institute of Science & Technology
Ann Arbor, Michigan
Attn: Tech Documents Serv (Box 618)

Ohio State University
M.E. Department Library
206 W. 18th Ave
Columbus 10, Ohio

University of New Mexico
Albuquerque, New Mexico
Attn: Dr. A. H. Koschmann

Case Institute of Technology
Pittsburgh, Pennsylvania
Attn: E. M. Williams

Catholic University
Department of Mech Engineering
Washington, D. C.
Attn: Prof. P. K. Chang

University of Nebraska
Lincoln 8, Nebraska
Attn: Prof. T. Sarpkaya

Oklahoma State University
Stillwater, Oklahoma
Attn: Dr. Glen Zumwalt

New York State University
School of Engineering
6 Chemistry Road
Buffalo 14, N. Y.
Attn: Tech Library

Rutgers University
University Library
New Brunswick, N. J.
Attn: Dr. D. F. Cameron

University of Arizona
Physics Department
Tucson, Arizona
Attn: Prof. Ulrich H. Bents

Linda Hall Library
5109 Cherry Street
Kansas City 10, Mo.
Attn: Joseph C. Shipman

Ohio State University
1858 Neil Avenue
Columbus 10, Ohio
Attn: Documents Division

Pennsylvania State University
201 Hammond Bldg
University Park, Pennsylvania 16802
Attn: Engineering Librarian
Attn: David P. Margolis

University of Notre Dame
Notre Dame, Indiana
Attn: Prof F. N. M. Brown
Dept of Aeronautical Eng

Minneapolis-Honeywell Regulator Co.
Military Products Group Research Dept
2600 Ridgway Rd. Mail Station 340
Minneapolis, Minnesota

NASA
Langley Research Center
Langley Station
Hampton, Virginia
Attn: Tech Library

Horton, B. M./Hochmuth, M. S., Lt. Col.
Apstein, M./Gerwin, H. L./Guarino, P. A./Kalmus, H. P.
Hardin, C. D., Lab 100
Sommer, H., Lab 200
Hatcher, R. D., Lab 300
Hoff, R. S., Lab 400
Nilson, H., Lab 500
Flyer, I. N., Lab 600
Campagna, J. H., Div 700
DeMasi, R., Div 800
Landis, P. E., Lab 900
Seaton, J. W., 260
Kirshner, J., 310 (50 copies)
Garver, R. V., 250
Harris, F. T., 320
Technical Reports Unit, 800
Technical Information Office, 010 (5 copies)
HDL Library (5 copies)
Rotkin, I./Godfrey, T. D./Bryant, W. T.
Distad, M. F./McCoskey, R. E./Moorhead, J. G.
Bonnell, R., 040

1 copy each to all persons listed on pages 195-211